

Ministry of Education and Science of the Russian Federation
Saint Petersburg National Research University of Information
Technologies, Mechanics, and Optics

NANOSYSTEMS:
PHYSICS, CHEMISTRY, MATHEMATICS

2017, volume 8(5)

Наносистемы: физика, химия, математика

2017, том 8, № 5



NANOSYSTEMS:

PHYSICS, CHEMISTRY, MATHEMATICS

ADVISORY BOARD MEMBERS

Chairman: V.N. Vasiliev (*St. Petersburg, Russia*),
V.M. Buznik (*Moscow, Russia*); V.M. Ievlev (*Voronezh, Russia*), P.S. Kop'ev (*St. Petersburg, Russia*), N.F. Morozov (*St. Petersburg, Russia*), V.N. Parmon (*Novosibirsk, Russia*),
A.I. Rusanov (*St. Petersburg, Russia*),

EDITORIAL BOARD

Editor-in-Chief: I.Yu. Popov (*St. Petersburg, Russia*)

Section Co-Editors:

Physics – V.M. Uzdin (*St. Petersburg, Russia*),
Chemistry, material science – V.V. Gusarov (*St. Petersburg, Russia*),
Mathematics – I.Yu. Popov (*St. Petersburg, Russia*).

Editorial Board Members:

V.M. Adamyan (*Odessa, Ukraine*); O.V. Al'myasheva (*St. Petersburg, Russia*);
A.P. Alodjants (*Vladimir, Russia*); S. Bechta (*Stockholm, Sweden*); J. Behrndt (*Graz, Austria*);
M.B. Belonenko (*Volgograd, Russia*); V.G. Bepalov (*St. Petersburg, Russia*); J. Brasche (*Clausthal, Germany*);
A. Chatterjee (*Hyderabad, India*); S.A. Chivilikhin (*St. Petersburg, Russia*); A.V. Chizhov (*Dubna, Russia*);
A.N. Enyashin (*Ekaterinburg, Russia*), P.P. Fedorov (*Moscow, Russia*); E.A. Gudilin (*Moscow, Russia*);
V.K. Ivanov (*Moscow, Russia*), H. Jónsson (*Reykjavik, Iceland*); A.A. Kiselev (*Madison, USA*); Yu.S. Kivshar (*Canberra, Australia*);
S.A. Kozlov (*St. Petersburg, Russia*); P.A. Kurasov (*Stockholm, Sweden*); A.V. Lukashin (*Moscow, Russia*);
V.A. Margulis (*Saransk, Russia*); I.V. Melikhov (*Moscow, Russia*); G.P. Miroshnichenko (*St. Petersburg, Russia*);
I.Ya. Mittova (*Voronezh, Russia*); H. Neidhardt (*Berlin, Germany*); V.V. Pankov (*Minsk, Belarus*); K. Pankrashkin (*Orsay, France*);
A.V. Ragulya (*Kiev, Ukraine*); V. Rajendran (*Tamil Nadu, India*); A.A. Rempel (*Ekaterinburg, Russia*);
V.Ya. Rudyak (*Novosibirsk, Russia*); D. Shoikhet (*Karmiel, Israel*); P. Stovicek (*Prague, Czech Republic*);
V.M. Talanov (*Novocherkassk, Russia*); A.Ya. Vul' (*St. Petersburg, Russia*); A.V. Yakimansky (*St. Petersburg, Russia*), V.A. Zagrebnev (*Marseille, France*).

Editors:

I.V. Blinova; A.I. Popov; A.I. Trifanov; E.S. Trifanova (*St. Petersburg, Russia*),
R. Simoneaux (*Philadelphia, Pennsylvania, USA*).

Address: University ITMO, Kronverkskiy pr., 49, St. Petersburg 197101, Russia.

Phone: +7(812)232-67-65, **Journal site:** <http://nanojournal.ifmo.ru/>,

E-mail: popov1955@gmail.com

AIM AND SCOPE

The scope of the journal includes all areas of nano-sciences. Papers devoted to basic problems of physics, chemistry, material science and mathematics inspired by nanosystems investigations are welcomed. Both theoretical and experimental works concerning the properties and behavior of nanosystems, problems of its creation and application, mathematical methods of nanosystem studies are considered.

The journal publishes scientific reviews (up to 30 journal pages), research papers (up to 15 pages) and letters (up to 5 pages). All manuscripts are peer-reviewed. Authors are informed about the referee opinion and the Editorial decision.

CONTENT

MATHEMATICS

- Yu.Kh. Eshkabilov, F.H. Haydarov
Lyapunov operator L with degenerate kernel and Gibbs measures 553

PHYSICS

- G. Alber, A.V. Chizhov
Spectral properties of spontaneous photon emission by a material two-level system in a parabolic cavity 559
- D.S. Golovina, S.A. Chivilikhin
Reproduction of the evolution of the liquid front profile in inhomogeneous nanoporous media 567
- S.Y. Liashko, I.S. Lobanov, V.M. Uzdin, H.Jónsson
Thermal stability of magnetic states in submicron magnetic islands 572
- A.S. Sarycheva, A.A. Semenova, E.A. Goodilin
Vapor phase SERS sensor based on mesoporous silica decorated with silver nanoparticles 579
- I.S. Lobanov, M.N. Potkina, H. Jónsson, V.M. Uzdin
Truncated minimum energy path method for finding first order saddle points 586
- A.I. Mikhailov, V.F. Kabanov, N.D. Zhukov, E.G. Glukhovskoy
Features of the energy spectrum of indium antimonide quantum dots 596
- R. Soorat, K. Madhuri, A. Vudayagiri
Random number generator for cryptography 600
- S. Saini, Y.D. Sharma
The effect of vertical throughflow in Rivlin-Ericksen elastico-viscous nanofluid in a non-Darcy porous medium 606
- S.V. Smirnov, M.S. Kulya, A.N. Tcypkin,
S.E. Putilin, V.G. Bespalov
Detection of the polarization spatial distribution of THz radiation generated by two-color laser filamentation 613
- ## CHEMISTRY AND MATERIAL SCIENCE
- A.A. Krasilin, V.V. Gusarov
Redistribution of Mg and Ni cations in crystal lattice of conical nanotube with chrysotile structure 620

A.Yu. Polyakov, V.A. Lebedev, L. Yadgarov, E.A. Goodilin Two facile routes for functionalization of WS₂ nanotubes with silver nanoparticles	628
V.G. Zavodinsky, O.A. Gorkusha, A.P. Kuz'menko Energetics of carbon nanotubes with open edges: Modeling and experiment	635
S.S. Moliver Modeling chemisorption of carbon dimer at (8,0) nanotube	641
A. Bachina, V.A. Ivanov, V.I. Popkov Peculiarities of LaFeO₃ nanocrystals formation via glycine-nitrate combustion	647
A.G. Kyazim-zade, V.M. Salmanov, A.G. Huseynov, R.M. Mamedov, A.A. Salmanova, F.Sh. Ahmedova Nonlinear optical and quanta-dimensional effects in monoselenide of gallium and indium	654
S.S. Nath, A. Ganguly, G. Gope, M.R. Kanjilal SnO₂ quantum dots for nano light emitting devices	661
M.N. Nikolaeva, E.V. Gushchina, M.S. Dunaevskii, A.T. Dideikin, A.N. Bugrov, T.D. Anan'eva The influence of substrate material on the resistance of composite films based on reduced graphene oxide and polystyrene	665
A.A. Semenova, I.A. Semenova, A.P. Semenov, E.A. Gudilina, E.A. Goodilin Revisiting preparation routes of SERS materials	670
M.V. Talanov, V.M. Talanov Universal mechanism of tetrahedral metal cluster formation in structures with breathing pyrochlore sublattices	677
Information for authors	688

Lyapunov operator \mathcal{L} with degenerate kernel and Gibbs measures

Yu. Kh. Eshkabilov¹, F. H. Haydarov²

¹Karshi State University, Kashkadarya, Uzbekistan

²National University of Uzbekistan, Tashkent, Uzbekistan

yusup62@mail.ru, haydarov_imc@mail.ru

DOI 10.17586/2220-8054-2017-8-5-553-558

In this paper, we studied the fixed points of the Lyapunov operator with degenerate kernel, in which each fixed point of the operator corresponds to a *translation-invariant* Gibbs measure with four competing interactions of models with uncountable set of spin values on the Cayley tree of order two. Also, it was proved that Lyapunov operator with degenerate kernel has at most three positive fixed points.

Keywords: Cayley tree, Gibbs measure, translation-invariant Gibbs measure, Lyapunov operator, degenerate kernel, fixed point.

Received: 11 September 2017

Revised: 6 October 2017

1. Introduction

The existence of Gibbs measures for a wide class of Hamiltonians was established in the groundbreaking work of Dobrushin. A complete analysis of the set of limiting Gibbs measures for a specific Hamiltonian is a difficult problem. Also, Spin systems on lattices are a large class of systems considered in statistical mechanics. Some of them have a real physical meaning, others are studied as suitably simplified models of more complicated systems [1,2].

The Ising model is an important model in statistical mechanics. The various partial cases of Ising model have been investigated in numerous works. For example, In [3] and [4], the exact solutions of an Ising model with competing restricted interactions with zero external field was presented. Also, it was proved that there are two translation-invariant and uncountable number of distinct non-translation-invariant extreme Gibbs measures and considered Ising model with four competing interactions on the Cayley tree of order two (see [5–7]). In [8], other important results are given on a Cayley tree. Mainly, these papers are devoted to models with a finite set of spin values. In [9], the Potts model, with a countable set of spin values on a Cayley tree is considered and it was shown that the set of translation-invariant splitting Gibbs measures of the model contains at most one point, independent of the parameters for the Potts model with a countable set of spin values on the Cayley tree.

Gibbs measures have been considered for models with uncountable sets of spin values for the last five years. Until now, models with nearest-neighbor interactions have been considered (i.e., $J_3 = J = \alpha = 0$, $J_1 \neq 0$) and with the set $[0, 1]$ of spin values on a Cayley tree, we obtained the following results: "Splitting Gibbs measures" of the model on a Cayley tree of order k is described by the solutions of a nonlinear integral equation. For $k = 1$ it has been shown that the integral equation has a unique solution (i.e., there is a unique Gibbs measure). For periodic splitting Gibbs measures, a sufficient condition was found under which the measure is unique and proved the existence of phase transitions on a Cayley tree of order $k \geq 2$ (see [10–13]).

In [14] it was described splitting Gibbs measures on Γ_2 were described by solutions to a nonlinear integral equation for the case $J_3^2 + J_1^2 + J^2 + \alpha^2 \neq 0$ which is a generalization of the case $J_3 = J = \alpha = 0$, $J_1 \neq 0$. Also, it was proved that periodic Gibbs measure for the Hamiltonian with four competing interactions is either *translation-invariant* or $G_k^{(2)}$ -*periodic*, and given examples of non-uniqueness for Hamiltonian (2.1) in the case $J_3 \neq 0$, $J = J_1 = \alpha = 0$. Gibbs measures for the Hamiltonian which corresponds to the degenerate kernel was not considered in the paper.

In this paper, we provide a connection between Gibbs measures for the model which is defined in [14] and positive solutions of the Lyapunov integral equations. Also we study the fixed points of the Lyapunov operator with degenerate kernel. Using each fixed point for the operator, the *translation-invariant* Gibbs measure for the Hamiltonian can be founded which corresponds to the degenerate kernel.

2. Preliminaries

A Cayley tree $\Gamma^k = (V, L)$ of order $k \in \mathbb{N}$ is an infinitely homogeneous tree, i.e., a graph without cycles, with exactly $k + 1$ edges incident to each vertex. Here, V is the set of vertices and L that of edges (arcs). Two vertices x and y are called nearest neighbors if there exists an edge $l \in L$ connecting them. We will use the notation $l = \langle x, y \rangle$. The distance $d(x, y)$, $x, y \in V$ on the Cayley tree is defined by the formula

$$d(x, y) = \min\{d \mid x = x_0, x_1, \dots, x_{d-1}, x_d = y \in V \text{ such that the pairs } \langle x_0, x_1 \rangle, \dots, \langle x_{d-1}, x_d \rangle \text{ are neighboring vertices}\}.$$

Let $x^0 \in V$ be a fixed and we set

$$W_n = \{x \in V \mid d(x, x^0) = n\}, \quad V_n = \{x \in V \mid d(x, x^0) \leq n\}, \\ L_n = \{l = \langle x, y \rangle \in L \mid x, y \in V_n\},$$

The set of the direct successors of x is denoted by $S(x)$, i.e.

$$S(x) = \{y \in W_{n+1} \mid d(x, y) = 1\}, \quad x \in W_n.$$

We observe that for any vertex $x \neq x^0$, x has k direct successors and x^0 has $k + 1$. The vertices x and y are called second neighbor which is denoted by $\rangle x, y \langle$, if there exist a vertex $z \in V$ such that x, z and y, z are nearest neighbors. We will consider only second neighbors $\rangle x, y \langle$, for which there exist n such that $x, y \in W_n$. Three vertices x, y and z are called a triple of neighbors and they are denoted by $\langle x, y, z \rangle$, if $\langle x, y \rangle, \langle y, z \rangle$ are nearest neighbors and $x, z \in W_n, y \in W_{n-1}$, for some $n \in \mathbb{N}$.

Now we consider models with four competing interactions where the spin takes values in the set $[0, 1]$. For some set $A \subset V$ an arbitrary function $\sigma_A : A \rightarrow [0, 1]$ is called a configuration and the set of all configurations on A we denote by $\Omega_A = [0, 1]^A$. Let $\sigma(\cdot)$ belong to $\Omega_V = \Omega$ and $\xi_1 : (t, u, v) \in [0, 1]^3 \rightarrow \xi_1(t, u, v) \in R$, $\xi_i : (u, v) \in [0, 1]^2 \rightarrow \xi_i(u, v) \in R, i \in \{2, 3\}$ are given bounded, measurable functions. Next, we consider the model with four competing interactions on the Cayley tree which is defined by following Hamiltonian

$$H(\sigma) = -J_3 \sum_{\langle x, y, z \rangle} \xi_1(\sigma(x), \sigma(y), \sigma(z)) - J \sum_{\rangle x, y \langle} \xi_2(\sigma(x), \sigma(y)) - J_1 \sum_{\langle x, y \rangle} \xi_3(\sigma(x), \sigma(y)) - \alpha \sum_{x \in V} \sigma(x), \quad (2.1)$$

where the sum in the first term ranges all triples of neighbors, the second sum ranges all second neighbors, the third sum ranges all nearest neighbors and $J, J_1, J_3, \alpha \in R \setminus \{0\}$. Let $h : [0, 1] \times V \setminus \{x^0\} \rightarrow \mathbb{R}$ and $|h(t, x)| = |h_{t,x}| < C$ where x_0 is a root of Cayley tree and C is a constant which does not depend on t . For some $n \in \mathbb{N}$, $\sigma_n : x \in V_n \mapsto \sigma(x)$ and Z_n is the corresponding partition function we consider the probability distribution $\mu^{(n)}$ on Ω_{V_n} defined by

$$\mu^{(n)}(\sigma_n) = Z_n^{-1} \exp \left(-\beta H(\sigma_n) + \sum_{x \in W_n} h_{\sigma(x), x} \right), \quad (2.2)$$

$$Z_n = \int \dots \int_{\Omega_{V_{n-1}}^{(p)}} \exp \left(-\beta H(\tilde{\sigma}_n) + \sum_{x \in W_n} h_{\tilde{\sigma}(x), x} \right) \lambda_{V_{n-1}}^{(p)}(d\tilde{\sigma}_n), \quad (2.3)$$

where

$$\underbrace{\Omega_{W_n} \times \Omega_{W_n} \times \dots \times \Omega_{W_n}}_{3 \cdot 2^{p-1}} = \Omega_{W_n}^{(p)}, \quad \underbrace{\lambda_{W_n} \times \lambda_{W_n} \times \dots \times \lambda_{W_n}}_{3 \cdot 2^{p-1}} = \lambda_{W_n}^{(p)}, \quad n, p \in \mathbb{N},$$

Let $\sigma_{n-1} \in \Omega_{V_{n-1}}$ and $\sigma_{n-1} \vee \omega_n \in \Omega_{V_n}$ is the concatenation of σ_{n-1} and ω_n . For $n \in \mathbb{N}$ we say that the probability distributions $\mu^{(n)}$ are compatible if $\mu^{(n)}$ satisfies the following condition:

$$\int \int_{\Omega_{W_n} \times \Omega_{W_n}} \mu^{(n)}(\sigma_{n-1} \vee \omega_n) (\lambda_{W_n} \times \lambda_{W_n})(d\omega_n) = \mu^{(n-1)}(\sigma_{n-1}). \quad (2.4)$$

By Kolmogorov's extension theorem there exists a unique measure μ on Ω_V such that, for any n and $\sigma_n \in \Omega_{V_n}$, $\mu(\{\sigma|_{V_n} = \sigma_n\}) = \mu^{(n)}(\sigma_n)$. The measure μ is called *splitting Gibbs measure* corresponding to Hamiltonian (2.1)

and function $x \mapsto h_x, x \neq x^0$.

We denote

$$K(u, t, v) = \exp \{ J_3 \beta \xi_1(t, u, v) + J \beta \xi_2(u, v) + J_1 \beta (\xi_3(t, u) + \xi_3(t, v)) + \alpha \beta (u + v) \}, \tag{2.5}$$

and

$$f(t, x) = \exp(h_{t,x} - h_{0,x}), \quad (t, u, v) \in [0, 1]^3, \quad x \in V \setminus \{x^0\}.$$

The following statement describes conditions on h_x guaranteeing the compatibility of the corresponding distributions $\mu^{(n)}(\sigma_n)$.

Theorem 2.1. *The measure $\mu^{(n)}(\sigma_n), n = 1, 2, \dots$ satisfies the consistency condition (2.4) iff for any $x \in V \setminus \{x^0\}$ the following equation holds:*

$$f(t, x) = \prod_{\langle y, z \rangle \in S(x)} \frac{\int_0^1 \int_0^1 K(t, u, v) f(u, y) f(v, z) du dv}{\int_0^1 \int_0^1 K(0, u, v) f(u, y) f(v, z) du dv}, \tag{2.6}$$

where $S(x) = \{y, z\}, \langle y, x, z \rangle$ is a ternary neighbor and $du = \lambda(du)$ is the Lebesgue measure.

3. Lyapunov’s operator \mathcal{L} with degenerate kernel

Now we consider the case $J_3 \neq 0, J = J_1 = \alpha = 0$ for the model (2.1) in the class of translational-invariant functions $f(t, x)$ i.e $f(t, x) = f(t)$, for any $x \in V$. For such functions, equation (2.1) can be written as

$$f(t) = \frac{\int_0^1 \int_0^1 K(t, u, v) f(u) f(v) du dv}{\int_0^1 \int_0^1 K(0, u, v) f(u) f(v) du dv}, \tag{3.1}$$

where $K(t, u, v) = \exp \{ J_3 \beta \xi_1(t, u, v) + J \beta \xi_2(u, v) + J_1 \beta (\xi_3(t, u) + \xi_3(t, v)) + \alpha \beta (u + v) \}, f(t) > 0, t, u \in [0, 1]$.

We shall find positive continuous solutions to (3.1) i.e. such that $f \in C^+[0, 1] = \{f \in C[0, 1] : f(x) \geq 0\}$.

We define a nonlinear operator H on the cone of positive continuous functions on $[0, 1]$:

$$(Hf)(t) = \frac{\int_0^1 \int_0^1 K(t, s, u) f(s) f(u) ds du}{\int_0^1 \int_0^1 K(0, s, u) f(s) f(u) ds du}.$$

We’ll study the existence of positive fixed points for the nonlinear operator H (i.e., solutions of the equation (3.1)). Put $C_0^+[0, 1] = C^+[0, 1] \setminus \{\theta \equiv 0\}$. Then the set $C^+[0, 1]$ is the cone of positive continuous functions on $[0, 1]$.

We define the Lyapunov integral operator \mathcal{L} on $C[0, 1]$ by the equality (see [15])

$$\mathcal{L}f(t) = \int_0^1 K(t, s, u) f(s) f(u) ds du.$$

We put

$$\mathcal{M}_0 = \{f \in C^+[0, 1] : f(0) = 1\}.$$

We denote by $N_{fix.p}(H)$ and $N_{fix.p}(\mathcal{L})$ are the set of positive numbers of nontrivial positive fixed points of the operators $N_{fix.p}(H)$ and $N_{fix.p}(\mathcal{L})$, respectively.

Theorem 3.1. [14]

i) *The equation*

$$Hf = f, \quad f \in C_0^+[0, 1] \tag{3.2}$$

has a positive solution iff the Lyapunov equation

$$\mathcal{L}g = \lambda g, \quad g \in C^+[0, 1] \tag{3.3}$$

has a positive solution in \mathcal{M}_0 for some $\lambda > 0$.

ii) *The equation $Hf = f$ has a nontrivial positive solution iff the Lyapunov equation $\mathcal{L}g = g$ has a nontrivial positive solution.*

iii) *The equation*

$$\mathcal{L}f = \lambda f, \quad \lambda > 0 \tag{3.4}$$

has at least one solution in $C_0^+[0, 1]$.

iv) *The equation (3.2) has at least one solution in $C_0^+[0, 1]$.*

v) The equality $N_{fix.p}(H) = N_{fix.p}(\mathcal{L})$ holds.

Let $\varphi_1(t)$, $\varphi_2(t)$ and $\psi_1(t)$, $\psi_2(t)$ are positive functions from $C_0^+[0, 1]$. We consider Lyapunov's operator \mathcal{L}

$$(\mathcal{L}f)(t) = \int_0^1 (\psi_1(t)\varphi_1(u) + \psi_2(t)\varphi_2(v))f(u)f(v)dudv, \tag{3.5}$$

and quadratic operator P on \mathbb{R}^2 by the rule

$$P(x, y) = (\alpha_{11}x^2 + \alpha_{12}xy + \alpha_{22}y^2, \quad \beta_{11}x^2 + \beta_{12}xy + \beta_{22}y^2).$$

$$\alpha_{11} = \int_0^1 \int_0^1 \psi_1(u)\psi_1(v)\varphi_2(v)dudv, \quad \alpha_{12} = \int_0^1 \int_0^1 (\psi_1(v)\psi_2(u) + \psi_1(u)\psi_2(v))\varphi_2(v)dudv,$$

$$\alpha_{22} = \int_0^1 \int_0^1 \psi_2(u)\psi_2(v)\varphi_2(v)dudv, \quad \beta_{11} = \int_0^1 \int_0^1 \psi_1(u)\psi_1(v)\varphi_1(u)dudv,$$

$$\beta_{12} = \int_0^1 \int_0^1 (\psi_1(u)\psi_2(v) + \psi_1(v)\psi_2(u))\varphi_1(u)dudv, \quad \beta_{22} = \int_0^1 \int_0^1 \psi_2(u)\psi_2(v)\varphi_1(u)dudv.$$

Lemma 3.2. *Lyapunov's operator \mathcal{L} has a nontrivial positive fixed point iff the quadratic operator P has a nontrivial positive fixed point, moreover $N_{fix}^+(H_k) = N_{fix}^+(P)$.*

Proof. a) Put

$$\mathbb{R}_2^+ = \{(x, y) \in \mathbb{R}^2 : x \geq 0, y \geq 0\}, \quad \mathbb{R}_2^> = \{(x, y) \in \mathbb{R}^2 : x > 0, y > 0\}.$$

Let $f(t) \in C_0^+[0, 1]$ be a nontrivial positive fixed point of \mathcal{L} . Let

$$c_1 = \int_0^1 \varphi_1(u)f(u)f(v)dudv, \quad c_2 = \int_0^1 \varphi_2(u)f(u)f(v)dudv$$

Clearly, $c_1 > 0$, $c_2 > 0$ and $f(t) = c_1\psi_1(t) + c_2\psi_2(t)$. If we put $f(t) = c_1\psi_1(t) + c_2\psi_2(t)$ to the equation (3.5) we'll get

$$c_1 = \alpha_{11}c_1^2 + \alpha_{12}c_1c_2 + \alpha_{22}c_2^2, \quad c_2 = \beta_{11}c_1^2 + \beta_{12}c_1c_2 + \beta_{22}c_2^2.$$

Therefore, the point (c_1, c_2) is fixed point of the quadratic operator P .

b) Assume, that the point (x_0, y_0) is a nontrivial positive fixed point of the quadratic operator P , i.e. $(x_0, y_0) \in \mathbb{R}_2^+ \setminus \{\theta\}$ and numbers x_0, y_0 satisfies following equalities

$$\alpha_{11}x_0^2 + \alpha_{12}x_0y_0 + \alpha_{22}y_0^2 = x_0, \quad \beta_{11}x_0^2 + \beta_{12}x_0y_0 + \beta_{22}y_0^2 = y_0.$$

Similarly, we can prove that the function $f_0(t) = x_0\psi_1(t) + y_0\psi_2(t)$ is a fixed point of the operator \mathcal{L} and $f_0(t) \in C_0^+[0, 1]$. This completes the proof. □

We define positive quadratic operator \mathcal{Q} :

$$\mathcal{Q}(x, y) = (a_{11}x^2 + a_{12}xy + a_{22}y^2, \quad b_{11}x^2 + b_{12}xy + b_{22}y^2).$$

Proposition 3.3.

i) If $\omega = (x_0, y_0) \in \mathbb{R}_2^+$ is a positive fixed point of \mathcal{Q} , then $\lambda_0 = \frac{x_0}{y_0}$ is a root of the following equation

$$a_{11}\lambda^3 + (a_{12} - b_{11})\lambda^2 + (a_{22} - b_{12})\lambda - b_{22} = 0. \tag{3.6}$$

ii) If the positive number λ_0 is a positive root of the equation (3.6), then the point $\omega_0 = (\lambda_0y_0, y_0)$ is a positive fixed point of \mathcal{Q} , where $y_0^{-1} = a_{11} + a_{12}\lambda_0 + a_{22}\lambda_0^2$.

Proof. i) Let the point $\omega = (y_0, x_0) \in \mathbb{R}_2^+$ be a fixed point of \mathcal{Q} . Then

$$a_{11}x_0^2 + a_{12}x_0y_0 + a_{22}y_0^2 = x_0, \quad b_{11}x_0^2 + b_{12}x_0y_0 + b_{22}y_0^2 = y_0$$

Using the equality $\frac{x_0}{y_0} = \lambda_0$, we obtain

$$a_{11}\lambda_0^2y_0^2 + a_{12}\lambda_0y_0^2 + a_{22}y_0^2 = \lambda_0y_0, \quad b_{11}\lambda_0^2y_0^2 + b_{12}\lambda_0^2y_0^2 + b_{22}y_0^2 = y_0.$$

Thus we get

$$\frac{a_{11}\lambda_0^2 + a_{12}\lambda_0 + a_{22}}{b_{11}\lambda_0^2 + b_{12}\lambda_0 + b_{22}} = \lambda_0.$$

Consequently,

$$a_{22} + (a_{12} - b_{22})\lambda_0 + (a_{11} - b_{12})\lambda_0^2 - b_{11}\lambda_0^3 = 0.$$

ii) Let $\lambda_0 > 0$ be a root of the cubic equation (3.6). We set $x_0 = \lambda_0 y_0$, where

$$x_0 = \frac{\lambda_0}{a_{11}\lambda_0^2 + 2a_{12}\lambda_0 + a_{22}}.$$

Since

$$a_{11}x_0^2 + 2a_{12}x_0y_0 + a_{22}y_0^2 = \frac{1}{a_{11}\lambda_0^2 + 2a_{12}\lambda_0 + a_{22}},$$

we get

$$a_{11}x_0^2 + 2a_{12}x_0y_0 + a_{22}y_0^2 = y_0.$$

Alternatively, we get:

$$a_{22} + (a_{12} - b_{22})\lambda_0 + (a_{11} - b_{12})\lambda_0^2 - b_{11}\lambda_0^3 = 0.$$

Then, we get

$$b_{11}\lambda_0^2 + b_{12}\lambda_0 + b_{22} = \lambda_0(a_{11}\lambda_0^2 + a_{12}\lambda_0 + a_{22}).$$

From the last equality we get

$$\frac{\lambda_0}{a_{11}\lambda_0^2 + a_{12}\lambda_0 + a_{22}} = \frac{b_{11}\lambda_0^2 + b_{12}\lambda_0 + b_{22}}{(a_{11}\lambda_0^2 + a_{12}\lambda_0 + a_{22})^2} = b_{11}x_0^2 + 2b_{12}x_0y_0 + b_{22}y_0^2 = y_0.$$

This completes the proof. \square

We denote

$$\begin{aligned} P(\lambda) &= \alpha_{11}\lambda^3 + (\alpha_{12} - \beta_{11})\lambda^2 + (\alpha_{22} - \beta_{12})\lambda - \beta_{22} = 0, \\ \mu_0 &= \alpha_{11}, \quad \mu_1 = \alpha_{12} - \beta_{11}, \quad \mu_2 = \alpha_{22} - \beta_{12}, \quad \mu_3 = \beta_{22}, \\ P_3(\xi) &= \mu_0\xi^3 + \mu_1\xi^2 + \mu_2\xi - \mu_3, \\ D &= \mu_1^2 - 3\mu_0\mu_2, \quad \alpha = -\frac{\mu_1 + \sqrt{D}}{3\mu_0}, \quad \beta = -\frac{\mu_1 - \sqrt{D}}{3\mu_0}. \end{aligned} \tag{3.7}$$

Theorem 3.4. Let \mathcal{Q} satisfy one of the following conditions

- i) $D \leq 0$;
- ii) $D > 0, \beta \leq 0$;
- iii) $D > 0, \alpha \leq 0, \beta > 0$;
- iv) $D > 0, \alpha > 0, P_3(\alpha) < 0$;
- v) $D > 0, \alpha > 0, P_3(\alpha) > 0, P_3(\beta) > 0$, then \mathcal{Q} has a unique nontrivial positive fixed point.

Proof. The proof of Theorem 3.4 is basis on monotonous property of the function $P_3(\xi)$. Clearly,

$$(P_3(\xi))' = 3\mu_0\xi^2 + 2\mu_1\xi + \mu_2. \tag{3.8}$$

and $P_3'(\alpha) = P_3'(\beta) = 0$. Moreover,

i) In the case $D \leq 0$, by the equality (3.8) the function $P_3(\xi)$ is an increasing function on \mathbb{R} and $P_3(0) = -b_{11} < 0$. Therefore, the polynomial $P_3(\xi)$ has a unique positive root.

ii) Let $D > 0$ and $\beta \leq 0$. For the case $D > 0$ the function $P_3(\xi)$ is an increasing function on $(-\infty, \alpha) \cup (\beta, \infty)$ and it is a decreasing function on (α, β) . Hence, from the inequality $P_3(0) < 0$ the polynomial $P_3(\xi)$ has a unique positive root.

iii) Let $D > 0, \alpha \leq 0$ and $\beta > 0$. Since the function $P_3(\xi)$ is decreasing on (α, β) and increasing on (β, ∞) , the polynomial $P_3(\xi)$ has a unique positive root as $P_3(0) < 0$.

iv) Let $D > 0, \alpha > 0$ and $P_3(\alpha) < 0$. Then $\max_{\xi \in (-\infty, \beta)} P_3(\xi) = P_3(\alpha) < 0$. Consequently, by the function $P_3(\xi)$ is increasing on (β, ∞) the polynomial $P_3(\xi)$ has a unique positive root $\xi_0 \in (\beta, \infty)$.

v) Let $D > 0, \alpha > 0, P_3(\alpha) > 0$ and $P_3(\beta) > 0$. Then $\min_{\xi \in (\alpha, \infty)} P_3(\xi) = P_3(\beta) > 0$. From the function $P_3(\xi)$ on $(-\infty, \alpha)$, $P_3(\xi)$ has a unique positive root $\xi_0 \in (0, \alpha)$, as $P_3(0) < 0$ and $P_3(\alpha) > 0$.

From the upper analysis and by Lemmas 3.3, it follows that the Theorem 3.4. \square

Theorem 3.5. Let be $D > 0$. If \mathcal{Q} satisfies one of the following conditions

i) $\alpha > 0, P_3(\alpha) = 0, P_3(\beta) < 0$;

ii) $\alpha > 0, P_3(\alpha) > 0, P_3(\beta) = 0$, then $\mathcal{Q} \in \mathcal{Q}$ has two nontrivial positive fixed points and $N_{fix}^+(\mathcal{Q}) = N_{fix}^>(\mathcal{Q}) = 2$.

Proof. i) Let $\alpha > 0, P_3(\alpha) = 0$ and $P_3(\beta) < 0$. Then $\max_{\xi \in (-\infty, \beta)} P_3(\xi) = P_3(\alpha) = 0$ and $\xi_1 = \alpha$ is the root of the polynomial $P_3(\xi)$. By the increase property on (β, ∞) of the function $P_3(\xi)$ the polynomial $P_3(\xi)$ has a root $\xi_2 \in (\beta, \infty)$, as $\beta > 0$ and $P_3(\beta) < 0$. There are no other positive roots of the polynomial $P_3(\xi)$.

ii) Let $\alpha > 0, P_3(\alpha) > 0$ and $P_3(\beta) = 0$. Then by the increase property on $(-\infty, \alpha)$ of the function $P_3(\xi)$ the polynomial $P_3(\xi)$ has a root $\xi_1 \in (0, \alpha)$. Alternatively, $\min_{\xi \in (\alpha, \infty)} P_3(\xi) = P_3(\beta) = 0$ and the number $\xi_2 = \alpha$ is the second positive root of the polynomial $P_3(\xi)$. The polynomial $P_3(\xi)$ has no other roots. From above, and by Lemmas 3.3, we get Theorem 3.6. \square

Theorem 3.6. Let be $D > 0$. If \mathcal{Q} satisfies one of the following conditions

i) $\alpha > 0, P_3(\alpha) = 0, P_3(\beta) < 0$;

ii) $\alpha > 0, P_3(\alpha) > 0, P_3(\beta) = 0$,

then \mathcal{Q} has two nontrivial positive fixed points and $N_{fix}^+(\mathcal{Q}) = N_{fix}^>(\mathcal{Q}) = 2$.

Proof. i) Let $\alpha > 0, P_3(\alpha) = 0$ and $P_3(\beta) < 0$. Then $\max_{\xi \in (-\infty, \beta)} P_3(\xi) = P_3(\alpha) = 0$ and $\xi_1 = \alpha$ is the root of the polynomial $P_3(\xi)$. By the increase property on (β, ∞) of the function $P_3(\xi)$ the polynomial $P_3(\xi)$ has a root $\xi_2 \in (\beta, \infty)$, as $\beta > 0$ and $P_3(\beta) < 0$. There are no other positive roots of the polynomial $P_3(\xi)$.

ii) Let $\alpha > 0, P_3(\alpha) > 0$ and $P_3(\beta) = 0$. Then by the increase property on $(-\infty, \alpha)$ of the function $P_3(\xi)$ the polynomial $P_3(\xi)$ has a root $\xi_1 \in (0, \alpha)$. Alternatively, $\min_{\xi \in (\alpha, \infty)} P_3(\xi) = P_3(\beta) = 0$ and the number $\xi_2 = \alpha$ is the second positive root of the polynomial $P_3(\xi)$. The polynomial $P_3(\xi)$ has no other roots. From above, and by Lemmas 3.3, we get Theorem 3.6. \square

Acknowledgments

We thank the referee for their careful reading of the manuscript and useful comments.

References

- [1] Georgii H.O. *Gibbs measures and phase transitions*. Second edition. de Gruyter Studies in Mathematics, 9. Walter de Gruyter, Berlin, 2011.
- [2] Preston C. *Gibbs states on countable sets*. Cambridge University Press, London, 1974.
- [3] Monroe J.L. Phase diagrams of Ising models on Husime trees two. *J.Statist.Phys.*, 1992, **67**, P. 1185–2000.
- [4] Monroe J.L. A new criterion for the location of phase transitions for spin system on a recursive lattice. *Phys.Lett.A.*, 1994, **188**, P. 80–84.
- [5] Mukhamedov F.M., Rozikov U.A. On Gibbs measures of models with completing ternary and binary interactions and corresponding von Neumann algebras. *J.Statist.Phys.*, 2004, **114**, P. 825–848.
- [6] Ganikhodjaev N.N., Pah C.H., Wahiddin M.R.B. An Ising model with three competing interactions on a Cayley tree. *J. Math. Phys.*, 2004, **45**, P. 3645–3658.
- [7] Ganikhodjaev N.N., Rozikov U.A. On Ising model with four competing interactions on Cayley tree. *Math. Phys. Anal. Geom.*, 2009, **12**, P. 141–156.
- [8] Utkir A. Rozikov. *Gibbs measures on a Cayley trees*. World Sci. Pub., Singapore, 2013.
- [9] Ganikhodjaev N.N., Rozikov U.A. The Potts model with countable set of spin values on a Cayley Tree. *Letters Math. Phys.*, 2006, **75**, P. 99–109.
- [10] Eshkabilov Yu.Kh., Haydarov F.H., Rozikov U.A. Uniqueness of Gibbs Measure for Models With Uncountable Set of Spin Values on a Cayley Tree. *Math. Phys. Anal. Geom.*, 2013, **16**(1), P. 1–17.
- [11] Eshkabilov Yu.Kh., Haydarov F.H., Rozikov U.A. Non-uniqueness of Gibbs Measure for Models With Uncountable Set of Spin Values on a Cayley Tree. *J. Stat. Phys.*, 2012, **147**, P. 779–794.
- [12] Eshkabilov Yu.Kh., Haydarov F.H. On positive solutions of the homogenous Hammerstein integral equation. *Nanosystems: Physics, Chemistry, Mathematics*, 2015, **6**(5), P. 618–627.
- [13] Rozikov U.A., Haydarov F.H. Periodic Gibbs measures for models with uncountable set of spin values on a Cayley tree. *Inf.Dim.Anal.Quan.Prob.*, 2015, **18**, P. 1–22.
- [14] Rozikov U.A., Haydarov F.H. Four competing interactions for models with an uncountable set of spin values on a Cayley tree. *Theor. Math. Phys.*, 2017, **191**(2), P. 748–761.
- [15] Krasnosel'ski M.A. *Positive solutions of operator equations*. Gos. Izd., Moscow, 1969 (in Russian).

Spectral properties of spontaneous photon emission by a material two-level system in a parabolic cavity

G. Alber¹, A. V. Chizhov^{2,3}

¹Institut für Angewandte Physik, Technische Universität Darmstadt,
Darmstadt, 64289, Germany

²Bogoliubov Laboratory of Theoretical Physics, Joint Institute for Nuclear Research,
Joliot-Curie, 6, Dubna, 141980, Russia

³Dubna State University, Universitetskaya, 19, Dubna, 141980, Russia
chizhov@theor.jinr.ru

PACS 37.30.+i, 42.50.Pq

DOI 10.17586/2220-8054-2017-8-5-559-566

The spectral properties of a photon spontaneously emitted by a material two-level system, modelling an atom or ion, in a parabolic cavity are investigated. In particular, we concentrate on the special case of a motionless two-level system positioned exactly at the focus of a parabolic cavity with a dipole moment oriented along the symmetry axis of this cavity. Treating the corresponding atom-field coupling in the dipole- and rotating wave approximation, it is demonstrated that inside the parabolic cavity the position and frequency dependence of the spectrum of the spontaneously emitted photon exhibits interesting interference patterns. These patterns are explored in detail with the help of a photon path representation of the first-order electric field correlation function. In the radiation zone the spatial behavior of the spectrum reveals strong interference in particular at distances from the two-level system of the order of the focal length of the parabola. With increasing distances, these interference patterns decay except for an undepleted component surrounding the symmetry axis at an almost constant radius. Furthermore, the maximum of the frequency dependence of the spectrum exhibits a position-dependent frequency shift with respect to the atomic resonance frequency.

Keywords: cavity QED, spontaneous emission.

Received: 30 August 2017

Revised: 11 September 2017

1. Introduction

A material two-level system, modelling an atom or ion, interacting with the quantized radiation field is the paradigm of an elementary quantum optical system. Despite its simplicity, it exhibits many fundamental phenomena characteristic for quantum theory which also offer interesting possibilities for innovative quantum technological applications [1]. Within this scenario, the almost resonant exchange of energy between a single photon of the radiation field and a trapped motionless two-level system represents the simplest physically realizable model system. Particularly interesting phenomena occur in this simple model system if the photonic mode structure is engineered by the presence of a cavity which imposes additional physical boundary conditions.

In quantum electrodynamical experiments [2], manipulations of the photonic mode structure have already been pushed to the extreme case that approximately only a single mode of the electromagnetic radiation field is capable of exchanging energy with a trapped motionless atom almost resonantly. In these cases, which can be described within the Jaynes-Cummings-Paul model [3,4], the cavity induced modification of the interaction between a two-level system and a photon can lead to vacuum Rabi oscillations or to collapse and revival phenomena [5].

A series of recent experiments [6] has started to explore a different dynamical regime in which a single approximately motionless two-level ion is trapped at the focus of a parabolic mirror. In view of the peculiar focusing properties of a parabolic mirror an intense exchange of energy between a single photon and the trapped material two-level system is expected in this scenario. In addition, this physical system offers interesting possibilities for applications in quantum communication [7], for example, as it allows for an almost lossless coupling in and coupling out of the electromagnetic field energy into and out of the cavity. Contrary to the case of extreme mode selection, in this scenario this half open cavity supports a continuum of photonic modes which can couple to the trapped material two-level system. This continuum of modes, however, is structured by the presence of the parabolic cavity so that interesting dynamical modifications take place, which range from modifications of the spontaneous decay rate of the trapped two-level system in comparison with the free-space scenario by the Purcell effect [8] to intricate recurrence effects observable in the time evolution of the trapped two-level system originating from photonic reflections at the boundary of the cavity [9,10].

In this paper we generalize previous investigations into the interaction of a trapped approximately motionless material two-level system with a single photon inside a parabolic cavity [10] and explore the spectral properties of a spontaneously emitted photon inside this cavity. For this purpose, we apply our recently developed classical path representation of photonic transition amplitudes to the description of the electric field correlation function of a single photon and to the corresponding spectrum. This position-dependent photonic correlation function and its corresponding spectrum produced by the trapped spontaneously decaying two-level system can be measured by positioning a photon detector with appropriate spectral properties at various positions inside the parabolic cavity. Our subsequent investigations demonstrate that in the radiation zone, the spatial behavior of the spectrum reveals strong interference effects. These interference effects reflect the intricate photonic dynamics inside the parabolic cavity in the presence of the trapped material two-level system which originates from the interference of probability amplitudes associated with different photon paths.

This paper is organized as follows: In Sec. 2, the quantum optical model of a trapped motionless two-level system interacting with the quantized radiation field inside a parabolic cavity is introduced and previous results are summarized briefly. Based on these previous results, characteristic dynamical properties of the spontaneous decay process and its influence on the first-order electric field correlation function of the radiation field are discussed in Sec. 3. Subsequently, the resulting spectrum of a photon spontaneously emitted by the two-level system trapped in the focus of the parabolic cavity is explored in Sec. 4.

2. The quantum optical model

In this section, we introduce the quantum optical model describing a two-level system positioned in the focus of a parabolic cavity and interacting with the quantized radiation field.

In particular, we consider a motionless material two-level system placed at a fixed position in a parabolic optical cavity with an ideally conducting wall. The Hamiltonian describing the dynamics of its interaction with the quantized radiation field is given by [10]:

$$\hat{H} = \hat{H}_A + \hat{H}_F + \hat{H}_{AF}, \quad (1)$$

with the (free) Hamiltonian:

$$\hat{H}_A = E_e |e\rangle\langle e| + E_g |g\rangle\langle g|, \quad (2)$$

of the two-level system with its ground $|g\rangle$ and its excited state $|e\rangle$. These two states are assumed to be of opposite parity. The (free) dynamics of the quantized radiation field inside the parabolic cavity is described by the Hamiltonian:

$$\hat{H}_F = \sum_n \int d\omega \hbar\omega \hat{a}_{\omega,n}^\dagger \hat{a}_{\omega,n}. \quad (3)$$

The creation and destruction operators of the field modes are denoted by $\hat{a}_{\omega,n}^\dagger$ and $\hat{a}_{\omega,n}$. These modes are labeled by their continuous frequencies ω and by the discrete, integer-valued parameter n originating from the boundary conditions imposed by the parabolic cavity. Consistent with the Coulomb gauge the corresponding orthonormal and frequency normalized mode functions $\mathbf{g}_{\omega,n}(\mathbf{x})$ fulfill the transversality condition $\nabla \cdot \mathbf{g}_{\omega,n}(\mathbf{x}) = 0$ and are solutions of the Helmholtz equation:

$$\left(\nabla^2 + \frac{\omega^2}{c^2} \right) \mathbf{g}_{\omega,n}(\mathbf{x}) = 0, \quad (4)$$

with boundary conditions of an ideally conducting parabolic mirror with focal length f . (c denotes the speed of light in vacuum.) The interaction between the two-level system positioned at \mathbf{x}_A and the quantized radiation field is treated in the dipole- and rotating-wave approximations and is described by the Hamiltonian:

$$\hat{H}_{AF} = -i \sum_n \int d\omega \sqrt{\frac{\hbar\omega}{2\epsilon_0}} \mathbf{d} \cdot \mathbf{g}_{\omega,n}(\mathbf{x}_A) \hat{a}_{\omega,n} |e\rangle\langle g| + \text{h.c.}, \quad (5)$$

with the atomic dipole matrix element $\mathbf{d} = \langle e | \hat{\mathbf{d}} | g \rangle$ between the excited state $|e\rangle$ and the ground state $|g\rangle$.

In our subsequent discussion, we assume that the atom is located at the focus of the parabolic mirror, i.e. $\mathbf{x}_A = 0$, and that its dipole moment is oriented along the symmetry axis of the parabolic cavity, i.e. $\mathbf{d} = d\mathbf{e}_z$. As a consequence, the mode functions $\mathbf{g}_{\omega,n}(\mathbf{x})$ solving Eq. (4) and capable of coupling to this atomic dipole can be written in the form [10]:

$$\mathbf{g}_{\omega,n}(\mathbf{x}) = \nabla \times \mathbf{G}_{\omega,n}(\mathbf{x}), \quad (6)$$

with

$$\begin{aligned} \mathbf{G}_{\omega,n}(\mathbf{x}) &= \frac{1}{\sqrt{2\pi\omega\mathcal{N}_{\omega,n}}} \frac{\chi_{\omega,n}(\xi)}{\sqrt{\xi}} \frac{\chi_{\omega,n}(\eta)}{\sqrt{\eta}} \mathbf{e}_\phi, \\ \chi_{\omega,n}(\xi) &= \sqrt{\frac{4}{\pi k}} F_0(\alpha_n/k, k\xi/2), \\ \chi_{\omega,n}(\eta) &= \sqrt{\frac{4}{\pi k}} F_0(-\alpha_n/k, k\eta/2). \end{aligned} \quad (7)$$

Thereby, we have introduced parabolic coordinates (ξ, η, z) which are related to the corresponding symmetry adapted cylindrical coordinates (ρ, ϕ, z) by $\xi = r + z$ and $\eta = r - z$ with $r = \sqrt{\rho^2 + z^2}$. The relevant mode functions involve the Coulomb functions $F_L(\mu, x)$ [11] in these parabolic coordinates with $L = 0$ and with wave number $k = \omega/c$. The normalization factors appearing in Eq. (7) are given by:

$$\mathcal{N}_{\omega,n} = \int_0^{2f} d\eta \frac{\chi_{\omega,n}^2(\eta)}{\eta}. \quad (8)$$

The separation constants α_n are determined by the relevant boundary conditions at the surface of the ideally conducting parabola described by the equation $\eta = 2f$, i.e.:

$$\left. \frac{d\chi_{\omega,n}(\eta)}{d\eta} \right|_{\eta=2f} = 0. \quad (9)$$

Eq. (9) ensures the absence of the tangential component of the electric-field operator $\hat{E}_\xi(\mathbf{x}) \equiv \mathbf{e}_\xi \cdot \hat{\mathbf{E}}(\mathbf{x})$ on the surface of the parabola, where:

$$\hat{\mathbf{E}}(\mathbf{x}) = i \sum_n \int d\omega \sqrt{\frac{\hbar\omega}{2\epsilon_0}} \mathbf{g}_{\omega,n}(\mathbf{x}) \hat{a}_{\omega,n} + \text{h.c.} \equiv \hat{\mathbf{E}}^+(\mathbf{x}) + \hat{\mathbf{E}}^-(\mathbf{x}). \quad (10)$$

3. Photon path representation of the electric-field correlation function

Based on the results of Sec. 2, we explore the first-order electric-field correlation function of a photon spontaneously emitted by the two-level system. For this purpose, we develop a classical photon path representation for the relevant one-photon transition amplitude in the radiation zone, i.e. at distances from the radiating two-level system large in comparison with the wave length of the spontaneously emitted photon. This classical photon path representation exhibits the intricate photonic dynamics inside the parabola with sequences of reflections at the boundary and elastic scatterings by the two-level system [9].

If the two-level system is initially in its excited state $|e\rangle$ without any photon in the radiation field, the subsequent time evolution of the quantum state of the atom-field system is of the general form:

$$|\psi(t)\rangle = A_e(t)|e\rangle|0\rangle + \sum_n \int_0^\infty d\omega A_{\omega,n}(t)|g\rangle\hat{a}_{\omega,n}^\dagger|0\rangle. \quad (11)$$

The time-dependent coefficients $A_e(t)$ and $A_{\omega,n}(t)$ fulfill the Schrödinger equation with Hamiltonian (1). In the long-time limit, i.e. $t \gg 1/\Gamma_0$ with Γ_0 denoting the spontaneous decay rate of state $|e\rangle$, one obtains the result [10]:

$$A_{\omega,n}(t) = i \sqrt{\frac{\omega}{2\hbar\epsilon_0}} e^{-i\omega t} \frac{\mathbf{d} \cdot \mathbf{g}_{\omega,n}(\mathbf{x}_A)}{\omega - \omega_0 - i\Gamma_0/2}. \quad (12)$$

Information on the dynamics of the spontaneously emitted photon is contained in the first-order electric-field correlation function which is related to this probability amplitude by:

$$\langle \psi(t_1) | \hat{\mathbf{E}}^-(\mathbf{x}_1) \otimes \hat{\mathbf{E}}^+(\mathbf{x}_2) | \psi(t_2) \rangle = \nabla \times \mathbf{F}^*(\mathbf{x}_1, t_1) \otimes \nabla \times \mathbf{F}(\mathbf{x}_2, t_2), \quad (13)$$

with the effective one-photon amplitude:

$$\mathbf{F}(\mathbf{x}, t) = -i \sum_n \int_0^\infty d\omega \sqrt{\frac{\hbar\omega}{2\epsilon_0}} A_{\omega,n}^*(t) \mathbf{G}_{\omega,n}(\mathbf{x}). \quad (14)$$

If the focal length f of the parabolic cavity is not too large in the sense $c/\omega_0 \ll f \ll c/\Gamma_0$, in the radiation zone this effective one-photon amplitude is given by [10]:

$$\mathbf{F}(\mathbf{x}, t) = -i \mathbf{e}_\phi \frac{k_0 d}{4\pi\epsilon_0 \rho} \sum_{M=0}^\infty e^{-i2\pi M n_0} e^{(i\omega_0 - \Gamma_0/2)(t-r/c)} \left[\frac{\theta(t-r/c-MT)}{\cosh \Lambda_M(\rho, z; k_0)} - \frac{\theta(t-z/c-MT)}{\cosh \Theta_{M-1}(\rho, z; k_0)} \right], \quad (15)$$

with:

$$\begin{aligned} \Lambda_L(\rho, z; k_0) &= \ln \left(\frac{r-z}{r+z} \right) + 2L\mathcal{S}(k_0 f), \\ \Theta_L(\rho, z; k_0) &= \ln \left(\frac{2f}{\rho} \right)^2 + 2L\mathcal{S}(k_0 f), \end{aligned} \quad (16)$$

and with the diffraction function:

$$\mathcal{S}(u) = \int_0^u dy \frac{\sin^2 y}{y}.$$

In Eq. (15), the radiation zone refers to distances from the radiating two-level system which are large in comparison to the optical wave length characterizing the resonant atomic transition.

Eq. (15) represents the effective one-photon amplitude determining the electric-field correlation function as a sum of contributions M which can be associated with repeated returns of the spontaneously emitted photon back to the atom. Thereby, this photon evolves periodically along a straight-line classical path extending along the symmetry axis of the parabolic cavity from its focal point, where the two-level system is positioned, to its boundary and back again. The time the photon requires for this motion is given by the period $T = 2f/c$ and $2\pi n_0$ with $n_0 = k_0 f/\pi - 1/2$ is the corresponding classical eikonal associated with this photon path. The integer M enumerates the number of reflections of this photon path at the boundary of the parabola.

4. Spectrum of the spontaneously emitted photon

Based on the results of Sec. 3, we explore characteristic properties of the spectrum of the radiation field produced by the spontaneously emitted photon in the radiation zone, i.e. at distances from the radiating two-level system large in comparison with the wave length of the spontaneously emitted photon.

In general, the power spectrum of a photon spontaneously emitted by the material two-level system and detected at position \mathbf{x} with frequency ω_S is related to the first-order electric-field correlation function of Eq. (13) by [12]:

$$S(\mathbf{x}, \omega_S) = \int_0^\infty dt_1 \int_0^\infty dt_2 e^{-i\omega_S(t_1-t_2)} \langle \psi(t_1) | \hat{\mathbf{E}}^-(\mathbf{x}) \cdot \hat{\mathbf{E}}^+(\mathbf{x}) | \psi(t_2) \rangle. \quad (17)$$

Performing the time integrations, we find from Eqs. (13) and (15) the final result, which is conveniently represented in the form:

$$S(\mathbf{x}, \omega_S) = \left(\frac{\omega_0^2 d}{4\pi\epsilon_0 c^2} \right)^2 \cdot \frac{1}{(\omega_0 - \omega_S)^2 + \Gamma_0^2/4} \cdot I_{\text{mir}}(\rho, z; \omega_S, k_0), \quad (18)$$

with the mirror influence function being defined by:

$$\begin{aligned}
I_{\text{mir}}(\rho, z; \omega_S, k_0) &= \frac{1}{2r} \cdot \sum_{L, M=0}^{\infty} e^{-i(M-L)[2\pi n_0 - T(\omega_0 - \omega_S)] - (M+L)T\Gamma_0/2} \\
&\times \left\{ \frac{1}{\cosh \Lambda_M(\rho, z; k_0) \cosh \Lambda_L(\rho, z; k_0)} \right. \\
&\times \left(\frac{1}{r+z} \cdot \left[1 - \frac{2i \tanh \Lambda_M(\rho, z; k_0)}{k_0(r-z)} \right] \left[1 + \frac{2i \tanh \Lambda_L(\rho, z; k_0)}{k_0(r-z)} \right] \right. \\
&+ \left. \frac{1}{r-z} \cdot \left[1 + \frac{2i \tanh \Lambda_M(\rho, z; k_0)}{k_0(r+z)} \right] \left[1 - \frac{2i \tanh \Lambda_L(\rho, z; k_0)}{k_0(r+z)} \right] \right) \\
&+ \frac{1}{\cosh \Theta_{M-1}(\rho, z; k_0) \cosh \Theta_{L-1}(\rho, z; k_0)} \\
&\times \left(\frac{1}{r+z} \cdot \left[1 - \frac{2i \tanh \Theta_{M-1}(\rho, z; k_0)}{k_0(r-z)} \right] \left[1 + \frac{2i \tanh \Theta_{L-1}(\rho, z; k_0)}{k_0(r-z)} \right] \right. \\
&+ \left. \frac{1}{r-z} \cdot \left[1 + \frac{2i \tanh \Theta_{M-1}(\rho, z; k_0)}{k_0(r+z)} \right] \left[1 - \frac{2i \tanh \Theta_{L-1}(\rho, z; k_0)}{k_0(r+z)} \right] \right) \\
&+ 2\text{Re} \left[\frac{e^{-i\omega_S(r-z)/c}}{\cosh \Lambda_M(\rho, z; k_0) \cosh \Theta_{L-1}(\rho, z; k_0)} \right. \\
&\times \left(\frac{1}{r+z} \cdot \left[1 - \frac{2i \tanh \Lambda_M(\rho, z; k_0)}{k_0(r-z)} \right] \left[1 + \frac{2i \tanh \Theta_{L-1}(\rho, z; k_0)}{k_0(r-z)} \right] \right. \\
&- \left. \left. \frac{1}{r-z} \cdot \left[1 + \frac{2i \tanh \Lambda_M(\rho, z; k_0)}{k_0(r+z)} \right] \left[1 - \frac{2i \tanh \Theta_{L-1}(\rho, z; k_0)}{k_0(r+z)} \right] \right) \right] \left. \right\}. \tag{19}
\end{aligned}$$

Eqs. (18) and (19) represent the main result of this section.

In the extreme far-field zone in the sense of $\rho \gg f$ Eq. (19) reduces to the well-known free-space result:

$$I_{\text{free}}(\rho, z) = \left(\frac{\rho}{\rho^2 + z^2} \right)^2,$$

so that the spectrum (18) assumes the characteristic positional intensity distribution of dipolar radiation, i.e.:

$$S_{\text{free}}(\mathbf{x}, \omega_S) = \left(\frac{\omega_0^2 d \rho}{4\pi \epsilon_0 c^2 r^2} \right)^2 \cdot \frac{1}{(\omega_0 - \omega_S)^2 + \Gamma_0^2/4}. \tag{20}$$

As a consequence of the rotating wave approximation, in this limit the frequency distribution exhibits a purely Lorentzian lineshape. However, in more general cases which do not correspond to the extreme far-field condition the function $I_{\text{mir}}(\rho, z; \omega_S, k_0)$ is not only position dependent but also depends on the atomic transition frequency $\omega_0 = k_0 c$ and on the frequency ω_S at which the spontaneously emitted photon is observed. This additional frequency dependence reveals the influence of the parabolic mirror on the spatial behavior of the atomic photon emission.

The spatial behavior of $I_{\text{mir}}(\rho, z; \omega_S = \omega_0, k_0)$ at the atomic resonance frequency is depicted in Fig. 1. Apparently, pronounced interference effects take place in the radiation zone at positions of the photon detector from the radiating two-level system comparable to the focal length of the parabola. Due to the specific structure of the field modes capable of coupling to the atomic dipole oriented along the symmetry axis of the parabolic cavity, the spectrum is exactly zero on the axis of symmetry. However, there is a ring zone around the symmetry axis approximately at $\rho/f \sim 2/\sqrt{3} \approx 1.15$ at which the spectrum is maximal. Along this ring, the spectrum remains appreciable even at asymptotically large distances from the radiating two-level system. However, in all other directions the probability of detecting a photon diminishes quickly with increasing distance from the radiating two-level system.

The dependence of the spectrum of Eq. (18) on frequency and distance orthogonal to the symmetry axis is depicted in Fig. 2. Characteristic spatial interference patterns originating from the presence of the parabolic cavity are again visible. The contour plot of Fig. 2 indicates a small asymmetry of the frequency dependence with respect to the atomic resonance frequency ω_0 . To a good degree of approximation this asymmetry can be described by a position-dependent frequency shift Δ according to the relation:

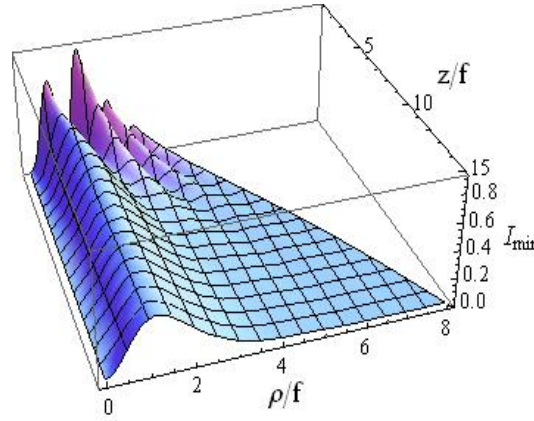


FIG. 1. Position dependence of the mirror influence function $I_{\text{mir}}(\rho, z; \omega_S, k_0)$ as defined by Eq. (19) at frequency $\omega_S = \omega_0$ for a parabolic mirror. The parameters are $T = 20/\omega_0$ and $T = 0.1/\Gamma_0$ so that the focal length f is large in comparison to the resonant inverse wave number k_0 , i.e. $f = 10/k_0$, and the spontaneously emitted photon is reflected at the boundary of the parabolic mirror many times during time T (compare with Eq. (15)). The boundary of the figure is given by the equation of the parabolic mirror of the form $z/f + 1 = (\rho/2f)^2$

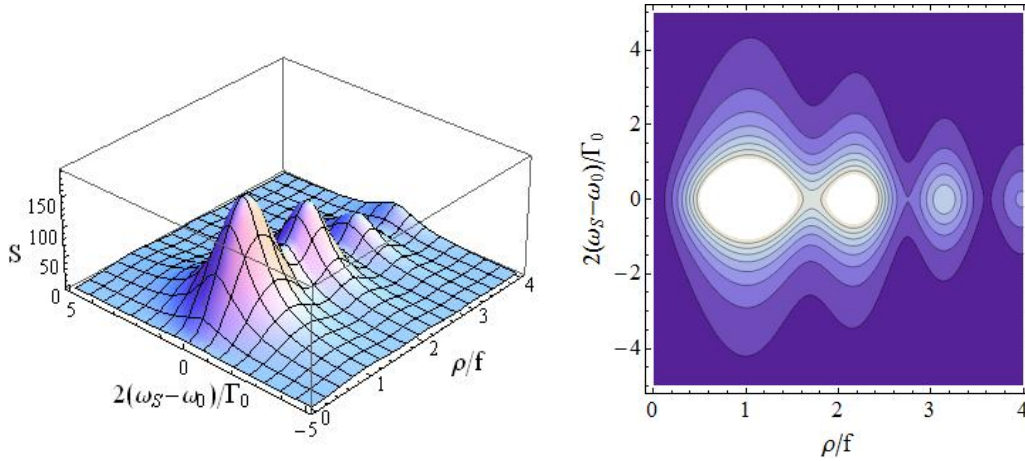


FIG. 2. Dependence of the spectrum of Eq. (18) and of its contour plot on the dimensionless frequency $2(\omega_S - \omega_0)/\Gamma_0$ and on the distance orthogonal to the symmetry axis at $z/f = 3$. The parameters are $\omega_0 T = 20$ and $\Gamma_0 T = 0.1$ as in Fig. 1

$$S(\mathbf{x}, \omega_S) = \left(\frac{\omega_0^2 d}{4\pi\epsilon_0 c^2} \right)^2 \cdot \frac{I_{\text{mir}}(\rho, z; \omega_0, k_0)}{(\omega_0 - \omega_S - \Delta)^2 + \Gamma_0^2/4}, \quad (21)$$

with the frequency shift Δ being determined by the equation:

$$\frac{\partial I_{\text{mir}}(\rho, z; \omega_0 + \Delta, k_0)/\partial \omega_S}{I_{\text{mir}}(\rho, z; \omega_0 + \Delta, k_0)} = \frac{2\Delta}{\Delta^2 + \Gamma_0^2/4}. \quad (22)$$

In Fig. 3, the spatial dependence of this frequency shift Δ is depicted. The modifications of the spectrum originating from the presence of the parabolic cavity give rise to an oscillatory spatial dependence of this frequency shift which reflects once again characteristic interference effects taking place inside the parabolic cavity.

In order to demonstrate the accuracy of the approximation of Eqs. (21) and (22) a cut of Fig. 2 at position $\rho/f = 0.5, z/f = 3$ is depicted in detail in Fig. 4 (left) with its top part being amplified in Fig. 4 (right). Although this shift is small, i.e. $2\Delta/\Gamma_0 \approx -0.003$, it is clearly visible.

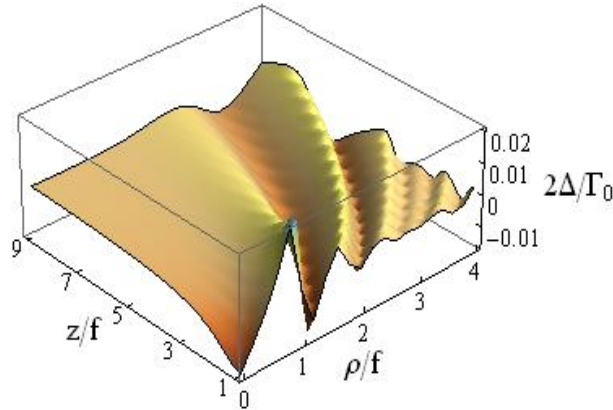


FIG. 3. Position dependence of the effective shift $2\Delta/\Gamma_0$ as defined by Eqs. (21) and (22). The parameters are $\omega_0 T = 20$ and $\Gamma_0 T = 0.1$ as in Fig. 1

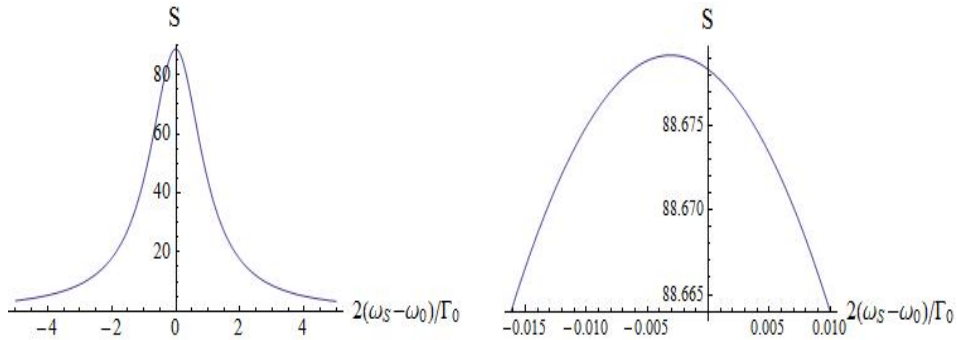


FIG. 4. Spectrum of Fig. 2 and its dependence on the dimensionless spectral frequency $2(\omega_S - \omega_0)/\Gamma_0$ at the fixed position $\rho/f = 0.5$ and $z/f = 3$. The parameters are $\omega_0 T = 20$ and $\Gamma_0 T = 0.1$ as in Fig. 1. The right part of this figure shows the frequency dependence around the maximum on a finer scale

5. Summary and conclusion

We have investigated the spectral properties of a photon spontaneously emitted by a motionless two-level atom positioned at the focus of a parabolic cavity with a dipole moment oriented along the symmetry axis of the parabola. Within a quantum optical model we have studied the spectrum of the spontaneously emitted radiation with the help of a photon path representation of the first-order electric field correlation function. In this manner, the influence of the parabolic mirror on the spontaneous photon emission process is described in terms of photon path contributions originating from repeated reflections of the spontaneously emitted photon at the boundary of the parabolic mirror. It has been demonstrated that inside the parabolic cavity, the position and frequency dependence of the spectrum of the spontaneously emitted photon exhibits interesting interference patterns. In the radiation zone, the spatial behavior of the spectrum reveals strong interference at distances from the atom of the order of the focal length of the parabola. With increasing distances, these interference patterns decay in all directions except for an undepleted component along the axis of symmetry. Furthermore, the maximum of the spectral line-shape exhibits a position-dependent frequency shift with respect to the atomic resonance frequency.

Acknowledgements

This work is supported by the Heisenberg–Landau Program (JINR, Russia).

References

- [1] Bruss D., Leuchs G. *Lectures on Quantum Information*. Wiley-VCH, Weinheim, 2008.
- [2] Haroche S., Raimond J.M. *Exploring the Quantum: Atoms, Cavities and Photons*. Oxford UP, Oxford, 2006.
- [3] Jaynes E.T., Cummings F.W. Comparison of quantum and semiclassical radiation theories with application to the beam maser. *Proceedings of the IEEE*, 1963, **51** (1), P. 89–109.
- [4] Paul H. Induzierte Emission bei starker Einstrahlung. *Annalen der Physik*, 1963, **466** (7–8), P. 411–412.
- [5] Schleich W.P. *Quantum Optics in Phase Space*. Wiley-VCH, Weinheim, 2001.
- [6] Maiwald R., Golla A., et al. Collecting more than half the fluorescence photons from a single ion. *Phys. Rev. A*, 2012, **86** (4), 043431–5.
- [7] Trautmann N., Bernad J.Z., et al. Generation of entangled matter qubits in two opposing parabolic mirrors. *Phys. Rev. A*, 2014, **90** (6), 063814–9.
- [8] Purcell E.M. Spontaneous emission probabilities at radio frequencies. *Phys. Rev.*, 1946, **69** (8), P. 681.
- [9] Alber G. Photon wave packets and spontaneous decay in a cavity. *Phys. Rev. A*, 1992, **46** (9), R5338–R5341.
- [10] Alber G., Bernad J.Z., et al. QED with a parabolic mirror. *Phys. Rev. A*, 2013, **88** (2), 023825–11.
- [11] Abramowitz M., Stegun I.A. *Handbook of Mathematical Functions*. Dover, New York, 1965.
- [12] Eberly J.H., Wódkiewicz K. The time-dependent physical spectrum of light. *J. Opt. Soc. Am.*, 1977, **67** (12), P. 1252–1261.

Reproduction of the evolution of the liquid front profile in inhomogeneous nanoporous media

D. S. Golovina, S. A. Chivilikhin

ITMO University, Kronverkskiy, 49, St. Petersburg, 197101, Russia

dheaddd@gmail.com, sergey.chivilikhin@gmail.com

PACS 68.03.-g

DOI 10.17586/2220-8054-2017-8-5-567-571

In recent years possible applications of nanoporous materials in biophysics and biomedicine have become a topic of intense scientific interest. One of the main problems in this field is that of transport processes in inhomogeneous nanoporous media. Another one is the reproduction of the specific evolution of the liquid front profile, observed in one medium, in another medium. In this paper, we present a model which simulates two-dimensional liquid front propagation in inhomogeneous nanoporous media; we also propose a method to evaluate the parameters of the nanoporous medium required for reproduction of the given liquid front propagation.

Keywords: inhomogeneous nanoporous media, transport processes, liquid front propagation.

Received: 15 September 2017

Revised: 9 October 2017

1. Introduction

In last decade, nanoporous materials have become a point of considerable scientific interest. They are widely studied and used in biophysics and biomedicine; nanoporous materials are applied in drug delivery [1, 2], tissue engineering [3], as biosensors [4], have great potential for usage in pharmacology [5], etc.

One significant problem in this field is the analysis of transport processes, which are considered to be more complex than in porous media, especially if nanoporous media in question are inhomogeneous [6]. Also, in biophysics and biomedicine, it is often necessary to reproduce in synthesized non-organic nanoporous medium the specific pattern of evolution of the liquid front profile observed in organic nanoporous medium.

The purpose of our work is to propose a model for simulation of the two-dimensional liquid front propagation in inhomogeneous nanoporous media and a method to evaluate the parameters of the medium in which a liquid will flow in a specific manner.

2. Mathematical model and its numerical realization

In this paper, we consider the flow in a thin nanoporous slab with thickness < 1 mm. We introduce the Cartesian coordinates along the slab – horizontal coordinate x and vertical coordinate y . The width of slab is L , the vertical coordinate of the boundary of the liquid front is $H(x, t)$ – see Fig. 1.

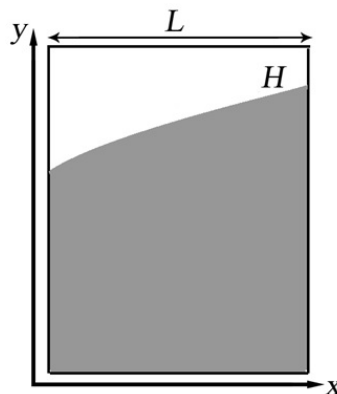


FIG. 1. Thin nanoporous slab. Gray area is the part of the medium permeated by liquid

While liquid flow permeates through a medium, the capillary forces in the liquid surface create the pressure $P_H = -\frac{2\sigma}{R}$, where σ is the surface tension coefficient of the liquid and R is the pore radius. The process of flowing also creates the pressure in the volume of the propagating liquid.

The proposed mathematical model for describing the two-dimensional propagation of the liquid in inhomogeneous nanoporous media is based on the approximation of Darcy's law $\vec{v} = -\gamma \nabla P$, where \vec{v} is the velocity of the flow and P is the pressure in the liquid, and on the continuity equation for the incompressible flow $\nabla \vec{v} = 0$. In the two-dimensional case, the combination of these equations gives us the linear differential equation:

$$\nabla(\gamma \nabla P) = 0, \tag{1}$$

with boundary conditions – definite pressure on the bottom of the thin slab ($y = 0$) and on the boundary of the liquid front ($y = H(x, t)$) plus the impermeability of the sidewalls ($x = 0, x = L$):

$$\begin{aligned} P|_{y=0} &= 0, \\ P|_{y=H} &= -\frac{2\sigma}{R}, \\ \frac{\partial P}{\partial x}\Big|_{x=0} &= \frac{\partial P}{\partial x}\Big|_{x=L} = 0. \end{aligned} \tag{2}$$

The coefficient γ in (1) describes the permeability of the medium [7]:

$$\gamma = \frac{\Omega R^2}{8\mu}, \tag{3}$$

where Ω is the porosity of medium (volume ratio of the pore space to the total volume of the material), R is the average pore radius and μ is the dynamic viscosity coefficient of the fluid.

The coefficient γ describes the structural properties of the nanoporous medium. By changing γ values in every grid point, we take into consideration the changes in porosity or/and pore size in the medium and their influence on the shape and transition of the boundary of the front.

On the whole, the numerical calculation procedure consists of two parts. First, by solving linear differential equation (1) we obtain the pressure distribution in the part of the medium which has been permeated by liquid. While pressure and distance values for grid points which are remote from border can be obtained directly from adjacent grid points, calculation of those values for grid points which are adjoined to the border requires an interpolation procedure.

Once the pressure distribution is obtained, we shift the boundary of the front on the basis of the pressure derivatives. Since we consider inhomogeneous nanoporous media, capillary pressure P_u changes with the motion of the front and thus, must be recalculated after each iteration.

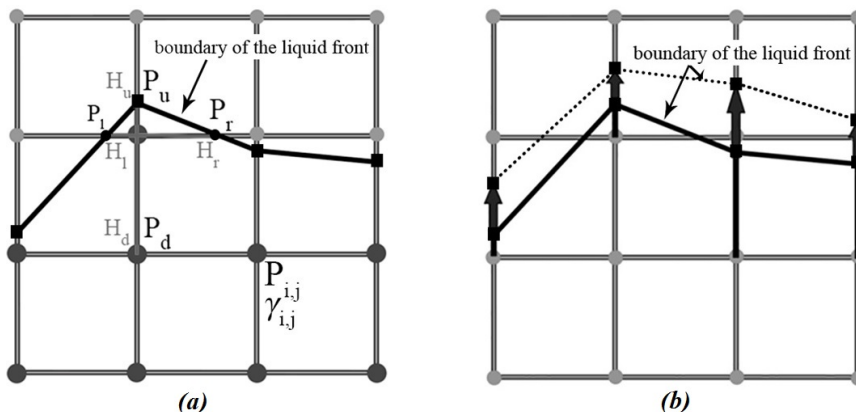


FIG. 2. (a) The numerical calculation procedure, step 1: solving linear differential equation (1) by finite-difference method. Pressure values P_r, P_l and distance values H_u, H_d, H_r, H_l are obtained by linear interpolation between central grid point and upper, lower, right and left grid points accordingly with P_u being the capillary pressure and P_d being the pressure obtained directly from lower grid point. (b) The numerical calculation procedure, step 2: translocation of boundary of the front

Figure 2 shows the result of numerical simulation of the water ($\sigma = 0.07$ N/m, $\mu = 0.8$ mPa s) propagation in nanoporous thin film (20×20 mm) with constant porosity $\Omega = 0.5$ and pore radius changing randomly from 10 to 13 nm.

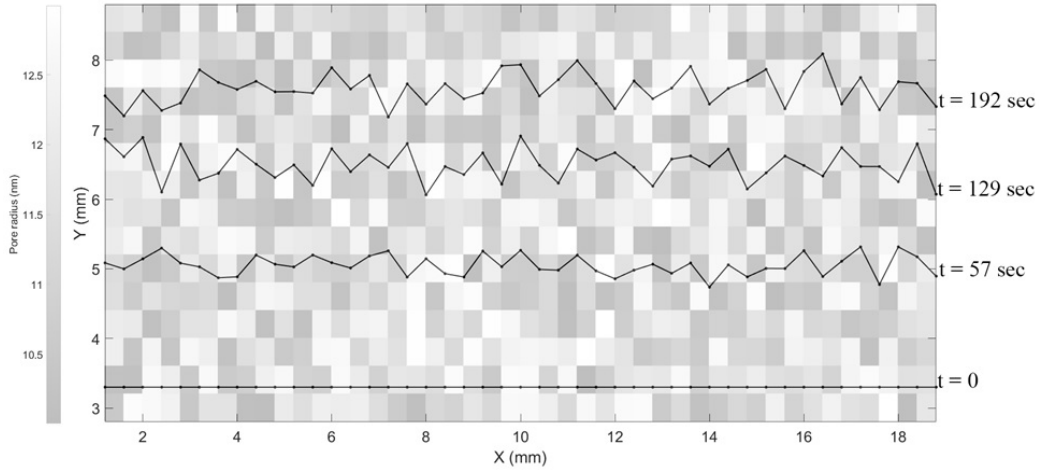


FIG. 3. Evolution of the water front profile in nanoporous thin film (20×20 mm) with constant porosity $\Omega = 0.5$ and pore radius changing randomly from 10 to 13 nm. Darker areas on the background indicate the smaller pore radius and lighter ones, accordingly, larger

Figures 3, 4 show the simulations for the same scenario, only with porosity not being constant, but changing stepwise relative to x . $\Omega = 0.2$ while $x < 6.8$ mm, $\Omega = 0.8$ while $6.8 \leq x < 13.6$ mm and $\Omega = 0.2$ while $x \geq 13.6$ mm. As expected, the increase of porosity leads to additional rise of the front boundary, although while the porosity changes strictly stepwise, the deformation of the boundary of the front is gradually linear.

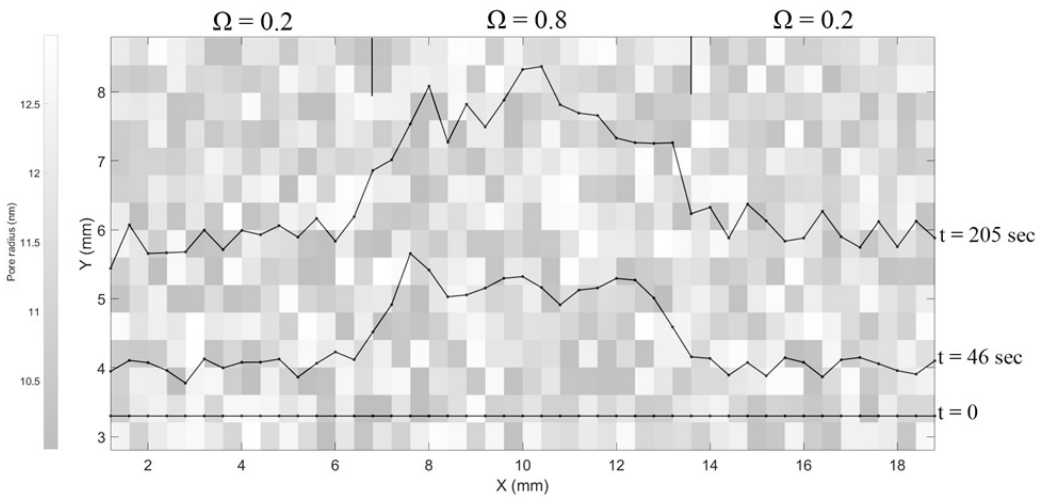


FIG. 4. Evolution of the water front profile in nanoporous thin film (20×20 mm) with porosity changing stepwise from 0.2 to 0.8 and back to 0.2 and pore radius changing randomly from 10 to 13 nm. Darker areas on the background indicate the smaller pore radius and lighter ones, accordingly, larger

3. Evaluation of the parameters of the inhomogeneous nanoporous medium required for reproduction of the specific liquid front propagation

On the basis of the model described above we propose a method of evaluating the parameters of the inhomogeneous nanoporous medium in which the liquid will flow as it is required.

The porosity distribution or/and pore radius distribution in inhomogeneous nanoporous medium can be viewed as polynomial of some degree:

$$R_{x,y}(\Omega_{x,y}) = A_{1,1}x^n + A_{1,2}y^n + A_{2,1}x^{n-1} + A_{2,2}y^{n-1} + \dots + A_{n-1,1}x + A_{n-1,2}y + A_n, \quad (4)$$

where $A_{j,k}$ are the coefficients of the polynomial and x, y are the coordinates of the medium.

Any set of the polynomials' coefficients correspond to a certain evolution of the liquid front profile. The task of finding suitable parameters reduces to the problem of function minimization; the coefficients of the polynomial are being adjusted until the difference between resulting evolution of the liquid front and sought-for one becomes minimal. As a measure of difference, we considered the standard deviation between the points of the reproduced boundary of the front and original one.

An example of such reproduction is shown in Fig. 5. The original evolution of the water front profile was modelled in nanoporous thin film (40×40 mm) with constant porosity $\Omega = 0.5$ and pore radius increasing quadratically from 7 nm to 23 nm relatively to x (mm): $R(\text{nm}) = 9.38 \cdot 10^{-3}x^2 + 2.5 \cdot 10^{-2}x + 7$. The reproduction process has been simulated for the 4th degree polynomial – the resulting reproduced pore size distribution is 4th-degree increase from 7 nm to 28 nm.

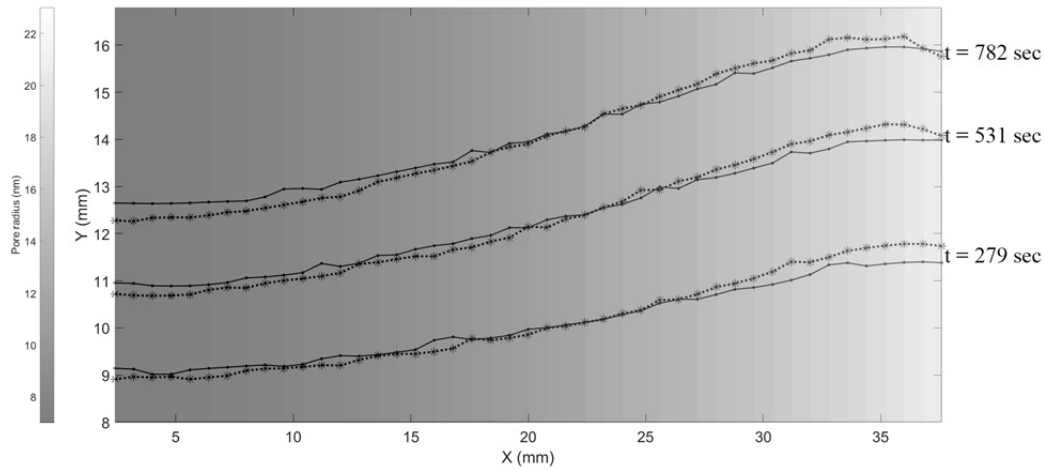


FIG. 5. The original evolution of the water front profile in nanoporous thin film with constant porosity $\Omega = 0.5$ and pore radius increasing quadratically from 7 nm to 23 nm (point markers, solid line) and reproduced evolution front profile in thin film with the same porosity and pore radius distribution being 4th-degree increase from 7 nm to 28 nm (asterisk markers, dotted line). Darker areas on the background indicate the smaller pore radius and lighter ones, accordingly, larger

As can be seen, the results are in good correspondence with each other.

This method can also be used if the required porosity and pore radius distributions are known, but synthesis of such medium is impossible or if for analysis/modelling purposes, the calculation time is too large because of distribution complexity. If simpler distributions are required, this method can be used for finding an alternative solution, suited for the task at hand.

Figure 6 shows the original evolution of the water front profile in a thin nanoporous film (40×40 nm) with constant porosity $\Omega = 0.5$ and pore radius increasing cubically from 8 nm to 20 nm relative to x (mm): $R(\text{nm}) = 13.67 \cdot 10^{-5}x^3 + 15.63 \cdot 10^{-4}x^2 + 2.5 \cdot 10^{-2}x + 8$, which was considered original, and “reproduced” evolution of the water front profile in nanoporous thin film with porosity $\Omega = 0.7$ and pore radius increasing linearly from 6 nm to 13 nm relative to x .

4. Conclusion

The mathematical model which describes the two-dimensional propagation of liquid in inhomogeneous nanoporous media has been presented along with its numerical realization. On the basis of this model a method of evaluating the parameters of the inhomogeneous nanoporous medium resulting in sought-for specific pattern of the liquid front propagation has been proposed. Several scenarios of reproduction of the specific evolutions of the liquid front profile have been presented – it has been shown that proposed method is effective for both

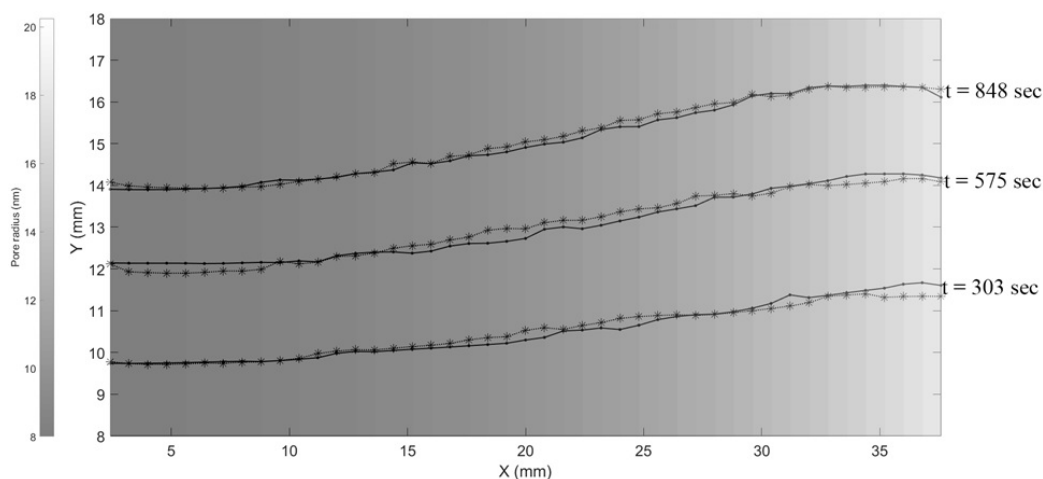


FIG. 6. The original evolution of the water front profile in nanoporous thin film with constant porosity $\Omega = 0.5$ and pore radius increasing cubically from 8 nm to 20 nm (point markers, solid line) and reproduced evolution front profile in thin film with porosity $\Omega = 0.7$ and pore radius increasing linearly from 6 nm to 13 nm (asterisk markers, dotted line). Darker background areas indicate smaller pore radius and lighter ones, accordingly, larger

evaluating the needed parameters as accurately as possible (which can be used for further mathematical analysis and modelling) and finding distributions which can be synthesized with greater ease at lower costs.

References

- [1] Solomatin A.S., Yakovlev R.Yu., Efremenkova O.V., Sumarukova I.G., Kulakova I.I., Lisichkin G.V. Antibacterial activity of Amikacin-immobilized detonation nanodiamond. *Nanosystems: physics, chemistry, mathematics*, 2017, **8**(4), P. 531–534.
- [2] Sun C.Y., Qin C., Wang C.G., Su Z.M., Wang S., Wang X.L., Yang G.S., Shao K.Z., Lan Y.Q., Wang E.B. Chiral Nanoporous Metal-Organic Frameworks with High Porosity as Materials for Drug Delivery. *Advanced Materials*, 2011, **53**, P. 5629–5632.
- [3] Cardea S., Pisanti P., Reverchon E. Generation of chitosan nanoporous structures for tissue engineering applications using a supercritical fluid assisted process. *The Journal of Supercritical Fluids*, 2010, **54**, P. 290–295.
- [4] Hu K, Lan D, Li X and Zhang S. Electrochemical DNA Biosensor Based on Nanoporous Gold Electrode and Multifunctional Encoded DNA-Au Bio Bar Codes. *Analytical Chemistry*, 2008, **80**(23), P. 9124–9130.
- [5] Almjashveva O.V., Garabadzhiu A.V., Kozina Yu.V., Litvinchuk L.F., Dobritsa V.P. Biological effect of zirconium dioxidebased nanoparticles. *Nanosystems: physics, chemistry, mathematics*, 2017, **8**(3), P. 391–396.
- [6] Conner W.C., Fraissard J. *Fluid Transport in Nanoporous Materials: Proceedings of the NATO Advanced Study Institute, held in La Colle sur Loup, France, 16-28 June 2003* (Nato Science Series II:). Springer, 2006, 686 p.
- [7] Scheidegger A.E. *The Physics of Flow Through Porous Media*. University of Toronto Press, Toronto, 1974, 353 p.

Thermal stability of magnetic states in submicron magnetic islands

S. Y. Liashko^{1,2}, I. S. Lobanov¹, V. M. Uzdin^{1,3}, H. Jónsson^{2,4}

¹ITMO University, Kronverkskiy, 49, St. Petersburg, 197101, Russia
Kronverkskiy, 49, St. Petersburg, 197101, Russia

²Science Institute and Faculty of Physical Sciences, University of Iceland
107 Reykjavík, Iceland

³St. Petersburg State University, St. Petersburg, 198504, Russia

⁴Center for Nonlinear Studies, Los Alamos, NM 87545, USA

sergei.liashko@gmail.com, lobanov.igor@gmail.com, v_uzdin@mail.ru, hj@hi.is

PACS 75.75.-c, 75.75.Jn, 75.60.Jk

DOI 10.17586/2220-8054-2017-8-5-572-578

The lifetime of magnetic states in single domain micromagnetic islands is calculated within the harmonic approximation to transition state theory. Stable magnetic states, minimum energy paths between them and first order saddle points determining the activation energy are analyzed and visualized on two-dimensional energy surfaces. An analytical expression is derived for the pre-exponential factor in the Arrhenius rate expression for the reversal of the magnetic moment when the external field is directed either along the anisotropy axis or perpendicular to it.

Keywords: pre-exponential factor, magnetic islands, activation energy, rate theory, spin ice.

Received: 19 September 2017

Revised: 14 October 2017

1. Introduction

The stability of magnetic states with respect to thermal fluctuations and external perturbations is an important topic in fundamental science as well as for technological applications [1, 2]. Thermal stability is a particularly important issue in the context of nanoscale information storage devices. The thermal stability of the magnetic states decreases as the size of such devices is reduced. Estimates of the rate of magnetic transitions are, therefore, important when designing such systems.

In this context, thermally-activated magnetic transitions are rare events on the time scale of oscillations of the magnetic moments, making direct simulations of spin dynamics an impractical way to estimate the lifetime. This separation of time scales, however, makes it possible to apply statistical approaches such as transition state theory (TST) [3] or Kramers theory [4]. The transitions are slow enough that a Boltzmann distribution is established and maintained in the initial state of the system. Within the harmonic approximation to TST (HTST) [5] and within Kramers theory, the activation energy of a transition is given by the energy difference between the local minimum on the energy surface corresponding to the initial state and the highest energy on the minimum energy path (MEP) connecting the initial and final state minima. The MEPs between minima are the transition paths of largest statistical weight and characterize the mechanism of the corresponding transitions. A maximum along an MEP corresponds to a first order saddle point on the energy surface and gives an estimate of the activation energy within HTST. In adaptations of these rate theories to magnetic systems [6–12], the magnitude of the magnetic vectors is either assumed to be constant as orientation changes, or it is treated as a fast variable obtained from self-consistency calculations for fixed values of the slow variables specifying orientation [13]. The energy surface of a system of N magnetic moments is then a function of $2N$ degrees of freedom defining the orientation of the magnetic moments.

If all degrees of freedom in the system can be included within the harmonic approximation (no zero modes, i.e. degrees of freedom for which the energy is constant) HTST and Kramers estimate give an Arrhenius expression for the rate constant, $k(T) = f_0 \exp[-\Delta E/k_B T]$ where ΔE is the energy difference between the relevant first order saddle point and the initial state minimum. The pre-exponential factor, f_0 , often referred to as the attempt frequency, can be determined by calculating the eigenvalues of the Hessian matrix, the matrix of second derivatives of the energy with respect to the angles specifying the orientation of the magnetic moments, at the first order saddle point and at the initial state minimum [11].

While the activation energy for magnetic transitions has frequently been calculated, fewer estimates of the pre-exponential factor have been reported. Brown [6, 7] estimated the pre-exponential factor for remagnetization

transitions in a single domain, uniaxial magnetic particle to be on the order of $10^9 - 10^{12} \text{ sec}^{-1}$. The size and shape of the particle as well as the materials properties will affect the value. Experimental measurements by Wernsdorfer et al. [14] on 30 nm diameter Co nanoparticles gave an estimate of $4 \times 10^9 \text{ sec}^{-1}$.

Recently, the HTST approach has been used to estimate the pre-exponential factor as well as the activation energy for various magnetic transitions. For remagnetization transitions in small Fe nanoislands on W(110), significantly larger values of the pre-exponential factor were obtained, ranging from 10^{13} to 10^{18} sec^{-1} , depending on the size and shape of the islands [15]. The higher range of values was found where the remagnetization occurs via formation of a temporary domain wall ('soliton' mechanism [2]). Experimental estimates for islands falling within a more limited range in shape and size are in close agreement with the calculated values [16]. An HTST estimate for larger permalloy islands used in kagome spin ice systems [17] gave a smaller value, $9.9 \times 10^8 \text{ sec}^{-1}$ [18] while analysis of the experimental data had assumed a value of 10^{12} sec^{-1} [17].

On the other hand, HTST calculations of magnetization reversal in a small Fe cluster at a tip interacting with an antiferromagnetic surface gave values in the range of 10^{12} to 10^{18} sec^{-1} [19], while previous analysis of such measurements had assumed a pre-exponential factor of 10^9 sec^{-1} [20]. Since the values of the pre-exponential factor quoted here range over several orders of magnitude, it is clearly important to carry out calculations based on the energy landscape characterizing the magnetic system of interest, rather than just assuming some value *a priori*.

Calculations of the value of the pre-exponential factor using HTST are in principle straightforward, even when the energy of the system is obtained from iterative self-consistent calculations [12, 13]. Other examples of HTST calculations of transition rates include magnetic skyrmion annihilation in CoPt(111) films [21], skyrmion lifetime in narrow magnetic tracks [22] and the effect of impurities on skyrmion lifetime [23]. The dimensionality of the energy surface used for those calculations ranged from several hundreds up to tens of thousands. Good agreement has been found between HTST calculations and experimental measurements of lifetimes of both single and double kagome rings when the parameters in the calculations were determined from basic properties of a single island and no adjustment made to fit the data [18].

While robust methods are available for finding MEPs in complex magnetic systems [24, 25], the visualization of the transition mechanism is in general a difficult task. To simplify the problem, one can consider a projection of the multidimensional surface on a two-dimensional surface, where the energy is given by a two-parameter function specifying the orientation of the magnetic moments in the system. This has, for example, been done in studies of magnetization reversals in an exchange spring magnet, where the mechanism was described as propagation of a temporary domain wall along the soft magnet toward the interface with the hard magnet and beyond [26]. The position and the width of the wall are the two parameters used to parametrize the projection of the energy surface.

A particularly simple and yet important example of a magnetic system is a single domain magnetic particle with shape anisotropy, possibly in the presence of a magnetic field. This system has been studied over a long period of time and is often referred to as a Stoner-Wohlfarth particle [27]. It is, for example, relevant for modeling of transitions in artificial spin ice systems which consist of arrays of magnetic islands on a solid surface. The energy of the magnetic particle can be described by two angles in a spherical coordinate system so the energy surface can be visualized easily. Previously, thermal effects on the lifetime of the magnetic states of such a particle have been studied using kinetic equations [7] and by calculations of the smallest non-vanishing eigenvalue of the Fokker-Plank equation [28]. Theoretical and experimental studies of the effect of temperature on dynamic hysteresis [29] have been carried out as well as studies of the effect of thermal fluctuations on magnetic anisotropy determinations [30]. However, the dependence of the pre-exponential factor in the rate constant on the size and shape of the magnetic particle as well as the materials properties is not well known and, as mentioned above, analysis of experimental data often relies on assumed values rather than accurate estimates.

In the present article, we report HTST calculations of the lifetime of magnetic states of a single domain magnetic particle with shape anisotropy with and without an applied magnetic field. The activation energy and pre-exponential factor for magnetic transitions are reported for various values of the anisotropy parameters. For the cases where the applied magnetic field is directed either along the anisotropy axis or perpendicular to it, explicit analytical expressions are obtained for the pre-exponential factor as well as the activation energy.

2. Model

We will consider a single domain magnetic island supported on a solid surface in the presence of an external magnetic field \mathbf{H} . The direction of the magnetic moment of the island is determined by two angles, θ and ϕ , as shown in Fig. 1. The direction of the magnetic field will be characterized by angles θ_H and ϕ_H .

The energy density can be written as the sum of an anisotropy term and a Zeeman term

$$E/V = E_{anis}/V + E_Z/V. \quad (1)$$

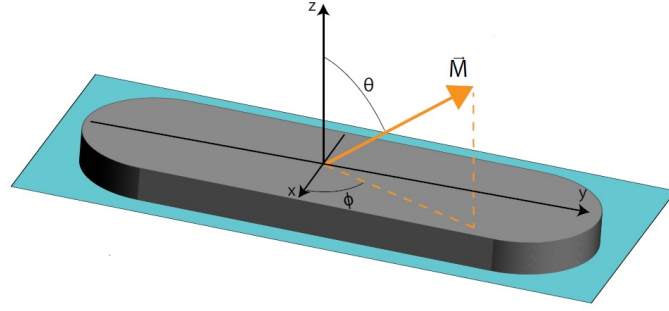


FIG. 1. Single domain magnetic island on a solid surface. \vec{M} is the total magnetic moment of the island and its direction with respect to the anisotropy axis and the surface normal is given by the spherical polar angles θ and ϕ .

Here, the anisotropy term can be written as

$$E_{anis}/V = -K_1 \sin^2 \theta \sin^2 \phi + K_2 \cos^2 \theta, \quad (2)$$

where K_1 and K_2 are anisotropy constants. For a permalloy island in a spin ice structure [17], $K_1 > 0$ and $K_2 > 0$ describe easy axis shape anisotropy and easy plane shape anisotropy, respectively. For CoPt islands [31,32], there is an intrinsic out of plane anisotropy and $K_2 < 0$ whereas $K_1 \approx 0$ due to the round shape of the islands. The same system can be described by $K_1 < 0$ and $K_2 \approx 0$ when the y -axis is chosen to be perpendicular to the island plane.

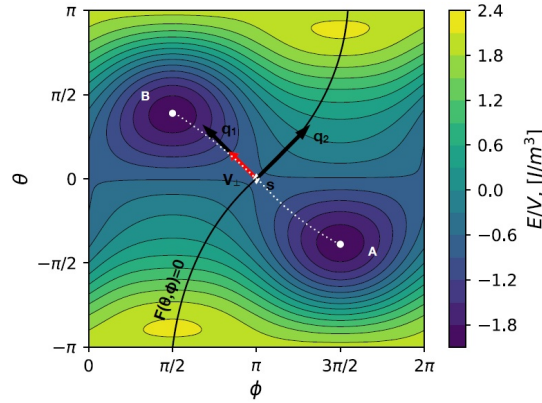


FIG. 2. Energy surface determined by eqs. (1-3) for parameters mimicking CoPt islands [31,32], $c = 1.3$ and $h = 1.8$ with magnetic field $H = 1.33$ MA/m in a direction given by $\theta_H = \pi/10$ and $\phi_H = \pi/2$ (the parameters used in the calculations are $M_0 = 836$ kA/m, $K_1 = 386$ kJ/m³ and $K_2 = 501.8$ kJ/m³). The local minima corresponding to the two stable states, A and B, are marked with white disks and the minimum energy path connecting them is shown with a white dotted line. The first order saddle point is marked with s and a dividing surface separating the A and B states, defined by $F(\theta, \phi) = 0$, is shown with a black line. The velocity perpendicular to the dividing surface, V_{\perp} , near the saddle point is shown with a red arrow. The two normal mode vectors at the saddle point are shown as black arrows labeled q_1 and q_2 .

The Zeeman energy is given by the equation

$$E_Z/V = -\mu_0 H M_0 (\sin \theta \sin \theta_H \sin \phi \sin \phi_H + \sin \theta \sin \theta_H \cos \phi \cos \phi_H + \cos \theta \cos \theta_H), \quad (3)$$

where M_0 is the magnetization of the material and H is the magnetic field strength.

An example energy surface determined by eq. (1-3) is depicted in Fig. 2. The values of parameters are $c \equiv K_2/K_1 = 1.3$ and $h \equiv \mu_0 M_0 H / 2K_1 = 1.8$ (The parameters used in the calculations shown in Fig. 2 are $M_0 = 836$ kA/m, $K_1 = 386$ kJ/m³ and $K_2 = 501.8$ kJ/m³. In the calculations shown in Fig. 3 the value of K_2 is different, 116 kJ/m³, to roughly correspond to CoPt islands [31,32]), and the magnetic field is chosen to have strength of $H = 1.33$ MA/m and direction given by $\theta_H = \pi/10$ and $\phi_H = \pi/2$. There are two local minima

A and B on the energy surface corresponding to the stable magnetic states. The dividing surface separating the orientations that correspond to the A and B states can be represented as a continuous curve $F(\theta, \phi) = 0$. The MEP between the stable states was found using the geodesic nudged elastic band method [24], a generalization of the frequently used NEB method for atomic rearrangements [33]. The exact position of the first order saddle point was determined with the climbing image algorithm [34].

When the magnetic field is applied along or perpendicular to the easy axis and in the plane of the island, the energy surface is more symmetric and the values of the angles corresponding to stable states, the MEP and saddle point can be obtained analytically. Fig. 3 shows such a case for a magnetic field of $H = 100$ kA/m. If the field is directed perpendicular to the easy axis (the y-axis), the local minima are at $\theta = \pi/2$ and $\phi = \pi \pm \arccos h$. The value of θ is constant along the MEP and the saddle point is at $\theta = \pi/2$, $\phi = \pi$. The activation energy is the same in this case for transitions in both directions $\Delta E/V = K_1(1-h)^2$. If the field is directed parallel to the easy axis, the local minima are at $\theta = \pi/2$ and $\phi = \pi \pm \pi/2$ and the saddle point is at $\theta = \pi/2$, $\phi = \pi + \arcsin(-h)$.

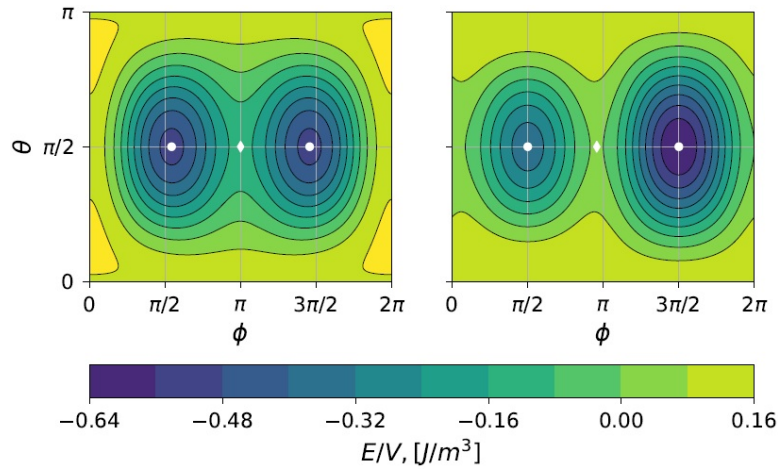


FIG. 3. Energy surface of a single domain magnetic island with parameter values the same as for Fig. 2 except that $c = 0.3$ and the field strength is $H = 100$ kA/m (the parameters used in the calculations are $M_0 = 836$ kA/m, $K_1 = 386$ kJ/m³ and $K_2 = 116$ kJ/m³). The field is pointing perpendicular to the easy axis (the y-axis) on the left side, but parallel to the easy axis on the right side. The local minima and the first order saddle point are marked with white dots.

The two wells corresponding to the stable states are not equally deep. For transitions from the metastable state to the ground state, the activation energy is again $\Delta E/V = K_1(1-h)^2$. Note that the positions of the minima and saddle point as well as the activation energy do not depend on the in-plane anisotropy, K_2 . The direction of the MEP is along $\theta = \pi/2$, also independent of K_2 . However, K_2 affects the shape of the energy surface, the variation of the energy with respect to θ when ϕ is constant, so the rate constant ends up being dependent on K_2 , see below.

3. Rate constant

Within TST, the rate of transitions can be found as the product of the probability of reaching the transition state, a thin ribbon of configuration space around the dividing surface, $F(\theta, \phi) = 0$, and the flux out of the transition state. The key approximation of TST is that a dynamical trajectory starting from the initial state only crosses the dividing surface once until the system thermalizes in the product state. Recrossing events during the traversal over the energy barrier are neglected. Dynamical trajectories started at the transition state, can be used to correct the TST estimate of the rate constant. The TST estimate of the rate constant is

$$k^{TST} = \frac{1}{Z} \iint_S e^{-E(\theta, \phi)/k_B T} V_{\perp} \sin \theta d\theta d\phi, \quad (4)$$

where S denotes the dividing surface and

$$Z = \iint_A e^{-E(\theta, \phi)/k_B T} \sin \theta d\theta d\phi \quad (5)$$

is the configuration integral for the system in the initial state, A, and V_{\perp} is the projection of the velocity vector, \vec{V} , onto the local normal of the dividing surface (that points to the final state B),

$$V_{\perp} = \frac{\nabla \vec{F}}{\|\nabla \vec{F}\|} \cdot \vec{V}. \quad (6)$$

When the harmonic approximation is used, i.e. in HTST, the dividing surface is taken to be a hyperplane going through the first order saddle point with normal pointing along the MEP. A quadratic approximation of the energy surface in terms of θ and ϕ around the initial state minimum and the first order saddle point are used to estimate the activation energy and the flux out of the transition state. In order to eliminate mixed terms in the quadratic approximation, it is convenient to define a new coordinate system in terms of the eigenvectors of the Hessian matrix, the vibrational normal coordinates q_1^{β} and q_2^{β} , where $\beta = s$ at the saddle point and $\beta = m$ at the initial state minimum

$$E(q_1^{\beta}, q_2^{\beta}) = E(\theta_{\beta}, \phi_{\beta}) + \frac{1}{2}[\epsilon_{\beta 1}(q_1^{\beta})^2 + \epsilon_{\beta 2}(q_2^{\beta})^2], \quad (7)$$

where, $\epsilon_{\beta 1}$ and $\epsilon_{\beta 2}$ are the eigenvalues of the Hessian matrix at the saddle point or initial state minimum. The velocity is given by the Landau-Lifshitz equation, which in the vicinity of the first order saddle point, can be written in terms of the normal coordinates as

$$\dot{q}_1^s = \frac{\gamma \epsilon_{s2}}{VM_0 \sin \theta_s} q_2^s \quad (8)$$

and

$$\dot{q}_2^s = -\frac{\gamma \epsilon_{s1}}{VM_0 \sin \theta_s} q_1^s. \quad (9)$$

where γ is the gyromagnetic ratio. If at the saddle point $\epsilon_{s1} < 0$ and $\epsilon_{s2} > 0$, then $V_{\perp} = \dot{q}_1^s \sin(\theta_s)$. Otherwise, if $\epsilon_{s1} > 0$ and $\epsilon_{s2} < 0$, then $V_{\perp} = \dot{q}_2^s \sin \theta_s$. The integral over the dividing surface in eqn. (4) needs to be carried out only for regions where $V_{\perp} > 0$, i.e. for trajectories that are heading away from the initial state and towards the product state [11]. The velocity is zero at the saddle point, but non-zero contributions to the flux are obtained from one half of the hyperplanar dividing surface. Integration gives

$$k^{HTST} = \frac{\gamma \sqrt{\epsilon_{m1} \epsilon_{m2}}}{2\pi M_0 V \sin \theta_m} e^{-\Delta E/k_B T}. \quad (10)$$

It is interesting to note that the pre-exponential factor does not depend on the Hessian at the saddle point, only at the initial minimum through the eigenvalues ϵ_{m1} and ϵ_{m2} . This occurs for two-dimensional energy surfaces because $V_{\perp} > 0$ is proportional to the one positive eigenvalue of the Hessian at the saddle point, but the same eigenvalue also appears in the denominator and thus cancels out. The pre-exponential factor also does not depend on the volume, V , because the eigenvalues of the Hessian at the minimum are proportional to the volume, and the volume also appears in the denominator, so it cancels out.

For the cases when the applied magnetic field is directed either parallel or perpendicular to the easy axis, an analytical expression for the rate constant in terms of the parameters characterizing the energy surface can be obtained. When the magnetic field is perpendicular to the easy axis, the result is

$$k_{\perp}^{HTST} = f_{0\perp} e^{-\Delta E/k_B T} = \frac{\gamma K_1 \sqrt{(1-h^2)(2c+1)}}{\pi M_0} \exp\left[-\frac{VK_1}{k_B T}(1-h)^2\right], \quad (11)$$

and when it is parallel to the easy axis, the result is

$$k_{\parallel}^{HTST} = f_{0\parallel} e^{-\Delta E/k_B T} = \frac{\gamma K_1 \sqrt{(1-h)(2c-h+1)}}{\pi M_0} \exp\left[-\frac{VK_1}{k_B T}(1-h)^2\right]. \quad (12)$$

Figure 4 shows the dependence of the pre-exponential factor, f_0 , on the anisotropy parameters, K_1 and K_2 in the absence of an external magnetic field, when $M_0 = 200$ kA/m. A decrease of K_1 leads to a decrease of the pre-exponential factor but reduces at the same time the activation energy. These results show that a value of 10^9 Hz as was assumed in refs. [31,32] gives reasonable approximation.

4. Conclusion

We have presented here simple equations that can be easily evaluated to estimate to estimate the rate constant for remagnetization transitions in a single domain magnetic particle where the transition occurs by uniform rotation. While the saddle point needs to be found in order to estimate the activation energy, ΔE , the eigenvalues of the Hessian are not needed there, only at the initial state minimum.

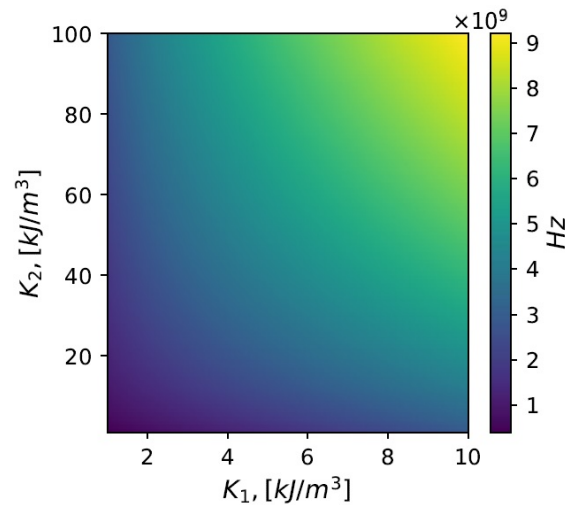


FIG. 4. Dependence of the pre-exponential factor on the anisotropy parameters K_1 and K_2 when the saturation magnetization is $M_0 = 200$ kA/m and no external magnetic field is present, $H = 0$

Especially simple analytical equations were obtained for the cases where the applied field is directed in either a parallel or perpendicular manner to the easy axis, or is absent. All that is needed to evaluate the rate constant in such cases is the saturation magnetization of the material and the two anisotropy constants. The rate constant turns out to be independent of the volume of the magnetic particle.

These results should be of value for theoretical estimates of magnetic transition rates in, for example, artificial spin ice systems, where previously, values of the pre-exponential factor have usually simply been assumed to have some value without relating to the basic properties of the individual islands. The approach presented here has already been shown to be accurate in calculations of the lifetime of single and double kagome rings [18].

For large enough islands compared with the strength of the magnetic interaction between the spins within the island, a uniform rotation is not the preferred transition mechanism, but rather a temporary domain wall. The results presented here do not apply to such situations. Calculations of Fe islands indicate that the pre-exponential factor can be substantially larger in such cases [15]. The reason may be that lower frequency modes then appear at the saddle point. Further analysis of the systematic trends in the pre-exponential factor in such cases as a function of the materials properties and the size and shape of the islands remains a topic of future studies.

Also, for low enough temperatures, quantum mechanical tunneling as opposed to the over-the-barrier mechanism considered here, will become the preferred transition mechanism. Recently, general equations for estimating the onset temperature for tunneling have been presented [35,36] and can be used to give a lower bound on the temperature range for which the equations presented here remain reliable approximations.

5. Acknowledgements

This work was supported by the Icelandic Research Fund, the Academy of Finland (grant 278260) and the Government of the Russian Federation (grant 074-U01) and by grant 16-11-10330 of Russian Science Foundation.

References

- [1] Coffey W.T., Garanin D.A. and McCarthy D.J. Crossover formulas in the Kramers theory of thermally activated escape rates - Application to spin systems. *Advances in Chemical Physics*, 2001, **117**, P. 483.
- [2] Braun H.B. Topological effects in nanomagnetism: from superparamagnetism to chiral quantum solitons. *Advances in Physics*, 2012, **61**, P. 1.
- [3] Wigner E. The transition state method. *Trans. Faraday Soc.*, 1938, **34**, P. 29–41.
- [4] Kramers H.A. Brownian motion in a field of force and the diffusion model of chemical reactions. *Physica*, 1940, **7**, P. 284–304.
- [5] Vineyard G.H. Frequency factors and isotope effects in solid state rate processes. *J. Phys. Chem. Solids*, 1957, **3**, P. 121.
- [6] Brown Jr.W.F. Thermal fluctuations of a single-domain particle. *Phys. Rev.*, 1963, **130**, P. 1677.
- [7] Brown Jr.W.F. Thermal Fluctuations of Fine Ferromagnetic Particles. *IEEE Trans. Magn.*, 1979, **MAG-15**, P. 1196–1208.
- [8] Braun H.-B. Kramers's rate theory, broken symmetries and magnetization reversal. *J. Appl. Physics*, 1994, **76**, P. 6310–6315.
- [9] Visscher P.B., Zhu R. Low-dimensionality energy landscapes: Magnetic switching mechanisms and rates. *Physica B*, 2012, **407**, P. 1340–1344.
- [10] Fiedler G., Fidler J., Lee J., Schrefl T., Stamps R.L., Braun H.B. and Suess D., Direct calculation of the attempt frequency of magnetic structures using the finite element method. *J. Appl. Phys.*, 2012, **111**, P. 093917(7).

- [11] Bessarab P.F., Uzdin V.M. and Jónsson H. Harmonic Transition State Theory of Thermal Spin Transitions. *Phys. Rev. B*, 2012, **85**, P. 184409(4).
- [12] Bessarab P.F., Uzdin V.M. and Jónsson H. Potential Energy Surfaces and Rates of Spin Transitions. *Z. Phys. Chem.*, 2013, **227**, P. 1543–1557.
- [13] Bessarab P.F., Uzdin V.M. and Jónsson H. Calculations of magnetic states and minimum energy paths of transitions using a noncollinear extension of the Alexander-Anderson model and a magnetic force theorem. *Phys. Rev. B*, 2014, **89**, P. 214424(12).
- [14] W. Wernsdorfer, E. Bonet Orozco, K. Hasselbach, A. Benoit, B. Barbara, N. Demoncy, A. Loiseau, H. Pascard and D. Maily. Experimental evidence of the Néel-Brown model of magnetization reversal. *Phys. Rev. Lett.*, 1997, **78**, P. 1791.
- [15] Bessarab P.F., Uzdin V.M. and Jónsson H. Size and Shape Dependence of Thermal Spin Transitions in Nanoislands. *Phys. Rev. Lett.*, 2013, **110**, P. 020604(5).
- [16] Krause S., Herzog G., Stapelfeldt T., Berbil-Bautista L., Bode M., Vedmedenko E. Y., Wiesendanger R. Magnetization reversal of nanoscale islands: How size and shape affect the Arrhenius Prefactor. *Phys. Rev. Lett.*, 2009, **103**, P. 127202(4).
- [17] Farhan A., Derlet P.M., Kleibert A., Balan A., Chopdekar R.V., Wyss M., Anghinolfi L., Nolting F., Heyderman L.J. Exploring hyper-cubic energy landscapes in thermally active finite artificial spin-ice systems. *Nature Physics*, 2013, **9**, P. 375(8).
- [18] Liashko S.Y., Uzdin V.M. and Jónsson H. The effect of temperature and external field on transitions in elements of kagome spin ice. *New J. Phys.*, 2017, (accepted) DOI: 10.1088/1367-2630/aa8b96.
- [19] Ivanov A., Bessarab P.F., Uzdin V.M. and Jónsson H. Magnetic exchange force microscopy: Theoretical analysis of induced magnetization reversals. *Nanoscale*, 2017, **9**, P. 13320–13325.
- [20] Schmidt R., Schwarz A., Wiesendanger R. Magnetization switching utilizing the magnetic exchange interaction. *Phys. Rev. B*, 2012, **86**, P. 174402(6).
- [21] Lobanov I.S., Jónsson H. and Uzdin V. M. Mechanism and activation energy of magnetic skyrmion annihilation obtained from minimum energy path calculations. *Phys. Rev. B*, 2016, **94**, P. 174418(7).
- [22] Uzdin V.M., Potkina M.N., Lobanov I.S., Bessarab P.F., Jónsson H. The effect of confinement and defects on the thermal stability of skyrmions. *Physica B*, 2017, (in press), DOI; 10.1016/j.physb.2017.09.040.
- [23] Uzdin V.M., Potkina M.N., Lobanov I.S., Bessarab P.F., Jónsson H. Energy surface and lifetime of magnetic skyrmions. *J. Magn. Magn. Mat.*, (accepted). Manuscript available at <https://arxiv.org/pdf/1707.00124.pdf>.
- [24] Bessarab P.F., Uzdin V.M. and Jónsson H. Method for finding mechanism and activation energy of magnetic transitions, applied to skyrmion and antivortex annihilation. *Comp. Phys. Commun.*, 2015, **196**, P. 335–347.
- [25] Bessarab P. F. Comment on “Path to collapse for an isolated Néel skyrmion”. *Phys. Rev. B*, 2017, **95**, P. 136401(2).
- [26] Moskalenko M., Bessarab P.F., Uzdin V.M. and Jónsson H. Qualitative Insight and Quantitative Analysis of the Effect of Temperature on the Coercivity of a Magnetic System. *AIP Advances*, 2016, **6**, P. 025213(8).
- [27] Stoner E.C., Wohlfarth E.P. A mechanism of magnetic hysteresis in heterogeneous alloys. *Phil. Trans. Roy. Soc. A*, 1948, **240**, P. 599–642.
- [28] Coffey W.T, Crothers D.S.F., Dormann J.L., Kalmykov Y.P., Kennedy E.C., Thermally activated relaxation time of a single domain ferromagnetic particle subjected to a uniform field at an oblique angle to the easy axis: Comparison with experimental observations. *Phys. Rev. Lett.*, 1998, **80**, P. 5655–5568.
- [29] Poperechny I.S., Raikher Yu.L., Stepanov V.I. Dynamic magnetic hysteresis in single-domain particles with uniaxial anisotropy. *Phys. Rev. B*, 2010, **82**, P. 174423(14).
- [30] Franco V., Conde A. Thermal effects in a StonerWohlfarth model and their influence on magnetic anisotropy determination. *J. Magn. Magn. Mat.*, 2004, **278**, P. 28–38.
- [31] De Vries J., Bolhuis T., Abelman L. Temperature dependence of the energy barrier and switching field of sub-micron magnetic islands with perpendicular anisotropy. *New J. Phys.*, 2017, (accepted) DOI:10.1088/1367-2630/aa8082.
- [32] Engelen J.B.C., Delalande M., le Febvre A.J., Bolhuis T., Shimatsu T., Kikuchi N., Abelman L., Lodder J.C. Thermally induced switching field distribution of a single CoPt dot in a large array. *Nanotechnology*, 2010, **21**, P. 035703(7).
- [33] Jónsson H., Mills G., Jacobsen K.W. *Classical and Quantum Dynamics in Condensed Phase Simulations*, edited by Berne B.J., Ciccotti G., Coker D.F. (World Scientific, Singapore, 1998), P. 385–404.
- [34] Henkelman G., Uberuaga B.P., Jónsson H. A climbing image nudged elastic band method for finding saddle points and minimum energy paths. *J. Chem. Phys.*, 2000, **113**, P. 9901–9904.
- [35] Vlasov S., Bessarab P.F., Uzdin V.M. and Jónsson H. Classical to quantum mechanical tunneling mechanism crossover in thermal transitions between magnetic states. *Faraday Discuss.*, 2016, **195**, P. 93–109.
- [36] Vlasov S., Bessarab P.F., Uzdin V.M. and Jónsson H. Calculations of the onset temperature for tunneling in multispin systems. *Nanosystems: Physics, Chemistry, Mathematics*, 2017, **8**, P. 454–461.

Vapor phase SERS sensor based on mesoporous silica decorated with silver nanoparticles

A. S. Sarycheva¹, A. A. Semenova², E. A. Goodilin^{2,3,*}

¹Department of Materials Science and Engineering and A. J. Drexel Nanomaterials Institute, Drexel University, Philadelphia, PA 19104, USA

²Lomonosov Moscow State University, Faculty of Materials Science, Lenin Hills, Moscow, 119991, Russia

³Kurnakov Institute of General and Inorganic Chemistry of the Russian Academy of Sciences, Moscow, 119991, Russia

*goodilin@yandex.ru

PACS 61.46.Hk, 62.23.St, 68.35.bd

DOI 10.17586/2220-8054-2017-8-5-579-585

For the first time, nanocomposite colloidosomes of mesoporous silica microspheres decorated with silver nanoparticles have been applied as a highly sensitive vapor phase optical sensors utilizing a semiquantitative analysis of surface-enhanced Raman spectra (SERS). The material was prepared using soft chemistry approaches and benefits from the intrinsic properties of both components: the mesoporous structure of the silica microspheres allows for capillary condensation of target analytes while the silver nanoparticles favor the great enhancement of Raman fingerprints of thus trapped and preconcentrated analytes. This approach seems to be highly promising for the further development of express gas phase sensors for heterocyclic or polycyclic aromatic hydrocarbon pollutants.

Keywords: SERS, silver, nanostructures, nanoparticles, preparation methods, background.

Received: 1 September 2017

Revised: 22 September 2017

1. Introduction

Recently, the rapid development of Surface-enhanced Raman spectroscopy (SERS) is supported greatly by its obvious advantageous features, such as remarkable sensitivity, label-free techniques of use, robust and express practical application routes [1,2]. At the same time, ordinary materials for SERS with ecological, pharmaceutical, biological and medical applications are commonly designed for the analysis of liquid analytes [1–10] while a limited number of actual research efforts has focused on vapor phase detection [11–29]. The latter challenge evidently widens the promising application area of SERS and therefore requires novel approaches for the design of SERS-active materials.

At present, most of the research advantages for SERS in the analysis of gaseous and vapor phases are based on simple chemical sorption of analytes on a highly developed silver or gold surface if they have high affinity to plasmonic nanoparticles being, for example, thiol derivatives or other similar molecules [11,13,14,19,20,25,27,29]. Accordingly, the sensitivity of the analysis becomes even higher if porous silver nanocubes [12], polymer coatings [15], anisotropic nanoparticle aggregates [16,24], metal – organic frameworks [21,26], multihole capillaries [23], graphene oxide surface [28], free – surface microfluidic chips [18], electrodynamic precipitation [17] are applied.

In this paper, nanocomposite colloidosomes of mesoporous silica microspheres [30,31] decorated with silver nanoparticles are applied for the first time as a highly sensitive vapor phase optical sensor utilizing a semiquantitative SERS analysis. We suggest that the material prepared using soft chemistry approaches benefits from the intrinsic properties of both the precursors: the silica microspheres' mesoporous structure allows for capillary condensation of target analytes; the silver nanoparticles favor the significant enhancement of Raman fingerprints of trapped and preconcentrated analytes.

2. Experimental

Highly pure water (Milli-Q, Millipore), tetraethylorthosilicate (TEOS), cetyl trimethylammonium bromide (CTAB), silver (I) nitrate (AgNO_3), sodium citrate, sodium hydroxide (NaOH), ethyl alcohol, methanol, hydrochloric acid (HCl), aqueous ammonia solution, polyvinylpyrrolidone (PVP), sodium borohydride (NaBH_4), ascorbic acid (Aldrich) were used as reagents.

Silica microspheres were synthesized by the Stöber method [30,31] using the ammonia-catalyzed hydrolysis of TEOS at 400 °C for 5 – 10 h with the molar ratio of the components $\text{C}_2\text{H}_5\text{OH} : \text{NH}_3 : \text{TEOS} : \text{H}_2\text{O} =$

63 : 13 : 4 : 1. Typically, to prepare 500 ml of suspension, solution of 367 ml of ethyl alcohol, 101 ml of 25 % ammonia and 10 ml of water was heated up to 40 °C with magnetic stirring (400 rpm) followed by addition of 9 ml of TEOS and maintaining the mixture overnight (12 hrs) to complete hydrolysis and silica microsphere growth. The as-prepared suspension was repeatedly centrifuged (6000 rpm, 15 min) and washed (redispersed) with water to remove residual reagents. Finally, the predried sample was slowly heated up to 550 °C in air (1 °C/min) and held for 5 hrs followed by furnace cooling. Similarly, MCM-41 mesoporous silica microspheres were prepared in the presence of CTAB as a structure-directing surfactant [30,31]. Typically, 7.5 g of CTAB was mixed with 150 ml of pure water and heated up to 40 °C under vigorous stirring. The resulting soap-like semitransparent liquid was kept at room temperature followed by addition of 47 ml of aqueous ammonia (25 – 27 %) and 77 ml of ethyl alcohol under stirring for 15 min. After that, 15 ml of dry TEOS was added under stirring and the mixture was stirred for 20 hrs. The resulting suspension was filtered, washed with pure water and methanol followed by drying for 20 hrs at 90 °C. An additional structure saving preparation stage of surfactant extraction at gentle temperatures was applied to enhance absorption of molecules in a gas state. In the most of cases 1 g of mesoporous silica microspheres was placed into 107 ml of methanol and 2.8 ml of 1 M HCl. The mixture was refluxed at 60 °C for 24 hrs followed by washing with ethanol and drying at 90 °C in air.

Soft chemistry decoration of silica microspheres was performed using their reaction with hot solutions of diamminesilver (I) hydroxide. To obtain diamminesilver (I) hydroxide, 0.1 M aqueous sodium hydroxide was added dropwise to a freshly prepared 0.01 M aqueous silver nitrate solution until complete precipitation of a black-brown silver (I) oxide. Thus, the prepared silver (I) oxide was thoroughly washed with water and dissolved in a two-fold molar excess of a 10 % aqueous ammonia solution, resulting in the formation of 0.01 M diamminesilver (I) hydroxide. The obtained transparent complex solution was filtered through Millex-LCR syringe driven filter units (Millipore, 0.45 mm pores). After that, typically 0.3 g of Stöber silica was redispersed in 10 ml of pure water by ultrasound treatment for 30 min. Such a suspension was mixed in the ratio of 1:1 with the preliminary prepared diamminesilver (I) hydroxide solution, heated at 95 – 97 °C, and held for 0.5 – 2.0 hrs, filtered, repeatedly washed with pure water and dried to prepare yellow-brown powder of mesoporous silica colloidosomes decorated with silver nanoparticles. In a number of cases, silver nanoparticles sizes were increased by their regrowth by additional reduction of silver nitrate with ascorbic acid in the presence of an aqueous suspension of the colloidosomes.

The obtained colloidosomes were characterized by scanning electron microscopy (Carl Zeiss NVision 40) at 0.5 – 5 kV accelerating voltage. The materials dried on alumina plates were examined using Rigaku D/MAX 2500 (Japan) with a rotating copper anode (CuK_{alpha} irradiation, 5 – 80 ° 2 Theta range, 0.02 ° step). Diffraction maxima were indexed using the PDF-2 database. UV-vis absorption spectra were recorded using the UV-vis spectrophotometer Lambda 35 (Perkin-Elmer) with an attached diffuse reflectance accessory. Size distribution and zeta potentials measurements were performed using Malvern Zetasizer Nano ZS. Thermal analysis assisted by evaluation of the exhausted products composition was utilized using the thermal analyzer STA 409 PC Luxx with an attached gas analyzer QMS 403 D *Aëolos* (NETZSCH) at a heating rate of 3 °C/min in air in the temperature range of 30 – 900 °C. BET and BJH analysis were done using the Quantachrome NOVA 4200e setup.

Raman and SERS experiments were performed using the InVia Raman microscope (Renishaw, UK) equipped with a 20 mW 514 nm argon laser and power neutral density filters. All the spectra were collected using ×5 objective, NA 0.15 and 10 – 30 s of acquisition time. A silicon wafer was used for calibration.

3. Results and discussion

Pyridine is a classical model compound for SERS measurements and it is selected in the present paper as a primary analyte because of several important reasons. First of all, this was the first compound detected by SERS in 1973 after its adsorption onto electrochemically deposited silver [32], also, it is known that affinity of pyridine to silver is high enough and the surface layer seems to be strong due to chemical bonding. The compound demonstrates high delocalization of π electrons and this effect, as well known, increases much SERS enhancement of such molecules. The pyridine normal modes with the largest Raman intensity are 983 and 1026 cm^{-1} corresponding to ring breathing; the mode at 598 cm^{-1} is a ring deformation mode; ring stretching modes appear at 1208, 1472 and 1583 cm^{-1} . The most intense peak at 1001 cm^{-1} appear usually in SERS spectra because of a shift by about 20 cm^{-1} due to a chemical interaction with silver surface. Therefore this particular mode could be selected as a reference peak for the estimation of the amount of pyridine. In addition, the boiling point of pyridine at 116 °C favors capillary adsorption. Finally, pyridine is a typical heterocyclic component of crude oil and its content is important to analyze to determine oil quality.

The samples prepared for the SERS analysis of pyridine represent silver – silica nanocomposites with a highly porous structure (Fig. 1). The nucleus of silver clusters are distributed homogeneously after the reaction of silica microspheres with hot diamminesilver (I) solution (Fig. 1(a, b)). Larger silver nanoparticles formed onto microporous

silver colloidosomes are attached to the surface (Fig. 1(c, d)). The overall silver content in the nanocomposites is dependent on preparation parameters in a complex way (Fig. 1(e)), the latter is connected with two competing processes – silver cluster deposition and superficial etching with alkali solution of diamminesilver (I) hydroxide. It seems that silver concentrations of 10 mM and reacting time of 20 – 60 min are suitable conditions for the formation of the nanocomposite. The most preferable treatment procedure of the silica microspheres with hot diamminesilver (I) hydroxide includes the shortest (20 min) reaction time (Fig. 1). As a result, it minimizes silica dissolution and its surface erosion while generation of uniformly distributed superficial silver nanoparticle of 3 – 5 nm remains effective. This is connected with remaining ethoxy groups of silica participating in silver reduction and nanoparticles attachment to the microspheres. The measured surface area of the mesoporous samples exceeds $1100 \text{ cm}^2/\text{g}$ and becomes by about 10 % higher after the surfactant extraction procedure compared to traditional annealing and therefore extraction seems to be a predominant technique for creation of open pores (Fig. 1(f)). The nanocomposite demonstrates plasmon resonance modes around 400 nm typical of isotropic silver nanoparticles (Fig. 1(g)) which is also confirmed either by an XRD analysis (Fig. 1(h)) demonstrating all clear diffraction peaks of cubic metallic silver or probe SERS measurements of a model Rhodamine 6G dye showing most intense Raman modes at low concentrations (Fig. 1(i)). The complex investigation of the colloidosomes thus confirms (Fig. 1) that they represent a SERS-active nanocomposite material with a high surface area.

Such a material is a good candidate for SERS investigation of gaseous phases and it was used then to detect pyridine in the vapor phase at different partial pressures of the analyte to determine a wide range of volumetric concentrations in a carrier gas (heptane) having a low Raman intensities compared to pyridine. Both the organic components, pyridine or heptane, could be absorbed by the colloidosomes but this process seems to be more preferable for pyridine due to its chemical nature while heptane plays the role of an inert diluting component (Fig. 2).

Figure 2 shows typical intensities of a narrow-selected region of raw measurements of the most intense enhanced Raman modes of pyridine, absorbed by the porous structure of the colloidosomes after exposure of the SERS-active material in a gaseous mixture of pyridine and heptane with different partial pressures (volumetric content) of pyridine. It is evident that there is a distinct correlation between the content of pyridine in vapor and the spectral features of this compound measured using plasmonic nanoparticles of silver decorating mesoporous silica. The inset of Fig. 2 demonstrates an almost linear dependence between the SERS intensities and concentrations under optimal measurement conditions at a low concentration end. The detection limit of this compound comprises a better mark than 10 – 100 ppm. It should be noted that this sensitivity level is found for a two-component mixture with heptane which seems to be generally similar with a gaseous atmosphere over some oil reforming products. Probably, a vapor over car fuel will contain, at least, several more components including benzene which would also be absorbed by the colloidosomes and will reveal itself in SERS spectra. However the discussed system is a simpler model example showing a possibility of such an analysis near pyridine safety concentration threshold using the prepared type of SERS materials.

Mesoporous channels, being definitely present in the colloidosomes (Fig. 1), favor capillary condensation of both the organic components of the vapor phase (Fig. 3). Boiling points of pyridine at $116 \text{ }^\circ\text{C}$ and heptane at $98 \text{ }^\circ\text{C}$ are very close and therefore it would be expected that they both will be equally absorbed however a distinct weight loss of about 4 % at $130 - 160 \text{ }^\circ\text{C}$ accompanied by desorption of constituents with a molecular mass of 79 proves that it is mostly pyridine that physically absorbed and releases slightly above its boiling temperature. Another event is observed at $300 - 450 \text{ }^\circ\text{C}$ and this wide temperature range most probably corresponds to oxidation of the residual organic with the formation of N_2 , H_2O , NH_3 , CO_2 , NO_2 and NO . It is not found also that bromine could be evolved from the pores meaning that the extraction procedure was effective and CTAB, which might be a generator of heavy bromine-containing vaporized compounds, is not really present in the colloidosomes. It is also important to note that it is known that thermal oxidation of pyridine studied using a matrix-isolation infrared spectroscopy gives almost similar products [33] as we found in our experiments: carbon monoxide or nitrogen, carbon dioxide, nitric oxides and some others evidencing for oxidation of a pseudoaromatic ring containing a nitrogen atom. In such a case, the molecules found are related to burning to either pyridine or heptane capillary condensed in the mesopores. This is the only phenomenon in this system which can keep organic molecules inside the colloidosomes at temperature as high as $400 \text{ }^\circ\text{C}$.

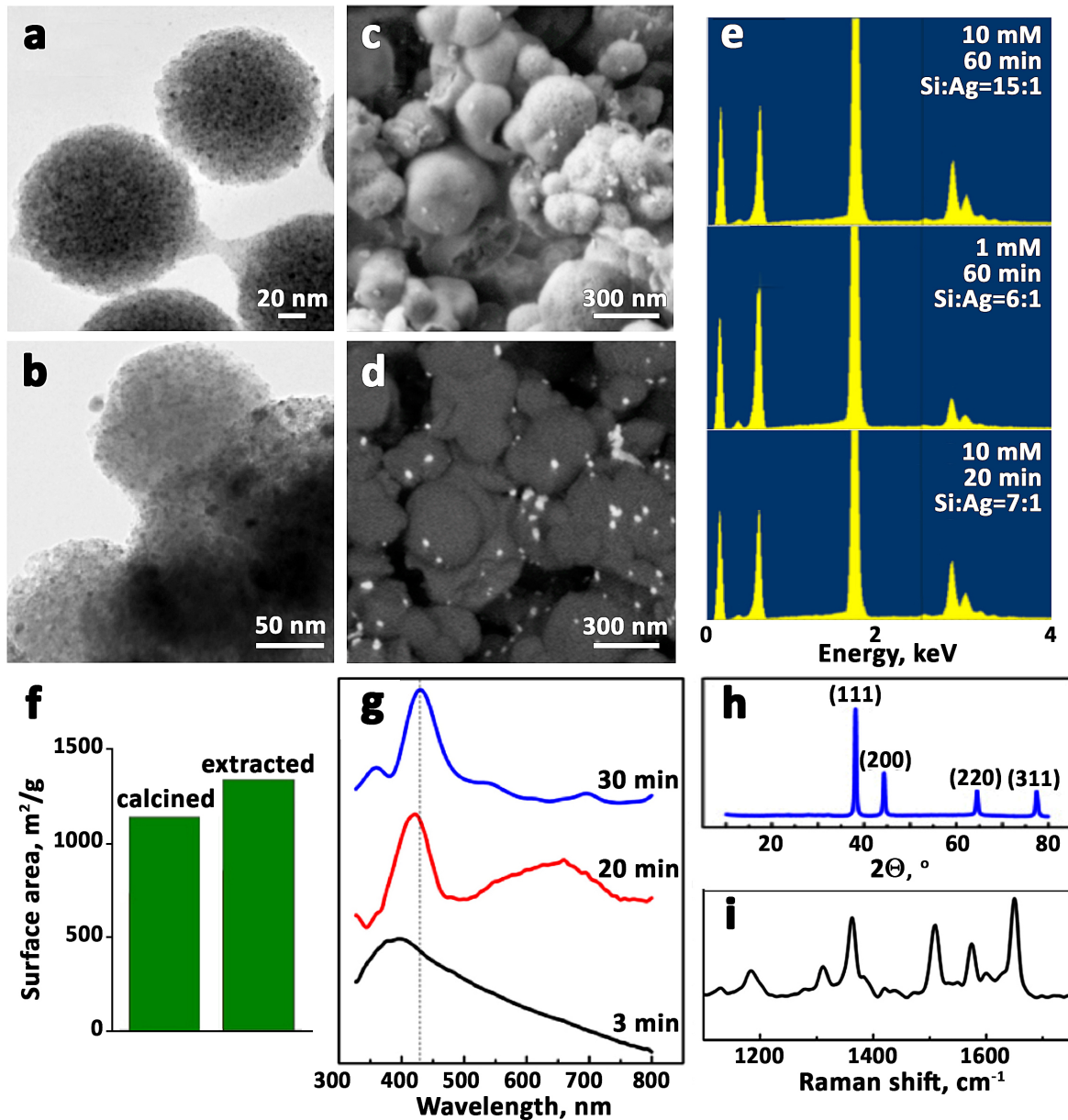


FIG. 1. Colloidosomal material characterization. (a, b) TEM images of silica microspheres decorated with silver nanoparticles; (c, d) SEM micrographs of mesoporous silica in SE and BSE modes demonstrating silver nanoparticle aggregates; (e) EDX analysis with respect to the Si:Ag ratio for the samples with a different preparation history; (f) comparison of porous structure of silica after surfactant thermal destruction or extraction; (g) plasmon resonance modes of the samples with different reaction time of pristine silica with a hot solution of diamminesilver (I) hydroxide; (h) typical XRD pattern of the composite; (i) SERS spectrum of a model dye Rhodamine 6G at 10^{-8} M concentration

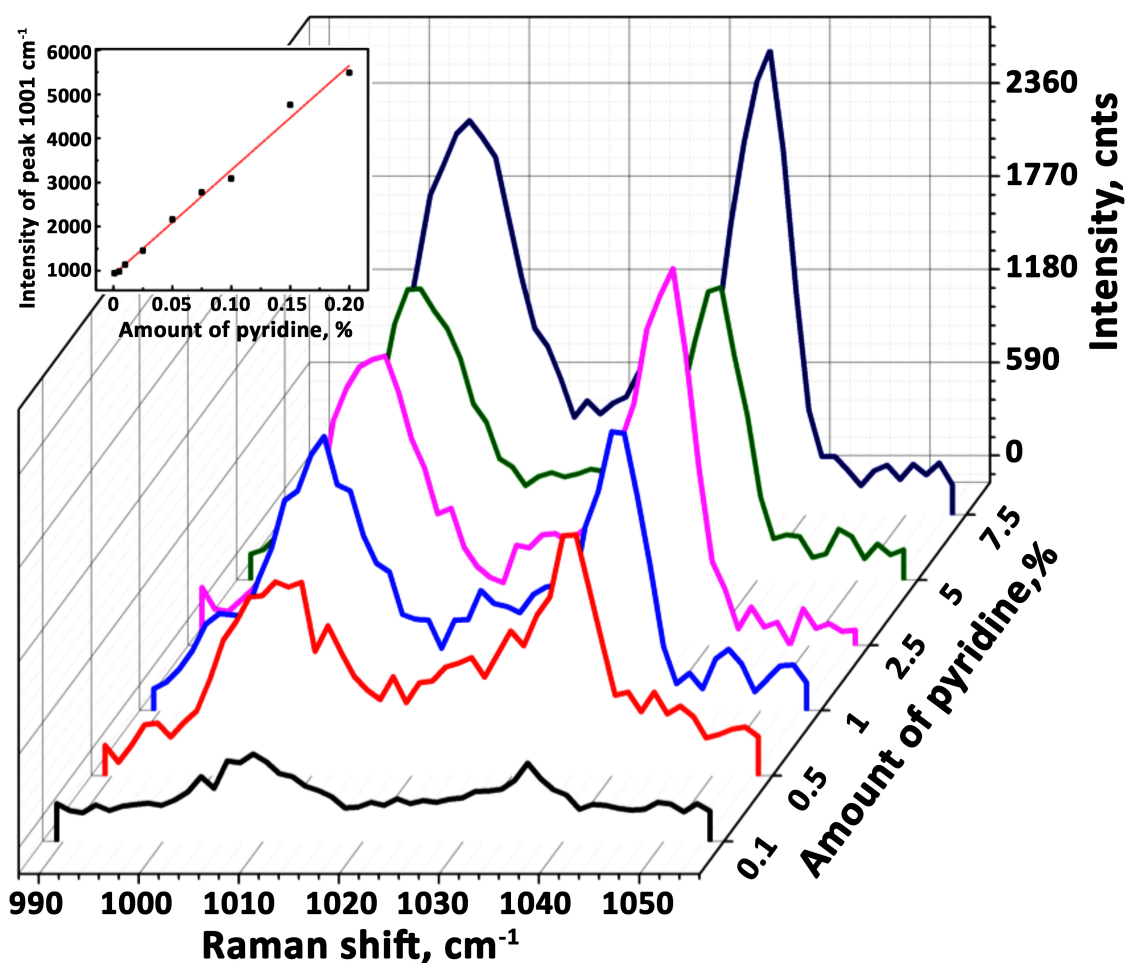


FIG. 2. Experimental data on SERS enhancement of typical spectral modes of pyridine absorbed by silver decorated colloidosomes of mesoporous silica exposed for 0.5 – 1 min in a mixed vapor phase of pyridine and heptane when varying volumetric (molar) content of the target analyte. The inset shows a nearly linear approximation of the dependence of the intensity of the 1001 cm^{-1} peak on concentration

4. Conclusions

Thus nanocomposite colloidosomes of mesoporous silica microspheres decorated with silver nanoparticles have been successfully applied as highly sensitive vapor phase optical sensors utilizing a semiquantitative analysis of surface-enhanced Raman spectra. The material was prepared using soft chemistry approaches and benefits from the intrinsic properties for both of the components: the mesoporous structure of the silica microspheres allows for capillary condensation of target analytes while the silver nanoparticles favor the great enhancement of Raman fingerprints of thus trapped and preconcentrated analytes at low concentrations in gaseous phase. This approach would be recommended as a further development of universal gas phase sensors for volatile organic compounds.

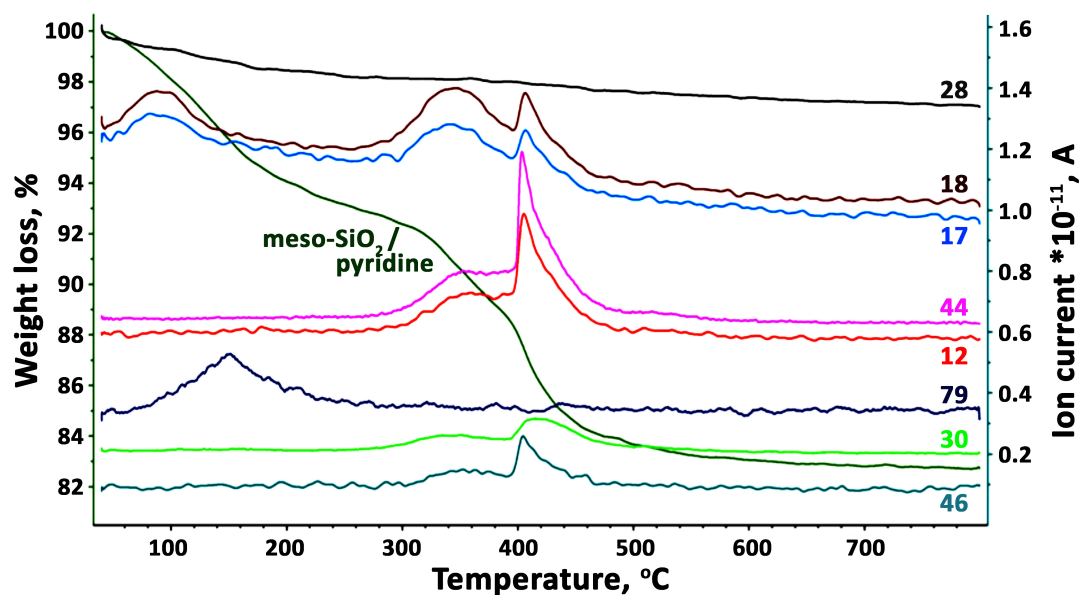


FIG. 3. Experimental data on a simultaneous TGA and mass-spectrometry analysis of outlet gases for silver-decorated colloidosomes of mesoporous silica with pyridine adsorbed upon their exposure in a vapor phase in SERS experiments. The TG curve is marked with the “meso-SiO₂/pyridine” label. Other curves show the amounts of different molecular fragments released from the colloidosomes, presumably, 28 means CO or N₂, 18 – H₂O, 17 – NH₃, 44 – CO₂, 79 – pyridine, 46 – NO₂, 30 – NO. Molecular bromine with a molecular mass of 158 and heptane itself with a molecular mass 100 are not detected

Acknowledgements

The work is supported by the Russian Science Foundation (grant 14-13-00871). Authors thank V.K. Ivanov and A. E. Baranchikov for SEM measurements and fruitful discussions.

References

- [1] Yuan Y., Panwar N., et al. SERS-based ultrasensitive sensing platform: An insight into design and practical applications. *Coord. Chem. Rev.*, 2017, **337**, P. 1–33.
- [2] Sharma B., Frontiera R.R., et al. SERS: Materials, applications, and the future. *Mater. Today*, 2012, **15** (1–2), P. 16–25.
- [3] Semenova A.A., Semenov A.P., et al. Nanostructured silver materials for noninvasive medical diagnostics by surface-enhanced Raman spectroscopy (focus article). *Mendeleev Commun.*, 2016, **26** (3), P. 177–186.
- [4] Brazhe N.A., Evlyukhin A.B., et al. Probing cytochrome c in living mitochondria with surface-enhanced Raman spectroscopy. *Sci. Rep.*, 2015, **5**, 13793.
- [5] Sarycheva A.S., Brazhe N.A., et al. New nanocomposites for SERS studies of living cells and mitochondria. *J. Mater. Chem. B*, 2016, **3** (4), P. 539–546.
- [6] Sarycheva A.S., Ivanov V.K., et al. Microbead silica decorated with polyhedral silver nanoparticles as a versatile component of sacrificial gel films for SERS applications. *RSC advances*, 2015, **5** (110), P. 90335–90342.
- [7] Semenova A.A., Ivanov V.K., Savilov S.V., Goodilin E.A. Unusual silver nanostructures prepared by aerosol spray pyrolysis. *Cryst. Eng. Comm.*, 2013, **15** (39), P. 7863–7871.
- [8] Semenova A.A., Brazhe N.A., et al. A new route of SERS analysis of intact erythrocytes using polydisperse silver nanoplatelets on biocompatible scaffolds. *RSC advances*, 2016, **6** (88), P. 85156–85164.
- [9] Semenova A.A., Goodilin E.A., et al. Planar SERS nanostructures with stochastic silver ring morphology for biosensor chips. *J. Mater. Chem.*, 2012, **22** (47), P. 24530–24544.
- [10] Semenova A.A., Semenova I.A., et al. Revisiting preparation routes of SERS materials. *Nanosystems: Physics, Chemistry, Mathematics*, 2017, **8** (5), P. 670–676.
- [11] Hill W., Wehling B., Klockow D. Analysis of odorous vapor exhaled from rubber by surface-enhanced Raman scattering. *Appl. Spectrosc.*, 1999, **53** (5), P. 547–550.
- [12] Kodyath R., Malak S.T., et al. Assemblies of silver nanocubes for highly sensitive SERS chemical vapor detection. *J. Mater. Chem. A*, 2013, **1** (8), P. 2777–2788.
- [13] Biggs K.B., Camden J.P., Anker J.N., Van Duyne R.P. Surface-enhanced Raman spectroscopy of benzenethiol adsorbed from the gas phase onto silver film over nanosphere surfaces: determination of the sticking probability and detection limit time. *J. Phys. Chem. A*, 2009, **113** (16), P. 4581–4586.

- [14] Zayak A.T., Hu Y.S., et al. Chemical Raman enhancement of organic adsorbates on metal surfaces. *Phys. Rev. Lett.*, 2001, **106** (8), 083003(1–4).
- [15] Stokes D.L., Pal A., Narayanan V.A., Vo-Dinh T. Evaluation of a chemical vapor dosimeter using polymer-coated SERS substrates. *Anal. Chim. Acta*, 1999, **399** (3), P. 265–274.
- [16] Mueller M., Tebbe M., et al. Large-area organization of pNIPAM-coated nanostars as SERS platforms for polycyclic aromatic hydrocarbons sensing in gas phase. *Langmuir*, 2012, **28** (24), P. 9168–9173.
- [17] Lin E.-C., Fang J., et al. Effective localized collection and identification of airborne species through electrodynamic precipitation and SERS-based detection. *Nat. Commun.*, 2013, **4**, 1636.
- [18] Piorek B.D., Lee S.J., et al. Free-surface microfluidic control of surface-enhanced Raman spectroscopy for the optimized detection of airborne molecules. *PNAS*, 2007, **104** (48), P. 18898–18901.
- [19] Rae S.I., Khan I. Surface enhanced Raman spectroscopy (SERS) sensors for gas analysis. *Analyst*, 2010, **135** (6), P. 1365–1369.
- [20] Khaing Oo M.K., Chang C.-F., Sun Y., Fan X. Rapid, sensitive DNT vapor detection with UV-assisted photo-chemically synthesized gold nanoparticle SERS substrates. *Analyst*, 2011, **136** (13), P. 2811–2817.
- [21] Kreno L.E., Greenelch N.G., et al. SERS of molecules that do not adsorb on Ag surfaces: a metalorganic framework-based functionalization strategy. *Analyst*, 2014, **139** (16), P. 4073–4080.
- [22] Chou A., Jaatinen E., et al. SERS substrate for detection of explosives. *Nanoscale*, 2012, **4** (23), P. 7419–7424.
- [23] Khaing Oo M.K., Guo Y., et al. Ultrasensitive vapor detection with surface-enhanced Raman scattering-active gold nanoparticle immobilized flow-through multihole capillaries. *Anal. Chem.*, 2012, **84** (7), P. 3376–3381.
- [24] Wang J., Yang L., et al. Spectroscopic ultra-trace detection of nitroaromatic gas vapor on rationally designed two-dimensional nanoparticle cluster arrays. *Anal. Chem.*, 2011, **83** (6), P. 2243–2249.
- [25] Zhu S., Fan C., et al. Realization of high sensitive SERS substrates with one-pot fabrication of Ag-Fe₃O₄ nanocomposites. *J. Colloid Interface Sci.*, 2015, **438**, P. 116–121.
- [26] Chong X., Kim K.J., et al. Plasmonic nanopatch array with integrated metal-organic framework for enhanced infrared absorption gas sensing. *Nanotechnology*, 2017, **28**, 26LT01.
- [27] Zhang Z., Yu W., et al. Ultrasensitive surface-enhanced Raman scattering sensor of gaseous aldehydes as biomarkers of lung cancer on dendritic ag nanocrystals. *Anal. Chem.*, 2017, **89** (3), P. 1416–1420.
- [28] Chen Y., Zhang Y., et al. Breath analysis based on surface-enhanced Raman scattering sensors distinguishes early and advanced gastric cancer patients from healthy persons. *ACS Nano*, 2016, **10** (9), P. 8169–8179.
- [29] Wong C.L., Dinish U.S., Schmidt M.S., Olivo M. Non-labeling multiplex surface enhanced Raman scattering (SERS) detection of volatile organic compounds (VOCs). *Anal. Chim. Acta*, 2014, **844**, P. 54–60.
- [30] Gerardin C., Reboul J., Bonne M., Lebeau B. Ecodesign of ordered mesoporous silica materials. *Chem. Soc. Rev.*, 2013, **42** (9), P. 4217–4255.
- [31] Innocenzi P., Malfatti L. Mesoporous thin films: properties and applications. *Chem. Soc. Rev.*, 2013, **42** (9), P. 4198–4216.
- [32] Fleishmann M., Hendra P.J., McQuillan A.J. Raman spectra of pyridine adsorbed at a silver electrode. *Chem. Phys. Lett.*, 1974, **26** (2), P. 163–166.
- [33] Morris V.R., Bhatia S.C., Stelson A.W., Hall J.H. Matrix - isolation study of thermal decomposition of pyridine. *Energy and Fuel*, 1991, **5**, P. 126–133.

Truncated minimum energy path method for finding first order saddle pointsI. S. Lobanov¹, M. N. Potkina^{2,3}, H. Jónsson^{3,4}, V. M. Uzdin^{1,2}¹ITMO University, Kronverkskiy, 49, St. Petersburg, 197101, Russia
Kronverkskiy, 49, St. Petersburg, 197101, Russia²St. Petersburg State University, St. Petersburg, 198504, Russia³Science Institute and Faculty of Physical Sciences, University of Iceland
107 Reykjavík, Iceland⁴Center for Nonlinear Studies, Los Alamos, NM 87545, USA
lobanov.igor@gmail.com, hj@hi.is, v_uzdin@mail.ru**PACS 82.20.Pm, 34.10.+x, 75.40.Mg****DOI 10.17586/2220-8054-2017-8-5-586-595**

A method for finding a selected region of the minimum energy path between two local minima on an energy surface is presented. It can be used to find the highest saddle point and thereby estimate the activation energy for the corresponding transition when the shape of the path is known reasonably well and a good guess can be made of the approximate location of the saddle point. The computational effort is then reduced significantly as compared with a calculation of the full minimum energy path by focusing the images on the selected part of the path and making one of the images, the climbing image, converge rigorously on the saddle point. Unlike the commonly used implementation where a restraint is used to distribute the images along the path, the present implementation makes use of a constraint where the distance between images is controlled based on a predefined overall length of the path. A relatively even density of images on each side of the climbing image is maintained by allowing images to move from one side to the other. Applications to magnetic skyrmion annihilation and escape through boundary are used to illustrate the savings in computational effort as compared with full minimum energy path calculations.

Keywords: saddle point, minimum energy path, constraint, rate theory, skyrmion.*Received: 9 October 2017**Revised: 19 October 2017***1. Introduction**

The mechanism of a transition between (meta)stable states of an atomic system, involving rearrangement of atomic coordinates and/or rotation of magnetic moments, can be characterized by the minimum energy path (MEP) connecting the corresponding (local) minima on the energy surface. The MEP represents the path of highest statistical weight and is a natural choice for a reaction coordinate. Typically, the primary task is to estimate the transition rate. Within the harmonic approximation to transition state theory (HTST) this requires the evaluation of the highest energy along the MEP, a first order saddle point (SP) on the energy surface. While the MEP may have more than one energy maximum, only the highest one is needed for the HTST rate estimate as it determines the activation energy. For this purpose, the MEP only needs to be known well enough to identify the point of highest energy.

The nudged elastic band (NEB) method is frequently used to find MEPs to determine transition mechanisms and at the same time estimate the activation energy for transitions [1,2]. Given initial and final state minima on the energy surface and some initial path between them, the NEB method can be used to iteratively converge on an MEP, typically the one nearest to the initial path. The MEP does not, however, need to be close to the initial path. An NEB calculation can reveal an unexpected transition mechanism and intermediate local (or even global) minima that were not known beforehand (see, for example, ref. [3]). If, on the other hand, the shape of the MEP is quite well known and the region where the (highest) SP lies can be identified beforehand, the calculation of the full MEP is not needed and the computational effort in estimating the activation energy can be reduced by launching a SP search starting from a best estimate of the SP. The NEB calculation can, for example, be carried out only to the extent that the rough shape of the MEP becomes evident, and then a minimum mode following (MMF) method [4–6] launched from the point of highest energy [7].

In the NEB method, the path is discretized using a set of replicas of the system, i.e. sets of values of the variables defining a system configuration. The replicas are referred to as images of the system. Starting with some initial path, an iterative procedure is used to bring the images to an MEP. In the climbing image NEB (CI-NEB) [8], the highest energy image is treated separately and made to converge on the highest SP. This modification of the NEB method is simple and easy to implement and is a popular alternative to a saddle point search method such as

MMF. In either case, the computational effort of converging accurately on the whole MEP can be avoided if the primary goal is to find the SP and estimate the activation energy for the transition.

Another option for reducing the computational effort compared with a full MEP calculation is to focus the convergence on a limited region of the MEP, one that is known to contain the (highest) SP. There have been several different implementations of this approach. In its simplest form, intermediate images of partly converged NEB calculation are chosen to be the fixed endpoints instead of the local minima (see, for example, ref. [9]), but a better approach is to make the new endpoints follow selected equipotential contours towards the MEP [10, 11].

A key aspect of the NEB method is a clear separation of the adjustments in image positions that represent a change in the shape of the path and adjustments that affect the distribution of images along the path. This is referred to as 'nudging' and it requires a numerically stable estimate of the local tangent to the path [12]. Displacements representing changes in the shape of the path are only driven by the component of the energy gradient perpendicular to the local tangent. The distribution of the images along the path is then a separate issue and can be handled in various ways. The most common implementation makes use of a restraint approach, i.e. a harmonic penalty term in the energy which gives a spring force between adjacent images acting only in the direction of the tangent [1, 2]. Alternatively, a constraint approach can be used where the total length of the path is estimated and the images placed along the path so as to obtain a desired (usually even) distribution [13]. This is one of many examples in computational methodology where a desired feature of the simulation can be implemented either with a restraint or a constraint (see, for example, ref. [14]). Tests indicate that the restraint approach can converge with fewer iterations when a small but typical number of images is included in the MEP calculation, while the constraint approach ensures better distribution of the images along the path when a large number of images is included (because the springs only act between adjacent images) [15]. While the restraint approach has become widely used, the constraint approach is used less frequently. The reason for this may partly be that useful features such as the CI and ways to focus the convergence onto a limited region of the MEP have not, as far as we know, been formulated for the constraint approach. In the present article, we describe how this can be done.

The applications we present involve annihilation and escape of a magnetic skyrmion. The NEB method with restraints has been adapted to magnetic systems, the so-called geodesic NEB (GNEB) [16] and applied to various types of magnetic systems, in particular skyrmions [16–18]. Magnetic skyrmions are topologically nontrivial states of magnetic systems. The states are localized in the sense that only in a finite domain (called the support) the vectors are not directed along the external magnetic field direction. The support can be large (containing millions of spins), making the simulation domain large, thus numerical modelling of the skyrmions requires significant computational effort. During annihilation in the interior of the domain, the skyrmion first shrinks before reaching the SP and then the spins rotate to form the ferromagnetic (FM) state. We are primarily interested here in the activation energy, hence the part of the MEP close to the SP is of primary importance. The shape of the MEP is simple, has a single maximum, and is well known from previous calculations of similar systems. In calculations of skyrmion annihilation, the support can be reduced by an order of magnitude by focusing on a limited region of the MEP, thereby reducing the simulation domain and the computational effort. The skyrmion escape through a free boundary of the simulated system has similar properties: The skyrmion is repelled by the boundary, so the local energy minimum corresponds to a skyrmion located far from the boundary. Large part of the MEP represents movement of the skyrmion towards the boundary while the interesting part of the MEP is in a small region near the boundary. By focusing on a limited region of the MEP, the calculation can be carried out for a smaller simulation domain without loss of precision in the estimate of the SP energy. Calculations of these two skyrmion transitions are used here as benchmarks to calibrate the efficiency.

In the following section, we review briefly the NEB method and then discuss the constraint approach for distributing the images along the path. The formulation of the CI variant of the method within the context of the constraint approach is then described and finally the method for focusing on only a limited part of the MEP, a method we will refer to as truncated MEP (TMPEP). Applications to skyrmion annihilation and escape through the boundary of the simulated system are then presented and the computational effort compared with full MEP calculations.

2. Method

2.1. Nudging and image distribution

Let E denote the energy of the system, and p^n denote a set of values of all the variables defining a configuration of the system. This will be referred to as an image of the system. A path in configuration space is defined as a sequence of images $p = (p^n)$, $n = 0 \dots N$. The path p is an MEP between two states if

$$(1) \quad p^0 \text{ and } p^N \text{ are local minima of } E,$$

(2) p^n for $n = 1 \dots N - 1$ is a local minimum of energy in the plane orthogonal to the path p .

The first condition implies that the gradient of energy at the first and the last image is zero: $g^0 = g^N = 0$, $g^n = \nabla E[p^n]$. Given a unit tangent τ^n to the path at the image p^n , the second condition implies that the projection of the gradient of energy on the space orthogonal to τ^n is zero:

$$P_{\tau^n}(g^n) = g^n - \tau^n(\tau^n \cdot g^n) = 0.$$

Care must be taken in the estimation of the the tangent. A simple and numerically stable way has been presented in ref. [12]:

$$\hat{\tau}^n = \begin{cases} \tau_+^n, & E^{n+1} > E^n > E^{n-1}, \\ \tau_-^n, & E^{n+1} < E^n < E^{n-1}, \end{cases}$$

where $\tau_+^n = p^{n+1} - p^n$ is the right tangent, $\tau_-^n = p^n - p^{n-1}$ is the left tangent. If E^n is a local maximum $E^{n-1} < E^n \wedge E^{n+1} < E^n$ or a local minimum $E^n < E^{n-1} \wedge E^n < E^{n+1}$ on the path, then the tangent should be a weighted sum of τ_+^n and τ_-^n that transforms continuously between the definition above as energy becomes monotone. The tangent vector $\hat{\tau}^n$ should be normalized:

$$\tau^n = \hat{\tau}^n / \|\hat{\tau}^n\|.$$

Given some initial path p^n , the images are moved towards the MEP using an iterative procedure. The projected gradient $P_{\tau^n}(g^n)$ can be used as a measure of convergence to the MEP, the smaller the norm, the closer the convergence. The images are moved in the direction of the antigradient,

$$w^n = p^n - \alpha g^n$$

where $\alpha > 0$ controls the length of an optimization step. This displacement of the images should only change the shape of the path, but not affect directly the distribution of the images along the path. Therefore, the gradient is projected on the orthogonal plane of the path (nudging):

$$w^n = p^n - \alpha h^n, \quad h^n = P_{\tau^n}(g^n).$$

If the configuration space is constrained (for example the fixed norm of the spins in the applications presented here), then additional steps need to be carried out to satisfy the constrains. Let $q_n = \pi(g^n)$ be projection of g^n to the tangent space of the manifold defined by the constrains, $\tau_\pi^n = \pi(\tau_n) / \|\pi(\tau_n)\|$ be projection of the approximation of the tangent vector to the tangent space, and R be operator projecting arbitrary point to the closest state satisfying the constrains. Then, the gradient descent step is defined as:

$$w^n = R(p^n - \alpha h^n), \quad h^n = P_{\tau_\pi^n}(q^n).$$

The procedure described above changes the location of the images so as to adjust the shape of the path. However, this does not specify how the images are distributed along the path. If this distribution is not controlled, the images will eventually slide down to the local energy minima. The nudging algorithm separates the distribution of the images along the path from the displacements of images affecting the shape of the path. While the distribution is most commonly controlled using a restraint method where a harmonic spring acts between adjacent images [1,2], we will here use a constraint method based on an estimate of the total length of the path [13]. A reparametrization step is introduced to distribute the images. Given pre-images w^n , piecewise linear interpolation of the path is constructed

$$w(t) = R\left(\frac{(t - d^n)w^{n+1} - (t - d^{n+1})w^n}{d^{n+1} - d^n}\right), \quad t \in [d^n, d^{n+1}],$$

where d^n is the distance from the pre-image w^n to the first image w^0 in the metric of the phase space:

$$d^{n+1} = d^n + \text{dist}(w^{n+1}, w^n), \quad d^0 = 0.$$

Almost equidistant distribution of the images on the next step is obtained by selecting images with constant step in terms of the distance d along the path:

$$p^n \mapsto w(d^n n/N).$$

2.2. Climbing image

The procedure described above will bring the images to the nearest MEP and make the magnitude of the projected gradient arbitrarily small for a sufficiently small α . But, the most important point on the MEP, the maximum which corresponds to the SP, may turn out to be in between images and the estimate of the SP energy thus inaccurate. The algorithm can be modified by making one of the images, the climbing image (CI), converge rigorously on the SP [8]. The CI is moved along the path in the uphill direction, to higher energy:

$$w^n = R(p^n - \alpha h^n), \quad h^n = q^n - 2\tau_\pi^n(\tau_\pi^n \cdot q^n).$$

It is desirable to choose the CI to be the highest energy image of the path. Hence every image on the path is marked as climbing $M^n = 2$ (closest to a maximum), descending $M^n = 0$ (closest to a minimum) or holding $M^n = 1$ (all other images). The general equation for the update of the images is then as follows:

$$w^n = R(p^n - \alpha h^n), \quad h^n = q^n - M^n \tau_\pi^n(\tau_\pi^n \cdot q^n).$$

Climbing and descending images should not be moved during the reparametrization, otherwise they will not reach stationary points. To save positions of climbing and descending images, every new image $w(d^N n/N)$ introduced during reparametrization that is closest to a climbing/descending image should be removed and the climbing/descending image should be used instead. This guaranties that climbing/descending images will not come too close to the holding images as that could cause problems in the estimation of the tangent. This approach allows for an image to move from one side of the climbing image to the other. This helps maintain similar resolution on both sides of the CI. (This feature has, as far as we know, not been implemented previously).

The norm of the gradient at the climbing and the descending images can be used to monitor convergence. If a climbing image reaches a SP, its gradient becomes zero. Hence another important measure of the convergence to an MEP is the maximum of norm of gradients at all extremes of the energy along the path.

2.3. Truncated MEP

Above, the calculation of a full MEP between local minima has been described. When enough information about the shape of the MEP has been obtained to identify the region where the (highest) SP is located, or it is known *a priori* that the shape is simple with only one maximum, computational effort can be reduced by focusing the calculation on the region near the SP. Only a part of the MEP is then calculated. We will refer to this as truncated MEP (TMEP). To specify the selected part, an image called an anchor is specified. It should always belong to the TMEP. The anchor can be a point of maximum energy, or a local minimum. To compute TMEP, the same steps are carried out as described above, namely compute w^n and then $w(t)$. But when new images are introduced, they are taken from the interval $t \in [t_{min}, t_{max}]$, the increment of t is still constant:

$$p^n = w(t_{min} + (t_{max} - t_{min})n/N).$$

Let $n = a$ be an anchor, then the part of the MEP used for reparametrization is chosen in such a way that image a lies in the middle of the TMEP and the length of the TMEP is a predefined constant μ , that is

$$t_{min} = d^a - \mu/2, \quad t_{max} = d^a + \mu/2.$$

If $d^a < \mu/2$, then the interval should be moved to the right, to preserve the length of the TMEP:

$$t_{min} = 0, \quad t_{max} = \min(\mu, d^N).$$

If $d^a + \mu/2 > d^N$, then the interval should be moved to the left:

$$t_{min} = \max(0, d^N - \mu), \quad t_{max} = d^N.$$

If the whole path is shorter than μ , then nothing is dropped and the interval is the same as for the computation of the full MEP:

$$t_{min} = 0, \quad t_{max} = d^N.$$

The length μ of the TMEP can be chosen to equal the length of the initial path or as some multiple of that length.

During computation of a full MEP the end images are fixed at local minima, and can be marked as descending images. The same can be done for TMEP, but the gradient at the end images will in general no longer become zero, only the projected gradient. The tangent at the ends can be found as left and right tangents:

$$\hat{\tau}^0 = \tau_+^0, \quad \hat{\tau}^N = \tau_-^N.$$

During reparametrization the indices of images can change, that should be taken into account when defining an anchor image for the next step. To preserve the anchor image, it is excluded from the reparametrization stage

in the same way as a climbing or descending image. Namely, after computation of a new image p^A , the image closest to the old anchor w^a , is replaced and the new anchor value set to A .

The selection of the TMEP can be done in various ways. MEP often can be divided to two parts: from the initial state to the SP, or from SP to the final state. One of the possible uses of TMEP is the calculation of only one of the two parts. In calculations of only the first part of the path, the TMEP should contain the initial state and at least one image lying on the other side of the energy ridge, possibly close to the SP. Another choice of TMEP is to find only the highest SP, i.e. the highest energy point on the MEP between two local minima. In that case, two images lying on opposite sides of the energy ridge need to be identified and the initial path set to a geodesic between the states. The anchor image in that case is the image with maximal energy. It is important to place the images at the ends of TMEP on opposite sides of the energy ridge, otherwise all images collapse to a metastable state. If the length of TMEP is insufficient and the anchor is set to an image different from the image with maximal energy, all images may end up on the same side of the energy ridge, even if initially they were separated by the energy ridge. This all requires considerable knowledge of the MEP, but can be useful when repeated calculations are carried out on similar systems or only slight changes have been made in the energy landscape, so previous knowledge can be used to speed up the calculation.

3. Applications

The TMEP method is applied here in studies of a magnetic skyrmion. Calculations of two example transitions are described below, annihilation of the skyrmion and escape of the skyrmion through a free boundary of the simulated system.

3.1. Model system

The energetics of the system are described by a Heisenberg model. Every state of the system is given by the vectors of magnetic moments μS_n of each atom n in the system, where μ is value of magnetic moment and S_n is a unit direction vector. The energy of the system is given by

$$E[S] = - \sum_{(j,k)} (J_{jk} S_k \cdot S_j + D_{j,k} \cdot (S_j \times S_k)) - \sum_j K(K^0 \cdot S_j)^2 - \sum_j \mu B_j \cdot S_j, \quad (1)$$

where the sum over (j, k) is taken over all pairs of neighboring atoms, B is strength of external magnetic field, J is Heisenberg exchange constant, D is Dzyaloshinskii-Moriya (DM) vector, K and K^0 are strength and direction of anisotropy.

In this case, the computation of an MEP involves a constraint, because the length of the magnetic moments is fixed, $\|S_n\| = 1$. The operator R projects to the manifold corresponding to this restriction and the projection g^n of the gradient on the tangent space of the manifold are

$$R(S_j) = \frac{S_j}{\|S_j\|}, \quad \pi(g_j^n) = g_j^n - S_j^n (S_j^n \cdot g_j^n).$$

The system is represented by a square lattice in the x-y plane, 100×100 . The parameters in the Heisenberg model are chosen as follows: Easy axis anisotropy constant of $K = 0.004 J$ with the axis perpendicular to the plane of the system, and DM vector directed along pairs of interacting spins of length $D = 0.05 J$. An external magnetic field is not applied. For these parameters, the skyrmion is a metastable state with a radius of ≈ 21 lattice constants.

3.2. Skyrmion annihilation

In the calculations of skyrmion annihilation, periodic boundary conditions are applied in the x-y plane. The initial path is generated as a geodesic between a single skyrmion and a ferromagnetic state where all spins are directed along z . The skyrmion annihilation process consists of two stages: First, skyrmion shrinkage and then collapse of the skyrmion core. The saddle point is located in the second stage where the radius has shrunk to about 3 lattice constants. A large part of the full MEP contains the first stage and, therefore, requires a large simulation domain. By using TMEP to focus on the part of the path between transition state and ferromagnetic state (FM) the calculation of the SP can be done quicker. To obtain the full MEP we first relaxed both ends of the path to the local minima and then applied the constraint method with steps $\alpha = 0.22$. TMEP was obtained as described in the previous section with the same α . FM state was set as the anchor and as one of the ends. The other end was set to a skyrmion like state of radius 10 lattice constants.

The calculated results are shown in Fig. 1. The TMEP calculation gives the same activation energy for FM to skyrmion transition as a full MEP calculation up to computational precision. Convergence of TMEP is several

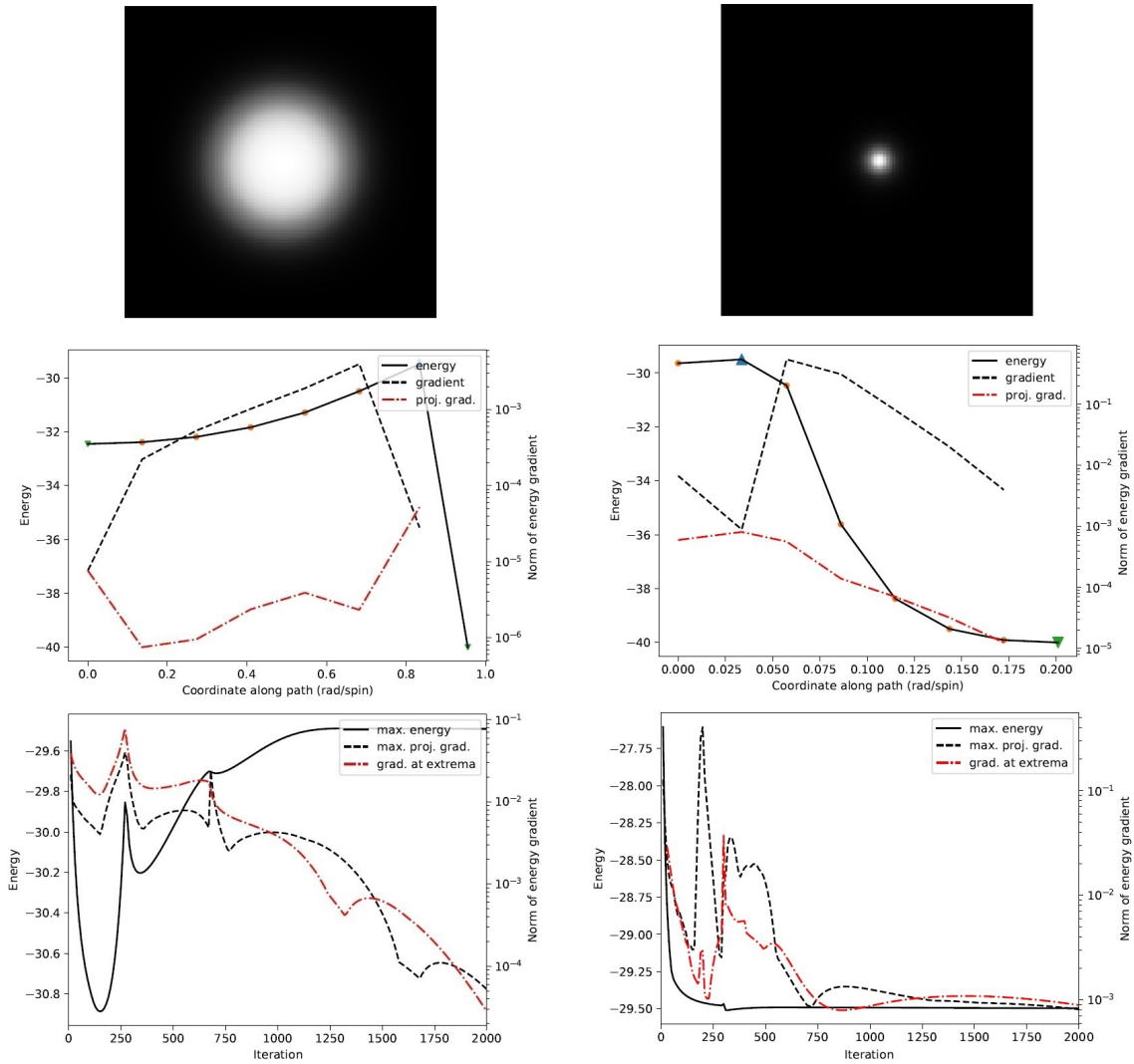


FIG. 1. MEP for skyrmion annihilation (100×100 lattice): (left) full MEP, (right) truncated path (TMEP) with anchor at ferromagnetic state (last image). (top) first images of MEP after 2000 iterations, (middle) MEP after 2000 iterations, (bottom) convergence history. Solid black line depicts energy, dash-dotted line is l^∞ norm of gradient, and dashed line is l^∞ norm of the gradient component perpendicular to the path. Down-pointing triangle, circle and up-pointing triangle markers show descending, climbing and holding images, respectively. Images with small markers are subjects of reparametrization step. Support of all images in TMEP is 10 times smaller and the resolution of the path in TMEP is higher than when the full MEP is calculated. SP energy was found with a precision of 0.1% five times faster using TMEP

times faster, probably because of better tangent estimate due to higher resolution of the path around the saddle point. Both the full MEP and TMEP were computed with the same number of images, a total of 8 images. Because of the lower resolution, the full MEP calculation does not contain intermediate points between the saddle point and FM state. Since the images are situated closer to the SP in the TMEP calculation, details of the transition are better resolved. First images of the paths have largest support, and the support for the full MEP calculation is two orders of magnitude larger than for TMEP. As a result, the computational effort of TMEP can be two orders of magnitude smaller under appropriate correction of simulation domain size. TMEP also gives almost correct value of the activation energy from the beginning, while the estimate of the activation energy given by the full MEP calculation slowly increases as climbing image reaches the saddle point.

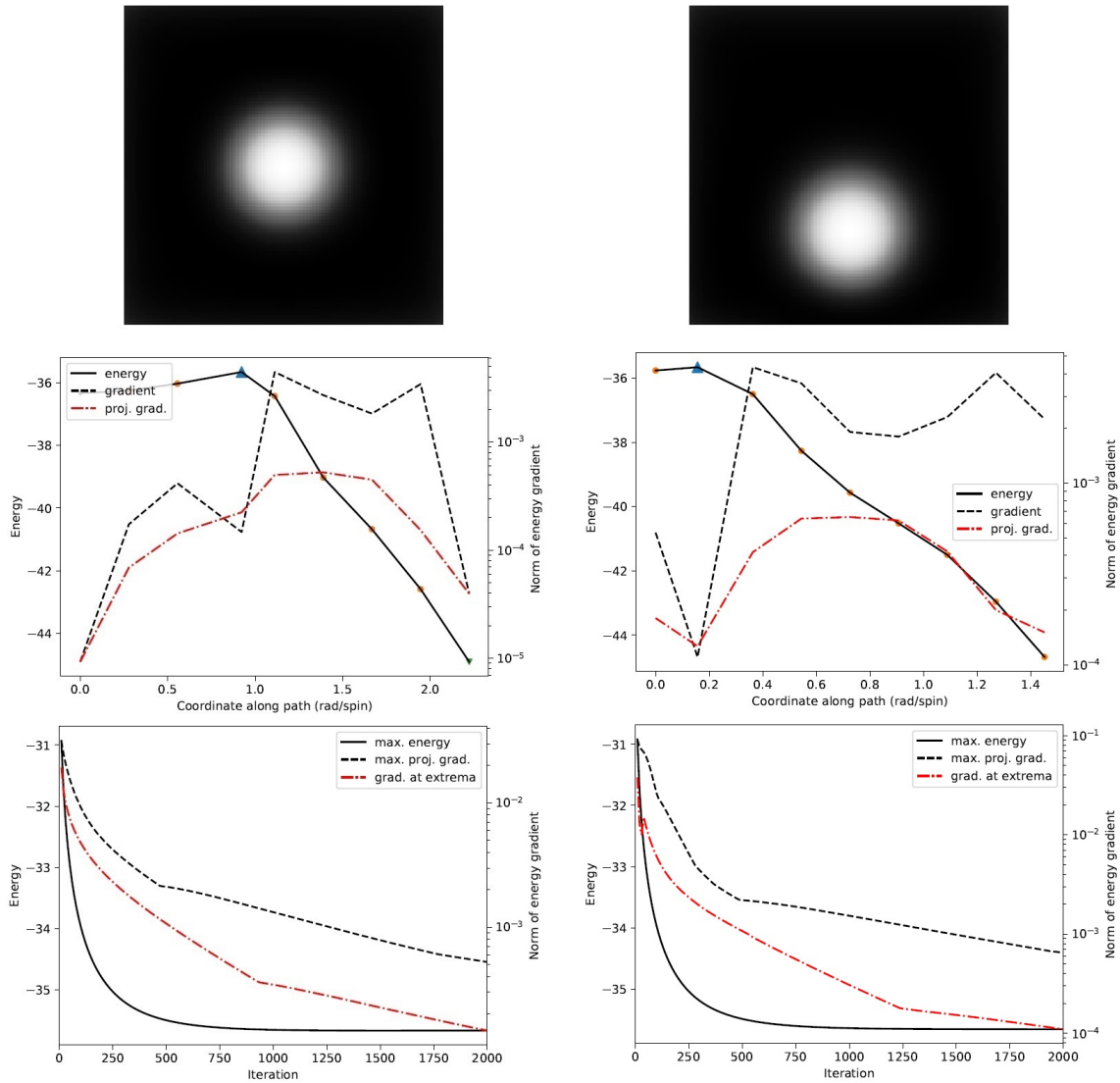


FIG. 2. MEP for skyrmion escape through a free boundary of the (100×100) lattice: (left) full MEP, (right) truncated path (TMEP) with anchor at ferromagnetic state (last image). (top) first images of MEP after 2000 iterations, (middle) MEP after 2000 iterations, (bottom) convergence history. Solid black line depicts energy, dash-dotted line is l^∞ norm of gradient, and dashed line is l^∞ norm of the gradient component perpendicular to the path. Down-pointing triangle, circle and up-pointing triangle markers show descending, climbing and holding images, respectively. Images with small markers are subjects of reparametrization step. All images of TMEP are closer to the boundary than those of the full MEP. Resolution in the part of interest is higher, convergence is faster and precision is higher for TMEP as compared with the full MEP calculation

3.3. Skyrmion escape

As a second application, the SP for a skyrmion escaping through free boundaries of the simulated system (periodic boundaries turned off). The initial path is generated from a skyrmion configuration having a radius of 30 lattice constants with center gradually moving from one radius toward center of the domain from the interface to one radius outside the domain. In the calculation of the full MEP, the endpoints of the path were relaxed, but for TMEP calculation the ends were not relaxed. The beginning of TMEP is relaxed to the single skyrmion state; since skyrmions are repelled by the boundary, the isolated skyrmion is located at the center of the simulated system. The final configuration is FM (all spins are directed along z axis except of spins near the boundary). The optimization methods and parameters were the same as in the previous application.

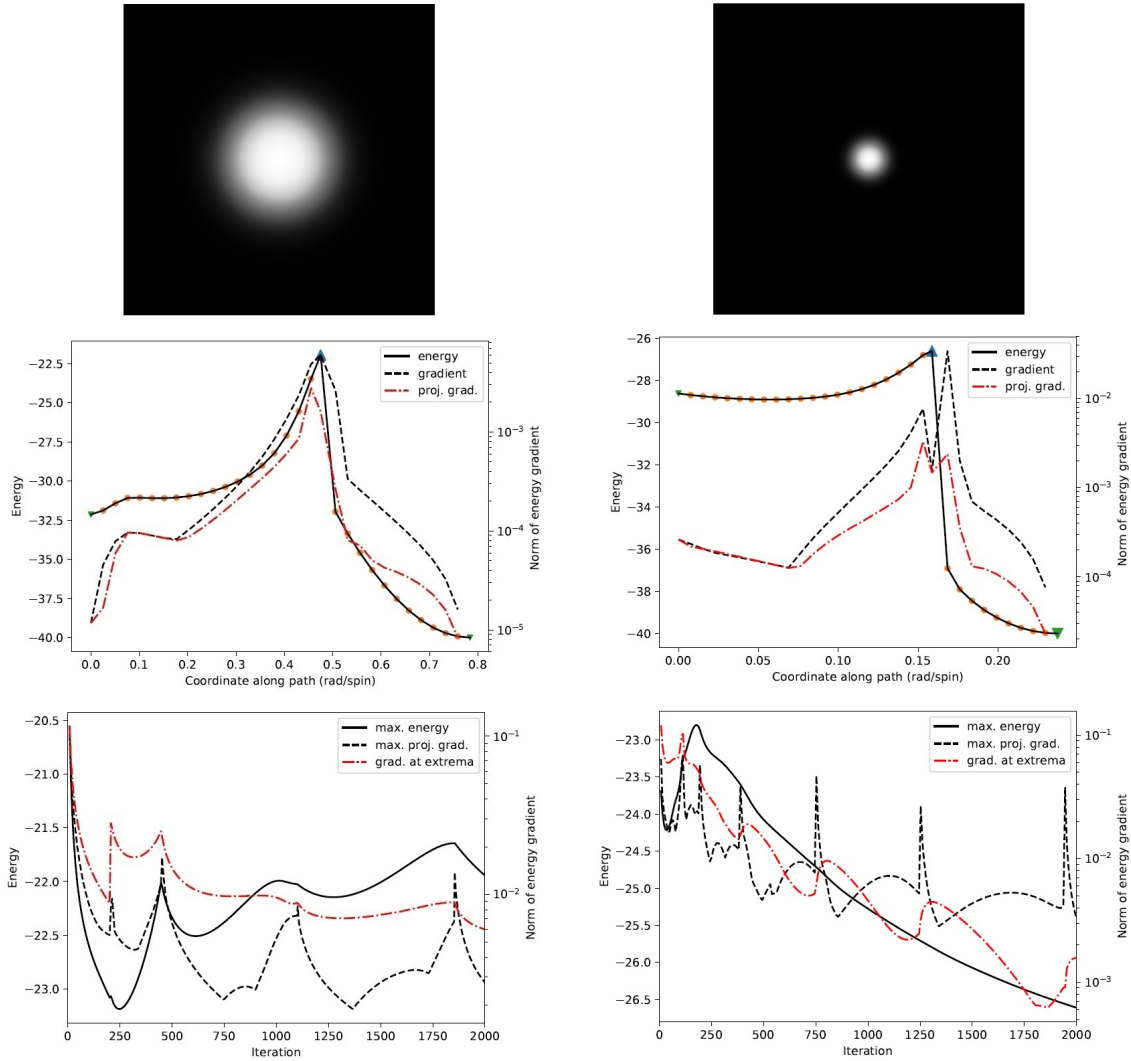


FIG. 3. MEP for skyrmion annihilation (1000×1000 lattice): (left) full MEP, (right) truncated path (TMEP) with anchor at ferromagnetic state (last image). (top) first images of MEP after 2000 iterations, (middle) MEP after 2000 iterations, (bottom) convergence history

The calculated results are shown in Fig. 2. Since the lowest energy configuration of the skyrmion is at the center of the simulated system, the first part of the MEP describes translation of the skyrmion with only a slight variation in the energy. This first part is of little interest, but can be long if the domain is large. Hence, most images of the full MEP belong to this first part. The second part of the MEP describes the escape of the skyrmion through one of the edges and is of main interest. In the TMEP calculation the focus is placed in the second part while the first part is not included. In this benchmark it is hard to estimate the length of the TMEP from the beginning, so the anchor is set to the image with maximal energy. TMEP again gives good resolution of the important part of the MEP. The precision of the calculation of the SP is several times higher using TMEP when the same number of images is used to represent the full MEP. The first image on the path is most distant from the interface, for the TMEP the image is located in the region about the interface of the width about three skyrmion radii, when for MEP the image occupies the region about half of the simulation domain. As before, the TMEP can be used to significantly decrease computational effort.

For comparison, the calculations described above are repeated for a denser lattice consisting of 1000×1000 atoms. All parameters are scaled accordingly to make the skyrmion have the same relative dimensions to the domain size as in the previous example. For a small number of images, the CI in this case does not converge on the SP (the gradient does not become zero), although the projected gradient at the CI becomes zero. This is a result of inaccuracy in the tangent estimate. To improve the tangent estimate, the number of images was increased

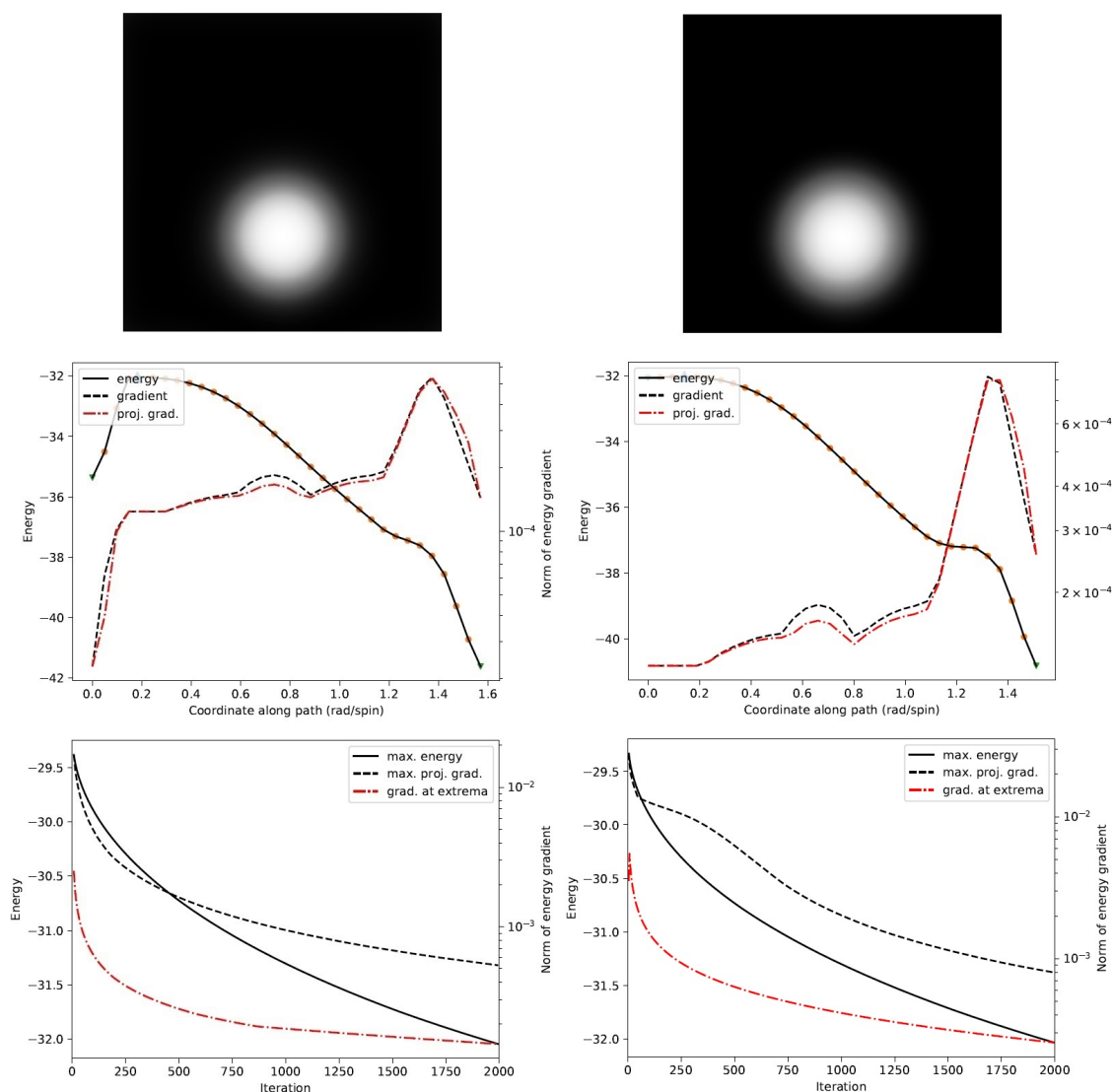


FIG. 4. MEP for skyrmion escape through a free boundary of the (1000×1000) lattice: (left) full MEP, (right) truncated path (TMEP) with anchor at ferromagnetic state (last image). (top) first images of MEP after 2000 iterations, (middle) MEP after 2000 iterations, (bottom) convergence history

to 32 and that enabled convergence of the CI to the SP. All optimization parameters are the same as in the previous example. The calculated results are shown in Fig. 3 and Fig. 4.

4. Acknowledgements

This work was supported by the Government of the Russian Federation (grant 074U01) and by grant 16-11-10330 of Russian Science Foundation.

References

- [1] Mills G., Jónsson H., Schenter G.K. Reversible work based transition state theory: Application to H_2 dissociative adsorption. *Surf. Sci.*, 1995, **324**, P. 305–337.
- [2] Jónsson H., Mills G., Jacobsen K.W., edited by Berne B.J., Ciccotti G., Coker D.F. Nudged elastic band method for finding minimum energy paths of transitions, in *Classical and Quantum Dynamics in Condensed Phase Simulations*. World Scientific, Singapore, 1998, P. 385–404.
- [3] Henkelman G., Arnaldsson A., Jónsson H. Theoretical calculations of CH_4 and H_2 associative desorption from Ni(111): Could subsurface hydrogen play an important role? *J. Chem. Phys.*, 2006, **124**, P. 044706(9).

- [4] Henkelman G., Jónsson H. A dimer method for finding saddle points on high dimensional potential surfaces using only first derivatives. *J. Chem. Phys.*, 1999, **111**(15), P. 7010–7022.
- [5] Olsen R.A., Kroes G.J., Henkelman G., Arnaldsson A., Jónsson H. Comparison of methods for finding saddle points without knowledge of the final states. *J. Chem. Phys.*, 2004, **121**(20), P. 9776–9792.
- [6] Gutiérrez M.P., Argáez C., Jónsson H. Improved minimum mode following method for finding first order saddle points. *J. Chem. Theo. Comput.*, 2017, **13**(1), P. 125–134.
- [7] Henkelman G., Jóhannesson G., Jónsson H. Methods for finding saddle points and minimum energy paths. in *Theoretical Methods in Condensed Phase Chemistry*, 2002, P. 269–302.
- [8] Henkelman G., Uberuaga B.P., Jónsson H. A climbing image nudged elastic band method for finding saddle points and minimum energy paths. *J. Chem. Phys.*, 2000, **113**(22), P. 9901–9904.
- [9] Maragakis P., Andreev S.A., Brumer Y., Reichman D.R., Kaxiras E. Adaptive nudged elastic band approach for transition state calculation. *J. Chem. Phys.* 2002, **117**, P. 4651–4658.
- [10] Zhu T., Li J., Samanta A., Kim H.G., Suresh S. Interfacial plasticity governs strain rate sensitivity and ductility in nanostructured metals. *PNAS*, 2007, **104** (9), P. 3031–3036.
- [11] Einarisdóttir D.M., Arnaldsson A., Óskarsson F. and Jónsson H. Path optimization with application to tunneling. *Lecture Notes in Computer Science*, 2012, **7134**, P. 45–55.
- [12] Henkelman G., Jónsson H. Improved tangent estimate in the nudged elastic band method for finding minimum energy paths and saddle points. *J. Chem. Phys.*, 2000, **113**(22), P. 9978–9985.
- [13] Weinan E., Weiqing R., Vanden-Eijnden E. String method for the study of rare events. *Phys. Rev. B*, 2002, **66**, P. 052301(4).
- [14] Ravishanker, et al. *Reviews in Computational Chemistry*, Volume 11, edited by Kenny B. Lipkowitz, Donald B. Boyd, John Wiley & Sons, Sep 22, 2009, chapter 6, P. 346–347.
- [15] Sheppard D., Terrell R., Henkelman G. Optimization methods for finding minimum energy paths. *J. Chem. Phys.*, 2008, **128**, P. 134106(10).
- [16] Bessarab P.F., Uzdin V.M. Jónsson H. Method for finding mechanism and activation energy of magnetic transitions, applied to skyrmion and antivortex annihilation. *Comp. Phys. Commun.*, 2015, **196**, P. 335–347.
- [17] Bessarab P.F. Comment on “Path to collapse for an isolated Néel skyrmion”. *Phys. Rev. B* , 2017, **95**(13), P. 136401(2).
- [18] Malottki S.V., Dupé B., Bessarab P.F., Delin A., Heinze S. Enhanced skyrmion stability due to exchange frustration. *Sci. Rep.*, 2017, **7**, P. 12299(10).

Features of the energy spectrum of indium antimonide quantum dots

A. I. Mikhailov, V. F. Kabanov, N. D. Zhukov, E. G. Glukhovskoy

Saratov State University, Department of Nano- and Biomedical Technologies,
Astrakhanskaya, 83, Saratov, 410012, Russia
glukhovskoy@gmail.com

PACS 73.22.f, 73.21.La

DOI 10.17586/2220-8054-2017-8-5-596-599

Energy spectrum of indium antimonide (InSb) quantum dots (QD) was analyzed in this paper. Properties of energy spectrum levels were determined both by calculations and experiments using differential tunneling current-voltage characteristics (CVC) related to static conductivity. It was confirmed that relatively large QD (size of about 20–25 nm) exhibit quantum size effects. Critical values of the characteristic parameters of InSb QD are analyzed, in which application of the differential tunneling current-voltage characteristics method for express analysis of the characteristic sizes of QD leads to significant errors (more than 10 %).

Keywords: quantum dots, indium antimonide, differential tunneling current-voltage characteristics, energy spectrum.

Received: 17 July 2017

Revised: 5 August 2017

1. Introduction

Quantum dots QD are among the most interesting quantum-sized structures in terms of application in devices for nanoelectronics and optoelectronics (ultrafast transistors, light-emitting diodes, lasers, photoelectric converter cells). Several of the semiconductor compounds A_3B_5 are promising materials for these purposes due to its energy spectrum features and extremely low effective mass values for conduction electrons. Low values of effective mass provide high De Broglie wavelength for conduction electrons that is tens of nanometers. In this regard, specific phenomena caused by dimensional quantization of the energy spectrum of electrons can be observed in relatively large structures, primarily in InSb samples, that is a narrow-band semiconductor with record values of the effective mass of electrons in the conduction band [1, 2]. This makes it possible to substantially simplify the experimental studies and reduce the cost of technologies for the development of corresponding nanoelectronic structures.

2. Materials and methods

Indium antimonide QD samples were obtained by a technique similar to that used in [3, 4]. 0.0014 g of InSb powder ($M_r = 236.578$ g/mole) was dispersed in 1 ml of chloroform ($C_{(\text{InSb})} = 6$ mM) followed by ultrasonic treatment for 30 min. Suspension of colloid nanoparticles was mixed with Arachic acid solution with an initial concentration of 1 mM in a volume ratio of 1:1. Resulted suspension was used to form a Langmuir monolayer on the surface of deionized water. It was injected onto the surface of the water, kept for 10 minutes until complete evaporation of chloroform and then the monolayer was condensed and transferred the solid support by the Langmuir–Schaeffer method. Surface pressure during transfer was 20 mN/m² and it was kept constant. A glass slide with a conductive layer of indium-tin oxide (ITO) on the surface was used as the support. After complete drying under normal conditions, the obtained films were investigated with scanning electron microscopy (SEM) and scanning tunneling microscopy (STM).

3. Results and discussion

Tunneling of electrons from the ITO electrode into the probe of the tunneling microscope occurs by means of discrete levels of QD. Model representations of this process considered in the work of the authors [5] and shown on the Fig. 1(a, b) under applied voltages V_1 and V_2 , corresponding to tunneling through the 1st and 2nd electron energy levels of the discrete spectrum of QD.

In the case of quantum dots, the energy spectrum has a discrete nature, and the density of electronic states $g(\varepsilon)$ is described by the Dirac δ -function and theoretically it is a set of infinitesimally narrow and high peaks:

$$g(\varepsilon) = \sum_i \delta(\varepsilon - \varepsilon_i). \quad (1)$$

An exact calculation of the function $g(\varepsilon)$ is difficult in general, since the isoenergetic surfaces have a rather complex shape. However the problem usually reduces to solving the Schrödinger equation for a free particle with

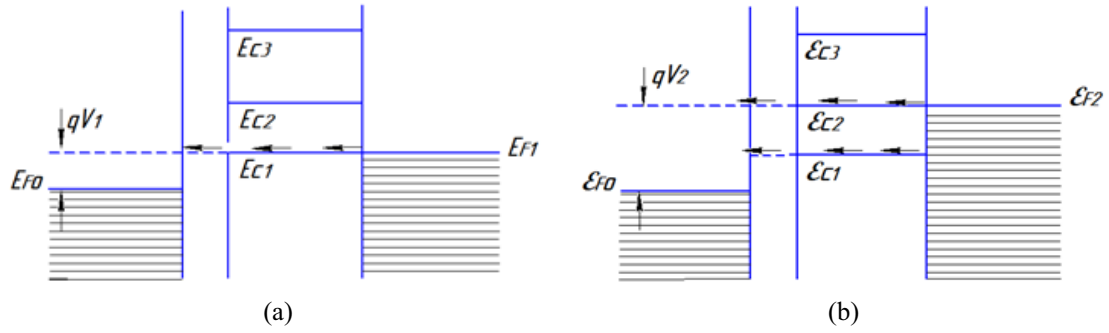


FIG. 1. Tunneling of electrons through a quantum dot

an effective mass m^* by the effective mass approximation [6]. Another approximation is the use of energy bands with a quadratic dispersion law. This is permissible in the case of small pulses and small electron energies, which is realized in the tasks under consideration.

When QD model of a cubic shape with edge d is used:

$$\varepsilon_i = \frac{(\pi\hbar)^2}{2m^*} \cdot \frac{1}{d^2} \cdot (l^2 + m^2 + n^2), \quad (2)$$

where $l, m, n = 1, 2, 3, \dots$ are positive natural numbers corresponding to the sub bands numbers; m^* is the effective mass of the electron, and d is the characteristic size of the quantum dot.

In case of a QD of a spherical shape with the radius d in the one-electron spectrum in a parabolic well approximation [7]:

$$\varepsilon_i = \frac{(\pi\hbar)^2}{2m^*} \cdot \frac{1}{d^2} \cdot (4n + 2l + 3), \quad (3)$$

where n is the radial quantum number ($n = 0, 1, 2, \dots$); l is the orbital quantum number ($l = 0, 1, 2, \dots$).

Calculated values of the electron energy for the first three allowed energy levels ($\varepsilon_1, \varepsilon_2, \varepsilon_3$) in accordance with (4), (5) for InSb are shown in Fig. 2(a, b). The value of the effective mass of electrons in the conduction band of InSb is used in the calculations: $m^* = 0.013m_0$, where m_0 is the mass of a free electron. Eqs. (2) and (3) (Fig. 2) imply that, as the QD size decreases, not only the “effective” width of the band-gap will increase, but also the energy distance between the allowed energy levels in the conduction band will increase. Presented in the [8] experimental results for InSb quantum dots with size 3 ± 7 nm confirming these conclusions.

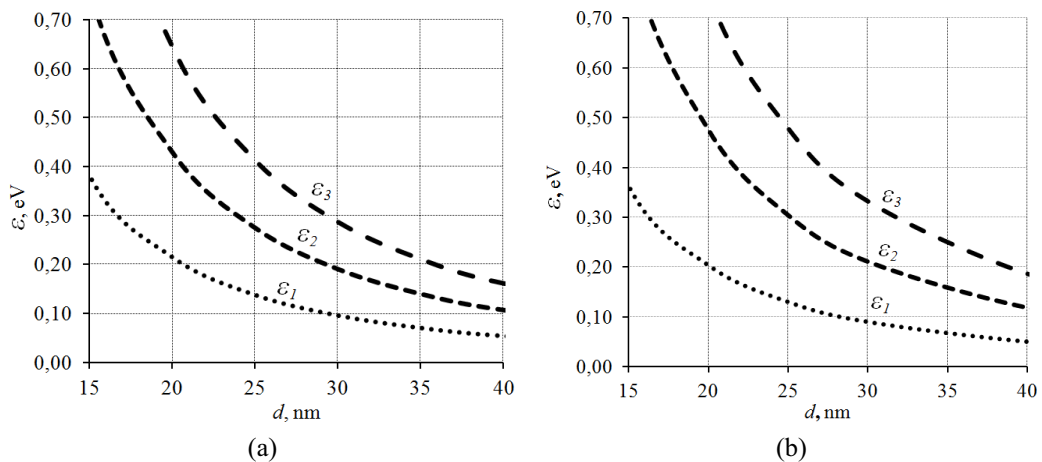


FIG. 2. Calculated values of the electron energy for the first allowed levels of QD InSb as a function of the characteristic size of the nanoobject d : (a) – according to the cubic QD model, (b) – according to the spherical QD model

Electron scattering leads to broadening of the energy levels $\Delta\varepsilon_i$ and limiting the amplitude of the peaks [9,10]: $\Delta\varepsilon_i \propto \hbar/\tau$, where τ is lifetime of an electron in quasi stationary states of QD.

Broadening of this kind in real QD occurs due to the finite lifetime of charge carriers caused by spontaneous emission, interaction with phonons, and a number of other processes [9, 11].

The magnitude of the broadening $\Delta\varepsilon_i$ is related to the value of ε_i . Both these parameters affect the form and nature of $g(\varepsilon)$.

The nature and the degree of the broadening $\Delta\varepsilon_i$ in accordance with representations of the authors [9] in case of simple energy bands with a quadratic dispersion law for the spherical QD model can be represented by the following equation according to the corresponding approximations:

$$\Delta\varepsilon_i \approx 16 \frac{\varepsilon_i^{1/2}}{\varepsilon_i} (\varepsilon_i - \varepsilon)^{3/2} \cdot e^{-2\Delta r \left(\frac{2m^*(\varepsilon_i - \varepsilon)^{1/2}}{\hbar} \right)}, \quad (4)$$

where Δr is the thickness of the QD shell.

The value ε_i is mainly determined by the characteristic size of QD d and hence by the technology of the synthesis.

SEM and optical spectroscopy methods do not provide correct interpretation of the experimental data if structure of the quantum particle is not homogeneous or several particles form a conglomerate. In this regard, STM method was additionally used to analyze the features of the electronic spectrum of the obtained InSb QDs films. Investigations were carried out with the scanning probe microscope SPM Nanoeducator II by the described methods [1, 10].

Localized energy levels ε_i associated with the properties of a quantum-dimensional object can be observed in differential tunneling CVC rated to static conductivity as individual peaks. To analyze the experimental tunneling CVC the dependence of $(dI/dV)/(I/V)$ on the voltage V was used in analogy with the approaches described in [1, 10, 12], since the method of normalized differential CVC is more informative. Typical results of measurements are shown in Fig. 3. Statistical processing of the values of the first three levels determined the following energies: $\varepsilon_1 \sim (0.15 - 0.20)$ eV, $\varepsilon_2 \sim (0.30 - 0.35)$ eV, $\varepsilon_3 \sim (0.55 - 0.65)$ eV (an error is on the level of kT). These values correspond to the characteristic size of the obtained QDs of 20–25 nm. It should be noticed that the difference between the cubic and spherical models did not exceed 8 %.

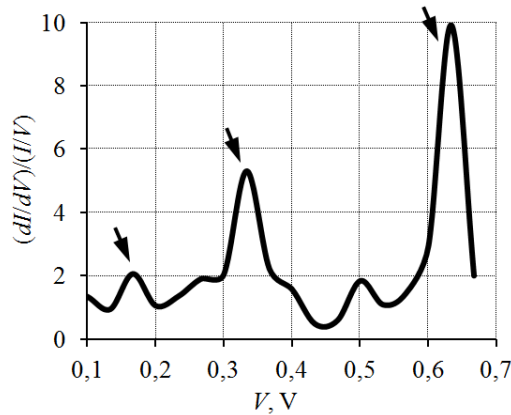


FIG. 3. Rated differential current-voltage characteristics of InSb QD

The value $\Delta\varepsilon_i$ should be taken into account in analysis of the experimental results for estimating the electron spectrum of QD by the method of rated differential tunneling CVC: the peaks corresponding to ε_i can be “smoothed”. In our opinion, this express analysis method of the characteristic size of QD is difficult at a value of $\Delta\varepsilon_i$ more than 10 %. Obviously, described broadening will be the most significant for the first level of QD, measured from the bottom of the conduction band for the bulk material. In this paper, we estimate the value $\Delta\varepsilon_1$ in accordance with Eq. (6), depending on the characteristic size of the nanoobject d . During the calculations, the value of the conduction electron kinetic energy was chosen on the level of $3/2kT$. The results are shown in Fig. 4.

The results of the calculations show that at QD shell thickness of about 1 nm (particles close to “open QD”) the magnitude of the broadening of the first energy level of the InSb QD becomes significant at the characteristic size d less than 10 nm. Errors of the of differential tunneling CVC method for express analysis of the QD characteristic size are significant (more than 10 %) in this case. If QD shell thickness is increased the magnitude of the energy level broadening from the characteristic size d of the quantum-dimensional object is substantially reduced. However in this case the lifetime of the charge carriers in the inner region of the QD, and, correspondingly, the value of $\Delta\varepsilon_i$ [9], will vary.

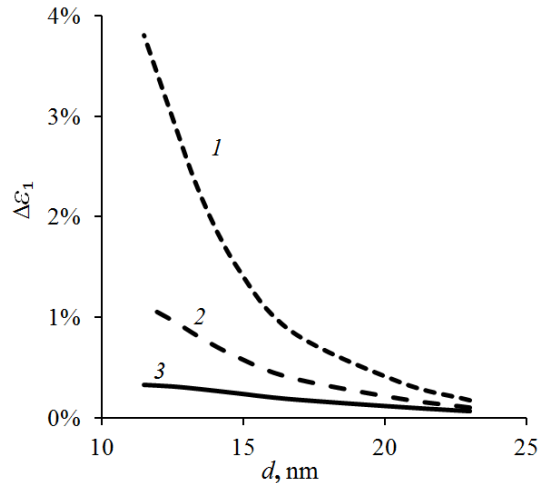


FIG. 4. Calculated values of the broadening of the 1st energy level of the InSb QD spectrum: 1 – QD shell thickness 1 nm; 2 – QD shell thickness 2 nm; 3 – QD shell thickness 3 nm

4. Conclusion

Thus, several features of the InSb quantum dots energy spectrum was analyzed, taking into account the broadening of the energy spectrum levels. Positions of the levels were determined by processing the experimental tunneling CVC. Estimation of the QD characteristic size was carried out using “cubic” and “spherical” models. Critical values for the characteristic sizes of InSb quantum dots are analyzed, which lead to significant (more than 10 %) errors for the differential tunneling CVC method for express analysis of the QD characteristic sizes. The obtained results can be used to clarify the understanding of the electronic processes features in the quantum-dimensional objects and its physical interpretation.

Acknowledgements

This work was supported by grants from the Russian Foundation for Basic Research Projects No. 16-07-00093 and No. 16-07-00185.

References

- [1] Mikhailov A.I., Kabanov V.F., Zhukov N.D. Peculiarities of field electron emission from submicron protrusions on a rough InSb surface. *Technical Physics Letters*, 2015, **41** (11), P. 1065–1067.
- [2] Chang A.Y., et al. Carrier Dynamics in Highly Quantum-Confined, Colloidal Indium Antimonide Nanocrystals. *ACS Nano*, 2014, **8** (8), P. 8513–8519.
- [3] Reiss P., Protière M., Li L. Core/shell semiconductor nanocrystals. *SMALL*, 2009, **5** (2), P. 154–168.
- [4] Speranskaya E.S., Beloglazova N.V., et al. Polymer-coated fluorescent CdSe-based quantum dots for application in immunoassay. *Biosensors and Bioelectronics*, 2014, **53**, P. 225–231.
- [5] Mikhailov A.I., Kabanov V.F. Electronic properties of A2B6 semiconductor quantum dots. – In the Collect.: Nano- and biomedical technologies. Quality management. Problems and prospects. Collection of scientific articles. Saratov, SGU Publishing house, 2016, 75 p. (in Russian)
- [6] Dragunov V.P., Neizvestny I.G., Gridchin V.A. *Fundamentals of nanoelectronics*. Fizmatkniga, Moscow, 2006, 496 p. (in Russian)
- [7] Kaputkina, N.E., Lozovik Y.E. “Spherical” quantum dots. *Phys. Solid State*, 1998, **40** (11), P. 1935–1936.
- [8] Wang T., et al. Size-dependent energy levels of InSb quantum dots measured by scanning tunneling spectroscopy. *ACS Nano*, 2015, **9** (1), P. 725–732.
- [9] Zegrya G.G., Samsvat D.M. Carrier energy spectrum and lifetime in quantum dots in electric field. *J. Exp. Theor. Phys.*, 2009, **108** (6), P. 907–916.
- [10] Mikhailov A.I., Kabanov V.F., Zhukov N.D. Peculiarities of field electron emission from submicron protrusions on a rough InSb surface. *Technical Physics Letters*, 2015, **41** (6), P. 568–570.
- [11] Korolev N.V., Starodubtsev S.E., Bormontov E.N., Klinskikh A.F. Features of the electron spectrum of an open spherical quantum dot with a delta potential. *Condensed media and interphase boundaries*, 2011, **13** (1), P. 67–71. (in Russian)
- [12] Mikhailov A.I., Kabanov V.F., Gorbachev I.A., Glukhovskoi E.G. A study of specific features of the electronic spectrum of quantum dots in CdSe semiconductor. *Technical Physics Letters*, 2016, **42** (8), P. 796–798.
- [13] Swart I., et al. Scanning probe microscopy and spectroscopy of colloidal semiconductor nanocrystals and assembled structures. *Chem. Rev.*, 2016, **116** (18), P. 11181–11219.

Random number generator for cryptography

R. Soorat^{1,2}, K. Madhuri¹, A. Vudayagiri¹

¹R. C. Bose centre for cryptology and security, Indian Statistical Institute, Kolkata, India

²School of Physics, University of Hyderabad, Hyderabad 500046, India

rsoorat@gmail.com

PACS 07.05.Hd

DOI 10.17586/2220-8054-2017-8-5-600-605

One key requirement for many cryptographic schemes is the generation of random numbers. Sequences of random numbers are used at several stages of a standard cryptographic protocol. One simple example is a Vernam cipher, where a string of random numbers is added to message string to generate encrypted code. $C = M \oplus K$. It has been mathematically shown that this simple scheme is unbreakable if key K is as long as M and is used only once. The security of a cryptosystem shall not be based on keeping the algorithm secret but solely on keeping the key secret. The security of a random number generator (RNG) is related to the difficulty of predicting its future sequence values from past values. The quality and unpredictability of secret data is critical to securing communication by modern cryptographic techniques. The generation of such data for cryptographic purposes typically requires an unpredictable physical source of random data. We studied a chaotic circuit which consisted of an inductor, capacitance, diode and thus used for the BB84 protocol. We have studied both pseudo random and true random number generators and evaluated them through various tests like frequency, correlation, NIST etc.

Keywords: Hardware random number generator, cryptography, chaos, chaotic circuit.

Received: 18 September 2017

Revised: 25 September 2017

1. Introduction

A random process is a repeating process in which output is difficult to find a describable deterministic pattern. The term randomness is quite often used in statistics to signify well defined statistical properties, such as correlation. Saying that a variable is random means that the variable follows a given probability distribution; under these terms, random is different from arbitrary, because to say that a variable is arbitrary does not imply that there is such determinable probability distribution. A good RNG should work efficiently, which means it should be able to produce a large amount of random numbers in a short period of time. Random numbers are widely used in many applications, such as cryptography [1, 2], spread-spectrum communications [3], Monte Carlo numerical simulations [4], statistical analysis [5], information security, stochastic simulation, stream ciphers, ranging signal in a radar system, controlling signal in remote control, encryption codes or keys in digital communication, address codes and spread spectrum codes in code division multiple access (CDMA) and many others. So for simulations, the generation of large amounts of random numbers is crucial, and thus fast RNGs are required. RNGs are also used in the statistics to solve problems in many fields such as nuclear medicine, finance and computer graphics.

Since traditional random numbers are generated by algorithms and are essentially pseudo-random, they have potential danger in security-related fields like quantum key distribution. There are, in general, two types of generators for producing random sequences: true random number generators (TRNGs) and pseudo random number generators (PRNGs). PRNGs require some input called seeds, along with some deterministic algorithms to generate multiple pseudo random numbers. They are usually faster than TRNGs and are preferable when several random-like numbers are required. TRNGs make use of non-deterministic sources along with some post-processing functions for generating randomness. Such sources include physical phenomena such as thermal noise, atmospheric noise, radioactive decay and even coin tossing. such as electrical noises [6], frequency jitters in electrical oscillators [7] and chaotic circuits [8, 9], which can produce unpredictable random numbers of high quality yet at much lower rates than PRNGs because of the narrow bandwidth of these physical entropy sources. In addition, a number of documents exist which provide general advice on using and choosing random number sources [10–13]. Further discussions on the nature of randomness, pseudo random number generators (PRNGs), and cryptographic randomness are available from a number of sources [14–16].

Truly random numbers are the basis of many cryptographic applications like QKD, especially for the generation of keys that cannot be penetrated by hackers or other attackers it is important that the random numbers used be unpredictable. The BB84 protocol makes use of polarization states of single photons to map the bits 0, 1 of the encryption key, in two mutually unbiased bases. These bases should be random, which means we need to design a

physical source for RNG to perform better than the available computer Pseudo random number generators (PRNG), but also should be compact and easy to integrate into the QKD device prototype. This requires a controller that generates four random states and its deterministic critically endangers the security of the entire protocol. For most applications, it is desirable to have fast random number generators (RNGs) that produce numbers which are as random as possible. There are different types of statistical tests that can be applied to a sequence to compare and evaluate the sequence to that of a truly random sequence [17–20].

2. Chaos based hardware random number generator

We are using a chaos based hardware random number generator which consists of a capacitor, a diode and an inductor. Fig. 1 is a simple LCR circuit built around a varactor diode. The voltage dependent capacitance acts as a nonlinear element, thus providing a chaotic oscillation. Generally, a hardware random number generator is based on sampling noise sources such as thermal noise or a reverse biased diode. Different circuits have been described, but these methods are difficult, since their amplitudes are usually small and often masked by deterministic disturbances; as a result, another alternative is to use a chaotic oscillator for pseudo random generator due to its unpredictable behavior and relatively simplicity. We have built a chaotic circuit based RNG (CCRNG), based on an earlier design by T. Kuusela [22], which in turn, was built around the chaos generator of Matsumoto et al. [23]. We use chaotic circuits which are extremely simple, consisting of an inductor and a capacitor diode, the nonlinear element is the capacitor whose capacitance is varied as a function of voltage across it. The nonlinear capacitance of the diode is seen earlier in many papers. The capacitance is varied as $C(V) = C/(1 + V/\theta)^\gamma$. Here, V is the voltage across the diode. If the circuit parameters and the external drive are suitably chosen, the system exhibits period doubling and chaotic behavior.

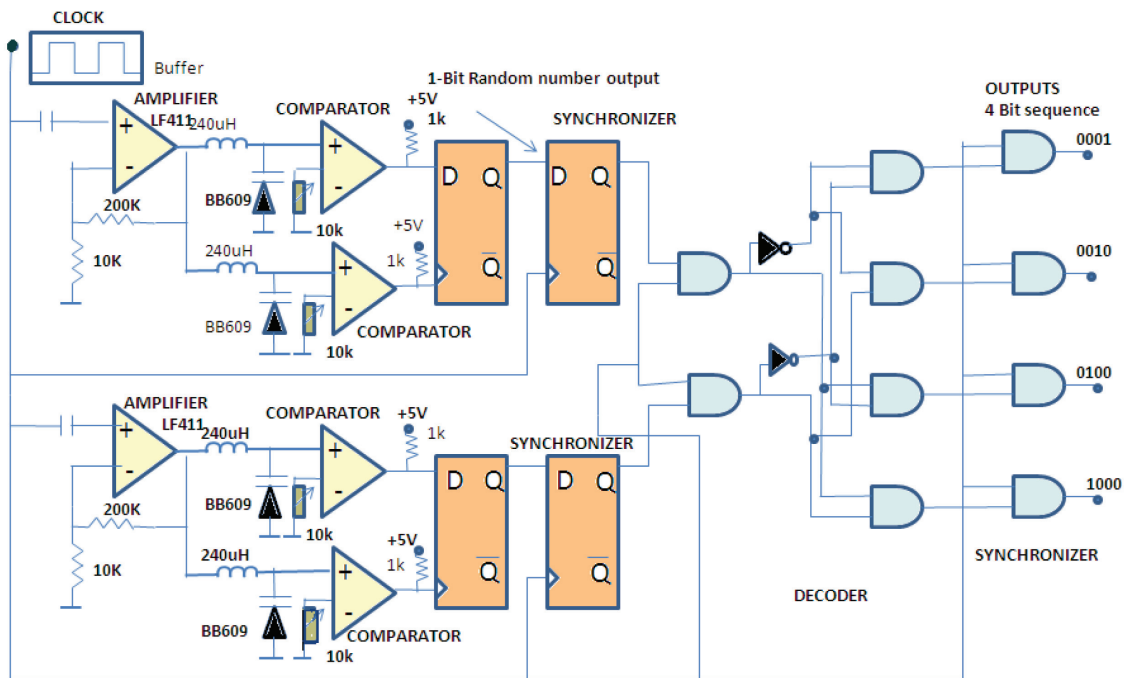


FIG. 1. Circuit diagram

The chaotic first-order differential equation and modified construction of chaotic clock Generator (CCG) by kuusela is as shown in Fig. 1. It has an external clock signal (a square wave of 500–600 KHz is used as a clock in this case). The CCG includes two identical chaotic oscillators; it consists of an inductor 240 μH and a varactor diode BB609 (nonlinear element). We are using two CCRNGs to generate a sequence of four bit structure in a random fashion, viz., 0001, 0010, 0100, and 1000. An amplifier is used to raise the signal level so that if the frequency and the amplitude of the driving clock are properly chosen, the circuit goes to a chaotic state and reliable operation is guaranteed, even the case of large tolerance. The fast operational amplifier with a large bandwidth is used as an amplifier (the LF 411 is used because of its high bandwidth and rapid response). The voltage across the capacitor diode is a random signal when the circuit exhibits period doubling and chaotic behavior. A comparator

is used to convert analog signal into a digital signal (LM 311 response time is 200 ns). Even though the output of comparators is quite randomly generated, it does not generate all the possible bit sequences for all possible values. We use two comparators for each CCRNG; one of them takes a bit sample from the other. This is done by a simple D-flip flop (1st D-flip flop). To synchronize the output bit sequences with the driven clock, one more D-flip flop is used and an AND gate is used to avoid continuous 1's and 0's. A decoder is used to generate four bits structures using two CCRNGs.

Using this circuit we generate several sets of random sequence of 0's and 1's and tested its behavior. Initially, we tapped the voltage at the output of the chaotic circuit and at the edge of the varactor. This data was stored in the computer as a function of time and then, its variation was computed $\frac{dv}{dt}$. Plotting $\frac{dv}{dt}$ against V , giving a phase plot Fig. 2. This showed the behavior of the generated signal. The plot on left side shows the raw data of voltage v/s time, while those on right side shown the phase plot, $\frac{dV}{dt} v/s V$. As the frequency is changed, the circuit becomes chaotic and we can see the bifurcation as shown in Fig. 2. The data is for different clock frequencies as output of chaos base random number generator before chaos up to (C); the output of chaos base random number generator at 500 kHz (D); the output of chaos base random number generator at 650 kHz (E). It can be seen from the phase plot in Fig. 2 (A) oscillation is constant as frequency is increased as in (B) the oscillation spreads. As frequency is further increased, in the phase plot, a clear frequency doubling behavior is shown, indicated by double loops. A further increase in frequency shows a multiple frequency regime in (D) and finally the chaotic oscillation in (E). The output of varactor is fed in to the comparator which maps the signal to 1 if the voltage is above a certain threshold and to 0 if it is a below the threshold. The sequence of 0's and 1's generated by the comparator, after being synchronized to the clock pulse, are recorded by the computer and analyzed. These data are obtained at the clock speed of about 650 kHz, since this is the region when chaos circuit is giving a proper chaotic output.

Figure 3 shows two different types of distribution. The total number of 1's and 0's are shown in (a) left side. For this run, it is asymmetric since there are more 1's than 0. This happens only for a few runs and can easily be corrected by changing the threshold. The graph on right (b) is more important, since it depicts the probability of getting zero following 1, getting 1 after 1 and simply of 0 after 0 and 1 after 0. The graph shows a slight higher frequency for the occurrence of 1-1, but this is due to fact that there is a higher occurrence of 1's as opposed to 0's. However, the graph clearly shows the same frequency for 1-0 and 0-1. This means that the system does not have any preference for 1 over 0.

In addition, we studied the bit correlation of random numbers from hardware module. Correlation $c_{ij}^{00} = \langle P_i(0)P_j(0) \rangle$, where $P_i(0)$ and $P_j(0)$ are the probability of finding 0 at i -th position and j -th position respectively. Extending this calculation, we can write $c_{ij}^{kl} = \langle P_i(k)P_j(l) \rangle$ for $k = 1, 0$ and $l = 1, 0$. For an ideal case, this should all be equal and have a value 0.25. The distance is the difference between i and j .

However, for Fig. 4, the closed square indicates correlation for 0-0, open square for correlation 0-1, solid line for 1-0 and closed circle for 1-1. Correlations for 0-1 and 1-0 are exactly identical at 0.25, indicating equal probability of getting pairs 0-1 and 1-0. The probability of getting 1-1 is higher, due to a systematic bias in the module for producing more 1's than 0's. This indicates the circuit is a near perfect coin toss system. It can be noticed from Fig. 4 bit correlation that the correlation has a small distribution around a mean value. We have passed this random sequence through the NIST test, and very few of the test pass through it.

3. Pseudo random number generator using LabVIEW

LabVIEW produces a double precision, floating-point number between 0 and 1, exclusively which has a uniform distribution. We have generated 50,000 random points between 0 and 1 from LabVIEW software and studied their random properties. We have plotted $\frac{dn}{dt}$ vs n which is phase and number sequence between 0 and 1.

Fig. 5 phase plot $\frac{dn}{dt}$ shows a highly non periodic behavior which is a clear indication of randomness.

Figure 6 (a) is a histogram graph which is a specific visual representation of data that measures the number of incidents of 0 and 1 for a sample set. The left side shows the distribution of 1's and 0's. We observe the same frequency for 1's and 0's, which is truly random behavior. The graph on right shows the probability of 1-1 is higher than 0-0 while that of 0-1 and 1-0 are the same.

Figure 7 bit correlation test shows the same correlation value of 0.25. This is a clear indication of a very good random number generator. It can be observed from Fig. 7 that the correlation has a small distribution around a mean value. In order to investigate this, we plotted the histogram of the correlation values. This distribution is very narrow about the mean value. In addition to the correlation test, we collected a bit stream of 0's and 1's from the circuit and processed them through the NIST test suite, with most of the tests being passed.

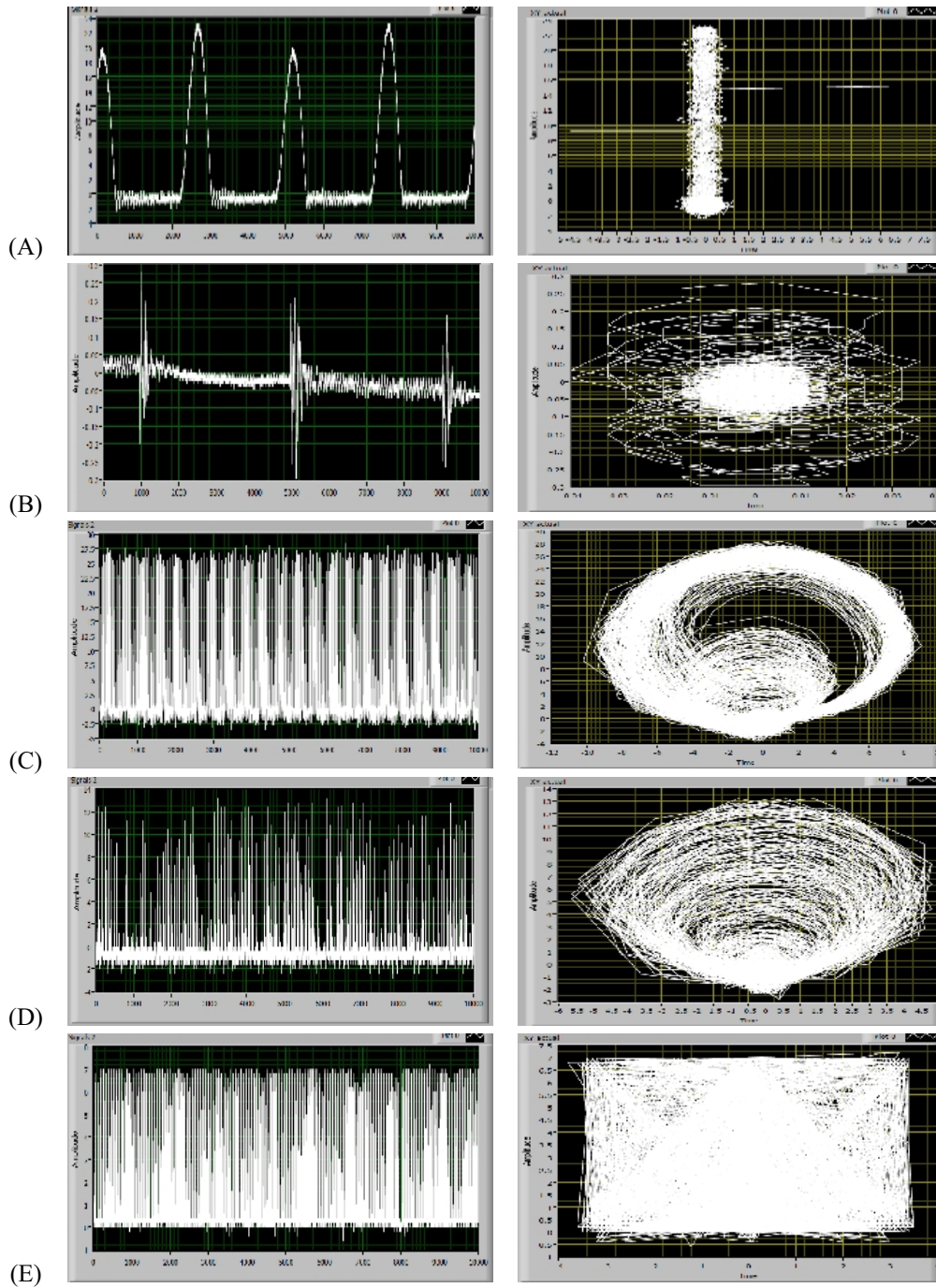


FIG. 2. Analog signal output of the chaos clock generator at different frequencies and corresponding phase plots

4. Conclusion

Since software methods only offer pseudo-random number codes, the need for other sources is important. We have therefore analyzed hardware and software based random number generators. We have compared and analyzed the randomness behavior between software and hardware random number generators. Although the correlation test gives very good results, the NIST test showed that some of them test pass through it. We have implemented this method for quantum key distribution based on BB84 protocol.

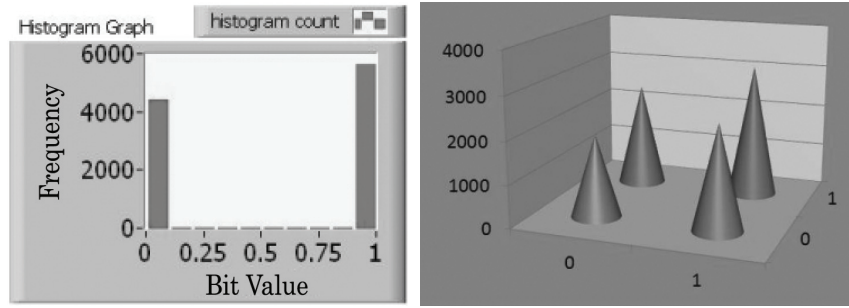


FIG. 3. (a) Histogram distribution of 0 and 1 (b) bit correlation

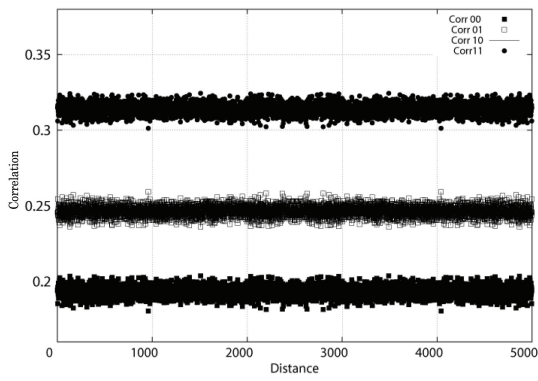


FIG. 4. Successive bit correlation of hardware module

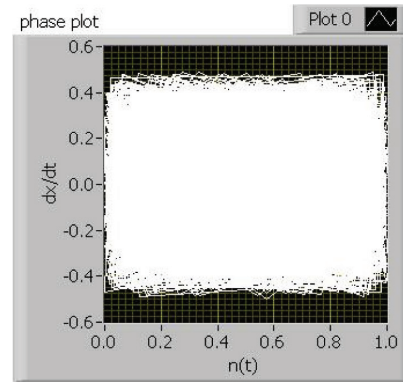


FIG. 5. Phase plots

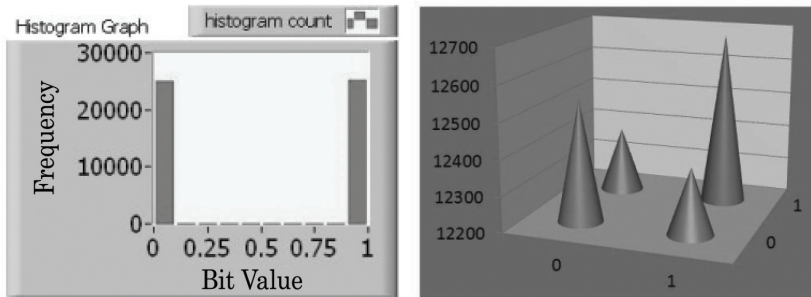


FIG. 6. Histogram distribution of 0 and 1 (b) bit correlation

Acknowledgements

This work was supported by department of information technology, Government of India. We thanks to Sunitha for her support.

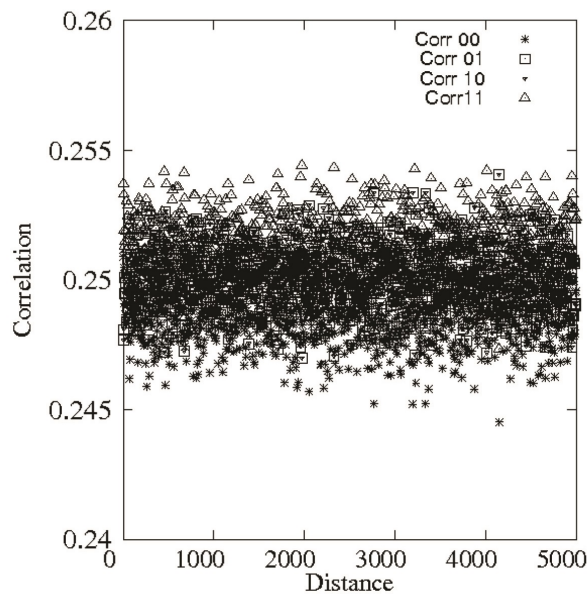


FIG. 7. Successive bit correlation of software module

References

- [1] Bennett C.H., Brassard G. Quantum cryptography: Public key distribution and coin tossing. *Proceedings of IEEE International Conference on Computers, Systems and Signal Processing*, New York, 1984, P. 8.
- [2] Burrows J.H. *Security requirements for cryptographic modules*. FIPS, Gaithersburg, 2001, 56 p.
- [3] Pickholtz R.L., Schilling D.L., Milstein L.B. Theory of spread-spectrum communications-a tutorial. *IEEE Trans. Commun.*, 1982, **30** (5), P. 855–884.
- [4] Metropolis N., Ulam S. The Monte Carlo method. *J. Am. Stat. Assoc.*, 1949, **44** (247), P. 335–341.
- [5] Nazarathy M., Newton S.A., et al. Realtime long range complementary correlation optical time domain reflectometer. *J. Lightwave Technol.*, 1989, **7** (1), P. 24–38.
- [6] Petrie C., Connelly J. A noise-based IC random number generator for applications in cryptography. *IEEE Trans. Circ. Syst. I Fundam. Theory Appl.*, 2000, **47** (5), P. 615–621.
- [7] Bucci M., Germani L., et al. A high-speed oscillator-based truly random number source for cryptographic applications on a smart card IC. *IEEE Trans. Comput.*, 2003, **52** (4), P. 403–409.
- [8] Stojanovski T., Kocarev L. Chaos-based random number generators-Part I: analysis. *IEEE Trans. Circ. Syst. I Fundam. Theory Appl.*, 2001, **48** (3), P. 281–288.
- [9] Stojanovski T., Pihl J., Kocarev L. Chaos-based random number generators-Part II: Practical realization. *IEEE Trans. Circ. Syst. I Fundam. Theory Appl.*, 2001, **48** (3), P. 382–385.
- [10] Krhovjak J. *Cryptographic random and pseudorandom data generators*. Brno, 2009.
- [11] Matthews T. Suggestions for random number generation in software. *RSA Laboratories' Bulletin*, 1996, **1**.
- [12] Ellison C. *Cryptographic Random Numbers*. IEEE P1363 Working Draft, 1997, 11 p.
- [13] Buchovecká S. *Analysis of a True Random Number Generator*. Master's thesis. Czech Technical University in Prague, Faculty of Information Technology, 2012.
- [14] Knuth D. *The Art of Computer Programming: Volume 2, Seminumerical Algorithms*, Addison-Wesley, 1981.
- [15] Menezes A., van Oorschot P., Vanstone S. *Handbook of Applied Cryptography*, CRC Press, 1996.
- [16] Goldreich O. *Foundations of Cryptography Fragments of a Book*, 1995, 290 p.
- [17] Rukhin A. *A Statistical Test Suite for Random and Pseudorandom Number Generators for Cryptographic Applications*. U.S. Department of Commerce, Technology Administration, National Institute of Standards and Technology, 2000, 152 p.
- [18] Marsaglia G. *Random Number CDROM, with The Diehard Battery of Tests of Randomness*. Florida State University, 1985.
- [19] Good I.J. The serial test for sampling numbers and other tests for randomness. *Proc. Cambridge Philos. Soc.*, 1953, **47**, P. 276–284.
- [20] Baron M., Rukhin A.L. Distribution of the Number of Visits For a Random Walk. *Communications in Statistics: Stochastic Models*, 1999, **15**, P. 593–597.
- [21] Spitzer F. *Principles of Random Walk*. Princeton: Van Nostrand, especially, 1964, 269 p.
- [22] Kuusela T. Random Number Generation Using a Chaotic Circuit. *J. Nonlinear Sci.*, 1993, **3**, P. 445–458.
- [23] Matsumoto T., Chua L.O., Tanaka S. Simmplex chaotic nonautonomous circuit. *Phys. Rev. A*, 1984, **30**, 1155.

The effect of vertical throughflow in Rivlin–Ericksen elastico-viscous nanofluid in a non-Darcy porous medium

S. Saini, Y. D. Sharma

Department of Mathematics, National Institute of Technology Hamirpur,
Hamirpur (H.P.), India-177005

shivani2291993@gmail.com

DOI 10.17586/2220-8054-2017-8-5-606-612

The instability of convection in a Rivlin–Ericksen elastico-viscous nanofluid with vertical throughflow is investigated using the linear stability theory. A modified Brinkman model is employed and single-term Galerkin method is used to solve the conservation equations. Nine dominating parameters are extracted from the analysis. Due to the combined effect of vertical throughflow, Brownian motion, and thermophoresis, the Rayleigh number is reduced by a substantial amount. It is found that through flow delays the convection while other nanofluid parameter enhance the convection. The thermal capacity ratio, kinematics viscoelasticity, and Vadasz number do not govern stationary convection. Using the convective component of nanoparticle flux, the critical wave number is a function of nanofluid parameters as well as throughflow parameter. Major trends are investigated briefly by plotting the graphs.

Keywords: heat transfer, porous layer, throughflow.

Received: 4 October 2017.

Revised: 9 October 2017

1. Introduction

Rivlin and Erickson [1] were the first to propose the theoretical and rheological model for elastic-viscous fluid. Rudraiah et al. [2] studied the overstable convection of an Oldroyd fluid and they found that effect of elasticity is to elongate the cells. Kim et al. [3] found that elasticity parameters have a destabilizing effect on the onset of convection. The effect of permeability, magnetic field, and rotation on Rivlin–Ericksin elastico-viscous fluid was studied by [4, 5] and they found that rotation, and magnetic field diminish the instability, while permeability enhances the instability. Sheu [6, 7] examined the linear stability in Visco-Elastic nanofluids and studied the combined effects of Brownian diffusion, thermophoresis diffusion, and viscoelasticity. Viscoelastic fluids are widely used in paper coating, chemical industries, and manufacturing processes.

A nanofluid contains nano-sized particles (diameter less than 100 nm) which are suspended in the base fluid. The term, “nanofluid” was first coined, by Choi [8] and Buongiorno [9] to describe the importance of the various transport mechanisms in nanofluids. Using the model given by [9], Nield and Kuznetsov [10, 11] analyzed the thermal stability problem and found that nanoparticles have a destabilizing effect.

The effect of throughflow was generally stabilizing, however, for a small amount of throughflow, it shows the destabilizing effect [12, 13]. Nield [14] found that destabilization occurs when the throughflow is away from impermeable boundaries. In the absence of internal heat generation, throughflow destabilized the system in a very small amount of throughflow at the different boundary conditions (top and bottom layer are not identical) [1]. Barletta et al. [15] studied the effect of vertical throughflow with viscous dissipation. Nield and Kuznetsov [16, 17] investigated the effect of vertical throughflow on both the boundaries (isoflux and isothermal). By using the Buongiorno model [16], we studied the effect of vertical throughflow on the onset of nanofluid convection, later it, this model was revised by using more realistic boundary conditions [18–20].

From the above brief review, it is clear that many researchers have carried out extensive studies on the onset of convection in Rivlin–Ericksin elastico-viscous nanofluids recently; however, the effect of vertical throughflow in Rivlin–Ericksin elastico-viscous nanofluid using the new boundary conditions (in which nanoparticle flux is the sum of diffusive, connective, and thermophoretic terms) has not been yet studied. Therefore, in this paper, the effects of viscoelastic parameters, nanofluid parameters, and throughflow parameters are investigated analytically and numerically for Rigid-rigid boundary conditions in a non-Darcy porous media.

2. Analysis

2.1. Mathematical formulation

An infinite horizontal Rivlin–Ericksen elastico-viscous nanofluid confined between rigid impermeable boundaries $z = 0$ and $z = H$ is considered. The pore sizes are large compared to nanoparticles. We use the modified Brinkman–Darcy model to define the nature of the porous medium and the Oberbeck–Boussinesq approximations are employed. We take temperatures T_0 and T_1 ($T_1 > T_0$) at the lower and the upper wall. The homogeneity and local thermal equilibrium in the porous medium is also assumed. The governing equations for mass, momentum, energy and nanoparticles for Rivlin–Ericksen elastico-viscous nanofluid in porous medium are written below (details of following equations can be seen in the articles given by [6,7,11]):

$$\nabla \cdot \mathbf{V}_D = 0, \tag{1}$$

$$\frac{\rho_f}{\varepsilon} \frac{d\mathbf{V}_D}{dt} = -\nabla \mathbf{P} - \frac{1}{k} \left(\mu + \mu' \frac{\partial}{\partial t} \right) \mathbf{V}_D + \left[\varphi \rho_p + (1 - \varphi) \{ \rho (1 - \beta(T - T_0)) \} \right] \mathbf{g}, \tag{2}$$

$$\frac{\partial T}{\partial t} + \frac{(\rho c)_f}{(\rho c)_m} \mathbf{V}_D \cdot \nabla T = k_m \nabla^2 T + \frac{\varepsilon (\rho c)_p}{(\rho c)_m} \left(D_B \nabla \varphi \cdot \nabla T - \frac{(\varphi - \varphi_0) \mathbf{V}_D}{\varepsilon} + \frac{D_T}{T_1} \nabla T \cdot \nabla T \right), \tag{3}$$

$$\frac{\partial \varphi}{\partial t} + \frac{1}{\varepsilon} \mathbf{V}_D \cdot \nabla \varphi = D_B \nabla^2 \varphi + \frac{D_T}{T_1} \nabla^2 T, \tag{4}$$

where \mathbf{V}_D is the Darcy velocity, μ and μ' are viscosity and kinematic viscoelasticity, ε is the porosity of the porous medium, p , t and \mathbf{g} are the pressure, time and gravity vector, T is the nanofluid temperature, φ is the nanoparticles volume fraction, ρ is the density of the nanofluid, ρ_p is the density of nanoparticles, $(\rho c)_p$ is the volumetric heat capacity for the nanoparticles, $(\rho c)_f$ is the volumetric heat capacity for the nanofluid, $(\rho c)_m$ is the effective heat capacity of the porous medium, (k_m) is the effective thermal conductivity of porous media, (β) is the volumetric thermal expansion coefficient, (D_B) is the Brownian diffusion coefficient, (D_T) is the thermophoresis diffusion coefficient.

On the boundaries, it is assumed that the temperature and throughflow velocity are constant. The total nanoparticle flux (sum of diffusive, thermophoretic, and connective terms) is assumed to be zero at the boundaries.

The boundary conditions are:

$$\begin{aligned} w = W_c, \quad T = T_0, \quad D_B \frac{\partial \varphi}{\partial z} - (\varphi - \varphi_0) W_c + \frac{D_B}{T_0} \frac{\partial T}{\partial z} &= 0 \quad \text{at } z = 0, \\ w = W_c, \quad T = T_1, \quad D_B \frac{\partial \varphi}{\partial z} - (\varphi - \varphi_0) W_c + \frac{D_B}{T_1} \frac{\partial T}{\partial z} &= 0 \quad \text{at } z = 1. \end{aligned} \tag{5}$$

Defining the dimensionless variables as follows:

$$\begin{aligned} (x', y', z') &= \frac{(x, y, z)}{H}, \quad \mathbf{V}(u', v', w') = \frac{\mathbf{V}_D(u, v, w) H}{\kappa}, \quad t' = \frac{t \kappa}{\sigma H^2}, \\ p' &= \frac{p K}{\mu \kappa}, \quad \varphi' = \frac{\varphi - \varphi_0}{\varphi_0}, \quad T' = \frac{T - T_1}{T_0 - T_1}, \end{aligned} \tag{6}$$

where $\kappa = \frac{k_m}{(\rho c_p)_f}$.

Eqs. (1)–(4) in non-dimensionless form (after dropping the primes) can be written as:

$$\nabla \cdot \mathbf{V} = 0, \tag{7}$$

$$\frac{1}{V_a} \frac{d\mathbf{V}}{dt} = -\nabla \mathbf{P} - \left(1 + F \frac{\partial}{\partial T} \right) \mathbf{V} - R_m \hat{\mathbf{k}} + R_a T \hat{\mathbf{k}} - R_n \varphi \hat{\mathbf{k}}, \tag{8}$$

$$\left(\frac{\partial}{\partial t} + \mathbf{V} \cdot \nabla \right) T = \nabla^2 T + \frac{N_B}{L_e} \nabla \varphi \cdot \nabla T - N_B \varphi \mathbf{V} + \frac{N_A N_B}{L_e} \nabla T \cdot \nabla T \tag{9}$$

$$\frac{1}{\sigma} \frac{\partial \varphi}{\partial t} + \frac{1}{\varepsilon} \mathbf{V} \cdot \nabla \varphi = \frac{1}{L_e} \nabla^2 \varphi + \frac{N_A}{L_e} \nabla^2 T. \tag{10}$$

The dimensionless parameters in Eqs. (8)–(10) namely, Prandtl number. (Pr), modified Darcy number (\tilde{D}_a), Rayleigh number (R_a), basic density Rayleigh number (R_m), nanoparticle Rayleigh number (R_n), Lewis number (L_e), Péclet number Q , Modified diffusivity Ratio (N_A), modified particle-density increment (N_B), Vadasz

number (Va), Thermal capacity ratio(σ), kinematics viscoelasticity (F) are defined as follows:

$$\begin{aligned} Pr &= \frac{\mu}{\rho\kappa}, \quad \tilde{D}_a = \frac{K}{H^2}, \quad R_a = \frac{\rho g \alpha H (T_0 - T_1)}{\mu\kappa}, \quad R_m = \frac{[\rho_p \varphi_0 + \rho(1 - \varphi_0)]gH}{\mu\kappa}, \quad R_n = \frac{\{(\rho_p - \rho)\varphi_0\}gH}{\mu\kappa}, \\ L_e &= \frac{\alpha_m}{D_B}, \quad Q = \frac{HV}{k_m}, \quad N_A = \frac{D_T(T_0 - T_1)}{D_B T_1 \varphi_0}, \quad N_B = \frac{(\rho c)_p \varphi_0}{(\rho c)_f}, \quad Va = \frac{\varepsilon Pr}{Da}, \quad \sigma = \frac{(\rho c_p)_m}{(\rho c_p)_f}, \quad F = \frac{\mu' K}{\mu \sigma H^2}. \end{aligned} \tag{11}$$

The dimensionless form of boundary conditions are written as:

$$\begin{aligned} w = Q, \quad T = 1, \quad \frac{\partial \varphi}{\partial z} - QL_e \varphi + N_A \frac{\partial T}{\partial z} &= 0 \quad \text{at } z = 0, \\ w = Q, \quad T = 0, \quad \frac{\partial \varphi}{\partial z} - QL_e \varphi + N_A \frac{\partial T}{\partial z} &= 0 \quad \text{at } z = 1. \end{aligned} \tag{12}$$

2.2. Basic solutions

The basic state of nanofluid is assumed to be time independent and is described by:

$$\mathbf{V} = \mathbf{V}_b = (0, 0, Q), \quad p = p_b(z), \quad T = T_b(z), \varphi = \varphi_b(z). \tag{13}$$

Then, Eqs. (8)–(10) are simplified as:

$$\frac{d^2 T_b}{dz^2} + \frac{N_B}{L_e} \frac{d\varphi_b}{dz} \frac{dT_b}{dz} + \frac{N_A N_B}{L_e} \left(\frac{dT_b}{dz} \right)^2 - Q_v \frac{dT_b}{dz} - Q_v N_B \varphi_b \frac{dT_b}{dz} = 0, \tag{14}$$

$$\frac{d^2 \varphi_b}{dz^2} + N_A \frac{d^2 T_b}{dz^2} - Q_v L_e \frac{d\varphi_b}{dz} = 0. \tag{15}$$

Solving Eq. (15) and Eq. (16) with boundary condition gives:

$$T_b = \frac{e^{Q_v z} - e^{Q_v z}}{e^{Q_v} - 1}, \tag{16}$$

$$\varphi_b = \frac{(1 - L_e - N_A)(e^{Q_v L_e z} - 1)}{(1 - L_e)(e^{Q_v L_e} - 1)} + \frac{N_A(e^{Q_v z} - 1)}{(1 - L_e)(e^{Q_v} - 1)}. \tag{17}$$

We differentiate the T_b, φ_b with respect to z :

$$\frac{dT_b}{dz} = \frac{Q e^{Q_v z}}{(1 - e^Q)}, \tag{18}$$

$$\frac{d\varphi_b}{dz} = \frac{QL_e(\varepsilon - L_e - N_A)e^{\frac{QL_e z}{\varepsilon}}}{(1 - L_e)\varepsilon(e^{\frac{QL_e}{\varepsilon}} - 1)} + \frac{\varepsilon N_A Q e^{Q_v z}}{(\varepsilon - L_e)(e^Q - 1)}. \tag{19}$$

Using the limit $Q \rightarrow 0$, the basic solution becomes $T_b = 1 - z, \varphi_b = z$; this is same solution as obtained by [11].

2.3. Perturbed solutions

For perturbations of small disturbance onto the base fluid, we assume that:

$$\mathbf{V} = \mathbf{V}_b + \mathbf{V}', \quad T = T_b + T', \quad \varphi = \varphi_b + \varphi', \quad p = p_b + p'. \tag{20}$$

Substituting the perturbed solutions in Eqs. (7)–(10) and Eq. (12), we get:

$$\nabla \cdot \mathbf{V}' = 0, \tag{21}$$

$$\frac{1}{V_a} \frac{\partial \mathbf{V}'}{\partial t} + w' = -\frac{\partial p'}{\partial z} - \left(1 + F \frac{\partial}{\partial t} \right) + R_a T' \hat{\mathbf{k}} - R_n \varphi' \hat{\mathbf{k}}', \tag{22}$$

$$\begin{aligned} \frac{\partial T'}{\partial t} + \frac{dT_b}{dz} w' + Q \frac{\partial T'}{\partial z} &= \nabla^2 T' + \frac{N_B}{L_e} \left(\frac{d\varphi_b}{dz} \frac{\partial T'}{\partial z} - \frac{dT_b}{dz} \frac{\partial \varphi'}{\partial z} \right) + \frac{2N_A N_B}{L_e} \frac{dT_b}{dz} \frac{\partial T'}{\partial z} \\ &\quad - N_B \left(Q \frac{dT_b}{dz} \varphi' + \varphi_b \frac{dT'}{dz} w' + Q \varphi_b \frac{\partial T'}{\partial z} \right), \end{aligned} \tag{23}$$

$$\frac{\partial \varphi'}{\partial t} + Q \frac{\partial \varphi'}{\partial z} + \frac{d\varphi_b}{dz} w' = \frac{1}{L_e} \nabla^2 \varphi' + \frac{N_A}{L_e} \nabla^2 T'. \tag{24}$$

Eq. (22) is operated with $\hat{\mathbf{k}} \cdot \text{curl curl}$ and the use is made of the identity $\text{curl curl} = \text{grad div} - \nabla^2$ together with Eq. (21). As a result of this procedure, pressure is eliminated from Eq. (22) and we get:

$$\frac{1}{Pr} \frac{\partial}{\partial t} \nabla^2 w' + \left(1 + M + F \frac{\partial}{\partial t} \right) \nabla^2 w' = R_a \nabla_H^2 T' - R_n \nabla_H^2 \varphi'. \tag{25}$$

In Eq. (25) ∇_H^2 is the 2-D Laplacian operator in the horizontal plane.

Analyzing the disturbance into the normal modes, perturbation equations are introduced as the following form:

$$[w', T', \varphi'] = [W(z), \Theta(z), \Phi(z)]f(x, y) \exp(st). \tag{26}$$

Using the normal mode analysis, the following equations for the amplitudes Θ, Φ, W are obtained:

$$(D^2 - a^2) \left(1 + \frac{s}{V_a} + sF \right) W + R_a a^2 \Theta - R_n a^2 \Phi = 0, \tag{27}$$

$$\begin{aligned} (-1 + N_B Q) \frac{dT_b}{dz} W + \left(D^2 + \frac{N_B}{L_e} \frac{d\varphi_b}{dz} D + \frac{2N_A N_B}{L_e} \frac{dT_b}{dz} D - N_B Q \varphi_b D - Q_v D - a^2 - s \right) \Theta \\ + \left(\frac{N_B}{L_e} \frac{dT_b}{dz} D - N_B Q \frac{dT_b}{dz} \right) \Phi = 0, \end{aligned} \tag{28}$$

$$\frac{d\varphi_b}{dz} W - \frac{N_A}{L_e} (D^2 - a^2) \Theta - \frac{1}{L_e} \left((D^2 - a^2) - Q_v D - \frac{s}{\sigma} \Phi \right) = 0, \tag{29}$$

with boundary conditions as:

$$W = 0, \quad \Theta = 0, \quad D\Phi - \frac{QL_e}{\varepsilon} \Phi + N_A D\Theta = 0, \quad \text{at } z = 0, 1. \tag{30}$$

Here, a is a dimensionless wave number, and $s = i\omega$ is a complex growth factor, where ω is a dimensionless frequency (it is a real number).

Single-term Galerkin-type weighted residuals method is used to obtain approximate solutions to the system of Eqs. (27)–(29). Accordingly Θ, W, Φ (satisfying the boundary conditions exactly) are chosen as:

$$\Theta_1 = z - z^2, \quad W_1 = z(1 - z)^2, \quad \Phi_1 = \frac{-N_A(QL_e - 2 - 2QL_e z)}{QL_e^2}.$$

We substitute this minimal polynomial into Eqs. (27)–(29) and using the Orthogonality of trial functions, we obtain a system of 3 linear algebraic equations in the 3 unknowns. We get:

$$\begin{bmatrix} G1 & \frac{R_a a^2}{140} & \frac{R_n N_A a^2}{15\eta^2} \\ (-1 + N_B Q) A_{TW} & G2 & \frac{N_B}{L_e} B_{T\Phi} - N_B Q A_{T\Phi} \\ A_{\varphi W} & -\frac{N_A^2(12 + a^2)}{3L_e \eta^2} & \frac{N_A^2 a^2(12 + \eta^2) - 3 - s(12 + \eta^2)}{3L_e \eta^4} \end{bmatrix} \begin{bmatrix} W \\ \Theta \\ \Phi \end{bmatrix} = \begin{bmatrix} 0 \\ 0 \\ 0 \end{bmatrix}, \tag{31}$$

where

$$G1 = \left(\frac{S}{V_a} + 1 \right) (504 + 24a^2 + a^4 + \tilde{D}_a(12 + a^2)),$$

$$G2 = \frac{-(10 + a^2)}{30} + \frac{N_B}{L_e} B_{\varphi\Theta} + \frac{2N_A N_B}{L_e} B_{T\Theta} - \frac{s}{30},$$

$$A_{TW} = \int_0^1 \left(\frac{dT_b}{dz} W \right) \Theta dz = \frac{6(120 + 60Q + 12Q^2 + Q^3) + e^Q(-120 + Q(60 + (-12 + Q)Q))}{Q^6(1 - e^Q)},$$

$$\begin{aligned} B_{\varphi\Theta} = \int_0^1 \left(\frac{d\varphi_b}{dz} D\Theta \right) \Theta dz = - \frac{\eta^2 + 6\eta + 12 - e^\eta(\eta^2 - 6\eta + 12)(Q - \eta - N_A Q)}{\eta^3(1 - e^\eta)(Q - \eta)} \\ - \frac{N_A(Q^2 + 6Q + 12 - e^Q(Q^2 - 6Q + 12))}{Q^2(1 - e^Q)(Q - \eta)}, \end{aligned}$$

$$B_{T\Theta} = \int_0^1 \left(\frac{dT_b}{dz} D\Theta \right) \Theta dz = \frac{Q^2 + 6Q + 12 - e^Q(Q^2 - 6Q + 12)}{Q^3(1 - e^Q)},$$

$$\begin{aligned} A_{\varphi\Theta} = \int_0^1 (\varphi_b D\Theta) \Theta dz = \frac{\eta^2 + 6\eta + 12 - e^\eta(\eta^2 - 6\eta + 12)(Q - \eta - N_A Q)}{\eta^4(1 - e^\eta)(Q - \eta)} \\ + \frac{N_A(Q^2 + 6Q + 12 - e^Q(Q^2 - 6Q + 12))}{Q^3(1 - e^Q)(Q - \eta)}, \end{aligned}$$

$$B_{T\Phi} = \int_0^1 \left(\frac{dT_b}{dz} D\Phi \right) \Theta dz = \frac{2\eta(2 + e^Q(-2 + Q) + Q)}{Q^2(1 - e^Q)},$$

$$A_{T\Phi} = \int_0^1 \left(\frac{dT_b}{dz} \Phi \right) \Theta dz = \frac{-2Q(2 + e^Q(-2 + Q) + Q) + \eta(12 + 6Q + Q^2 - e^Q(12 - 6Q + Q^2))}{Q^3(1 - e^Q)},$$

$$A_{\varphi\Phi} = \int_0^1 \left(\frac{d\varphi_b}{dz} W \right) \Phi dz = \frac{2(Q - \eta - N_A Q)(\eta - 2(1 + \eta z))(-12 - \eta(6 + \eta) + e^\eta(12 + (-6 + \eta)\eta))}{\eta^4(Q - \eta)(e^\eta - 1)}$$

$$+ \frac{2N_A(\eta - 2(1 + \eta z))(-12 - Q(6 + Q) + e^Q(12 + (-6 + Q)Q))}{Q^3(Q - \eta)(e^Q - 1)},$$

$$\eta = \frac{QL_e}{\varepsilon}.$$

For all considered set of boundary conditions, oscillatory convection cannot be occurring. In the absence of oscillatory convection ($s = 0$), we get the following expression for R_a :

$$R_a = \frac{14((504 + 24a^2 + a^4 + \tilde{D}_a(12 + a^2))\alpha - N_A R_n \beta)}{\gamma}, \quad (32)$$

where:

$$\alpha = \frac{30\eta^2 N_A^2 N_B(12 + a^2)(B_{T\Phi} - QA_{T\Theta}L_e) + A_{\varphi W}\eta^2(N_a^2 a^2(12 + \eta^2) - 3)(N_B(B_{\Phi\Theta} + 2B_{T\Theta}N_A) - (10 + a^2)L_e)}{9a^2 L_e^2 \eta^4},$$

$$\beta = \frac{A_{\varphi W}\eta^2(30N_B(B_{\Phi\Theta} + 2B_{T\Theta}N_A) - (10 + a^2)L_e)A_{\varphi W}\eta^2 + 10N_A^2 A_{TW}(-1 + N_B Q)(12 + a^2)}{45L_e \eta^4},$$

$$\gamma = \frac{3L_e \eta^4 N_B(B_{T\Phi} - QA_{T\Theta}L_e) - A_{TW}(N_a^2 a^2(12 + \eta^2) - 3)(-1 + N_B Q)}{3L_e \eta^4}.$$

The Rayleigh number (R_a) is a function of $a\varepsilon$, \tilde{D}_a , Q , L_e , N_A , a , R_n , and N_B and from Eq. (32), it is also clear that the Rayleigh number (R_a) is independent of viscoelastic parameters (V_a, F, σ). Thus, the effect of throughflow in Rivlin–Ericksin elastico-viscous nanofluid is independent of viscoelastic parameters. To simplify the above expression, we have assumed that $Q \ll 1$, so that first order Galerkin approximation leads to a useful result:

$$R_a = \frac{140(G3)(504 + 24a^2 + a^4 + \tilde{D}_a(12 + a^2)) - (105(12 + a^2)(1 + N_B Q)N_A - 98(G3)L_e)R_n}{135a^2(1 + N_B Q)}, \quad (33)$$

where $G3 = 10 + a^2 - \frac{N_A N_B Q}{L_e}$.

In Eq. (33), for the admissible range of parameters the Rayleigh number decreases as a nanoparticle Rayleigh number increases. The corresponding critical wave number can be obtained from Eq. (33), which in the presence of throughflow, critical wave number is a function of the Peclet number, modified Darcy number as well as nanofluid parameters.

In the absence of vertical throughflow, Eq. (33) reduces to the following form:

$$R_a = \frac{140(10 + a^2)(504 + 24a^2 + a^4 + \tilde{D}_a(12 + a^2)) - 105(12 + a^2)N_A R_n - 98(10 + a^2)L_e R_n}{135a^2}. \quad (34)$$

In the absence of vertical throughflow ($Q = 0$) the Rayleigh number is not a function of the modified particle density increment (N_B).

3. Results and discussions

To study the effect of various parameters on the stability, Eq. (33) is analyzed analytically and numerically. According to data given by [1, 11], the following threshold values for alumina/water nanofluids of 1–100 nm are utilized: $L_e = 500$, $Q = 0.5$, $R_n = 0.1$, $N_A = 5$, $N_b = 0.01$. Fig. 1 shows the plot of critical Rayleigh number ($R_{a,c}$) versus nanoparticle Rayleigh number R_n for vertical throughflow $Q = 0.1, 0.3, 0.7, 1$. It can be seen that R_n destabilizes the onset of convection. Fig. 1 also shows that $R_{a,c}$ increases with increasing value of Q . Vertical through flow delays the onset of nanofluid convection and this effect is larger for higher nanoparticle Rayleigh number values.

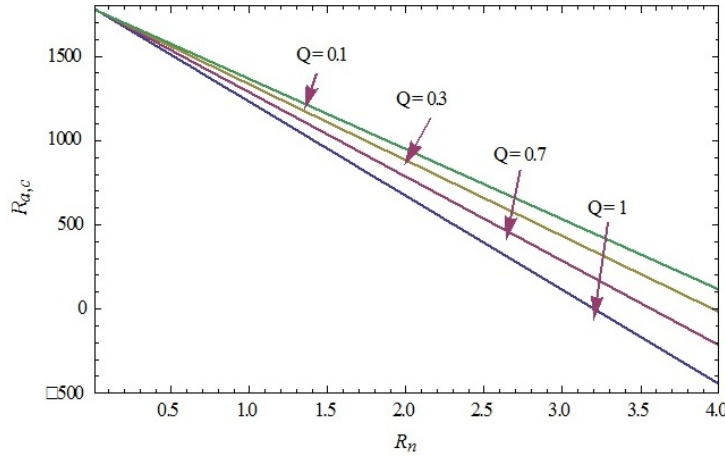


FIG. 1. Variation of $R_{a,c}$ with R_n for different values of Q

Figure 2 shows that the modified particle density increment (N_b) has no significant effect on the stability of Rivlin–Ericksin elasto-viscous nanofluid.

Figure 3 shows the variation of Rayleigh number R_a when $L_e = 500, 700$ and $N_A = 1.5$ respectively. It is seen that as the value of the Lewis number (L_e) increases, the Rayleigh number decreases. Thus, the Lewis number promotes nanofluid convection. The modified diffusivity ratio has a destabilizing effect on the onset of convection. This is because thermophoresis pushes the lighter nanoparticles upwards, which enhances the destabilizing effects on particle distributions.

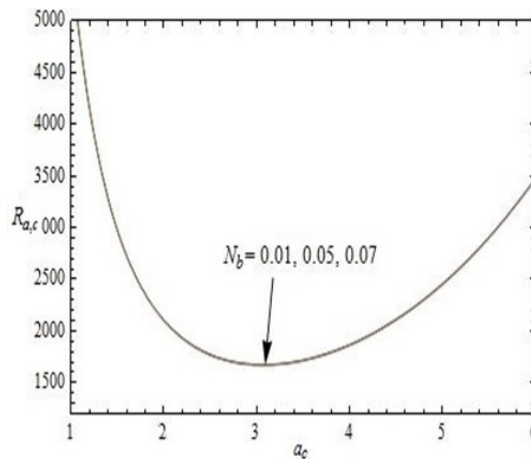


FIG. 2. Variation of $R_{a,c}$ with a_c for different values of N_b

4. Conclusions

In this paper, we investigate the effect of vertical throughflow in Rivlin–Ericksin elasto-viscous nanofluid for Rigid-rigid boundaries in a non-Darcy porous medium. It was observed that when using the convective term

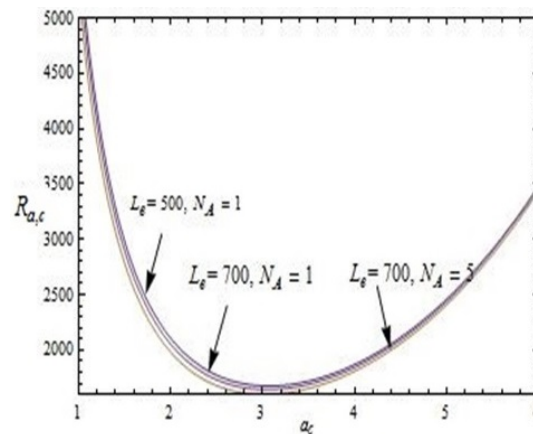


FIG. 3. Variation of $R_{a,c}$ with a_c for different values of N_b , L_e

of nanoparticle flux at the boundary, the Rayleigh number was independent of thermal capacity ratio, kinematics viscoelasticity parameter and Vadsaz number. The critical wave number was a function of the nanofluid parameters as well as Péclet number. Porosity, Lewis number, and nanoparticle Rayleigh number promotes instability while the modified particle-density increment had no significant effect on the stability. Vertical through flow delays the onset of nanofluid convection and this effect is larger for higher nanoparticle Rayleigh number values. New boundary conditions in terms of zero nanoparticle flux (the sum of the diffusive, thermophoretic, and connective terms) is more favourable for convection; however there is no drastic change in the magnitude of Rayleigh number.

References

- [1] Rivlin R., Ericksen J. Stress-Deformation Relations for Isotropic Materials. *J. Ration Mec.h Anal.*, 1955, **4**(2), P. 323–425.
- [2] Rudraiah N., Kaloni P.N., Radhadevi P.V. Oscillatory convection in a viscoelastic fluid through a porous layer heated from below. *Rheologica Acta.*, 1989, **28**(1), P. 48–53.
- [3] Kim M.C., Lee S.B., Chung B.J. Thermal instability of viscoelastic fluids in porous media. *Int. J. Heat Mass Transf.*, 2003, **46**, P. 5065–5072.
- [4] Sharma R.C., Kumar P. Effect of Rotation on Thermal Instability in Rivlin-Ericksen elastico-viscous Fluid. *Zeitschrift für Naturforschung A.*, 1996, **51**(7), P. 821–824.
- [5] Sharma R.C., Kumar P. Thermal Instability in Rivlin-Ericksen elastico-viscous Fluid in Hydromagnetic. *Z. Naturforsch.*, 1997, **52a**, P. 369–371.
- [6] Sheu L.J. Thermal Instability in a Porous Medium Layer Saturated with a Visco-Elastic Nanofluid. *Transp. Porous Med.*, 2011, **88**, P. 461–477.
- [7] Sheu L.J. Linear Stability of Convection in a Visco Elastic Nanofluid Layer. *World Acad. Sci. Eng. Technol.*, 2011, **58**, P. 289–295.
- [8] Choi S. Enhancing Thermal Conductivity of Fluids with Nanoparticles in Developments and Applications of Non-Newtonian Flows. *ASME*, 1995, **66**, P. 99–105.
- [9] Buongiorno J. Connective Transport in nanofluids. *J. Heat Transf.*, 2006, **128**, P. 240–250.
- [10] Nield D.A., Kuznetsov A.V. Thermal instability in a porous medium layer saturated by a nanofluid. *Int. J. Heat Mass Transf.*, 2009, **52**, P. 5796–5801.
- [11] Nield D.A., Kuznetsov A.V. The onset of convection in a horizontal layer of finite depth. *Eur. J. Mech. B/Fluids*, 2010, **29**, P. 217–223.
- [12] Homsy G.M., Sherwood A.E. Convective instabilities in porous media with throughflow. *AIChE J.*, 1976, **22**, P. 168–174.
- [13] Jones M.C., Persichetti J.M. Convective instability in packed beds with throughflow. *AIChE J.*, 1986, **32**, P. 1555–1557.
- [14] Nield D.A. Convective instability in porous media with throughflow. *AIChE J.*, 1987, **33**, P.1222–1224.
- [15] Barletta A., di Schio E. R., Storesletten L. Convective roll instabilities of vertical throughflow with viscous dissipation in a horizontal porous layer. *Transp. Porous Med.*, 1986, **81**, P. 461–77.
- [16] Nield D.A., Kuznetsov A.V. The effect of vertical through flow on thermal instability in a porous medium layer saturated by a nanofluid. *Transp. Porous Med.*, 2011, **87**, P. 765–775.
- [17] Nield D.A., Kuznetsov A.V. The onset of convection in a layered porous medium with vertical throughflow. *Transp. Porous Med.* 2013, **98**, P. 363–376.
- [18] Nield D.A., Kuznetsov A.V. The effect of vertical throughflow on thermal instability in a porous medium layer saturated by a nanofluid: a revised model. *ASME J. Heat Transf.*, 2015, **137**, P. 052601.
- [19] Khalili A., Shivakumara I.S. Onset of convection in a porous layer with net throughflow and internal heat generation. *Phys Fluids*, 1998, **10**, P. 315.
- [20] Nield D.A., Kuznetsov A.V. The effects of combined horizontal and vertical heterogeneity on the onset of convection in a porous medium with horizontal throughflow. *Int. J. Heat Mass Transf.*, 2010, **54**, P. 5595–5601.

Detection of the polarization spatial distribution of THz radiation generated by two-color laser filamentation

S. V. Smirnov, M. S. Kulya, A. N. Tsyarkin, S. E. Putilin, V. G. Bespalov

ITMO University, Kronverkskiy, 49, St. Petersburg, 197101, Russia

smirnov.semen@niuitmo.ru, mskulya@corp.ifmo.ru, tsypkinan@mail.ru,
seputilin@yandex.ru, victorbespaloff@gmail.com

PACS 52.38.-r, 42.25.Ja

DOI 10.17586/2220-8054-2017-8-5-613-619

The spatial distribution of the terahertz radiation polarization is experimentally measured from a femtosecond laser two-color filament in air. Terahertz radiation generation from two-color plasma filamentation with a β -BBO crystal located behind the lens leads to the spatial inhomogeneity of the polarization distribution. Inhomogeneity of the terahertz field polarization is determined by the polarization of the fundamental harmonic of the pump radiation after passing through the β -BBO crystal. A spatial inhomogeneity of the fundamental harmonic polarization is observed owing to the β -BBO crystal acting as a phase plate illuminated by a spherical front.

Keywords: filament generation, terahertz radiation, polarization.

Received: 18 August 2017

Revised: 21 August 2017

1. Introduction

Terahertz radiation (THz) is widely applied in biological diagnostics systems [1], chemistry [2], holography [3–5] and imaging [6, 7]. There are three main types of THz generation methods with femtosecond pulse pumping: nonlinear optical rectification [8], generation from the surface of a semiconductor layer based on the Demer effect (or by means of a photoconductive antenna) and femtosecond-laser-beam filamentation [9, 10]. One of the attractive features of filamentation is that the THz bandwidth is only determined by the exciting pulse duration and can reach up to 100 THz [11]. Filamentation deserves attention because it allows the generation of high-intensity THz radiation and management of its properties (intensity, polarization and radiation pattern) by varying the pump pulse duration and focusing conditions [12, 13]. The physical origin of the THz radiation is attributed to the transition Cherenkov emission process [14, 15]. One of the important properties of THz radiation is the polarization state. Previously [14, 16], it has been shown that the integrated field of the THz beam has a radial polarization. In the latest research, these results have been supplemented with the fact that the polarization of the THz field has an elliptic structure [17, 18]. This fact can be explained by a four-wave optical rectification [19]. The ellipticity of the integrated THz field polarization was recorded for the case of two-color filamentation [20, 21]. Moreover, it has been shown that THz radiation polarization is directly dependent on the polarization of the fundamental pump radiation [18]. However, all of this research was performed for an integrated THz beam profile and did not consider the possibility of mapping the local polarization of the THz beam. Recent research [22] demonstrated a method for generating broadband and few-cycle THz vortex beams through conversion of a radially polarized THz beam into a THz vortex beam. Thus, the polarization behavior in THz beams gains additional importance in the singular optics of THz spectral range [23, 24].

The current state of this technology demonstrates that it is possible to obtain a spatial distribution of the THz field in the time domain at different beam points independently and thus enables the mapping of the local properties of the investigated field, which is important in various imaging applications. In our research, we experimentally record the dependency of the polarization spatial distribution of the THz radiation generated in two-color filamentation. We identify the local THz field polarization inhomogeneity which is related to the inhomogeneity of the spatial distribution of laser fundamental pumping polarization state. Using this method, one can control the polarization inhomogeneity and thus vary the beam shape. One of the possible applications of such beam shaping is vortex beam generation, which can be realized by determining the polarization state distribution. Based on this method, the vortex beam properties can be used in a THz holographic imaging system [25].

2. Experimental setup and results

The pump radiation in the femtosecond laser system exhibited the following parameters: central wavelength of 800 nm, repetition rate of 1 kHz, pulse duration of 35 fs, pulse energy of 2 mJ, as well as horizontal polarization. To generate a filament, the femtosecond radiation was focused by a lens with a focal length of 25 cm. The β -BBO crystal with 300 μm thickness placed behind the lens focus was used for the second-harmonic generation. The β -BBO crystal was cut for type-I phase-matched second-harmonic generation with 800 nm pump light. Owing to the fact that the crystal was in a spherical beam, the efficiency of the second harmonic conversion for the horizontal and vertical polarization of the fundamental harmonic was 1 %. However, as described previously [26], the properties of the THz beam profile radiation can be regulated by varying the distance from the BBO to the filament, the azimuthal angle of BBO, the tilt angle of BBO and the tilt angle of the focusing lens. In our case, we determined the optimal parameters for the β -BBO crystal position as being when a maximum THz signal was observed. The filament length was measured from a photograph on the CCD camera and the value was approximately 15 mm. The polarization of the two-color radiation output is presented in Fig. 1(a,b). The orientation of the fundamental harmonic was set by the rotation of the half-wave plate at 90° before the focusing lens (L). Before measuring the polarization of the fundamental pump and the second harmonic, we reduced the pump radiation power so that there was no filamentation, and made experimental measurements at the correlating points of the space with terahertz radiation. Polarization and ellipticity measurements were made using a polarizer (Glan prism) fixed in rotational motion to determine the angle of inclination of the polarization, and a power meter to measure ellipticity. In the first case, the initial horizontal polarization of the fundamental harmonic passed through the β -BBO crystal and then was rotated at the angle $\alpha = -15^\circ$ in relation to the initial horizontal polarization axis of 800 nm. In the second case, the ellipticity in the beam profile was 0.12 (Fig. 2(b-I)) and the initial vertical polarization after passing through the β -BBO crystal was rotated at the angle $\alpha = 73^\circ$ with an ellipticity in the beam profile of 0.22 (Fig. 2(b-II)). The polarization of the second harmonic after the β -BBO crystal in both cases was linear, and its orientation was $\beta = 73^\circ$ (Fig. 2(b-I,II)).

The THz radiation was collimated by the parabolic mirror with a 10 cm focal length and 10 cm aperture size (PM 1). It was then focused by the second parabolic mirror (PM 2) on a 1 mm-thick $\langle 110 \rangle$ oriented ZnTe crystal [27]. The 35 fs, 800 nm pulse in conjunction with 300 μm -thick Type-I β -BBO should result in a THz emission with at least a 20 THz bandwidth. However, we used ZnTe with 1 mm-thickness, which has an acceptance bandwidth only up to 2 THz (Fig. 2(b-II)). The 1 mm-thick Teflon filter (F), placed between the mirrors, attenuated the white light radiation generated by the filament and the radiation of the fundamental and second harmonics. To obtain the THz amplitude as a function of time, we used a standard scheme of the electro-optical detection, consisting of a quarter-wave plane, a Wollaston prism (WP) and a balance detector (BD). The spatial dependence of the THz field polarization was measured by moving the diaphragm (D), connected to a THz polarizer (THzP) (wire grid) placed after the Teflon filter inside the collimated beam. Such an approach has been shown previously [3,28], even though it exhibits faster fall-off of the registered signal when moving from the center to the edge owing to the change of the angle between the signal wave vector and the optical axis. The projection of the signal is proportional to the cosine of this angle. The THz field intensity had a conical form [29] and the THz field measurement was performed on the maximum intensity of the ring.

Previously [19,30], the elliptical polarization of the THz radiation has been demonstrated for the two orthogonal polarization axes. The ellipticity parameter (eccentricity and main axis tilt) can be obtained by decomposing the two orthogonal polarizations. Fig. 1(c) demonstrates the measured THz field amplitude for two orthogonal polarization states, when a THz polarizer placed in a wide collimated beam is horizontally orientated (X state is 0°), and vertically orientated (Y state is 90°). The X-Y graph shows a closed curve, which can be depicted by the ellipse with an ellipticity parameter and an axis tilt [17,18]. Fig. 1 demonstrates the THz pulse polarization with horizontal (a) and vertical (b) pump beam orientation. In the first case, the ellipticity parameter of the polarization was 0.1 and in the second case, it was 0.23.

Figures 1(a) and 1(b) show that the main axis of the THz ellipse was in the same position as the fundamental pump polarization axis [19]. The ellipticity of the THz radiation increased with an increase in the fundamental pump polarization ellipticity. Varying the pump beam ellipticity, the ellipticity of the THz pulses could be controlled and changed. Additionally, doubling the fundamental harmonic ellipticity led to a doubling of the THz harmonic ellipticity. The THz radiation beam at the filament generation had high spatial homogeneity in the center of the filament [31]. Besides, the THz field propagation from the filament had a conical structure [29] that created a “donut” vortex beam shape after collimation. Using the THz pulse time-domain holography method [3] one could obtain the THz field distribution in each spatial coordinate, which provided the polarization distribution pictures. The measurement area of the THz signal at every point was 5 mm in diameter (Fig. 3(a)). Fig. 3(b,c) shows

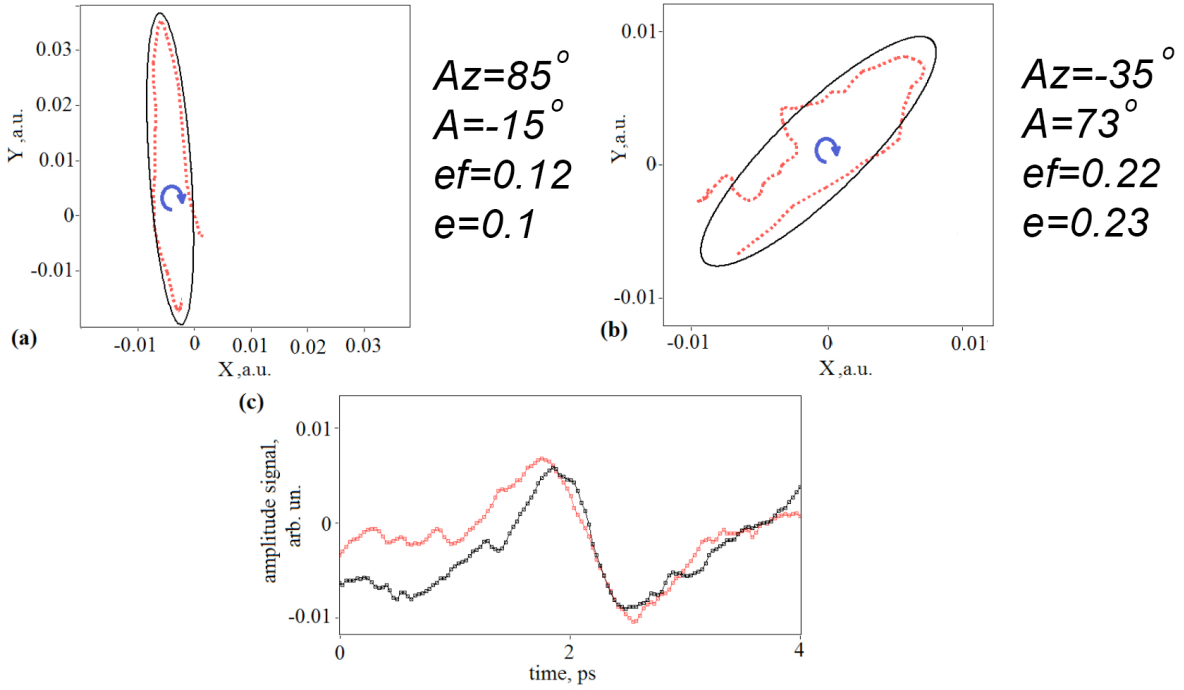


FIG. 1. (Color online) Measurement results (red dots) and approximation (black line) of the THz polarization for the case of horizontal pump polarization (a); Measurement results (red dots) and approximation (black line) of the THz polarization for the case of the vertical pump polarization (b); The THz field for two orthogonal THz polarizer states for the vertical pump polarization (red dots at 0° , black dots at 90°) (c). e is the ellipticity parameter of the THz beam profile polarization, Azimuth is the polarization angle of the THz beam profile radiation. ef is the ellipticity parameter of polarization of the fundamental harmonic, α is the angle of fundamental harmonic polarization

that spectra in different donut-beam profile positions are the same and temporal profiles differ only in phase shift which can be explained by the vortex structure of the generating beam in two-color filamentation. In the spectral domain, the polarization state of the generated THz beam exhibited no frequency dependency, for example, for point number 7 (Fig. 3(a)) the polarization had a constant value equal to ~ 0.09 in our frequency range of 0.15–2.00 THz. Therefore, it is possible to determine the polarization characteristics of the THz beam considering only a temporal form of the wave-packet. Fig. 4 illustrates the spatial distribution of the THz beam polarization for two polarization states of the pump beam radiation.

These results show that even though the THz polarization retained aperture integral ellipticity in the spatial distribution, there was still an inhomogeneity in the polarization states. However, the tilt angle for each spatial point of the THz field has the same value. Moreover, the polarization ellipse of the spatial distribution of the THz field changes from the quasi-linear state to the high-elliptical state and back during radial bypass with a period equal to 2π . Such spatial inhomogeneity is determined by the initial inhomogeneous spatial distribution of the polarization in the pump-fundamental harmonic. This was confirmed by the direct dependence of the polarization of the THz field on the polarization of the fundamental harmonic [14]. The observed inhomogeneity in the fundamental harmonic was determined by the fact that after the focusing lens, the fundamental harmonic beam became spherical and there was a polarization spatial dependence owing to the β -BBO crystal acting as a phase plate (Fig. 4).

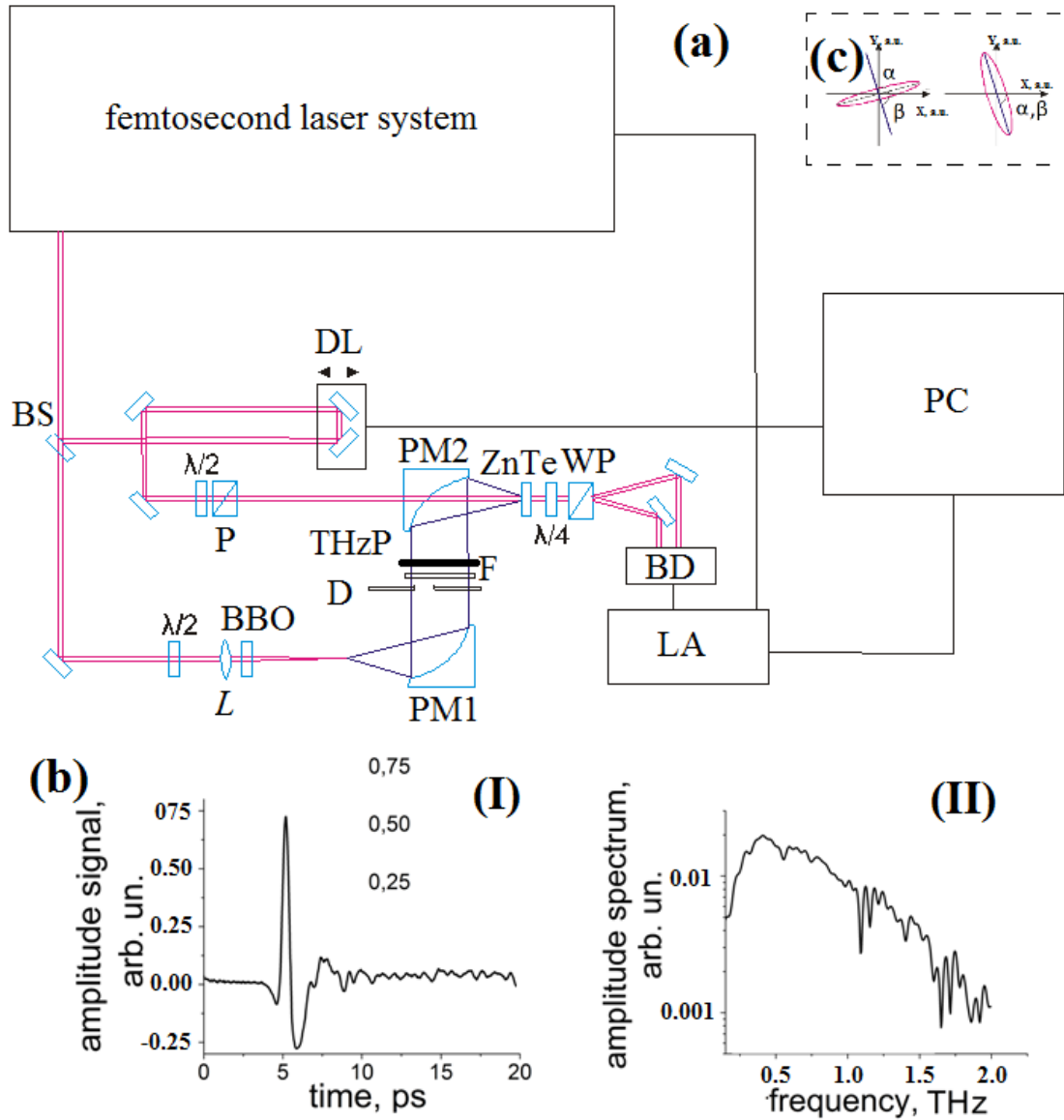


FIG. 2. (Color online) The experimental setup for measuring the spatial distribution of polarization of the THz radiation generated in two-color filamentation (a). BS is the beam splitter, DL is the time delay line, P is Glan prism, β -BBO is a nonlinear crystal for the second harmonic generation (Barium borate), L is a lens, PM1 and PM2 are parabolic mirrors, D is a diaphragm, THzP is a terahertz polarizer (wire grid), F is a Teflon filter, WP is a Wollaston prism, BD is a balance detector, LA is a Lock-in amplifier, PC is a computer. The temporal (I) and spectral (II) forms of the initial integrated beam profile THz pulse (b). Polarization of the fundamental and second harmonics (c): case of the initial horizontal (c-inset left) and vertical (c-inset right) polarization of the fundamental harmonic; α is the angle of the main axis inclination of the polarization ellipse of the fundamental harmonic after the β -BBO crystal ($\alpha = -15^\circ$ for horizontal polarization; $\alpha = 73^\circ$ for vertical polarization), β is the angle of inclination of the linear polarization of the second harmonic after the β -BBO crystal ($\beta = 73^\circ$)

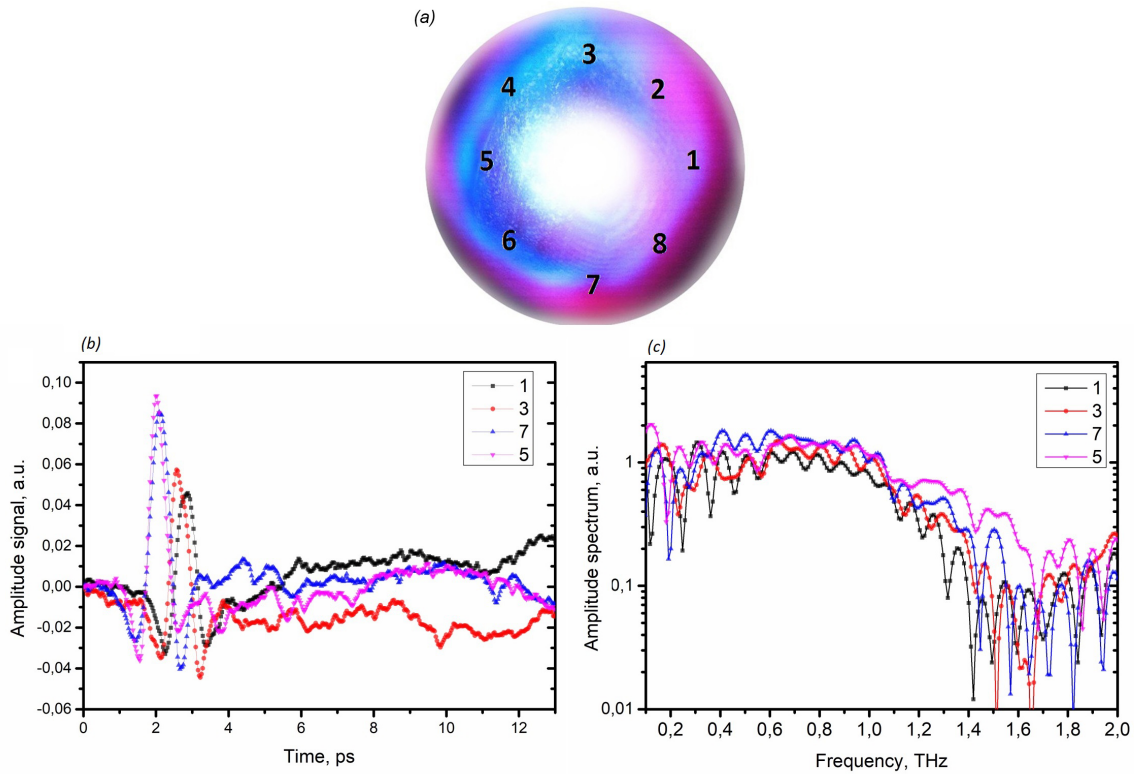


FIG. 3. (Color online) Measurement areas of a two-color filament and the areas of polarization measurement; Spatial polarization distribution of the THz beam for the two polarization states of the pump beam radiation corresponding to the points (1–8) from (a). Temporal (b) and spectral (c) form in different beam profile positions of the donut structure corresponding to (a)

3. Conclusion

Spatial distribution of the polarization of the terahertz radiation from a two-color filament in air generated by a femtosecond laser is experimentally measured in our study. We show that for this setup, the spatial inhomogeneity of the THz field is affected by the spatial inhomogeneity of the fundamental harmonic polarization. The inhomogeneity of the fundamental harmonic polarization is formed because of the passage of the spherical front after the focusing lens through the β -BBO crystal. In this case, the crystal acts as a phase plate for the beam profile. The management of the fundamental harmonic polarization can assist control of the polarization of the THz field and to form vortex beams. For instance, the conversion method of THz vortex beam generation was demonstrated in [22], where the sign of the topological charge could be controlled. This is made possible by conversion of the radially polarized THz beam via optical element achromatic polarization.

Acknowledgements

We thank X.-C. Zhang for consultation with the experiment. This work was partially financially supported by the Government of the Russian Federation, Grant 074-U01 and Project 3.9041.2017/7.8.

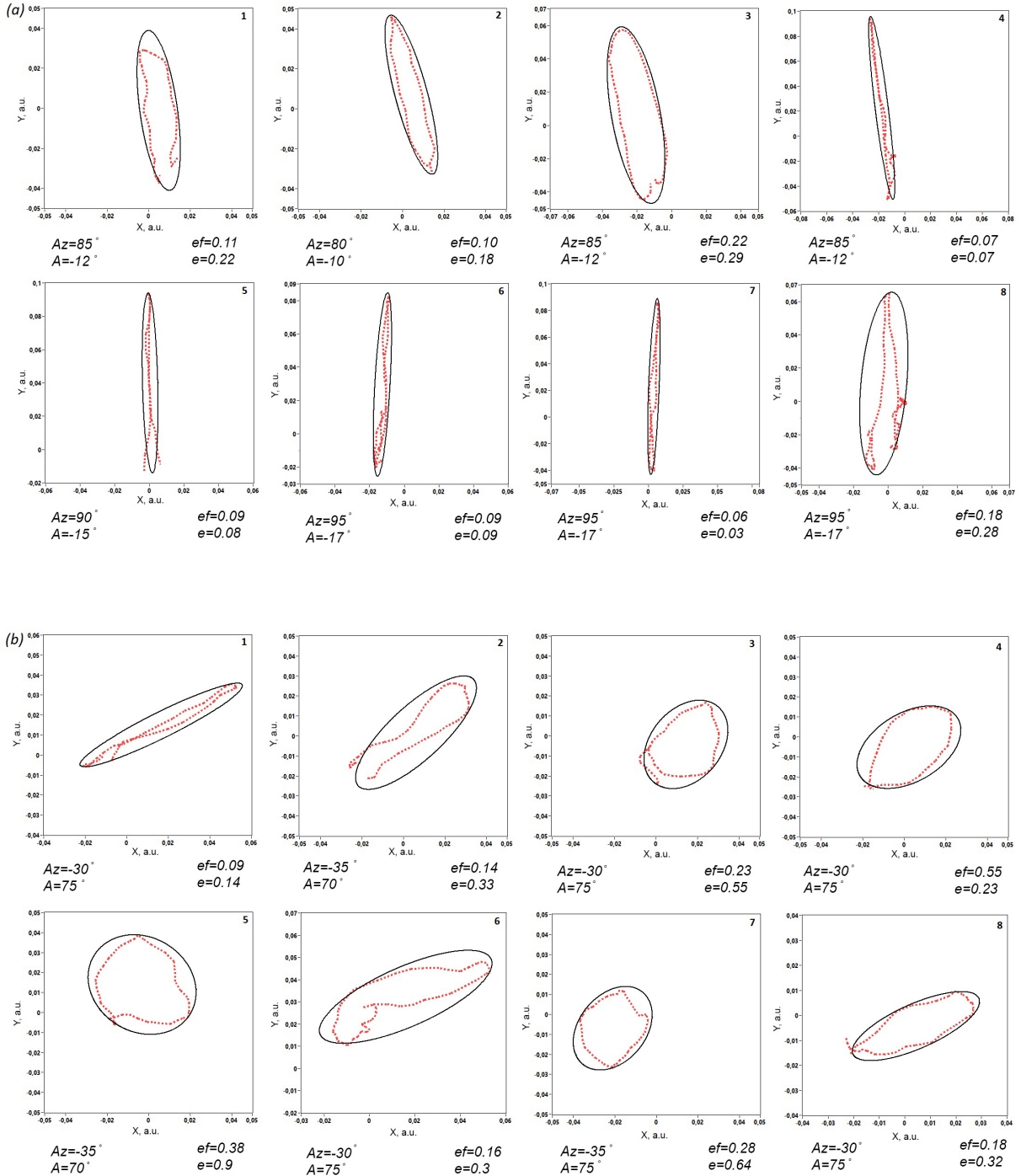


FIG. 4. (Color online) Spatial polarization distribution of the THz beam for the two polarization states of the pump beam radiation corresponding to the points (1–8) from (Fig. 3(a)). (a) – corresponds to the angle of the main axis inclination of the polarization ellipse of the fundamental harmonic after the β -BBO crystal $\alpha = -15^\circ$ with the ellipticity of 0.12 (see Fig. 2(b-I)). (b) – corresponds to the angle $\alpha = 73^\circ$ with the ellipticity of 0.22 (see Fig. 2(b-II)). e is ellipticity parameter of the polarization of the THz radiation, A_z is the angle of polarization of the THz radiation, ef is the ellipticity parameter of polarization of the fundamental harmonic, A is the angle of polarization of the fundamental harmonic

References

- [1] Siegel P.H. Terahertz technology in biology and medicine. *IEEE Transactions on Microwave Theory and Techniques*, 2004, **52** (10), P. 2438–2447.
- [2] Gredukhina I.V., Plotnikova L.V., et al. Influence of the degree of neutralization of acrylic acid and cross-linking agent on optical properties and swelling of sodium polyacrylate. *Optics and Spectroscopy*, 2017, **122** (6), P. 877–879.
- [3] Petrov N.V., Kulya M.S., et al. *IEEE Transactions on Terahertz Science and Technology*, 2016, **6** (3), P.464–472.
- [4] Balbekin N.S., Kulya M.S., Rogov P.Y., Petrov N.V. The modeling peculiarities of diffractive propagation of the broadband terahertz two-dimensional field. *Physics Procedia*, 2015, **73**, P. 49–53.
- [5] Kulya M.S., Balbekin N.S., et al. Computational terahertz imaging with dispersive objects. *Journal of Modern Optics*, 2017, **64**, P. 1283–1288.
- [6] Kulya M.S., Petrov N.V., Tcypkin A.N., Bepalov V.G. Influence of raster scan parameters on the image quality for the THz phase imaging in collimated beam with a wide aperture. *Journal of Physics: Conference Series*, 2014, **536** (1), P. 012010.
- [7] Semenova V.A., Kulya M.S., Bepalov V.G. Numerical simulation of broadband vortex terahertz beams propagation. *Journal of Physics: Conference Series*, 2016, **735** (1), P. 012064.
- [8] Cook D.J., Hochstrasser R.M. Intense terahertz pulses by four-wave rectification in air. *Optics Letters*, 2000, **25** (16), P. 1210–1212.
- [9] Lu X., Zhang X.C. Investigation of ultra-broadband terahertz time-domain spectroscopy with terahertz wave gas photonics. *Frontiers of Optoelectronics*, 2014, **7** (2), P. 121–155.
- [10] Roskos H.G., Thomson M.D., Kreß M., Löffler A.T. Broadband THz emission from gas plasmas induced by femtosecond optical pulses: From fundamentals to applications. *Laser & Photonics Reviews*, 2007, **1** (4), P. 349–368.
- [11] Thomson M.D., Blank V., Roskos H.G. Terahertz white-light pulses from an air plasma photo-induced by incommensurate two-color optical fields. *Optics Express*, 2010, **18** (22), P. 23173–23182.
- [12] Liu W., Théberge F., et al. An efficient control of ultrashort laser filament location in air for the purpose of remote sensing. *Applied Physics B: Lasers and Optics*, 2006, **85** (1), P. 55–58.
- [13] Couairon A., Mysyrowicz A. Femtosecond filamentation in transparent media. *Physics Reports*, 2007, **441** (2), P. 47–189.
- [14] D'Amico C., Houard A., et al. Conical forward THz emission from femtosecond-laser-beam filamentation in air. *Physical Review Letters*, 2007, **98** (23), P. 235002.
- [15] Andreev A.A., Bepalov V.G., et al. Generation of ultrabroadband terahertz radiation under optical breakdown of air by two femtosecond pulses of different frequencies. *Optics and Spectroscopy*, 2009, **107** (4), P. 538–544.
- [16] Amico C.D., Houard A., et al. Forward THz radiation emission by femtosecond filamentation in gases: theory and experiment. *New Journal of Physics*, 2008, **10** (1), P. 013015.
- [17] Zhang Y., Chen Y., et al. Non-radially polarized THz pulse emitted from femtosecond laser filament in air. *Optics Express*, 2008, **16** (20), P. 15483–15488.
- [18] Chen Y., Marceau C., et al. Elliptically polarized terahertz emission in the forward direction of a femtosecond laser filament in air. *Applied Physics Letters*, 2008, **93** (23), P. 231116.
- [19] Béjot P., Kasparian J., Wolf J.P. Dual-color co-filamentation in Argon. *Optics express*, 2008, **16** (18), P. 14115–14127.
- [20] Dietze D., Darmo J., et al. Polarization of terahertz radiation from laser generated plasma filaments. *JOSA B*, 2009, **26** (11), P. 2016–2027.
- [21] Stremoukhov S., Andreev A., et al. Origin of ellipticity of high-order harmonics generated by a two-color laser field in the cross-polarized configuration. *Physical Review A*, 2016, **94** (1), P. 013855.
- [22] Imai R., Kanda N., et al. Generation of broadband terahertz vortex beams. *Optics Letters*, 2014, **39** (13), P. 3714–3717.
- [23] Semenova V.A., Kulya M.S., Bepalov V.G. Numerical simulation of broadband vortex terahertz beams propagation. *Journal of Physics: Conference Series*, 2016, **735** (1), P. 012064
- [24] Semenova V.A., Kulya M.S., et al. Amplitude-phase imaging of pulsed broadband terahertz vortex beams generated by spiral phase plate. *41st International Conference on Infrared, Millimeter and Terahertz Waves (IRMMW-THz)*, 2016, 7758823.
- [25] He J., Wang X., et al. Generation and evolution of the terahertz vortex beam. *Optics Express*, 2013, **21** (17), P. 20230–20239.
- [26] Oh T.I., You Y.S., Kim K.Y. Two-dimensional plasma current and optimized terahertz generation in two-color photoionization. *Optics Express*, 2012, **20** (18), P. 19778–19786.
- [27] Wu Q., Hewitt T.D., Zhang X.C. Two-dimensional electro-optic imaging of THz beams. *Applied Physics Letters*, 1996, **69** (8), P. 1026–1028.
- [28] Gorodetsky A., Koulouklidis A.D., Massaoui M., Tzortzakis S. Physics of the conical broadband terahertz emission from two-color laser-induced plasma filaments. *Physical Review A*, 2014, **89** (3), P. 033838.
- [29] Zhang Y., Sun W., Zhang Y. Spectra modulation of terahertz radiation from air plasma. In *SPIE/COS Photonics Asia*, 2016, P. 1003025–1003025.
- [30] Chen Y., Marceau C., et al. Polarization separator created by a filament in air. *Optics Letters*, 2008, **33** (23), P. 2731–2733.
- [31] Théberge F., Aközbe N., et al. Tunable ultrashort laser pulses generated through filamentation in gases. *Physical Review Letters*, 2006, **97** (2), P. 023904.

Redistribution of Mg and Ni cations in crystal lattice of conical nanotube with chrysotile structure

A. A. Krasilin, V. V. Gusarov

Ioffe Institute, Politekhnikeskaya st., 26, St. Petersburg, 194021, Russia

ikrasilin@mail.ioffe.ru

PACS 64.70.Nd

DOI 10.17586/2220-8054-2017-8-5-620-627

Recently, nanotubular hydrosilicates have attracted attention due to numerous possible applications and intriguing formation mechanism. In this study we estimate energy effect of cylindrical and conical $(\text{Mg}_{0.5}\text{Ni}_{0.5})_3\text{Si}_2\text{O}_5(\text{OH})_4$ nanotube formation depending on their size parameters, cone angle, and Mg–Ni redistribution function. The calculations show that, as we expected, conical morphology is less preferable from an energy perspective than the cylindrical one, and the energy difference between them increases with the cone angle. Nevertheless, Mg and Ni cations redistribution along side length decreases strain energy of conical nanotube. This effect reaches its maximum of ~ -75 kJ/mol at a cone angle of 5° .

Keywords: hydrosilicate, chrysotile, nanotube, nanoscroll, hydrothermal synthesis, modeling, morphology.

Received: 30 August 2017

Revised: 2 September 2017

1. Introduction

The unusual behavior and properties of substances in nanotubes and related composite materials have resulted in wide scientific and technological interest [1–5]. In addition to well-known carbon [6], nitride [7], and chalcogenide nanotubes [8], researchers, using different approaches, have obtained new representative structures, termed micro- and nanoscrolls [9–16].

In the last few decades, spontaneously scrolling nanotubular hydrosilicates like imogolite, halloysite, and chrysotile have garnered increased attention due to their application as polymer fillers [17–19] (i.e. an alternative to carbon and chalcogenide nanotubes [20, 21]), sorbents and drug containers [22–24], catalyst materials [25–28], and materials for Li-ion energy sources [29]. The high specific surface (up to several hundred m^2/g [30–32]), abundance of OH-groups, and synthetic flexibility made hydrosilicate nanotubes and nanoscrolls suitable for these purposes. In addition, wide array of constituents (Mg, Al, Si) grants possibility of large-scale production and even industrial mining. The study of phase composition for hydrosilicate systems is of high importance for understanding of a number of geological processes [33, 34]. The potential of self-scrolling lies in one crystal structure peculiarity (Fig. 1, chrysotile structure as an example): one hydrosilicate layer consists of two sublayers (MgO_6 octahedra and SiO_4 tetrahedra) with slightly different lattice parameters. Covalent bonding of the sublayers causes internal stress in the layer, and nanotube formation is one effective relaxation mechanisms.

The bending, scrolling of crystal layer, and formation of chrysotile (and related minerals) nanotubes itself is of substantial interest. Since the middle of 20th century, various research groups have focused on synthesis of pure Mg-chrysotile [38–41], and related Fe [42, 43], Co [44], Ni-doped [45–49] structural analogs. The principal goal of recent studies in this field was to reveal pre-nucleus states that take part in the nanotube formation, and determine the role of their structure in the nanotube formation process. Other researches have opted to take theoretical consideration of the problem and performed hydrosilicate structure modeling [50–52] which yielded information about the preferred radius of curvature, electronic, and mechanical properties of those materials. Another theoretical approach involves phenomenological energy modeling [53–58], which focuses more on the morphological issues of single- and multiwalled nanotubes. In particular, it helps not only to predict preferable multiwalled nanotube size parameters, but to understand in deep the nanotubes' size distributions observed in electron microscopy experiments [59].

Varying the chemical composition affects morphology and properties of hydrosilicate nanotubes. Depending on its nature, the guest cation can increase the nanotube diameter, transform nanotubes into plates [43, 60–63], and provoke the formation of second nonsilicate phases. Apparently, the general trend for any cation doping of hydrosilicate nanotubes is formation of nanotubes and nanoscrolls with morphologies that deviate from cylinders. The SEM-image on Fig. 1 demonstrates particular example of this deviation: formation of conical $(\text{Mg}_{0.5}\text{Ni}_{0.5})_3\text{Si}_2\text{O}_5(\text{OH})_4$

nanoscrolls. Usually, the formation of conical nanotubes and nanoscrolls depends mainly on the pH of the hydrothermal medium [64]. Recently, we revealed [35] that partial Mg^{2+} to Ni^{2+} substitution yields a 3–5 fold increase of conical nanoscrolls content obtained in water and aqueous NaOH solutions. We try to investigate here possible mechanisms that stand behind this effect by further development of the energy approach proposed in [57, 59].

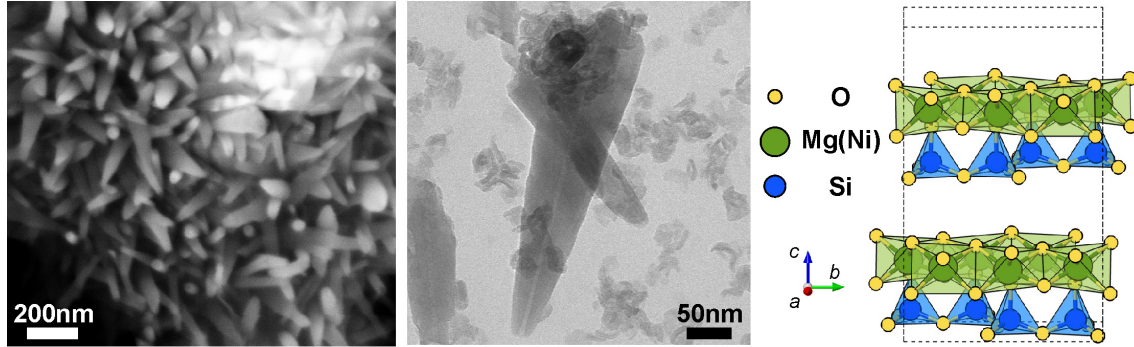


FIG. 1. SEM and TEM images of conical $(\text{Mg}_{0.5}, \text{Ni}_{0.5})_3\text{Si}_2\text{O}_5(\text{OH})_4$ nanoscrolls with chrysotile structure, obtained under hydrothermal conditions [35], and chrysotile unit cell (visualized using VESTA software [36]) according to data in [37]. Layers are joined by hydrogen bonds (not shown)

2. Energy model

The energy model proposed here relies on equations for the case of singlewalled hydrosilicate nanotube formation that were previously obtained in [57]. We compare four different states of hydrosilicate bilayer with chrysotile structure (Fig. 2): flat layer, cylindrical singlewalled nanotube, conical nanotube with uniform Mg^{2+} and Ni^{2+} ions distribution, and conical nanotube with cation gradient along its side length.

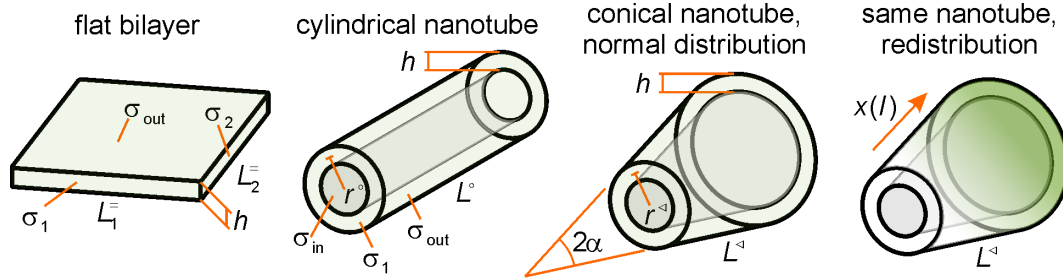


FIG. 2. Four morphological types of hydrosilicate particles and their size parameters. Color gradient denotes Mg^{2+} and Ni^{2+} ions redistribution along the side length of conical nanotube

The energy of each particle type includes strain energy and surface energy components. Before writing these equations, we must specify a number of principle assumptions made. First, processes like the formation of cylindrical and conical nanotubes by scrolling of flat layer, and also cations redistribution do not yield a mass (quantity of substance) change. For the cation redistribution process, the total concentration change must be equal to zero:

$$\frac{\int_0^{L^\triangleleft} dl (x(l) - \bar{x}) [r^\triangleleft / \sin(\alpha) + l] \tan(\alpha)}{\int_0^{L^\triangleleft} dl [r^\triangleleft / \sin(\alpha) + l] \tan(\alpha)} = 0, \quad (1)$$

where L^\triangleleft is side length of conical nanotube; $x(l)$ is length-dependent local molar content of Ni^{2+} ions; \bar{x} is average molar content of Ni^{2+} ions in respect to sum of Mg and Ni cations; r^\triangleleft is initial (smallest) cone radius of curvature on the half of wall thickness; α is half of cone angle. Integration in denominator returns the cone's surface area.

Second, scrolling process and transformation of flat layer into tube occurs without significant structural and chemical changes, except those mentioned above, and only morphological changes are under consideration here [57]. This also means that bending of the flat layer is small, and we can write strain energy equations in accordance with classic elastic theory [65]. Third, we assume that increase of curvature does not affect structural parameters like the Young's modulus and specific surface energies, although it is imprecise for curvature radii or layer thicknesses less than 3–4 nm [66,67]. Further assumptions and approximations will be given below.

In analogy with [57], the strain energy of cylindrical nanotube per 1 mol is:

$$E_s^\circ = \frac{1}{\nu(\bar{x})} \frac{D_s}{2} 2\pi r^\circ L^\circ \left(\frac{1}{r^\circ} - \frac{1}{r_0(\bar{x})} \right)^2 = \frac{Y h^3 M(\bar{x}) \pi r^\circ L^\circ}{12(1-\mu^2) V \rho(\bar{x})} \left(\frac{1}{r^\circ} - \frac{1}{r_0(\bar{x})} \right)^2, \quad (2)$$

where $\nu(\bar{x})$ is quantity of substance; D_s is bending stiffness; r° is cylinder radius on the half of wall thickness $h/2$; L° is cylinder length; Y is the Young's modulus; μ is the Poisson's ratio; $M(\bar{x})$ is molar mass; V is volume; and $\rho(\bar{x})$ is X-ray (bulk) density. The parameter $r_0(\bar{x})$ is radius of mechanically unstressed bilayer, which depends on cell parameters of octahedral and tetrahedral sublayers, thus, on interatomic distances [59].

Formally, we should denote Y , h , and μ as functions of \bar{x} , but the effect of chemical composition is either negligible or too uncertain, especially its influence on the Young's modulus [42]. Pure Mg- and Ni-hydrosilicates can have small difference in the Young's modulus, whereas bending stiffness of Mg- or Ni-doped hydrosilicates (or doped by other elements) is usually higher than that of pure ones [68]. For the rest of the parameters in (2), we assume linear dependence on \bar{x} (i.e. the Vegard's rule is valid). For the flat layer of the same volume and density, the strain energy is:

$$E_s^\circ = \frac{Y h^3 M(\bar{x}) L_1^\circ L_2^\circ}{24(1-\mu^2) V \rho(\bar{x}) r_0^2(\bar{x})} = \frac{Y h^2 M(\bar{x})}{24(1-\mu^2) \rho(\bar{x}) r_0^2(\bar{x})}, \quad (3)$$

where L_1° and L_2° are side lengths of the flat layer.

In the case of a conical tube (Fig. 2), calculation of strain energy goes through integration along the side length of the cone:

$$E_s^\triangleleft = \frac{D_s}{2\nu(\bar{x})} \int_0^{L^\triangleleft} dl \left(\frac{\cot(\alpha)}{[r^\triangleleft/\sin(\alpha) + l]} - \frac{1}{r_0(\bar{x})} \right)^2 2\pi [r^\triangleleft/\sin(\alpha) + l] \tan(\alpha). \quad (4)$$

Non-uniform distribution of Mg and Ni cations along the length transforms this equation into:

$$E_s^{\triangleleft g} = \int_0^{L^\triangleleft} dl \frac{D_s}{2\nu(x(l))} \left(\frac{\cot(\alpha)}{[r^\triangleleft/\sin(\alpha) + l]} - \frac{1}{r_0(x(l))} \right)^2 2\pi [r^\triangleleft/\sin(\alpha) + l] \tan(\alpha), \quad (5)$$

where r_0 becomes a function of l .

Once again, here we neglect possible dependence of Y , h , and μ on $x(l)$. Furthermore, in current approximation, we do not take into the account the function $\nu(x(l))$ and leave it beyond the integral as $\nu(\bar{x})$. Thus, the additional energy effect caused by special cation distribution might be realized due to minimization of squared difference of curvatures.

Full surface energy of the particles under consideration consists of partial surface energies of each of free surfaces (Fig. 2). For the cylindrical nanotube, it is:

$$\Sigma^\circ = \frac{2\pi}{\nu(\bar{x})} \left[\sigma_{\text{out}} \left(r^\circ + \frac{h}{2} \right) L^\circ + \sigma_{\text{in}} \left(r^\circ - \frac{h}{2} \right) L^\circ + 2\sigma_1 r^\circ h \right], \quad (6)$$

where σ_{out} , σ_{in} , and σ_1 are specific surface energies of outer, inner and cross-section surfaces, accordingly. In current approximation, we consider Mg- and Ni-rich hydrosilicate layers have close values of specific surface energies.

For the flat layer:

$$\Sigma^\circ = \frac{1}{\nu(\bar{x})} [L_1^\circ L_2^\circ (\sigma_{\text{out}} + \sigma_{\text{in}}) + 2\sigma_1 L_1^\circ h + 2\sigma_2 L_2^\circ h]. \quad (7)$$

TABLE 1. Structural parameters of the model

Parameter	Mg-chrysotile	Ni-pecoraite	Reference
m g	10^{-16}	10^{-16}	—
\bar{x}	0.5	0.5	—
M g/mol	277.1	380.3	—
ρ g/cm ³	2.5	3.5	[59]
r_0 nm	8.8	15	[52, 59]
h nm	0.4	0.4	[69]
t nm	0.3	0.3	[69]
Y GPa	300	300	[42, 51]
μ	0.2	0.2	[70]
σ_{out} J/m ²	0.6	0.6	[71–73]
σ_{in} J/m ²	0.4	0.4	[71–73]
σ_1, σ_2 J/m ²	1.2	1.2	[71–73]

For conical nanotube:

$$\Sigma^{\triangleleft} = \frac{2\pi}{\nu(\bar{x})} \left[\int_0^{L^{\triangleleft}} dl \sigma_{\text{out}} \left(r^{\triangleleft} + l \sin(\alpha) + \frac{h}{2 \cos(\alpha)} \right) + \int_0^{L^{\triangleleft}} dl \sigma_{\text{in}} \left(r^{\triangleleft} + l \sin(\alpha) - \frac{h}{2 \cos(\alpha)} \right) + \sigma_1 h (2r^{\triangleleft} + l \sin(\alpha)) \right]. \quad (8)$$

Due to the proximity of specific surface energies of Mg- and Ni-based lattices [59], we neglect changes in surface energy caused by their redistribution, i.e. $\Sigma^{\triangleleft \text{g}} \cong \Sigma^{\triangleleft}$. Energy effect of cation redistribution is:

$$\Delta E_{\triangleleft \text{g}}^{\triangleleft} = (E_s^{\triangleleft \text{g}} + \Sigma^{\triangleleft \text{g}}) - (E_s^{\triangleleft} + \Sigma^{\triangleleft})_{\text{min}} \cong E_s^{\triangleleft \text{g}} - E_{s, \text{min}}^{\triangleleft}. \quad (9)$$

This equation must be accompanied by constant composition condition (1). We can solve the system of (1) and (9) assuming $x(l)$ is two-parametric, for example, linear function of l :

$$x(l) = a + bl. \quad (10)$$

The choice of linear form of function allows one to not only integrate (5) analytically, but also assign clear physical meaning to the function parameters.

We suggest the following equation procedure: (a) as far as the integration leads to rather complicated forms of equations, we decide to assign numerical values to all structural parameters of energy model and visualize the results without writing analytical solution for energy minima; (b) we determine energy effect of cylindrical nanotube formation with respect to the energy minimum of flat layer:

$$\Delta E_{\circ}^{\circ} = (E_s^{\circ} + \Sigma^{\circ}) - (E_s^{\circ} + \Sigma^{\circ})_{\text{min}}, \quad (11)$$

and find the energy minimum of the tube with the values r_{min}° , L_{min}° , $E_{s, \text{min}}^{\circ}$, $\Sigma_{\text{min}}^{\circ}$; (c) we put these values in comparison with energy of conical nanotubes without and with linear distribution of the cations.

3. Results and discussion

Table 1 summarizes numerical values of structural parameters that we used in the calculation.

The choice of specific surface energy values becomes a sort of problem. Previous modeling cases (formation of multiwalled cylindrical nanoscrolls [58, 59]) were free from the influence of edges just because their surface areas were assumed to be constant during the scrolling process. Here, we cannot neglect difference in edges surface

areas between cone and cylinder. We chose edge values σ_1 and σ_2 at least 3 times higher the values related to outer and inner surfaces because of higher substance density along these directions.

Figure 3(a) shows the energy effect of cylindrical singledwalled nanotube formation with respect to flat layer (see equation (11)). The energy curve has an asymmetrical minimum with the with the parameters $\Delta E_{\circ}^{\circ} = -2$ kJ/mol, $r_{\min}^{\circ} = 14.6$ nm, $L_{\min}^{\circ} = 909$ nm. Relative to this point, conical nanotube of any morphology has higher energy (Fig. 3(b)): the larger is the cone angle, the more positive the energy effect is. This result correlates with numerous reports [38–49], in which mostly cylindrical form of chrysotile nanoscrolls and nanotubes has been observed after prolonged hydrothermal treatment. However, the energy effect of conical nanotube, especially when the angle is small ($2\alpha < 5^{\circ}$), does not exceed hundreds of J/mol. This feature also explains why high-angle ($2\alpha > 20^{\circ}$) conical tubes (scrolls) are rarely observed experimentally.

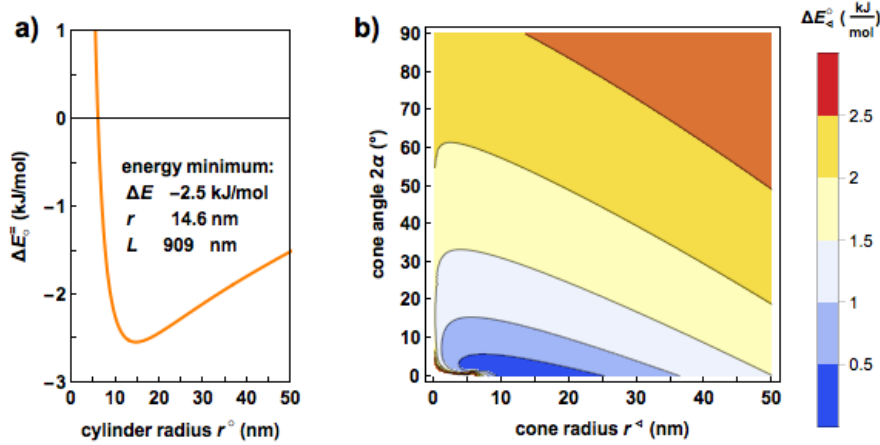


FIG. 3. (a) Energy effect of cylindrical nanotube formation from flat layer versus radius of curvature. (b) Energy effect of conical nanotube formation (with respect to the cylindrical nanotube energy minimum) versus initial radius of curvature and cone angle

Despite being less energetically preferable than the cylinder, the cone of certain angle 2α still has energy minimum (Fig. 3(b)). On the next calculation step, we compared this minimum with the conical nanotube with linear change of Ni^{2+} ion concentration (10).

Figure 4 shows the calculation results for cone angle $2\alpha = 5^{\circ}$. The case of parameter $a < 0.5$ corresponds to “direct” type of distribution (see inset on Fig. 4), in which the cation with bigger ionic radius (Mg^{2+}) concentrates at the small end of the tube, and the cation with smaller ionic radius (Ni^{2+}) – at the big end. $a \cong 0.5$ means absence of cation redistribution, and $a > 0.5$ represents “reverse” cation distribution. The redistribution causes change of energy preferable initial cone radius, which is optimal for certain chemical compositions. The maximal energy effect due to cation redistribution reaches 70–80 J/mol at 2α around 5° (Fig. 5). Interesting that there is a certain cone angle interval, in which the redistribution has maximal impact. If the angle is small, the redistribution does not make substantial contribution. Note there is no need for maximal possible concentration gradient – 0 % Ni at the small end of the nanotube, and 100 % Ni at its large end, i.e. $a = 0$ – in case of small angles ($2\alpha < 2^{\circ}$, Fig. 5(a)). During increase of cone angle the maximal cation gradient becomes less preferable energetically. This is because conical nanotube with large angle tends to increase its initial radius, which becomes unfavorable for only Mg^{2+} -rich hydrosilicate structure.

Choice of linear function $x(l)$ (10) seems to be close to the best way of cations redistribution. To minimize strain energy, according to our approximation, it is sufficient to be:

$$\left(\frac{\cot(\alpha)}{[r^{\circ}/\sin(\alpha) + l]} - \frac{1}{x(l)r_{0,\text{Ni}} + [1 - x(l)]r_{0,\text{Mg}}} \right)^2 = 0 \quad (12)$$

Solving this equation regarding $x(l)$ gives:

$$x(l) = \frac{r^{\circ}/\cos(\alpha) - r_{0,\text{Mg}}}{r_{0,\text{Ni}} - r_{0,\text{Mg}}} + l \frac{\tan(\alpha)}{r_{0,\text{Ni}} - r_{0,\text{Mg}}}, \quad (13)$$

which linearly depends on l .

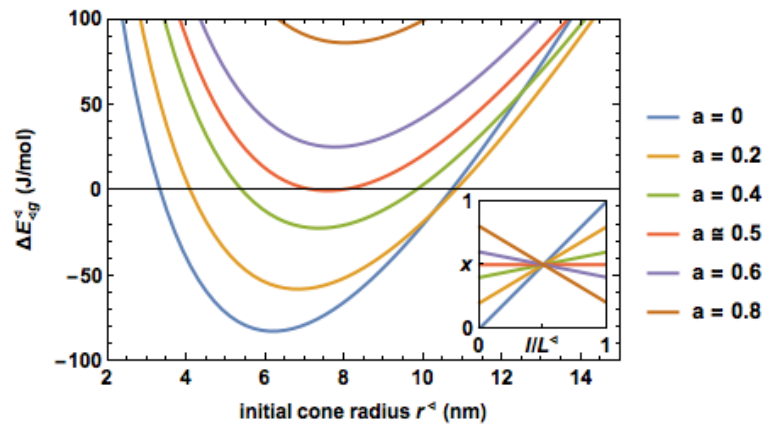


FIG. 4. Energy effect of cations redistribution in conical nanotube with $2\alpha = 5^\circ$. Inset: Ni^{2+} concentration profiles along conical nanotube side length (relative coordinates)

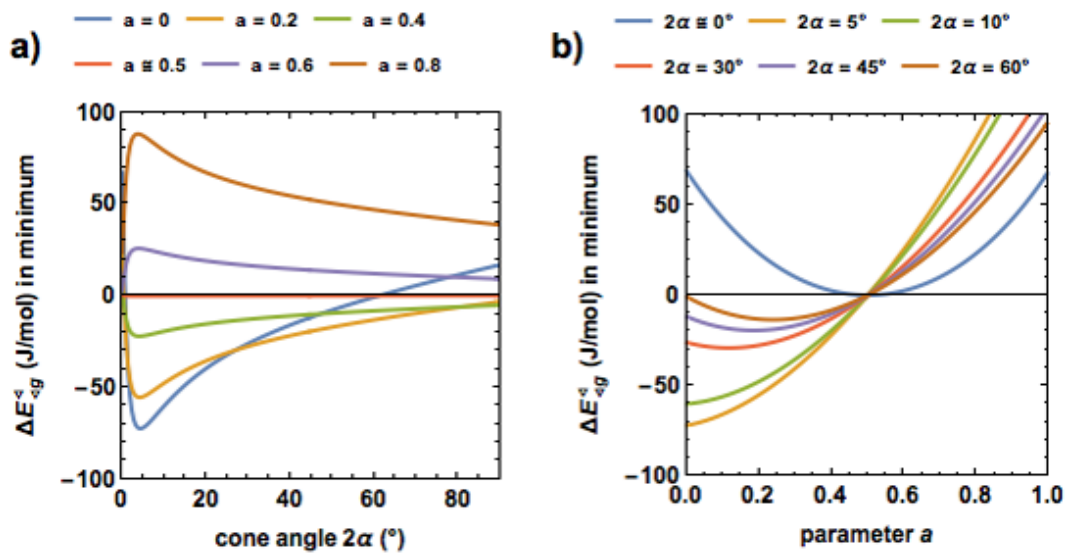


FIG. 5. (a) Depth of energy minimum vs cone angle. (b) Depth of energy minimum vs parameter a

4. Concluding remarks

Here, we developed an energy model for single-walled conical nanotube formation, and redistribution of cations inside its crystal structure as a mechanism to decrease its strain energy. These calculations showed that, in general, conical nanotubes are less energy favorable than the cylindrical nanotubes. At the same time, cation redistribution decreases conical nanotube's energy and make it slightly more preferable in comparison to the tube without redistribution. This additional energy effect, together with sophistication of chemical composition can probably inhibit recrystallization process and thus stabilize conical forms of hydrosilicates during long-time hydrothermal treatments.

Stabilization of conical morphology may occur not only in case of Ni^{2+} doping, but by the addition of other elements, for example, Co and Fe, which have their own preferable radii of curvatures and r_0 values, but among them Ni^{2+} possesses ionic radius closest to Mg^{2+} . This feature allows production of nanotubes in all ranges of Ni^{2+} concentrations, whereas in case of Fe^{3+} doping, there might be some difficulties regarding phase homogeneity.

Conical hydrosilicate nanotubes observed by electron microscopy often have walls consisting of two to tens of layers. Our approach can be extrapolated to those types of objects if we consider them as systems of embedded cones. Finally, cation redistribution may occur either in multi-walled cylindrical nanoscroll or nanotube just because the layers curvature changes from its inner surface to the outer one. The effect of redistribution here may reveal

itself by an increase in the outer diameter (number of layers inside the wall), including formation of cylindrical growth steps on the outer surface of the hydrosilicate nanotube.

Acknowledgements

The research was supported by Russian Science Foundation grant 16-13-10252.

References

- [1] Višić B., Panchakarla L.S., Tenne R. Inorganic nanotubes and fullerene-like nanoparticles at the crossroads between solid-state chemistry and nanotechnology. *JACS*, 2017, DOI: 10.1021/jacs.7b01652.
- [2] Jana M.K., et al. Two-dimensional inorganic analogues of graphene: transition metal dichalcogenides. *Philos. Trans. A*, 2016, **374** (2076), P. 162–163.
- [3] Tenne R., Seifert G. Recent progress in the study of inorganic nanotubes and fullerene-like structures. *Annu. Rev. Mater. Res.*, 2009, **39** (1), P. 387–413.
- [4] Tagliazucchi M., Szleifer I. Salt pumping by voltage-gated nanochannels. *J. Phys. Chem. Lett.*, 2015, **6** (18), P. 3534–3539.
- [5] Huang J.Y., et al. Nanowire liquid pumps. *Nat. Nanotechnol.*, 2013, **8** (4), P. 277–281.
- [6] Iijima S. Helical microtubules of graphitic carbon. *Nature*, 1991, **354** (6348), P. 56–58.
- [7] Enyashin A.N., Ivanovskii A.L. Electronic structure of nanotubes of layered modifications of carbon nitride C₃N₄. *Dokl. Phys. Chem.*, 2004, **398** (1–3), P. 211–215.
- [8] Tenne R., et al. Polyhedral and cylindrical structures of tungsten disulphide. *Nature*, 1992, **360** (6403), P. 444–446.
- [9] Prinz V.Y., et al. Free-standing and overgrown InGaAs/GaAs nanotubes, nanohelices and their arrays. *Physica E*, 2000, **6** (1–4), P. 828–831.
- [10] Prinz V.Y. A new concept in fabricating building blocks for nanoelectronic and nanomechanic devices. *Microelectron. Eng.*, 2003, **69** (2–4), P. 466–475.
- [11] Gurenko V.E., Tolstoy V.P., Gulina L.B. The effect of microtube formation with walls, containing Fe₃O₄ nanoparticles, via gassolution interface technique by hydrolysis of the FeCl₂ and FeCl₃ mixed solution with gaseous ammonia. *Nanosyst.: Phys. Chem. Math.*, 2017, **8** (4), P. 471–475.
- [12] Gulina L.B., et al. Facile synthesis of LaF₃ strained 2D nanoparticles and microtubes at solution–gas interface. *J. Fluor. Chem.*, 2015, **180**, P. 117–121.
- [13] Poluektov P.P., Dmitriev M.S. Model of nanotube formation in solution under molecular sorption conditions. *At. Energy*, 2009, **106** (5), P. 343–347.
- [14] Enyashin A.N., Ivanovskii A.L. Theoretical prediction of Al(OH)₃ nanotubes and their properties. *Physica E*, 2008, **41** (2), P. 320–323.
- [15] Grigor'eva A.V., et al. Micromorphology and structure of vanadium oxide nanotubes. *Dokl. Chem.*, 2006, **410** (2), P. 165–169.
- [16] Korytkova E.N., Pivovarova L.N. Hydrothermal synthesis of nanotubes based on (Mg,Fe,Co,Ni)₃Si₂O₅(OH)₄ hydrosilicates. *Glas. Phys. Chem.*, 2010, **36** (1), P. 53–60.
- [17] Vahedi V., Pasbakhsh P., Chai S.P. Toward high performance epoxy/halloysite nanocomposites: New insights based on rheological, curing, and impact properties. *Mater. Des.*, 2015, **68**, P. 42–53.
- [18] Yudin V.E., et al. Effects of nanofiller morphology and aspect ratio on the rheo-mechanical properties of polyimide nanocomposites. *Express Polym. Lett.*, 2008, **2** (7), P. 485–493.
- [19] Afanas'eva N.V., et al. Relaxation processes in an aromatic polyamide-imide and composites on its basis with hydrosilicate nanoparticles. *Polym. Sci. Ser. A*, 2016, **58** (6), P. 956–967.
- [20] Naffakh M., et al. New hybrid nanocomposites containing carbon nanotubes, inorganic fullerene-like WS₂ nanoparticles and poly(ether ether ketone) (PEEK). *J. Mater. Chem.*, 2011, **21** (20), P. 7425–7433.
- [21] Ksenevich V.K., et al. Electrical properties of carbon nanotubes/WS₂ nanotubes (nanoparticles) hybrid films. *Nanosyst.: Phys. Chem. Math.*, 2016, **7** (1), P. 37–43.
- [22] Lvov Y., et al. Halloysite clay nanotubes for loading and sustained release of functional compounds. *Adv. Mater.*, 2016, **28** (6), P. 1227–1250.
- [23] Cheng L., et al. Removal of simulated radionuclide Ce(III) from aqueous solution by as-synthesized chrysotile nanotubes. *Chem. Eng. J.*, 2012, **213**, P. 22–30.
- [24] Zheng Y., et al. Poly(methacrylic acid)-graft-Ni₃Si₂O₅(OH)₄ multiwalled nanotubes as a novel nanosorbent for effective removal of copper(II) ions. *Colloids Surfaces A*, 2016, **502**, P. 89–101.
- [25] Zhang Y., et al. Substitutional doping for aluminosilicate mineral and superior water splitting performance. *Nanoscale Res. Lett.*, 2017, **12** (1), P. 456.
- [26] Sarvaramini A., Larachi F. Mössbauer spectroscopy and catalytic reaction studies of shrysofile-catalyzed steam reforming of benzene. *J. Phys. Chem. C*, 2011, **115** (14), P. 6841–6848.
- [27] Bian Z., et al. A highly active and stable Ni–Mg phyllosilicate nanotubular catalyst for ultrahigh temperature water-gas shift reaction. *Chem. Commun.*, 2015, **51** (91), P. 16324–16326.
- [28] Peng H., et al. Facile synthesis and characterization of core-shell structured Ag₃PO₄@Hal nanocomposites for enhanced photocatalytic properties. *Appl. Clay Sci.*, 2017, **141**, P. 132–137.
- [29] Yang Y., et al. Ni₃Si₂O₅(OH)₄ multi-walled nanotubes with tunable magnetic properties and their application as anode materials for lithium batteries. *Nano Res.*, 2011, **4** (9), P. 882–890.
- [30] Shafia E., et al. Isomorphous substitution of aluminium by iron into single-walled aluminosilicate nanotubes: A physico-chemical insight into the structural and adsorption properties of Fe-doped imogolite. *Microp. Mesop. Mater.*, 2016, **224**, P. 229–238.
- [31] Lafay R., et al. Influence of trace elements on the textural properties of synthetic chrysotile: Complementary insights from macroscopic and nanoscopic measurements. *Microp. Mesop. Mater.*, 2014, **183**, P. 81–90.
- [32] Yuan P., Tan D., Annabi-Bergaya F. Properties and applications of halloysite nanotubes: recent research advances and future prospects. *Appl. Clay Sci.*, 2015, **112–113**, P. 75–93.

- [33] Pollastri S., et al. The crystal structure of mineral fibres: 1. Chrysotile. *Period. di Mineral.*, 2016, **85** (3), P. 249–259.
- [34] Villanova-de-Benavent C., et al. Ni-phylosilicates (garnierites) from the Falcondo Ni-laterite deposit (Dominican Republic): Mineralogy, nanotextures, and formation mechanisms by HRTEM and AEM. *Am. Mineral.*, 2016, **101** (6), P. 1460–1473.
- [35] Krasilin A.A., et al. Formation of conical $(\text{Mg,Ni})_3\text{Si}_2\text{O}_5(\text{OH})_4$ nanoscrolls. *Dokl. Phys. Chem.*, 2015, **460** (2), P. 42–44.
- [36] Momma K., Izumi F. VESTA 3 for three-dimensional visualization of crystal, volumetric and morphology data. *J. Appl. Crystallogr.*, 2011, **44** (6), P. 1272–1276.
- [37] Falini G., et al. Tubular-shaped stoichiometric chrysotile nanocrystals. *Chem. Eur. J.*, 2004, **10** (12), P. 3043–3049.
- [38] Korytkova E.N., et al. Formation of $\text{Mg}_3\text{Si}_2\text{O}_5(\text{OH})_4$ Nanotubes under hydrothermal conditions. *Glas. Phys. Chem.*, 2004, **30** (1), P. 51–55.
- [39] Jancar B., Suvorov D. The influence of hydrothermal-reaction parameters on the formation of chrysotile nanotubes. *Nanotechnology*, 2006, **17** (1), P. 25–29.
- [40] Krasilin A.A., Almajasheva O.V., Gusarov V.V. Effect of the structure of precursors on the formation of nanotubular magnesium hydrosilicate. *Inorg. Mater.*, 2011, **47** (10), P. 1111–1115.
- [41] Lafay R., et al. Dissolution-reprecipitation and self-assembly of serpentine nanoparticles preceding chrysotile formation: Insights into the structure of proto-serpentine. *Am. Mineral.*, 2016, **101** (12), P. 2666–2676.
- [42] Piperno S., et al. Characterization of geoinspired and synthetic chrysotile nanotubes by atomic force microscopy and transmission electron microscopy. *Adv. Funct. Mater.*, 2007, **17** (16), P. 3332–3338.
- [43] Bloise A., et al. Synthesis of Fe-doped chrysotile and characterization of the resulting chrysotile fibers. *Cryst. Res. Technol.*, 2009, **44** (6), P. 590–596.
- [44] Korytkova E.N., et al. Hydrothermal synthesis of nanotubular Co-Mg hydrosilicates with the chrysotile structure. *Russ. J. Gen. Chem.*, 2007, **77** (10), P. 1669–1676.
- [45] Bloise A., et al. Influence of synthesis conditions on growth of Ni-doped chrysotile. *Microp. Mesop. Mater.*, 2010, **132** (1-2), P. 239–245.
- [46] McDonald A., Scott B., Villemure G. Hydrothermal preparation of nanotubular particles of a 1:1 nickel phyllosilicate. *Microp. Mesop. Mater.*, 2009, **120** (3), P. 263–266.
- [47] Korytkova E.N., et al. Synthesis of nanotubular $\text{Mg}_3\text{Si}_2\text{O}_5(\text{OH})_4$ - $\text{Ni}_3\text{Si}_2\text{O}_5(\text{OH})_4$ silicates at elevated temperatures and pressures. *Inorg. Mater.*, 2005, **41** (7), P. 743–749.
- [48] Krasilin A.A., et al. Morphology vs. chemical composition of single Ni-doped hydrosilicate nanoscroll. *Mater. Lett.*, 2016, **171**, P. 68–71.
- [49] White R.D., Bavykin D.V., Walsh F.C. Morphological control of synthetic $\text{Ni}_3\text{Si}_2\text{O}_5(\text{OH})_4$ nanotubes in an alkaline hydrothermal environment. *J. Mater. Chem. A*, 2013, **1** (3), P. 548–556.
- [50] Guimarães L., et al. Structural, electronic, and mechanical properties of single-walled halloysite nanotube models. *J. Phys. Chem. C*, 2010, **114** (26), P. 11358–11363.
- [51] Loureno M.P., et al. Structural, electronic, and mechanical properties of single-walled chrysotile nanotube models. *J. Phys. Chem. C*, 2012, **116** (17), P. 9405–9411.
- [52] Demichelis R., et al. Serpentine polymorphism: a quantitative insight from first-principles calculations. *Cryst. Eng. Comm.*, 2016, **18** (23), P. 4412–4419.
- [53] Singh B. Why does halloysite roll? – A new model. *Clays Clay Miner.*, 1996, **44** (2), P. 191–196.
- [54] Chivilikhin S.A., Popov I.Yu., Gusarov V.V. Dynamics of nanotube twisting in a viscous fluid. *Doklady Physics*, 2007, **52** (1), P. 60–62.
- [55] Thill A., et al. How the diameter and structure of $(\text{OH})_3\text{Al}_2\text{O}_3\text{Si}_x\text{Ge}_{1-x}\text{OH}$ imogolite nanotubes are controlled by an adhesion versus curvature competition. *J. Phys. Chem. C*, 2012, **116** (51), P.26841–26849.
- [56] Thill A., Picot P., Belloni L. A mechanism for the sphere/tube shape transition of nanoparticles with an imogolite local structure (imogolite and allophane). *Appl. Clay Sci.*, 2017, **141**, P. 308–315.
- [57] Krasilin A.A., Gusarov V.V. Energy of formation of chrysotile nanotubes. *Russ. J. Gen. Chem.*, 2014, **84** (12), P. 2359–2363.
- [58] Krasilin A.A., Gusarov V.V. Energy model of radial growth of a nanotubular crystal. *Tech. Phys. Lett.*, 2016, **42** (1), P. 55–58.
- [59] Krasilin A.A., Nevedomsky V.N., Gusarov V.V. Comparative energy modeling of multiwalled $\text{Mg}_3\text{Si}_2\text{O}_5(\text{OH})_4$ and $\text{Ni}_3\text{Si}_2\text{O}_5(\text{OH})_4$ nanoscroll growth. *J. Phys. Chem. C*, 2017, **121** (22), P. 12495–12502.
- [60] Foresti E., et al. Morphological and chemical/physical characterization of Fe-doped synthetic chrysotile nanotubes. *Adv. Funct. Mater.*, 2005, **15** (6), P. 1009–1016.
- [61] Korytkova E.N., et al. Hydrothermal synthesis of nanotubular Mg–Fe hydrosilicate. *Russ. J. Inorg. Chem.*, 2007, **52** (3), P. 338–344.
- [62] Krasilin A.A., Gusarov V.V. Control over morphology of magnesium-aluminum hydrosilicate nanoscrolls. *Russ. J. Appl. Chem.*, 2015, **88** (12), P. 1928–1935.
- [63] Krasilin A.A., et al. Formation of variable-composition iron(III) hydrosilicates with the hrysotile structure. *Russ. J. Gen. Chem.*, 2016, **86** (12), P. 2581–2588.
- [64] Smolikov A., et al. Morphology of synthetic chrysotile nanofibers (Mg-hydro silicate). *J. Mater. Sci. Eng. A*, 2013, **3** (8), P. 523–530.
- [65] Landau L.D., et al. *Theory of elasticity*, third edition: Volume 7 (course of theoretical physics). Butterworth-Heinemann, Oxford, 1986, 187 p.
- [66] Tolman R.C. The effect of droplet size on surface tension. *J. Chem. Phys.*, 1949, **17** (3), P. 333.
- [67] Krivtsov A.M., Morozov N.F. On mechanical characteristics of nanocrystals. *Phys. Solid State*, 2002, **44** (12), P. 2260–2265.
- [68] Krasilin A.A., et al. Interconnection between composition, morphology and mechanics of chrysotile nanoscroll. *Proceedings of the Conference “12th Multinational Congress on Microscopy MCM 2015”*, Eger, Hungary, August 23–28, 2015, P. 459–460.
- [69] Roveri N., et al. Geoinspired synthetic chrysotile nanotubes. *J. Mater. Res.*, 2006, **21** (11), P. 2711–2725.
- [70] Cressey B.A., Whittaker E.J.W. Five-fold symmetry in chrysotile asbestos revealed by transmission electron microscopy. *Mineral. Mag.*, 1993, **57** (389), P. 729–732.
- [71] Tasker P.W., Duffy D.M. The structure and properties of the stepped surfaces of MgO and NiO. *Surf. Sci.*, 1984, **137** (1), P. 91–102.
- [72] Evarestov R.A., Bandura A.V. HF and DFT calculations of MgO surface energy and electrostatic potential using two- and three-periodic models. *Int. J. Quantum Chem.*, 2004, **100** (4), P. 452–459.
- [73] Shchupalov Y.K. Surface energy of crystalline and vitreous Silica. *Glas. Ceram.*, 2000, **57** (11/12), P. 374–377.

Two facile routes for functionalization of WS₂ nanotubes with silver nanoparticles

A. Yu. Polyakov¹, V. A. Lebedev¹, L. Yadgarov², E. A. Goodilin¹

¹Department of Materials Science, Lomonosov Moscow State University,
1-73 Leninskiye gory, Moscow, 119991, Russia

²Tel Aviv University, P.O. Box 39040, Tel Aviv 6997801, Israel
a.yu.polyakov@gmail.com, goodilin@gmail.com

PACS 81.10.-h, 88.30.mj

DOI 10.17586/2220-8054-2017-8-5-628-634

Silver-coated WS₂ nanotubes (NT-WS₂) were successfully synthesized via two wet chemistry techniques. The first employs spontaneous silver nanoparticle growth resulting from an interaction of disulfide nanotubes with AgNO₃ in aqueous suspensions at 100 °C without any additional reducing agents or stabilizers. The second utilizes [Ag(NH₃)₂]OH complex to produce silver nanoparticles upon thermal decomposition. Both techniques are capable of producing Ag-NT-WS₂ nanocomposites containing 5–60 nm silver nanoparticles tightly attached to the nanotubes' surfaces. The hexagonal arrangement of sulfur atoms of the outer WS₂ layer was postulated to facilitate crystallization of silver nanocrystals with hexagonal crystallographic system (4H–Ag). The physical-chemical model for spontaneous AgNP formation is proposed.

Keywords: WS₂ nanotubes, silver nanoparticles, plasmonic nanoparticles, nanocomposite, spontaneous growth, 4H silver.

Received: 30 September 2017

Revised: 6 October 2017

1. Introduction

Currently, much attention is paid to the nanocomposites of noble metals and semiconductors due to novel synergistic properties arising in such materials [1]. Among others, semiconducting nanotubes functionalized with silver nanoparticles (AgNPs) were successfully synthesized and became widely studied multifunctional composites. Due to the presence of bright plasmon resonance in Ag nanostructures, such nanocomposites can be employed in numerous optical applications. For example, carbon nanotubes (CNT) coated with Ag and Au nanoparticles have been found to be broad-band optical limiters [2]. Ag-CNT nanocomposites are widely used as mediators for highly-sensitive surface-enhanced Raman spectroscopy (SERS) [3–5]. AgNP-loaded CNT and TiO₂ nanotubes possess high efficiency in photocatalytic applications [6–8] including antibacterial photocatalysis in visible light [9]. Additionally, Ag-CNT nanocomposites are considered promising gas sensors [10, 11], catalysts [12], antibacterial agents [13–15] and drug delivery carriers [16].

WS₂ nanotubes (NT-WS₂) are the analogues of multiwalled CNT and represent folded and nested S-W-S sheets containing six-fold-bonded W atoms sandwiched between three-fold-bonded sulfur atoms [17]. Mass production of NT-WS₂ is based on reduction of WO₃ nanoparticles using a H₂S/H₂/N₂ gaseous mixture in fluidized-bed reactors [18]. A number of distinctive advantages of NT-WS₂ were reported. Contrary to CNT, disulfide nanotubes cannot be bent or entangled easily, therefore they are more easily dispersed in polymer blends and other matrices [19]. Individual NT-WS₂'s were also shown to be perfect torsional resonators with the highest quality factor (*Q*) and torsional resonant frequency in comparison to CNT and BN nanotubes [20]. Recently, the unique nonreciprocal superconductive behavior of individual chiral NT-WS₂ was also reported [21]. Surface modification of NT-WS₂ with inorganic nanoparticles expands application areas of disulfide nanotubes. Co@NT-WS₂ [22] and Ni@NT-WS₂ [23] nanocomposites effectively catalyze hydrodesulfurization reactions of thiophene and similar compounds. Additionally, Co@NT-WS₂ is considered as a promising visible-light photocatalyst [24]. Pd@NT-WS₂ nanocomposites were found to be efficient catalysts for cross-coupling (Heck and Suzuki) reactions [25]. FeWO₄ nanoparticles were successfully deposited onto NT-WS₂ resulting in magnetic nanocomposites [26]. Recently, CNT/NT-WS₂ electrically conductive hybrid films were also produced [27].

There are plenty of versatile techniques for CNT surface modification, e.g., generation of chemically active carboxylic groups by etching the CNT surface with HNO₃/H₂SO₄ [13, 28]. Similarly, many routes for coating of CNT with AgNPs have been reported, including deposition of pre-synthesized AgNPs [10, 11], magnetron sputtering of Ag and high-temperature annealing [3], E-beam coating in vacuum [2], Ag₂O reduction upon sonication in presence of CNT [29] and reduction of Ag(I) ions in aqueous CNT suspensions. The latter includes direct photoreduction, thermal decomposition [8], usage of reducing agents (e.g. glucose [14], formaldehyde [28], etc.)

and sacrificial layers [9], as well as spontaneous reduction of Ag⁺ ions on the surface of CNT [30]. On the contrary, the functionalization of NT-WS₂ with plasmonic silver nanoparticles has not been studied yet, despite several attempts having been made to synthesize Au-NT-WS₂ nanocomposites [31–34]. Moreover, it was suggested in our previous work [32], which focused on the functionalization of NT-WS₂ with AuNPs via spontaneous HAuCl₄ reduction on the disulfide surface, that the same technique could be applied using AgNO₃ solutions for the production of Ag-NT-WS₂ nanocomposites.

Going beyond this suggestion, here, we report two facile techniques for decoration of NT-WS₂ with AgNPs: the first is based on a reaction of AgNO₃ with aqueous NT-WS₂ suspension at 100 °C; the second employs the thermal decomposition of freshly prepared [Ag(NH₃)₂]OH complex solution in the presence of disulfide nanotubes. The resultant nanocomposites are carefully characterized using transmission electron microscopy (TEM).

2. Experimental

WS₂ nanotubes were kindly provided by NanoMaterials Ltd. (Israel) and personally by Prof. Reshef Tenne (Weizmann Institute of Science, Israel). The nanotubes are multiwalled, typically 1–20 μm long and 30–150 nm in diameter. Before all the syntheses the nanotubes were deagglomerated by sonication in acetone according to the common procedure [35].

Silver nitrate was of chemically pure (c.p.) grade. Sodium hydroxide standard solution was purchased from Merck (Germany). All other chemicals were purchased locally and were of analytical grade. All aqueous solutions and suspensions were prepared using high purity water (Milli-Q RG, 18.2 MΩ·cm resistivity, Millipore). Glassware and magnetic stirring bars utilized for AgNP synthesis were washed by 63 % HNO₃.

Within the first technique towards Ag-NT-WS₂ nanocomposites, 14 ml of 114 mM AgNO₃ solution were heated up to 100 °C in a foil-wrapped beaker to avoid photoinduced silver salt decomposition. Then, 2 ml of freshly prepared aqueous nanotube suspension (1.3 g/L NT-WS₂) were added to the beaker upon vigorous stirring. The reaction mixture was kept at 100 °C for 3 min and then cooled down to room temperature with continued stirring.

For the second NT-WS₂ decoration technique, freshly prepared [Ag(NH₃)₂]OH complex was used. This technique was adopted from the protocol for AgNP-decoration of SiO₂ microspheres reported elsewhere [36]. For the complex preparation, 0.1 M NaOH was added to 10 ml of 0.01 M AgNO₃ in a dropwise manner until the end of Ag₂O precipitation. The resulting brown sediment was centrifuged (4000 rpm, 10 min), redispersed in purified water by 1 min sonication and centrifuged again. This washing procedure was repeated three times. The purified sediment was dissolved in 10 % NH₃·H₂O to form 15 mM [Ag(NH₃)₂]OH solution, which was stored at 4 °C and used within 30 min after preparation.

For the nanocomposite synthesis, 2 ml of aqueous nanotube suspension (1.3 g/L NT-WS₂) were added to 13.89 ml of purified water pre-heated up to 100 °C under vigorous stirring. Then, 110 μl of freshly prepared 0.015 M [Ag(NH₃)₂]OH solution were added. The reaction mixture was kept in foil-wrapped beaker at 100 °C for 3 min and then cooled down to room temperature. In both procedures, the WS₂ concentration in reaction mixtures after addition of all the reactants was about 0.66 mM and the Ag concentration was about 0.1 mM.

The nanocomposite morphologies were analyzed using a Carl Zeiss Libra 200 MC transmission electron microscope (TEM) operating at 200 kV. Selected-area electron diffraction (SAED) patterns were registered for representative selection of the particles. For TEM analysis the aqueous composite suspensions were dripped on lacey-carbon copper grids (SPI, USA) and dried. Images were processed using open-source Gwyddion software [37] including calculation and processing of Fast Fourier Transforms.

Scanning electron microscopy (SEM) was performed using Carl Zeiss Leo Supra 55 microscope operating at 15 kV in secondary electron imaging (SE2) regime. For SEM analysis, the composite nanoparticle suspensions were dried on conductive silicon wafers.

3. Results and discussion

The silver-decorated nanotubes were multiwalled, 1–20 μm long and 30–150 nm in diameter. Both developed techniques resulted in functionalization of the NT-WS₂ sidewalls with a layer of silver nanoparticles (Fig. 1,2). If using AgNO₃, the size of the nanoparticles varied from 5 nm to 60 nm; the mean size is 30±8 nm (Fig. 1(a-d)). A synthesis with the same concentration of [Ag(NH₃)₂]OH resulted in smaller nanoparticles: from 5 to 35 nm, the mean size being 20±5 nm. As visualized by TEM, in both the cases the nanoparticles are uniformly distributed on the nanotube surface. A few AgNP agglomerates were also detected, especially near the tips of NT-WS₂. The AgNPs covering prepared from [Ag(NH₃)₂]OH looks more uniform and less agglomerated in comparison with those prepared at the same concentration of AgNO₃. SEM also revealed patterning of AgNPs along the

surface defects of disulfide (Fig. 1(c)). This suggestion is supported by AgNPs deposition on step defects of outer WS₂ layers observed by HRTEM (Fig. 1(d)). The same behavior was previously observed for gold nanoparticles grown on NT-WS₂[32]. The local composition of the Ag-NT-WS₂ nanocomposite prepared using AgNO₃ was also visualized using STEM-EDX mapping (Fig. 2). The AgNPs have a characteristic non-spherical shape indicating their heterogeneous nucleation and growth directly on the NT-WS₂ surface. Such growth results in a tight contact between AgNP and disulfide. Free AgNP detached from nanotube surface or formed in bulk solution are rare.

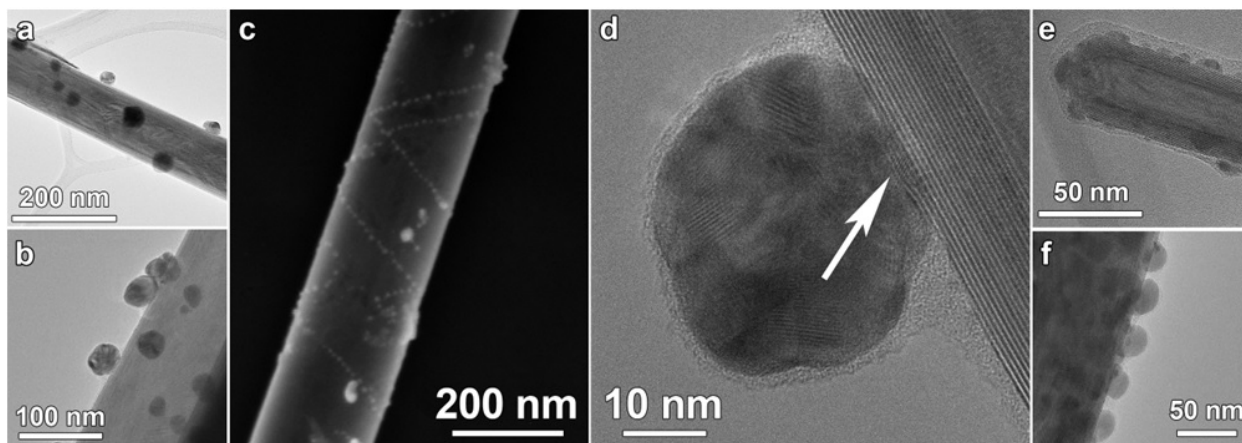


FIG. 1. Micrographs of Ag-NT-WS₂ nanocomposites synthesized using AgNO₃ (a-d) and [Au(NH₃)₂]OH (e, f) precursors. The arrow on (d) designates the step defect of NT-WS₂ surface underlying the grown AgNP

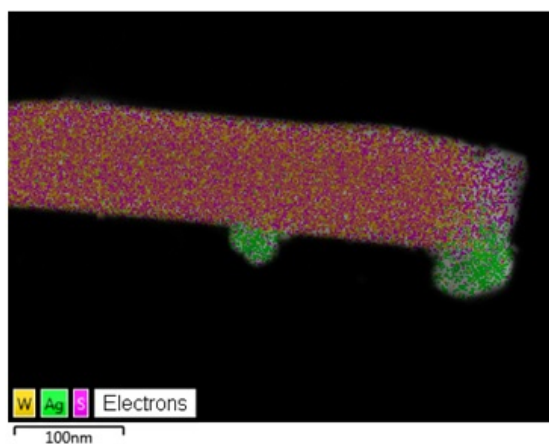


FIG. 2. STEM-EDX mapping of Ag-NT-WS₂ nanocomposite synthesized employing the AgNO₃ precursor

HRTEM analysis revealed that, while some grown particles exhibits “normal” (111) and (200) cubic silver (3C-Ag) plane arrays (Fig. 3(a)) with ca. 2.36 Å and ca. 2.00 Å spacings, respectively (Fig. 3(a-c)), the other particles have an unusual hexagonal (4H-Ag) structure. Distinct plane arrays with ca. 2.48 Å spacing were detected (Fig. 3(d-e)), coinciding well with 2.5 Å spacing of (004)-(100) 4H-Ag planes (entry #41-1402, ICDD PDF2 database [38]). To illustrate the difference in nanoparticle structures, Fast Fourier Transforms (FFTs) were calculated from HRTEM images of the selected “nanoparticle 1” (Fig. 3(a)) and “nanoparticle 2” (Fig. 3(d)). The integrated radial profiles of FFTs are shown on Fig. 3(g). It is clearly seen that “particle 1” is composed of 3C-Ag while the “particle 2” has the 4H-Ag structure.

Such a hexagonal structure of silver nanocrystals can be dictated by the arrangement of sulfur atoms on the surface of the outer WS₂ layer. Generally speaking, an arrangement of atoms in a sulfur layer in the S-W-S “sandwich” can be a perfect template for the growth of hexagonal close-packed (*hcp*) Ag atomic layers. Indeed, sulfur atoms of the WS₂ surface form a hexagonal array with a characteristic distance between the atoms of 3.15 Å. At the same time, the inter-atom distance in *hcp* Ag layer is about 2.9 Å (Fig. 3h). These *hcp* layers can be either

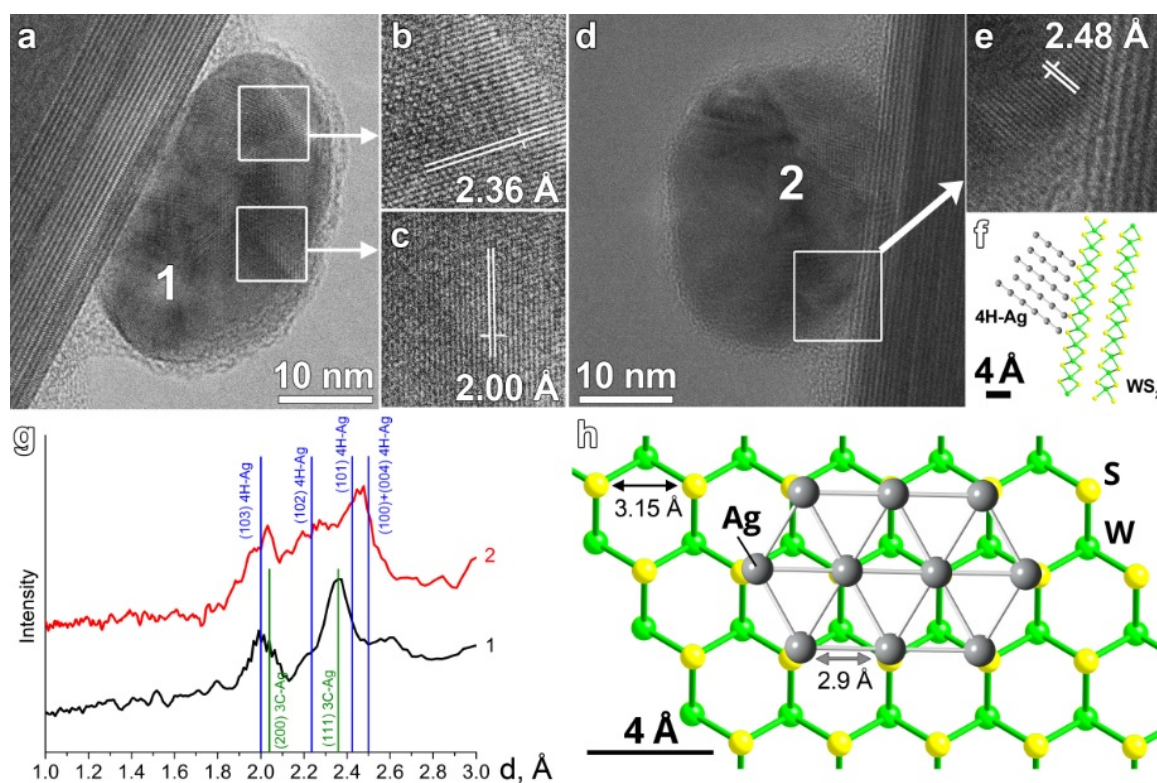


FIG. 3. (a-e) are HRTEM micrographs of AgNPs grown on the surface of NT-WS₂. (f) is a suggested crystallographic model for (e) in which (004) 4H-Ag planes continue the “chevrons” of outer WS₂ layers. (g) represents integrated radial profiles of FFTs calculated from nanoparticles 1 and 2 marked on (a) and (d), respectively. Data for 3C-Ag and 4H-Ag cells are taken from entries #4-783 and #41-1402 from ICDD PDF2 database [38]. The cif-files for crystallographic visualizations were taken from CrystalMaker Materials Library [43] and from the works [39,44] using Crystallography Open Database [45]. (h) depicts the suggested model of *hcp* atomic silver layers grown on the surface of WS₂. Please, refer to the article text for more details

(111) planes of cubic silver (3C-Ag) or (004) planes of hexagonal silver (4H-Ag). If the silver *hcp* layers propagate parallel to the surface of NT-WS₂, their spacing will not be influenced by the disulfide substrate. However, if the silver *hcp* planes propagate nearly perpendicularly to the disulfide surface, 4H structure becomes more preferable. Sulfur atomic rows on the WS₂ surface are located at 2.73 Å distances, so a 4H-Ag with 2.50 Å spacing between *hcp* Ag layers matches better with those rows than the 3C-Ag with a 2.35 Å spacing of equivalent atomic planes. In this case, a sulfur atoms arrangement of NT-WS₂ can pre-organize the 4H-Ag motifs. This also can explain the observation of (004) 4H-Ag planes continuing the “chevrons” of outer WS₂ layer (Fig. 3(e,f)). It should be noted that 4H-polytype was initially observed in natural silver samples from northern USSR [39] and later in a number of synthetic nanostructures: AgNPs prepared using *Rumex hymenosepalus* extracts [40], silver nanowires [41] and thin films [42].

Of great importance is the fact that Ag-NT-WS₂ preparation by the proposed techniques does not require any additional reducing agents or linkers, thus providing nanocomposite synthesis a material efficiency. Within the first technique, the spontaneous reaction of AgNO₃ with WS₂ takes place, resulting in heterogeneous silver nucleation. Obviously, the driving force of such chemical interaction originates from the energy difference of WS₂ Fermi level and the redox potential of dissolved Ag⁺ ions. The Fermi level of WS₂ is known to be of 4.7 range below the vacuum level [46]. The standard redox potential of Ag⁺ ions is +0.799 V against the standard hydrogen electrode (SHE) [47]. The absolute potential of SHE is, in turn, reported to be within the -4.73 to -4.43 V range [48]. Thus, the Fermi level of tungsten disulfide should be higher by 0.5–0.8 eV than the energy of missed valence electron in Ag⁺ ions (Fig. 4). This should result in spontaneous electron transfer from the NT-WS₂ surface to silver ions resulting in Ag⁺ → Ag⁰ reduction and nucleation of silver nanocrystals. Obviously, the first Ag atoms became bound by surface sulfur atoms, dictating hexagonal silver crystal symmetry as described above. The electron deficiency in the nanotubes can further be compensated by WS₂ oxidation, e.g. at the nearest surface

defects. $[\text{Ag}(\text{NH}_3)_2]\text{OH}$ has ca. twice lower reduction potential (+0.38 V) [47] than Ag^+ , so the energy difference with WS_2 Fermi level is lower but still negative. However at 100 °C, the diamminesilver(I) complex decomposes rapidly initiating silver nucleation as described in [36]. Previously, it was shown that the presence of excessive ammonia in the reaction mixture can prevent secondary nucleation during citrate-mediated AgNP synthesis, leading to the formation of smaller and quasi-monodisperse nanoparticles [49]. This was explained by the entrapment of residual free Ag^+ ions responsible for secondary nucleation. Possibly, the same moderating effect of ammonia leads to the aforementioned formation of smaller AgNPs on NT- WS_2 when $[\text{Ag}(\text{NH}_3)_2]\text{OH}$ is employed instead of AgNO_3 .

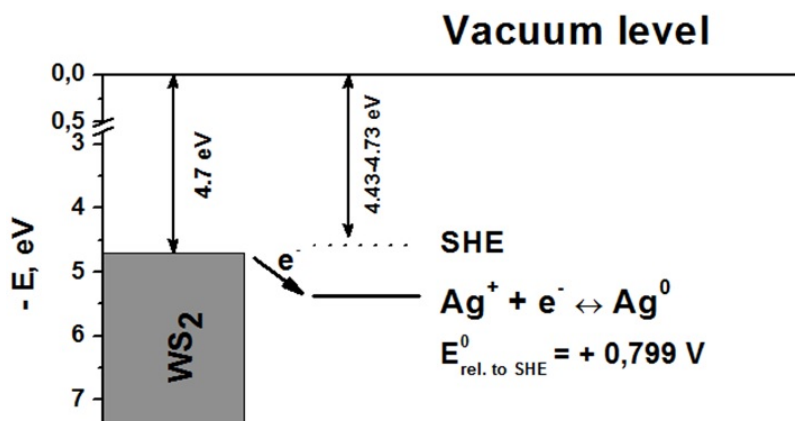


FIG. 4. Proposed energy diagram representing relative energies of WS_2 Fermi level and energy of missed valent electron in Ag^+ ion. The arrow designates possible electron transfer from NT- WS_2 to Ag^+ ions resulting in spontaneous AgNP growth on the sidewall of disulfide nanotubes

4. Conclusions

Reactions of aqueous AgNO_3 or $[\text{Ag}(\text{NH}_3)_2]\text{OH}$ solutions with NT- WS_2 resulted in functionalization of the nanotubes with a 5–60 nm layer of AgNPs without requiring any additional reducing agents. The spontaneous formation of AgNPs on NT- WS_2 surface is suggested to be driven by electron transfer from disulfide surface to dissolved Ag^+ ions. Part of the grown AgNPs exhibited unusual hexagonal crystal structure (4H-Ag). Based on careful HRTEM study, the hexagonal arrangement of sulfur atoms within the WS_2 layers, including the outer disulfide layer, is suggested to predict the observed formation of 4H-Ag nanocrystals. The prepared nanocomposites may have applications as sensors or antibacterial low-friction surface coatings.

Acknowledgements

This work is supported by the Russian Science Foundation (grant 14-13-00871), AYP acknowledges partial personal support by the Russian Foundation for Basic Research (project # 16-33-01058 mol_a) and Lomonosov Moscow State University Program of Development (the use of Carl Zeiss Libra 200 MC microscope). Authors thank Maria Poliakova (Tsukuba University, Japan) for the proof-reading.

References

- [1] Yang J., Liu H. *Metal-based composite nanomaterials*. Springer International Publishing, Cham, 2015, 259 p.
- [2] Chin K.C., Gohel A., Chen W.Z., Elim H.I., Ji W., Chong G.L., Sow C.H., Wee A.T.S. Gold and silver coated carbon nanotubes: An improved broad-band optical limiter. *Chem. Phys. Lett.*, 2005, **409** (1–3), P. 85–88.
- [3] Zhang J., Zhang X., Lai C., Zhou H., Zhu Y. Silver-decorated aligned CNT arrays as SERS substrates by high temperature annealing. *Optics Express*, 2014, **22**(18), P. 21157–21166.
- [4] Sanles-Sobrido M., Rodríguez-Lorenzo L., Lorenzo-Abalde S., González-Fernández Á., Correa-Duarte M.A., Alvarez-Puebla R.A., Liz-Marzán L.M. Label-free SERS detection of relevant bioanalytes on silver-coated carbon nanotubes: The case of cocaine. *Nanoscale*, 2009, **1**(1), P. 153–158.
- [5] Chen Y.-C., Young R.J., Macpherson J. V., Wilson N.R. Silver-decorated carbon nanotube networks as SERS substrates. *J. Raman Spectrosc.*, 2011, **42**(6), P. 1255–1262.
- [6] Chang W.-T., Hsueh Y.-C., Huang S.-H., Liu K.-I., Kei C.-C., Perng T.-P., Lin C., Chen Z. Fabrication of Ag-loaded multi-walled TiO_2 nanotube arrays and their photocatalytic activity. *J. Mater. Chem. A*, The Royal Society of Chemistry, 2013, **1**(6), P. 1987–1991.

- [7] Wu F., Hu X., Fan J., Liu E., Sun T., Kang L., Hou W., Zhu C., Liu H. Photocatalytic Activity of Ag/TiO₂ Nanotube Arrays Enhanced by Surface Plasmon Resonance and Application in Hydrogen Evolution by Water Splitting. *Plasmonics*, 2013, **8**(2), P. 501–508.
- [8] Yan Y., Sun H., Yao P., Kang S.-Z., Mu J. Effect of multi-walled carbon nanotubes loaded with Ag nanoparticles on the photocatalytic degradation of rhodamine B under visible light irradiation. *Appl. Surf. Sci.*, 2011, **257**(8), P. 3620–3626.
- [9] Liu W., Feng Y., Tang H., Yuan H., He S., Miao S. Immobilization of silver nanocrystals on carbon nanotubes using ultra-thin molybdenum sulfide sacrificial layers for antibacterial photocatalysis in visible light. *Carbon*, 2016, **96**, P. 303–310.
- [10] Cui S., Pu H., Mattson E.C., Lu G., Mao S., Weinert M., Hirschmugl C.J., Gajdardziska-Josifovska M., Chen J. Ag nanocrystal as a promoter for carbon nanotube-based room-temperature gas sensors. *Nanoscale*, The Royal Society of Chemistry, 2012, **4**(19), P. 5887–5894.
- [11] Cui S., Pu H., Lu G., Wen Z., Mattson E.C., Hirschmugl C., Gajdardziska-Josifovska M., Weinert M., Chen J. Fast and Selective Room-Temperature Ammonia Sensors Using Silver Nanocrystal-Functionalized Carbon Nanotubes. *ACS Appl. Mater. Interfaces*, 2012, **4**(9), P. 4898–4904.
- [12] Liu Y., Wu G., Cui Y. Ag/CNT-catalyzed hydroamination of activated alkynes with aromatic amines. *Appl. Organomet. Chem.*, 2013, **27**(4), P. 206–208.
- [13] Seo Y., Hwang J., Kim J., Jeong Y., Hwang M.P., Choi J. Antibacterial activity and cytotoxicity of multi-walled carbon nanotubes decorated with silver nanoparticles. *Int. J. Nanomedicine*, 2014, **9**, P. 4621–4629.
- [14] Dinh N.X., Quy N. Van, Huy T.Q., Le A.-T. Decoration of Silver Nanoparticles on Multiwalled Carbon Nanotubes: Antibacterial Mechanism and Ultrastructural Analysis. *J. Nanomater.*, 2015, **2015**, P. 1–11.
- [15] García B.O., Kharisova O.V., Rasika Dias H.V., Aguirre T. F.S., Hernández J.S. Nanocomposites with antibacterial properties using CNTs with magnetic nanoparticles. *Nanosyst. Physics, Chem. Math.*, 2016, **7**(1), P. 161–168.
- [16] Castle A.B., Gracia-Espino E., Nieto-Delgado C., Terrones H., Terrones M., Hussain S. Hydroxyl-Functionalized and N-Doped Multiwalled Carbon Nanotubes Decorated with Silver Nanoparticles Preserve Cellular Function. *ACS Nano*, 2011, **5** (4), P. 2458–2466.
- [17] Tenne R. Inorganic nanotubes and fullerene-like nanoparticles. *J. Mater. Res.*, 2006, **21**(11), P. 2726–2743.
- [18] Margolin A., Rosentsveig R., Albu-Yaron A., Popovitz-Biro R., Tenne R. Study of the growth mechanism of WS₂ nanotubes produced by a fluidized bed reactor. *J. Mater. Chem.*, 2004, **14**(4), P. 617–624.
- [19] Višić B., Panchakarla L.S., Tenne R. Inorganic Nanotubes and Fullerene-like Nanoparticles at the Crossroads between Solid-State Chemistry and Nanotechnology. *J. Am. Chem. Soc.*, 2017, **139**(37), P. 12865–12878.
- [20] Divon Y., Levi R., Garel J., Golberg D., Tenne R., Ya'akovovitz A., Joselevich E. Torsional Resonators Based on Inorganic Nanotubes. *Nano Lett.*, 2017, **17**(1), P. 28–35.
- [21] Qin F., Shi W., Ideue T., Yoshida M., Zak A., Tenne R., Kikitsu T., Inoue D., Hashizume D., Iwasa Y. Superconductivity in a chiral nanotube. *Nat. Commun.*, 2017, **8**, P. 14465.
- [22] Tsvetin Y., Popovitz-Biro R., Feldman Y., Tenne R., Komarneni M.R., Yu Z., Chakradhar A., Sand A., Burghaus U. Synthesis and characterization of WS₂ nanotube supported cobalt catalyst for hydrodesulfurization. *Mater. Res. Bull.*, 2012, **47**(7), P. 1653–1660.
- [23] Komarneni M.R., Yu Z., Burghaus U., Tsvetin Y., Zak A., Feldman Y., Tenne R. Characterization of Ni-Coated WS₂ Nanotubes for Hydrodesulfurization Catalysis. *Isr. J. Chem.*, 2012, **52**(11–12), P. 1053–1062.
- [24] Tsvetin Y., Livneh T., Rosentsveig R., Zak A., Pinkas I., Tenne R. Photocatalysis with hybrid Co-coated WS₂ nanotubes. *Nanomater. Energy*, 2013, **2**(1), P. 25–34.
- [25] Višić B., Cohen H., Popovitz-Biro R., Tenne R., Sokolov V.I., Abramova N. V., Buyanovskaya A.G., Dzvankovskii S.L., Lependina O.L. Direct Synthesis of Palladium Catalyst on Supporting WS₂ Nanotubes and its Reactivity in Cross-Coupling Reactions. *Chem. - An Asian J.*, 2015, **10**(10), P. 2234–2239.
- [26] Sedova A., Leitus G., Feldman Y., Bendikov T., Popovitz-Biro R., Khodorov S., Dodiuk H., Kenig S., Tenne R. Synthesis of magnetic FeWO₄ nanoparticles and their decoration of WS₂ nanotubes surface. *J. Mater. Sci.*, 2017, **52**(11), P. 6376–6387.
- [27] Ksenevich V.K., Gorbachuk N.I., Viet H., Shuba M.V., Kuzhir P.P., Maksimenko S.A., Paddubskaya A.G., Valusis G., Wieck A.D., Zak A., Tenne R. Electrical properties of carbon nanotubes/WS₂ nanotubes (nanoparticles) hybrid films. *Nanosyst. Physics, Chem. Math.*, 2016, **7**(1), P. 37–43.
- [28] Daoush W.M., Hong S.H. Synthesis of multi-walled carbon nanotube/silver nanocomposite powders by chemical reduction in aqueous solution. *J. Exp. Nanosci.*, 2013, **8**(5), P. 742–751.
- [29] Yamada T., Hayashi Y., Takizawa H. Synthesis of Carbon Nanotube/Silver Nanocomposites by Ultrasonication. *Mater. Trans.*, 2010, **51**(10), P. 1769–1772.
- [30] Maley J., Schatte G., Yang J., Sammynaiken R. Spontaneous Ag-Nanoparticle Growth at Single-Walled Carbon Nanotube Defect Sites: A Tool for *In Situ* Generation of SERS Substrate. *J. Nanotechnol.*, 2011, **2011**, P. 1–7.
- [31] Shahar C., Levi R., Cohen S.R., Tenne R. Gold Nanoparticles as Surface Defect Probes for WS₂ Nanostructures. *J. Phys. Chem. Lett.*, 2010, **1**(2), P. 540–543.
- [32] Polyakov A.Y., Yadgarov L., Popovitz-Biro R., Lebedev V.A., Pinkas I., Rosentsveig R., Feldman Y., Goldt A.E., Goodilin E.A., Tenne R. Decoration of WS₂ nanotubes and fullerene-like MoS₂ with gold nanoparticles. *J. Phys. Chem. C*, 2014, **118**(4), P. 2161–2169.
- [33] Polyakov A.Y., Nesterov A. V., Goldt A.E., Zubuyuk V., Dolgova T., Yadgarov L., Visic B., Fedyanin A.A., Tenne R., Goodilin E.A. Optical properties of multilayer films of nanocomposites based on WS₂ nanotubes decorated with gold nanoparticles. *J. Phys. Conf. Ser.*, 2015, **643**, P. 012046.
- [34] Tremel W., Spetter D., Hoshyargar F., Sahoo J., Tahir M.N., Branscheid R., Barton B., Panthöfer M., Kolb U. Surface Defects as a Tool to Solubilize and Functionalize WS₂ Nanotubes. *Eur. J. Inorg. Chem.*, 2017, **15**, P. 2190–2194.
- [35] Zak A., Ecker L.S., Efrati R., Drangai L., Fleischer N., Tenne R. Large-scale Synthesis of WS₂ Multiwall Nanotubes and their Dispersion, an Update. *J. Sensors Transducers*, 2011, **12** (Special Issue), P. 1–10.
- [36] Sarycheva A.S., Ivanov V.K., Baranchikov A.E., Savilov S. V., Sidorov A. V., Goodilin E.A., Grigorieva A. V., Maksimov G. V., Goodilin E.A., Egorov A. V., Brazhe A.R., Parshina E.Y., Luneva O.G., Maksimov G. V., Tretyakov Y.D. Microbead silica decorated with polyhedral silver nanoparticles as a versatile component of sacrificial gel films for SERS applications. *RSC Adv.*, 2015, **5**(110), P. 90335–90342.
- [37] Neas D., Klapetek P. Gwyddion: an open-source software for SPM data analysis. *Open Phys.*, 2012, **10**(1), P. 181–188.
- [38] ICDD Products - PDF-2 [Electronic resource], URL: <http://www.icdd.com/products/pdf2.htm> (accessed: 06.10.2017).

- [39] Novgorodova M.I., Gorshkov A.I., Mokhov A. V. Native Silver and Its New Structural Modifications. *Zap. Vsesoyuznogo Mineral. Obs.*, 1979, **108**, P. 552–563.
- [40] Rodríguez-León E., Iñiguez-Palomares R., Navarro R., Herrera-Urbina R., Tánori J., Iñiguez-Palomares C., Maldonado A. Synthesis of silver nanoparticles using reducing agents obtained from natural sources (*Rumex hymenosepalus* extracts). *Nanoscale Res. Lett.*, 2013, **8**(1), P. 318.
- [41] Liu X., Luo J., Zhu J. Size effect on the crystal structure of silver nanowires. *Nano Lett.*, 2006, **6**(3), P. 408–412.
- [42] Chakraborty I., Shirodkar S.N., Gohil S., Waghmare U. V, Ayyub P. A stable, quasi-2D modification of silver: optical, electronic, vibrational and mechanical properties, and first principles calculations. *J. Phys. Condens. Matter*, 2014, **26**(2), P. 25402.
- [43] CrystalMaker Structures Libraries: Materials Structures [Electronic resource], URL: <http://crystallmaker.com/library/chalcogenides.html> (accessed: 06.10.2017).
- [44] Jette E.R., Foote F. Precision Determination of Lattice Constants. *J. Chem. Phys.*, 1935, **3**(10), P. 605–616.
- [45] Crystallography Open Database [Electronic resource], URL: <http://www.crystallography.net/cod/index.php> (accessed: 05.10.2017).
- [46] Jaegermann W., Ohuchi F.S., Parkinson B.A. Interaction of Cu, Ag and Au with van der Waals faces of WS₂, and SnS₂. *Surf. Sci.*, 1988, **201**(1–2), P. 211–227.
- [47] Goia D. V., Matijević E. Preparation of monodispersed metal particles. *New J. Chem.*, 1998, **22** (11), P. 1203–1215.
- [48] Reiss H., Heller A. The absolute potential of the standard hydrogen electrode: a new estimate. *J. Phys. Chem.*, 1985, **89**(20), P. 4207–4213.
- [49] Gorup L.F., Longo E., Leite E.R., Camargo E.R. Moderating effect of ammonia on particle growth and stability of quasi-monodisperse silver nanoparticles synthesized by the Turkevich method. *J. Colloid Interface Sci.*, 2011, **360**(2), P. 355–358.

Energetics of carbon nanotubes with open edges: Modeling and experiment

V. G. Zavodinsky¹, O. A. Gorkusha², A. P. Kuz'menko³

¹Institute for Material Science, 153, Tikhoockeanskaya st., 680042, Khabarovsk, Russia

²Khabarovsk Department, Institute of Applied Mathematics, 54, Dzerzhinskogo st., 680000, Khabarovsk, Russia

³South-West State University, 94, 50 let Oktyabrya st., 305040 Kursk, Russia

vzavod@mail.ru, o_garok@rambler.ru, apk3527@mail.ru

PACS 61.48.De, 82.70.Dd

DOI 10.17586/2220-8054-2017-8-5-635-640

Modeling approaches based on the density functional theory (DFT): the Kohn–Sham (KS) method and orbital-free (OF) method are used to for calculation of the binding energies per atom as functions of the diameter of single-wall carbon nanotubes (SWCNTs) with the open ends. It is shown that this energy has a minimum at a diameter of about 1.1 – 1.2 nm. The experiments made by means of Raman spectroscopy have shown that diameters of SWCNTs mainly lie in the range of 1 – 1.5 nm.

Keywords: SWCNT, energy, diameter, modeling, Kohn–Sham, orbital free, Raman spectroscopy.

Received: 2 October 2017

Revised: 4 October 2017

1. Introduction

Single-wall carbon nanotubes (SWCNTs), discovered at the end of the last century are at the center of attention of many research groups. Many of those researchers are interested in the atomic and electronic structures of SWCNTs, their mechanical properties, interaction with other materials and among themselves, and many other things. However, despite huge number of the works devoted to the study of UNT, some of their main features are still obscure. In particular, one of main questions remains without answer: are the diameters of the tubes defined? Most often it is simply specified in literature that diameter of SWCNTs lies within 0.7 – 1.6 nanometers. At the same time there are data that it is possible to receive SWCNTs with the minimum diameter of 0.3 nanometers [1] and maximum of 12 nanometers [2]. Experimental distributions of SWCNTs on diameter values with maxima in the range from 1 to 1.5 nanometers are given in [3,4]. Energy dependence of the armchair tubes on their diameters is obtained in [5] by the semi-empirical PM3 method of computer modeling; the energy minimum is revealed for a diameter of about 0.8 nanometers.

We did not find other data regarding the dependence of the SWCNTs' energy on the diameter value, therefore we performed our own calculations from the first principles, using two methods based on DFT [6]: namely, the KS [7] method realized in the FHI96md [8] package and the orbital-free (OF) method described in [9–12].

2. Methods and models used for modeling

The KS method is widely known and does not need a detailed discussion here. It is enough to remind that in this approach, the system of the one-electron equations of Schrödinger is replaced with a set of the Kohn–Sham equations in which each electron interacts with total density $\rho(\mathbf{r})$, formed by all electrons:

$$-\frac{\hbar^2}{2m}\Delta\psi_i(\mathbf{r}) + V_{eff}(\mathbf{r})\psi_i(\mathbf{r}) = \varepsilon_i\psi_i(\mathbf{r}), \quad (1)$$

where

$$V_{eff}(\mathbf{r}) = \int \frac{\rho(\mathbf{r}')}{|\mathbf{r}' - \mathbf{r}|} d\mathbf{r}' + V_{xc}(\mathbf{r}), \quad \rho_e(\mathbf{r}) = \sum_{i=1}^{N_e} |\psi_i(\mathbf{r})|^2,$$

$V_{xc}(\mathbf{r})$ is the exchange-correlation potential which can be calculated in some approach, ψ_i is the wave function corresponding to the i -th one-electron state, ε_i is the energy of this state.

The OF approach does not operate with wave functions (orbitals), but with the total electron density only. Actually, this approach is consecutive development of the hypothesis of Hohenberg and Kohn [6], that the ground state of a quantum system can be described by means of only electronic density. Thus, the total energy of the system can be found by minimization of a certain functional:

$$E[\rho] = \int \varepsilon(\rho) d\mathbf{r} = \int V(\mathbf{r})\rho(\mathbf{r}) d\mathbf{r} + \frac{1}{2} \int \varphi(\rho)\rho(\mathbf{r}) d\mathbf{r} + \int \varepsilon^{ex-c}(\rho) d\mathbf{r} + \int \varepsilon^{kin}(\rho) d\mathbf{r}, \quad (2)$$

where ε^{ex-c} and ε^{kin} are the exchange-correlation and kinetic energy functionals.

A basis of the OF approach is finding of the density $\rho(\mathbf{r})$ turning into zero the functional $F[\rho]$, which is a variation derivative of the functional of energy (1):

$$F[\rho] \equiv \frac{\delta \varepsilon[\rho]}{\delta \rho} = V(\mathbf{r}) + \varphi(\mathbf{r}) + \mu_{kin}(\rho) + \mu_{ex-c}(\rho) = 0, \quad (3)$$

where the density $\rho(\mathbf{r})$ must satisfy the condition $\int \rho(\mathbf{r}) d\mathbf{r} = N$ (N is the number of electrons in the system);

the potentials $\mu_{kin}(\rho)$ and $\mu_{ex-c}(\rho)$ are the variation derivatives $\mu_{kin}(\rho) = \frac{\delta \varepsilon_{kin}(\rho)}{\delta \rho}$, $\mu_{ex-c}(\rho) = \frac{\delta \varepsilon_{ex-c}(\rho)}{\delta \rho}$. If ε^{kin} is known, equation (3) may be solved by any iteration method, and then the total energy may be calculated.

The OF approach gained noticeable development in the last 20 years (see for example [13–18]), however its supporters have not yet achieved serious success. In our opinion, the reason for difficulties is that their works rely on the authority of Hohenberg and Kohn, who declared that there is a universal functional of kinetic energy and the task consists only in that to find it.

However, as shown recently [19, 20], the idea of Hohenberg and Kohn about the existence of a universal density functional leading to the energy minimum is not strictly proved. Thus, there are bases to believe that attempts to construct an OF method based on use of any universal functional are obviously doomed to failure.

The OF method, based on the kinetic energy functionals ε^{kin} specified for the each type of atoms was developed in our previous works [9–12]. We demonstrated ability of our method to describe the structure and energy of atomic systems consisting of two, three, and four atoms of various types. In the present work, we use this method for more large systems: namely, for simulation of carbon nanotubes.

Taking into account the restrictions by the sizes of atomic systems which are available for the KS method and for observance of uniformity of calculations, we limited ourselves to consideration of nanotubes fragments of the armchair type in the form of rings consisted of the four atomic chains. Diameters of rings were varied from 0.41 nanometers to 1.55 nanometers. Thus, the number of the atoms included into the studied system changed from 48 to 176. The kinetic energy functional for carbon atoms were taken the same like in [10]. The cell sizes for calculations by the OF method were taken $40 \times 40 \times 40$ a.e.³ with splitting $150 \times 150 \times 150$ (1 a.u. = 0.529 Å). For calculations by the KS method, we used a cell of the same size; the cutting energy for the set of plane waves was equal 40 Rydberg; exchange and correlation interactions were calculated in both cases in the LDA approach [21]. In all cases, atoms of carbon could move under the influence of interatomic forces and find the equilibrium positions during of calculations.

3. Results of modeling

First of all, we compared interatomic distances d obtained in our calculations with literature data. Results are collected in Table 1.

TABLE 1. Interatomic distances d obtained by us for fragments of open SWCNTs compared with other data

Source	OF calculation	KS calculation	Other calculations	Experiment
d , inside, Å	1.42	1.39	1.42 [22]	1.42 [23]
d , edge, Å	1.32	1.28		

Our calculations give the sizes of distances between internal atoms of SWCNTs close to the literary data. Unfortunately, we did not find works in which experimental or theoretical data on interatomic distances at open edges of SWCNTs are provided. However in [24, 25] it is shown by modeling by various methods that in carbon systems of diamond type the distance between edge atoms decrease to 1.35 – 1.38 Å against 1.55 Å in the central part. Qualitatively it coordinates with our results about reduction of interatomic distance on the ends of nanotubes in comparison with distances between internal atoms.

In Fig. 1, the binding energies (per atom) are presented for the considered SWCNT fragments. First, we see that the values received by the OF method (the curve 1) and by the KS method (the curve 2) are well coordinated with each other, differing less than for 10 percent. Both methods show the existence of a minimum of energy at similar values of diameter: $D_{\min} = 1.1$ nanometer for the OF method, and $D_{\min} = 1.24$ nanometer for the KS method. For comparison, the semi-empirical PM3 method data [4] are given in the same Fig. 1 (the curve 4).

These data show a minimum at $D_{\min} = 0.8$ nanometer. In our opinion, this minimum is not very reliable as it is presented by only one point which obviously drops out of the values next to it.

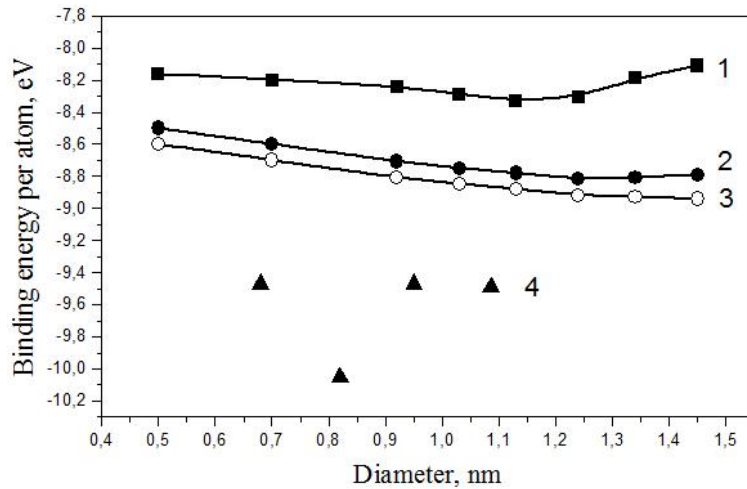


FIG. 1. The binding energy vs diameter of SWCNT. 1 – OF calculations; 2 – KS calculations with open ends; 3 – KS calculations of infinite tubes; 4 – PM3 calculations [4]

There is the remaining question: what is the physical reason for the emergence of a minimum of the atomic energy while diameter of a tube increases? Two counteracting mechanisms of energy change are necessary for the emergence of a minimum. The first mechanism is obvious: the total number of the system's atoms increases with increase of diameter. As a rule, it conducts to increasing of binding energy if is only not followed by specific reorganizations of atomic structure, like, for example, it is happened in "magic" clusters. In our case, the structure of the system does not change therefore the binding energy has to grow on the absolute value with increase of diameter. Besides, the increase in diameter automatically is followed by reduction of curvature of a tube that in addition lowers the energy of the system as it approaches to the energy of graphene. However in the case of SWCNTs of finite sizes having the open ends there is one more possible mechanism of the energy changing; this is the interaction of the atoms which are on the ends of a tube, among themselves. The greater the diameter, the greater the average distance between these atoms, and correspondingly, the lower their contribution to the system's total energy.

To verify this hypothesis, we carried out additional calculations by the KS method, using the fact that the FHI96md package, which we applied to calculations, is adapted for periodic calculations and at an appropriate choice of parameters of the supercell can model an infinite nanotube (i.e. not having the ends). In this case it appeared that the binding energy falling on one atom has no minimum, and monotonously grows on an absolute value (the curve 3). That is, interaction of the edge atoms really responsible for the energy minimum.

4. Technique of experiment

The colloidal solutions (CSs) with multi-walled carbon nanotubes (MWCNTs) (Nanocyl production, Belgium), synthesized by CCVD method with nanocatalysts on the basis of CoO, were used as a basis of investigation. Functionalization of MWCNTs was reached by hashing within 5 hours in an ultrasonic bathtub in the acid environment (H_2SO_4 and HNO_3 in the ratio 3:1) with a warming up no more than 42°C . Deionized water was added to solution after cooling in the equilibrium ratio; than it was filtering, washing, and the subsequent drying was carried out like [26]. The level of functionalization of MWCNTs was determined by use of the FT-IR spectra (Nicolet iS50, 0.125 cm^{-1}).

The produced CSs were put as drops within the interelectrode space (100, 500, 1000 and $1500\ \mu\text{m}$ of width) of the film chip made like [26]. The constant voltage (varied from 10 to 50 V) was applied to electrodes.

After evaporation of the drop some structures were formed in the electric field (Fig. 2). It is conditionally possible to divide them to fractals (with fractal dimensionality of $D_{FR} = 1.7 - 2.2$), fractal clusters ($D_{FR} = 1.6 - 1.8$) consisting, probably, of very small nanoparticles, and piecewise linear (threadlike) structures. According to SEM and ASM data, the simultaneous formation of both fractal clusters, and piecewise linear structures was observed in case of change of voltage from 20 to 45 V.

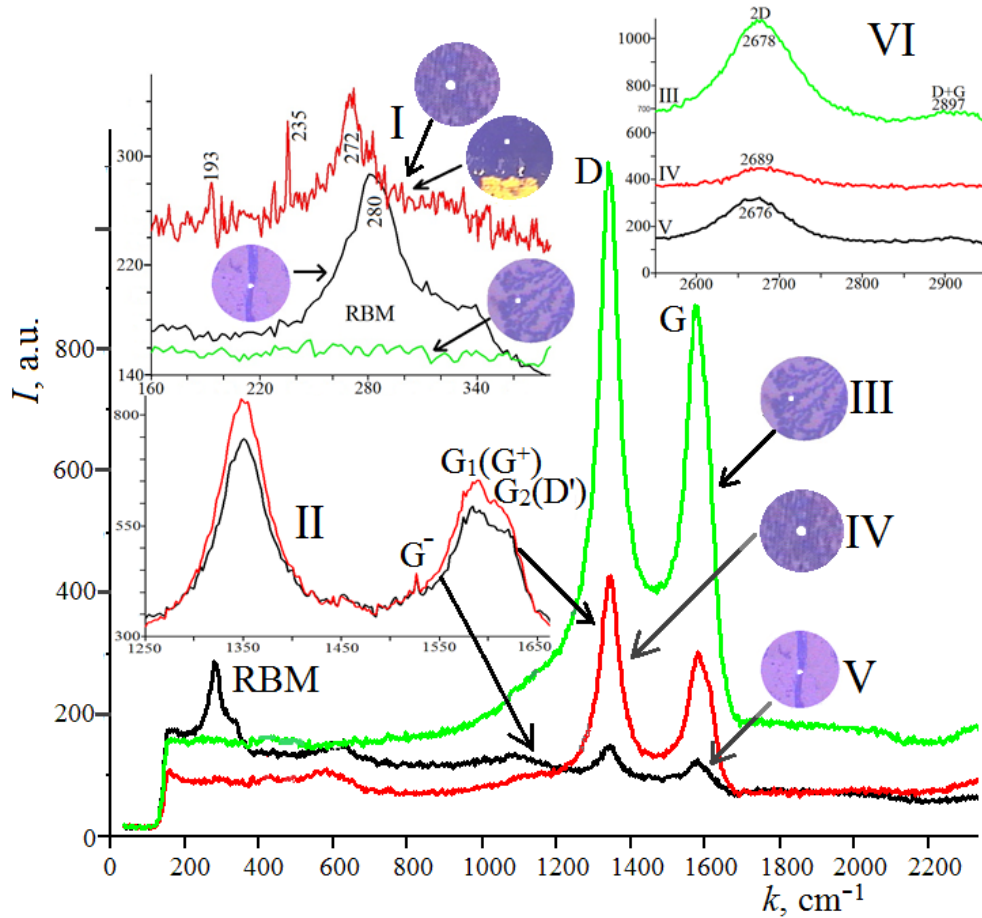


FIG. 2. Combinational Raman spectra (CRS) on the piecewise linear structures (V), on the fractal clusters (IV), and on the fractal structures (III) formed from MWCNT; CRS in the RBM area with pictures of structures (I); CRS in the area of lines G^- , $G_1(G^+)$, and $G_2(D')$ (II); CRS at frequencies higher than 2200 cm^{-1} (VI) for the cases III, IV, and V

In the combinational Raman spectra (CRS) (OmegaScopeTM the Raman microspectrometer, 532 nm , 0.8 cm^{-1}), lines $D = 1336 - 1353 \text{ cm}^{-1}$ and $G = 1567 - 1600 \text{ cm}^{-1}$, have been found (Fig. 3) (both with electric field, and without the field), which are typical for MWCNTs. However, in the low-frequency area of CLS so-called radial breath modes (RBM) have been found in the range of $100 - 360 \text{ cm}^{-1}$, typical only for SWCNTs [27] (see the insertion I in Fig. 3). RBM lines were observed for the particles formed directly on electrodes (193 , 235 and 272 cm^{-1}) and also for the fractal clusters and the piecewise linear structures (280 cm^{-1}) whereas they were absent for fractal structures (see the insertion I in Fig. 3). It directly indicates the perpendicular orientation of the SWCNTs to a substrate. Values of diameters of SWCNTs calculated as $d = 285 \text{ cm}^{-1}/\omega$ [27]: for the piecewise linear structures $d \approx 1 \text{ nm}$, and $d = 1 - 1.5 \text{ nm}$ for the fractal clusters and for SWCNTs formed on the electrodes.

5. Conclusion

The calculations which are carried out by two methods based on DFT, namely the Kohn–Sham method and the orbital-free method, showed that the binding energy of carbon nanotubes has an energy minimum with a diameter of tube about $1.1 - 1.2$ nanometers. It is revealed that interaction of atoms which are on the open ends of tubes is responsible for the emergence of an energy minimum. The experimental study, which was carried out by means of Raman spectroscopy has shown that SWCNTs which are formed in contact with multiwall carbon nanotubes have diameters in the range of $1 - 1.5$ nanometers irrespective of presence of electric voltage.

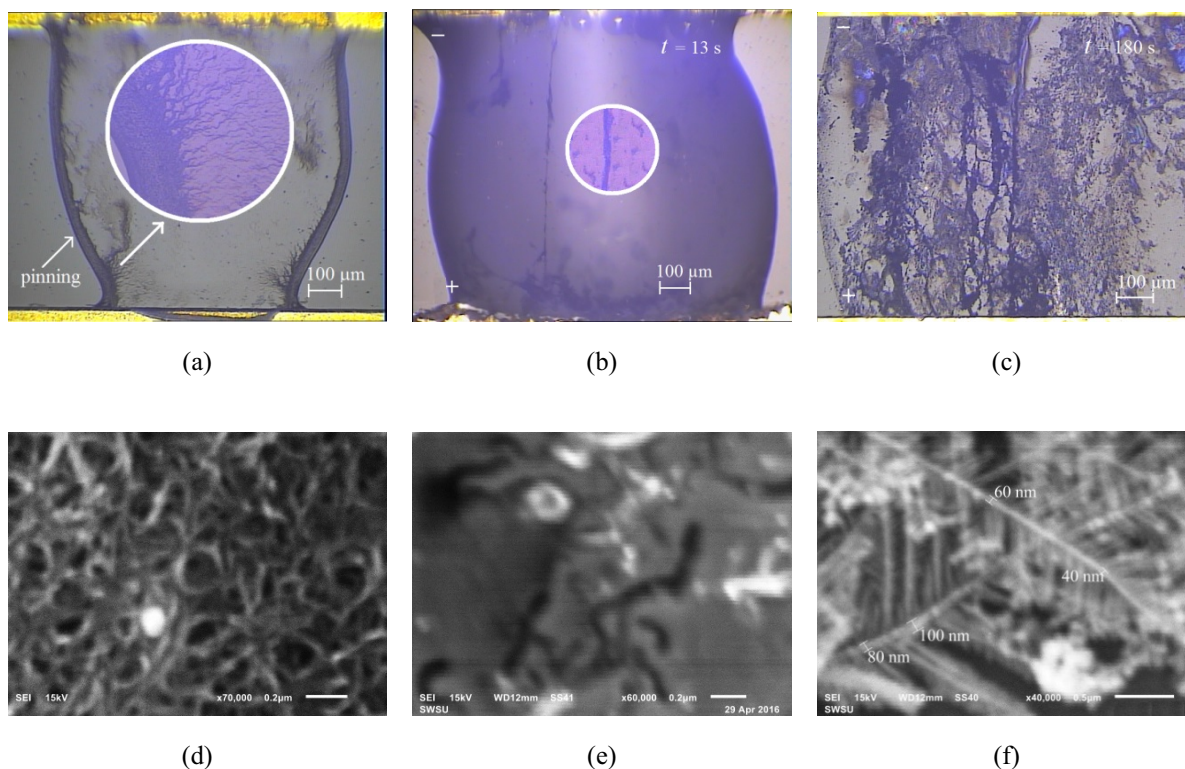


FIG. 3. Confocal and SEM images on polycrystalline glass: MWCNTs without voltage (a, d), piecewise linear structures (b), fractal clusters and diffusion structures at $U = 21$ V (c), and SEM images of MWCNTs at $U = 20$ V (e and f) with the similar structures having dark and light contrasts

Acknowledgements

This work is performed with financial support of the Ministry of Education and Science of the Russian Federation within the task No. 16.2814.2017/PCh. One of authors (A.P. Kuz'menko) expresses gratitude to employees of the South-West State University (Kursk, Russia) A. E. Kuzko, Thet Phyto Naing, and Myo Min Than.

References

- [1] Lee K., Chong Rae Park. Effects of chirality and diameter of single-walled carbon nanotubes on their structural stability and solubility parameters. *Royal Society of Chemistry Advances*, 2014, **4**, P. 33578–33581.
- [2] Chin Li Cheung, Andrea Kurtz, Hongkun Park, Charles M. Lieber. Diameter-Controlled Synthesis of Carbon Nanotubes. *J. Phys. Chem. B*, 2002, **106**, P. 2429–2433.
- [3] Eletskiy A.V. Carbon nanotubes. *Uspekhi Fizicheskikh Nauk*, 1997, **167** (9), P. 945–972 (in Russian).
- [4] Kiang C.-H., Goddard III W.A., Beyers R., Bethune D.S. Carbon nanotubes with single-layer walls. *Carbon*, **33** (7), P. 903–914.
- [5] Boguslavskaya E.S., Bazhin I.V. Mechanical properties of carbon nanotubes and of their contacts. *Fazovye perekhody, uporyadochennye sostoyaniya i novye materialy*, 2009, **11**, 4 p. (in Russian).
- [6] Hohenberg H., Kohn W. Inhomogeneous electron gas. *Phys. Rev. B*, 1964, **136**, P. 864–871.
- [7] Kohn W., Sham J.L. Self-consistent equations including exchange and correlation effects. *Phys. Rev. A*, 1965, **140**, P. 1133–1138.
- [8] Beckstedte M., Kley A., Neugebauer J., Scheffler M. Density functional theory calculations for poly-atomic systems: electronic structure, static and elastic properties and ab initio molecular dynamics. *Comp. Phys. Commun.*, 1997, **107**, P. 187–205.
- [9] Zavodinsky V.G., Gorkusha O.A. A simple quantum-mechanics way to simulate nanoparticles and nanosystems without calculation of wave functions. *International Scholarly Research Network Nanomaterials*, 2012, 531965, 3 p.
- [10] Zavodinsky V.G., Gorkusha O.A. Quantum-Mechanical Modeling without Wave Functions. *Physics of the Solid States*, 2014, **56** (11), P. 2329–2335.
- [11] Zavodinsky V.G., Gorkusha O.A. Development of an orbital free approach for simulation of multiatomic nanosystems with covalent bonds. *Nanosystems: Physics, Chemistry, Mathematics*, 2016, **7** (3), P. 427–432.
- [12] Zavodinsky V.G., Gorkusha O.A. Development of the orbital free approach for heteroatomic systems. *Nanosystems: Physics, Chemistry, Mathematics*, 2016, **7** (6), P. 1010–1016.
- [13] Wang Y.A., Carter E.A. Theoretical Methods in Condensed Phase Chemistry. In *Progress in Theoretical Chemistry and Physics*, Kluwer, Dordrecht, 2000, P. 117–184.

- [14] Huajie Chen, Aihui Zhou. Orbital-free density functional theory for molecular structure calculations. *Numerical Mathematics: Theory, Methods and Applications*, 2008, **1** (1), P. 1–28.
- [15] Karasiev V.V., Jones R.S., Trickey S.B., Harris F.E. Recent advances in developing orbital-free kinetic energy functionals. In *New Developments in Quantum Chemistry*, 2009, P. 25–54.
- [16] Chakraborty D. Computing the kinetic energy from electron distribution functions. Ph.D. (Chemistry) Thesis, McMaster University, Hamilton, Ontario, Canada, 2011.
- [17] Huang C., Carter E.A. Nonlocal orbital-free kinetic energy density functional for semiconductors. *Phys. Rev. B*, 2010, **81**, 045206–15.
- [18] Ho G.S., Ligneres V.L., Carter E.A. Introducing PROFESS: A new program for orbital-free density functional theory calculations. *Comp. Phys. Commun.*, 2008, **179**, P. 839–854.
- [19] Sarry A.M., Sarry M.F. On the density functional theory. *Fizika Tverdogo Tela*, 2012, **54** (6), P. 1237–1243 (in Russian).
- [20] Bobrov V.B., Trigger S.A. The problem of the universal density functional and the density matrix functional theory. *J. Exper. Theor. Phys.*, 2013, **116** (4), P. 635–640.
- [21] Perdew J.P., Wang Y.A. Accurate and simple density functional for the electronic exchange energy. *Phys. Rev. B*, 1986, **33**, P. 8800–8802.
- [22] Huhtala M., Kuronen A., Kimmo Kaski. Computational studies of carbon nanotube structures. *Computer Physics Communications*, 2002, **147**, P. 91–96.
- [23] Danilov C.V. Simulation of atomic structure and the X-Ray structure analysis of carbon nanotubes. PhD Thesis, Petrozavodsk State University, Petrozavodsk, Russia, 2013 (in Russian).
- [24] Barnard A.S., Russo S.P., Snook I.K. Surface structure of cubic diamond nanowires. *Surf. Sci.*, 2003, **538**, P. 204–210.
- [25] Cheng Yang, H. Chuan Kang. Cluster study of the dimer geometry on the C(100) surface. *Surf. Sci.*, 1998, **409**, P. 521–527.
- [26] Kuzmenko A.P., Thet Phyto Naing, et al. Self-assembly and Self-organization Processes of Carbon Nanotubes in the Colloidal Systems. *J. of Nano- and Electronic Physics*, 2015, **7** (4), P. 04014(3).
- [27] Thomsen C., Reich S. Raman scattering in carbon nanotubes. *Topics Appl. Physics*, 2007, **108**, P. 115–232.

Modeling chemisorption of carbon dimer at (8, 0) nanotube

S. S. Moliver

A. I. Alikhanov Institute for Theoretical and Experimental Physics NRC Kurchatov Institute,
Bol. Cheremush. 25, Moscow 117218, Russia
moliver.sergei@gmail.com

PACS 71.15.Ap, 71.15.Nc, 73.20.Hb, 74.20.Pq, 81.07.De

DOI 10.17586/2220-8054-2017-8-5-641-646

The electron structures of two forms of the grafted carbon dimer for the (8, 0) zigzag nanotube were calculated by the semi-empirical quantum-chemistry method applied to the supercell model. If the dimer adsorbs above the center of the tube's hexagon (h-grafting), it performs the topochemical transformation of the tube, according to the Stone–Wales scheme of inverse kind. B-grafting is a chemisorption above tube's bond, it is energetically lower, than h-grafting. Atomic structure of b-grafting is a splitted di-interstitial. Measuring the electronic density of states in the upper valence band has been shown to make it possible to distinguish between pure and grafted nanotubes, as well as between b- and h-graftings.

Keywords: Carbon nanotubes, quantum chemistry, chemisorption.

Received: 11 September 2017

Revised: 25 September 2017

1. Introduction

The carbon dimer (C_2 molecule, when isolated) is an important structural element of graphene and carbon nanotubes. Several point defects, occurring in these materials during growth or mechanical influence, can be represented by the carbon dimer (C–C bond) as a basic point defect. The well-known intrinsic topochemical defect (A. J. Stone, D. J. Wales, 1986) appears in an ideal hexagonal carbon net when dimer rotates on 90° . After the rotation the dimer is included in two 5- and two 7-membered carbon cycles: defect SW(55-77) [1], or (5-7-7-5) [2,3]. Ad-dimers (C_2 molecules after adsorption) produce interstitial defects in graphene and nanotubes; they may remain after growing the material, or may be entered purposely. Ion beam of C_2^- was used for structural modification of the fullerene film, and it has been found that new bonds were formed by dimers [4]. Hydrocarbon chemisorption could be the first stage of entering ad-dimers into graphene or nanotube: dehydrogenation is possible by electric current through the STM tip [5], or (supposedly) by tip-focused electron, X-ray, or molecular beam.

Theoretical models of the ad-dimer grafting by 2-dimensional-graphene net propose to place the dimer in the center of the bond's hexagon, in order to switch chemical bonds similarly to SW transformation. Such an interstitial-like defect is called (7-5-5-7) [2,3,6], or “inverse Stone–Wales” ISW [1,7]. (The dimer inside the SW is the common side of the 7-membered cycles, and inside the ISW is the common side of the 5-membered cycles.) This kind of dimer incorporation will be called below h-grafting.

The 3-dimensional-graphite problem of radiation defects, related to the interstitial dimer [8], also required models for dimer grafting. “Grafted interlayer bridge” di-interstitial [9], later marked $I_2(7557)$ [10], is similar to ISW in graphene. However, the alternative structure – splitted di-interstitial – was found [9], later marked $I_2(\alpha\beta)$ [10]. Suppose that the dimer is situated immediately above C–C bond of hexagonal net (basal atomic plane of graphite), so that it forms a 4-member cycle, perpendicular to basal plane. Splitting of di-interstitial means that the cycle slides as a whole, making dimer and the bond be equally spaced in the coordination-complex manner among 4 “ligand” neighbors of the net. This kind of dimer incorporation will be called below b-grafting.

2. Goal, method, and model

Theoretical calculations, presented here, are devoted to the covalent grafting of carbon dimer by the small-diameter SWNTs (single-wall carbon nanotubes) (8, 0) zigzag (chemisorption is equivalent to grafting in such low-dimensional system). Two possible above-mentioned ways of dimer incorporation are studied: h-grafting (dimer is placed above hexagon center), and b-grafting (dimer is placed along chemical bond). The tube's chirality allows high-symmetry models with degenerate electronic states, so insulating and metallic configurations may be compared. Although topologically similar, carbon nets of graphene and small-diameter SWNTs have different many-electron properties. The results of calculations of ad-dimer grafting in graphene and graphite [1,9,10] may be extrapolated to large-diameter SWNTs [2,3], but the case of large curvature should especially be considered.

The tool for the total-energy electron-structure calculations is a program set that:

- belongs to quantum chemistry,
- deals with MO-LCAO determinant wave function,
- uses the restricted Hartree–Fock–Roothaan algorithm for the self-consistent ground state,
- is advanced for open-shell configurations (several-determinant terms of a given symmetry),
- is constrained by semi-empirical basis of Slater-type atomic orbitals. Semi-empirical INDO parametrization was achieved previously, it is suitable for materials and macromolecules composed of Si and C, where impurities and chemical groups may contain H and N atoms. As to carbon materials, this tool had been used for: vacancy centers of diamond, molecular and crystalline fullerene [60], graphite and graphene, nanotubes. Modeling systems of 10^2 – 10^3 atoms on ab-initio level requires significant computing power and time, thus semi-empirical quantum chemistry is still useful, at least as a preliminary step. For example, properties of the SW defect in (8, 0) and (5, 5) nanotubes, exposed to fracture-like deformation, were successfully investigated using this tool [11].

The model of the SWNT was treated as a 1-dimensional supercell consisting of 8 primitive unit cells. Periodic boundary conditions require that every molecular orbital (MO) possesses a wave vector from the uniform k -set of 8 Brillouin-zone points. Since the primitive cell of SWNT (8, 0) consists of 4 circles of 8 atoms, the supercell model contains 256 atoms. To reach the goal, 4 ad-dimers were added to the tube's supercell; furthermore they were uniformly distributed over tube's length and axial angle with helical symmetry. Ad-dimers of such a model are identical and nearly independent. Due to 4-fold screw axis the model has degenerate electron states, which makes it possible to compare closed- and open-shell configurations. Figs. 1, 2 show the part of the model (2.5 primitive cells of 8) with one ad-dimer of 4. Atomic balls are drawn by the same program kit that fulfilled calculations (to help eliminate errors in input files), bonding sticks are hand-drawn.

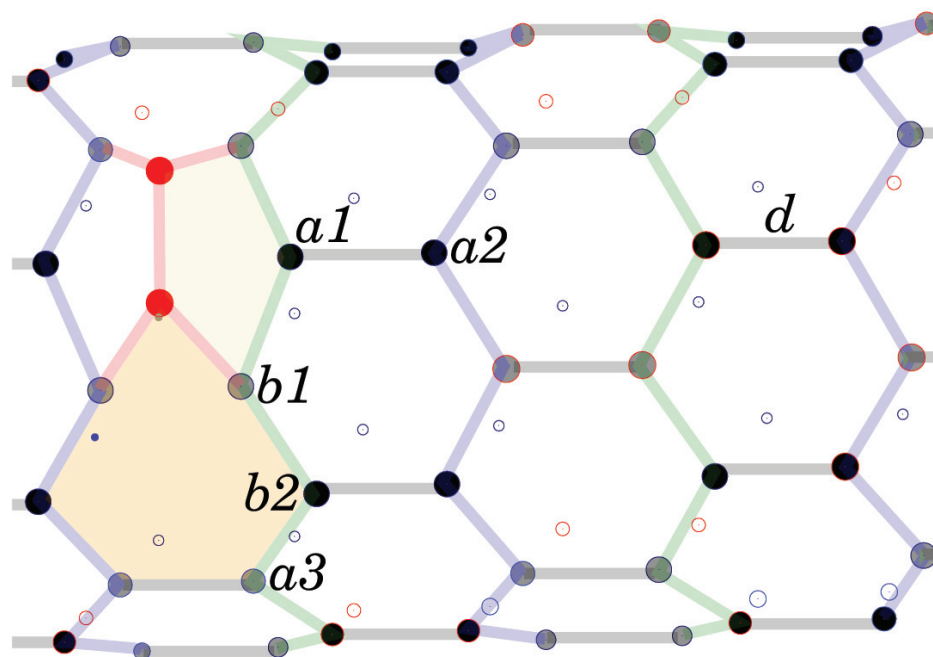


FIG. 1. Ad-dimer's h-grafting, or inverse Stone–Wales transformation. Longitudinal CC bond is used as a length unit d

Each mark in Figs. 1, 2 refers to several neighbors of equal symmetry (coordination star), their positions should be varied simultaneously, one coordination star after another, as well as dimer's length and height, until the total-energy minimum is found. See below about equilibrium structures of both graftings.

Colored 5- and 7-membered cycles around h-grafted dimer of Fig. 1 remind one about the topochemical Stone–Wales ability of ad-dimer placed above the center of hexagon. Colored cycles around the b-grafted dimer of Fig. 2 do not have usual chemical-structure sense. They help to visualize the coordination-complex-like geometry: a 4-member cycle, consisting of dimer and split bond $b2$, plays the role of the “center”; adjoint nested 6-member cycles are non-planar, contain “ligands” $c1$, and are flexed either to the dimer or to the split bond.

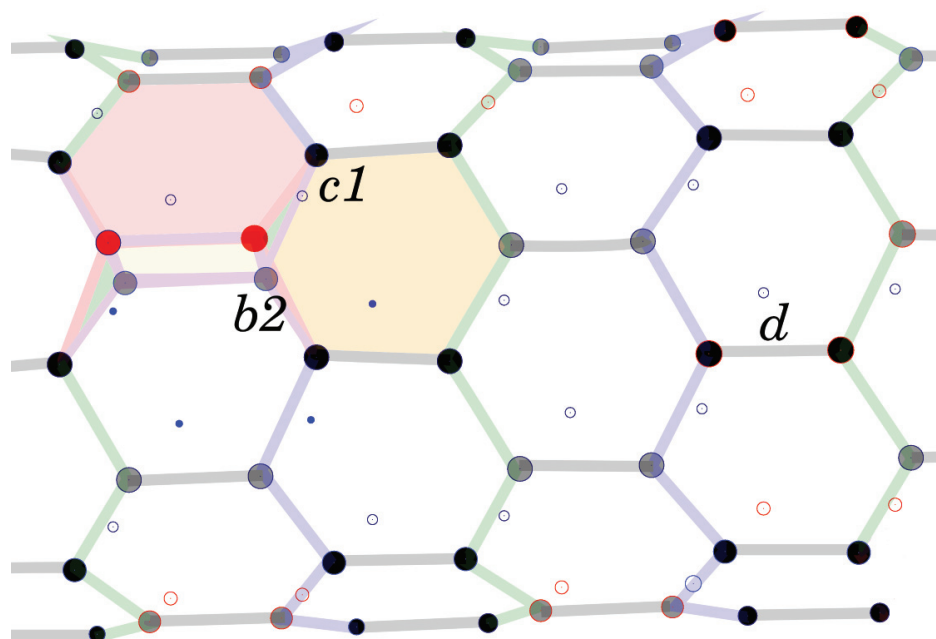


FIG. 2. Ad-dimer's b-grafting, or splitted di-interstitial

3. Atomic structures of grafted dimer

With the use of the same quantum-chemistry tool and the supercell models, optimal (i. e. giving minimal total energy to the model) lattice parameters of graphene and SWNT (8,0) were previously found. Calculated optimal lengths of the longitudinal tube's bond d and of graphene bond are very close, and rather close to the well-known experimental value 1.42 Å. Calculated SWNT (8,0) optimal radius $R = 2.24d$, and zigzag $Z = 0.49d$ (in graphene $Z = d/2$). Initially, the goal supercell was taken with large distance between dimers and the tube, thus the total-energy origin (free dimers and tube), as well as dimer's optimal length, were found. Total energies are given below as dimer-bonding energies in eV/dimer, obtained by formula of cohesive (binding) energy of defect, (*total energy* – *origin*) : 4, since 4 dimers are present in the supercell.

Calculations of the equilibrium (optimal) atomic structures were organized as a repeated search of 1-dimensional minimum of the total energy, taken as a function of a given parameter (length and height of dimer, and shifts of its neighbors). After the optimal value for the chosen parameter had been found, it was fixed, then 1-D minimization was repeated with the next parameter. Each 1-D minimization produces a difference of initial and final total energies, that determines “the cost” of given parameter. Parameters with negligible cost were excluded from optimization, thus the corresponding atoms maintained their positions. At last certain displacements, marked in Figs. 1, 2, with sufficient costs were found. The sequence of their optimization was ordered according to the cost, thus the accelerated the search for equilibrium. The results are gathered in Table 1.

Bonding energies of alternative dimer graftings are the main calculation results. According to the total-energy theory, in 3-D graphite [9, 10], both h- and b-graftings are possible, as having lower energy than independent substrate and dimer, that is also true for SWNT (8,0). But which of them has lower total energy? Our findings show that b-grafting is ~ 0.9 eV/dimer lower than h-grafting. In graphite, this is reversed: h-grafting is lower by ~ 1.4 eV/dimer [9] or ~ 2.0 eV/dimer [10].

4. Electronic structures of grafted dimer

The calculated energy spectra of self-consistent MOs are presented below in the form of observable densities of the occupied (valence-band) electronic states (DOS). Since spectra of our grafted-dimer model cover only 8 k-points of its supercell's k-set, they (spectra) are discrete and need smoothing to be transformed into DOS. Gaussian-type smoothing was used with parameter $\Delta = 0.3$ eV (the magnitude itself is not very important):

TABLE 1. Length, height, and shift along tube's axis are given in d (see Fig. 1). Angle of rotation around tube's axis is given in degrees. Signs refer to the marked representatives of coordination stars in Figs. 1, 2. The origin of height is tube's radius R . Positive shift is to the right. Positive angle is clockwise if looked at from the right

	h-grafting					b-grafting			
	dimer	$a1$	$a2$	$a3$	$b1$	$b2$	dimer	$b2$	$c1$
length	1.016						1.110	1.070	
height	0.606						0.365	-0.715	
shift		-0.086	-0.028	-0.010	+0.016	+0.038			-0.020
angle					-1.9	-1.3			-1.5
energy		-8.7 eV/dimer					-9.6 eV/dimer		

$$\nu(E) = \frac{1}{N} \sum_i^{\text{occ}} \exp \frac{-(E - E_i)^2}{2\Delta^2}, \quad (1)$$

where N is a number of electrons of the supercell; i numerates all MOs despite degeneration; "occ" means summation over occupied MOs. The results are gathered in Fig. 3. It should be mentioned that the energy origin is a "vacuum level" of a free electron at rest. The left portion of Fig. 3 shows the occupied part of MO-spectrum of the pure SWNT (8,0) with 1-, 2-, and 4-fold degenerate states ordered in columns. The left-most DOS curve is an application of (1) to this spectrum.

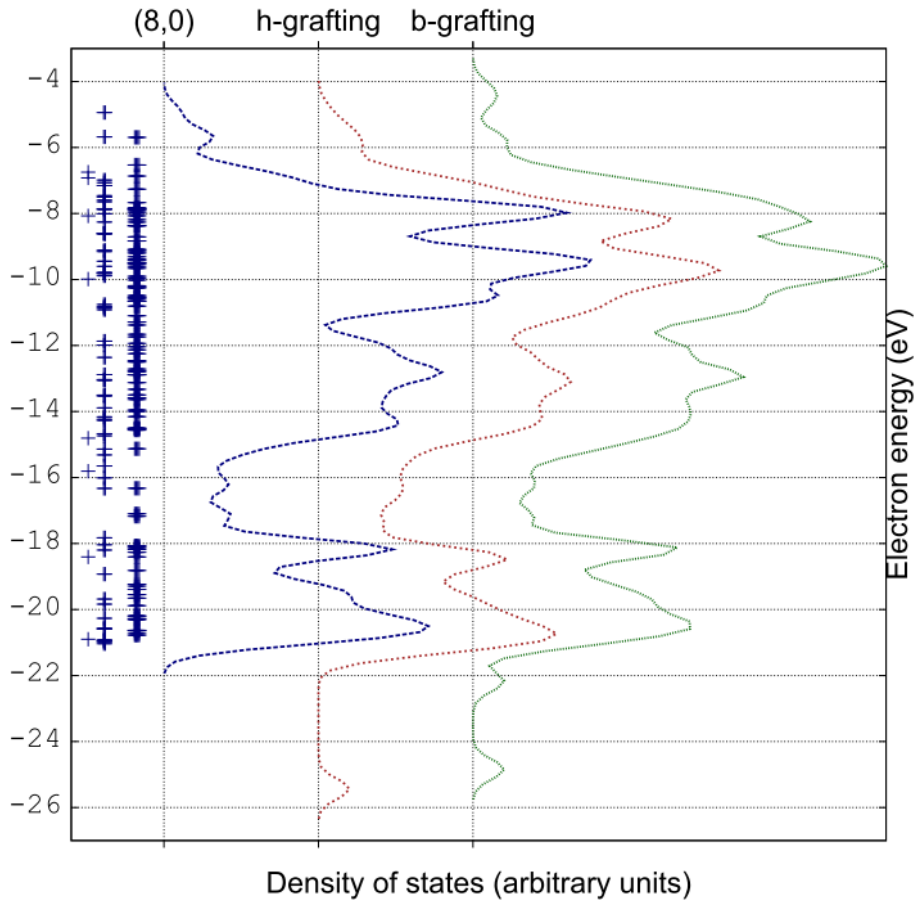


FIG. 3. Densities of occupied states calculated from MO spectra. Origins of three curves are shifted for the sake of comparing: pure SWNT (8,0), tube with h-grafted, and with b-grafted dimer

To extract DOS from measurements is a standard procedure in scanning-tunneling or atomic-force microscopy, in photoelectron emission spectroscopy, and the like. DOS at the top of occupied energy band is analyzed in the first place in order to fix structural changes, for example: incorporation of carbon dimer into a fullerene film [4], or hydrogenation of adsorbed molecules in STM [5]. Fig. 3 demonstrates DOS changes of this kind in $(-4, -6)$ eV band, where pure tube, as well as the tube with grafted dimer in both forms, do have distinct DOS features. Thus, dimer grafting can be identified indirectly, for instance, if b-grafted species looks in STM like the bond, which it splits down.

Electronic density $n(x, y, z)$ is another observable that can be calculated from occupied MOs. There are two ways to present this function of 3 arguments by a single drawing. Either one draws a 3-dimensional iso-surface, or a 2-dimensional (plain) map of iso-contours. The latter method demands simple graphical applications, so Fig. 4 is one of iso-contour maps that exhibits electronic density of the tube with b-grafted dimer. The plane of the map cuts the tube vertically and passes close to three points (see Fig. 2): one atom of dimer (the topmost), the nearest to it atom of the split bond $b2$ (inside the tube), and the nearest to them “ligand” atom of the tube $c1$. This plane was selected to display the covalent nature of b-grafting, whose structure resembles a chemical complex with a 4-member cycle as a center. Besides, it gives the same aspect of the tube’s bond before (bottom segment) and after splitting (top segment).

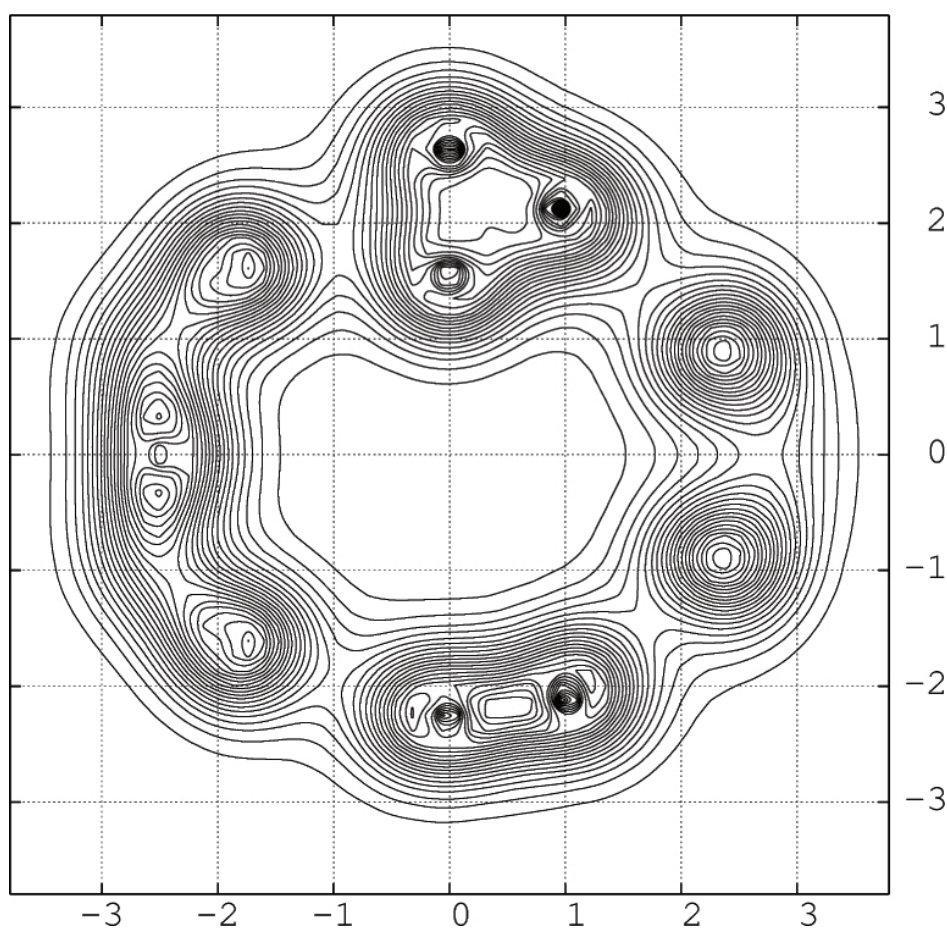


FIG. 4. Electron-density map of b-grafted dimer. The map’s plane passes through 3-member cycle (see Fig. 2): atom of dimer – atom $b2$ of the split bond – “ligand” atom $c1$

Other maps of electronic densities also assure the covalent character of the grafted dimer. 5- and 7-membered flexed cycles of h-grafting colored in Fig. 1, as well as 4-membered “central”, and 6-member flexed “ligand-center” cycles of b-grafting colored in Fig. 2, all them appear on electron-density maps as combinations of σ - and π -bonds. For example, the topochemical prediction of ISW in graphene is also true for h-grafting, though equilibrium height of ad-dimer, $\sim 0.6d$ above tube’s surface, makes 5- and 7-member cycles strongly flexed. If compared to other maps, the 3-member cycle of Fig. 4 could be called “cycle” in geometrical sense only, the electronic thickening around it corresponds to the covalent ligand-center bonding.

5. Discussion

To obtain good agreement with experimental data (not available for ad-dimer recently) may require calculations of a higher level than those presented above. However, quantum-chemistry results cover not only total energies and geometrical parameters (Table 1), which usually are rather difficult experimental goals. The present calculated energetical (Fig. 3) and spatial (Fig. 4) electron densities are complementary observables, which relate directly to experiment [4, 5].

One more argument pro the covalent character of ad-dimer incorporation into the tube may be found in the well-known feature of quantum chemistry called “atomic charges”. It is a standard output indicator of MO LCAO that shows the fraction (in sense of probability) of atomic orbitals of the given atom in occupied molecular orbitals. Small atomic charges support covalent bonding. Maximal absolute value of all atomic charges was < 0.2 for h-grafting, and < 0.1 for b-grafting (in atomic units).

At last it should be noted that the ad-dimer must overcome van-der-Waals barrier, before being covalently bonded (grafted) by the tube. This side of the problem is not addressed at all by our calculations at a semi-empirical level. Implementing certain corrections makes sense at the ab-initio level [10]. Therefore, the semi-empirical results (e. g. Table 1) are just a prelude to analysis and planning of experiment. Which form of grafting will take place depends on many circumstances of tube’s environment in future experiments.

6. Conclusion

Quantum-chemistry modeling of the carbon dimer chemisorption at carbon nanotube shows, that stereo-chemical assumption about covalent incorporation of dimer into graphene net is only sufficient for qualitative predictions. Previous calculations, guided by such assumption, had been performed for the topochemical inverse Stone–Wales grafting of ad-dimer at graphene and nanotubes. But alternative grafting, split di-interstitial, has not any simple stereo-chemical support, and was not studied before in the case of nanotubes. The calculations, presented above, were made for both kinds of ad-dimer grafting at the small-diameter SWNT (8, 0). The result is: total energy of b-grafting (split di-interstitial) is on ~ 0.9 eV/dimer lower than of h-grafting (inverse SW).

The electronic structures of both graftings are of the covalent type, though b-grafting with flexed, split, and nested 6-membered cycles is more like a chemical complex with a 4-member cycle as a center. In both cases, the ad-dimer is placed above tube’s surface, so terms “grafting” and “chemisorption” are fair. In h-grafting, the ad-dimer stays at $\sim 0.6d$ above tube’s surface (where d is the length of longitudinal CC bond), that could be called a chemisorption at the hexagon center, if its bonding energy was unknown. In b-grafting, the ad-dimers height is $\sim 0.4d$ above the tube’s surface, with the splitted bond at $\sim 0.7d$ under the tube’s surface.

References

- [1] Banhart F., Kotakoski J., Krasheninnikov A.V. Structural defects in graphene. *ACS Nano*, 2011, **5** (1), P. 26–41.
- [2] Orlikowski D., Buongiorno Nardelli M., Bernholc J., Roland C. Ad-dimer on strained carbon nanotubes: a new route for quantum dot formation? *Phys. Rev. Lett.*, 1999, **83** (20), P. 4132–4135.
- [3] Orlikowski D., Buongiorno Nardelli M., Bernholc J., Roland C. Theoretical STM signatures and transport properties of native defects in carbon nanotubes. *Phys. Rev. B*, 2000, **61** (20), P. 14194–14203.
- [4] Ulas S., Strelnikov D., et al. Incorporating C₂ into C₆₀ films. *J. Chem. Phys.*, 2012, **136** (1), 014701 (12).
- [5] Katano S., Kim Y., et al. Reversible control of hydrogenation of a single molecule. *Science*, 2007, **316** (5833), P. 1883–1886.
- [6] Sternberg M., Curtiss L.A., et al. Carbon ad-dimer defects in carbon nanotubes. *Phys. Rev. Lett.*, 2006, **96** (7), 075506 (4).
- [7] Lusk M.T., Carr L.D. Nanoengineering defect structures on graphene. *Phys. Rev. Lett.*, 2008, **100** (17), 175503 (4).
- [8] Iwata T., Watanabe M. Increase in specific heat and possible hindered rotation of interstitial C₂ molecules in neutron-irradiated graphite. *Phys. Rev. B*, 2010, **81** (1), 014105 (14).
- [9] Latham C.D., Heggie M.I., et al. The di-interstitial in graphite. *J. Phys.: Condens. Matter*, 2008, **20** (39), 395220 (8).
- [10] Teobaldi G., Tanimura K., Shluger A.L. Structure and properties of surface and subsurface defects in graphite accounting for van der Waals and spin-polarization effects. *Phys. Rev. B*, 2010, **82** (17), 174104 (14).
- [11] Moliver S.S. Stone–Wales defect generation in carbon nanotube being fractured. *Fullerenes, Nanotubes, and Carbon Nanostructures*, 2012, **20** (4–7), P. 531–537.

Peculiarities of LaFeO₃ nanocrystals formation via glycine-nitrate combustion

A. Bachina^{1,2}, V. A. Ivanov¹, V. I. Popkov^{1,2}

¹Saint Petersburg State Technological Institute (Technical University),
Moskovskiy 26, St. Petersburg, 190013, Russia

²Ioffe Institute, Russian Academy of Sciences,
Politekhnikeskaya 26, St. Petersburg, 194021 Russia
a.k.bachina@gmail.com

PACS 81.07.-b

DOI 10.17586/2220-8054-2017-8-5-647-653

Varying glycine to nitrate ratio in the initial solution the powders based on nanocrystalline LaFeO₃ were synthesized by solution combustion synthesis. The powders were studied by X-ray diffractometry, scanning electron microscopy, adsorption analysis and helium pycnometry. The average crystallite size of the synthesized LaFeO₃ nanocrystals ranged from 18±2 to 85±9 nm, and the specific surface area of the nanopowders based on them ranged from 8 to 33 m²/g. Based on the results, the influence of redox composition of the reaction solution on the nature of the combustion processes, as well as the composition, structure and properties of LaFeO₃ nanocrystals were analyzed. Here, it was shown, that the nanopowders have specific microstructure in terms of monocrystalline nanoscale layers of lanthanum orthoferrite, therefore it is allowed to consider them as a promising base for catalytically and magnetically functional materials.

Keywords: lanthanum orthoferrite, glycine-nitrate combustion, nanocrystals, formation mechanism, XRD, SEM.

Received: 15 September 2017

Revised: 9 October 2017

1. Introduction

Lanthanum orthoferrite is one of the rare-earth orthoferrites which has perovskite-like structure and crystallizes within the orthorhombic crystal system (*Pbnm* space group) [1]. Lanthanum orthoferrite, due to its wide prevalence in comparison with other rare-earth elements (REE) and its particular property set, is the basis for many functional materials applied in catalysis, solid-oxide fuel cells, chemical sensors, magnetic and electrode devices etc. [2–9]. Lately, materials based on LaFeO₃ are also considered as promising materials to obtain hydrogen by the photocatalytic decomposition of water under visible light irradiation [10–12]. In this case, the efficiency and the rate of H₂ generation are defined by the value of a specific surface area of photocatalyst and therefore the use of nanoscale lanthanum orthoferrite powders can be more advantageous relative to coarse-crystalline ones.

Nanocrystals of lanthanum orthoferrite and other rare-earth orthoferrites are conventionally obtained by soft chemistry methods: sol-gel synthesis [13, 14], hydrothermal synthesis [15–17], thermal treatment of precursors with different chemical composition [18, 19] and others [20]. In the most cases, the crystallite size and the specific surface area of successfully obtained LaFeO₃ nanocrystals are about 50 nm and 10 m²/g, correspondingly. However, to use materials based on lanthanum orthoferrite in real photocatalytic processes the value of crystallite size should be rather smaller.

Recently, the solution combustion method has been actively developed to obtain nanocrystalline oxides. The method is based on redox reaction, which occurs during the thermal treatment of solutions containing the respective metal nitrates and an organic reducing agent, for example, glycine, citric acid, urea, etc. The reaction is accompanied by enormous heat release which supports the process autonomously after combustion initiation by an external heating source. As a rule, the result of the reaction is the formation of single-phase oxide nanopowders with a high specific surface area and small crystallite size. Thus, application of this synthesis approach seems to be highly reasonable and promising.

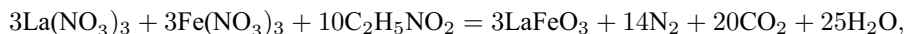
However, since the formation of the nanocrystalline oxides under the described conditions is a rather complicated combination of physical-chemical processes, the particular properties of nanopowders, in general, depend on different factors including the composition of a reaction mixture, material and shape of a reactor, composition of media, under which the synthesis occurs, etc. The most important factor among them is the redox composition of the initial solution, which was previously shown [21–23] to define the combustion conditions and temperature in the reaction zone. Despite much research [10, 24, 25] being focused on obtaining lanthanum orthoferrite by solution combustion synthesis, the influence of redox composition on processes of LaFeO₃ nanocrystal formation has not been studied in detail. Thus, the theoretical and practical goals of the present paper are the investigation of the

influence of redox composition on LaFeO_3 formation and synthesis of lanthanum orthoferrite nanopowders with a high specific surface area.

2. Experimental

2.1. Materials synthesis

The compositions based on LaFeO_3 were prepared by the solution combustion synthesis. The details of synthesis procedure have been previously described [26]. As starting materials, lanthanum and iron nitrates and glycine were used. All starting materials were analytic-grade purity. Lanthanum and iron nitrates were taken in a stoichiometric ratio according to the following reaction:



while the amount of glycine was varied towards to the total amount of nitrates (G/N) from 0.1 to 1.4. G/N ratio was calculated as follows:

$$G/N = \frac{n_{gly}}{n'_{\text{NO}_3^-} + n''_{\text{NO}_3^-}},$$

where n_{gly} – moles of glycine, $n'_{\text{NO}_3^-}$ and $n''_{\text{NO}_3^-}$ – moles of lanthanum and iron nitrates, correspondingly. Nitrates of iron and lanthanum and glycine were dissolved in distilled water under a vigorous stirring. Then, the solution was heated until water evaporation that caused the transition of solution into gel followed by its spontaneous ignition. The product of glycine-nitrate synthesis is foam-like substance, which becomes a brown powder after milling in a mortar.

2.2. Materials characterization

The prepared samples were characterized by the following techniques. Powder X-ray diffraction (PXRD) performed on a Rigaku SmartLab 3 diffractometer was used to identify the crystalline phases and estimate the average crystallite size and the crystallite size distribution. The Scherrer equation was used for crystallite size calculation. The fundamental parameters approach, which is implemented in standard Rigaku software supplied to the diffractometer, was used to find the crystallite size distribution. Scanning electron microscopy (SEM) with energy dispersive X-ray analysis (EDX) performed on a Tescan Vega 3 microscope was employed to characterize morphology and elemental composition. The specific surface area was measured by Brunauer–Emmett–Teller (BET) method using N_2 as adsorbed gas on an Micromeritics ASAP 2020 instrument. The density of the samples was determined with a helium pycnometer (Micromeritics AccuPyc 1330). The thickness of interpore partition was calculated from pycnometric density and specific surface area data in an approximation of an infinite plate of finite thickness [27,28] according to the following formula:

$$h = \frac{2}{S \cdot \rho},$$

where h – average interpore partition, S – specific surface area and ρ – density of the sample.

3. Results and discussion

According to EDX analysis, the lanthanum to iron ratio in all obtained powders answers to 1:1 ratio given by synthesis procedure within the method error. The phase composition of the powders evaluated from PXRD drastically differed, depending on G/N ratio. For instance, when the starting solution contains considerable excess or shortage of glycine ($G/N = 1.2, 1.4$ or $G/N = 0.1, 0.2$) the final solid products are completely or almost amorphous (Fig. 1). In the case of G/N ratio lying in between these edge points the crystalline phase of LaFeO_3 with orthorhombic structure is predominantly found in the final solid products (Fig. 1). Phase analysis is presented in details in Fig. 2(a). The data demonstrate that as G/N ratio comes closer to the stoichiometric point ($G/N = 0.6$) the amount of amorphous phase decreases to zero. It is worth noting that at $G/N = 0.2$, in addition to the amorphous phase, a trace amount of $\text{La}(\text{OH})_2\text{NO}_3$ crystalline phase is present. In the similar system based on YFeO_3 , the impurities of nitrate derivatives of REE were also found in the powders obtained by glycine-nitrate synthesis at non-stoichiometric G/N ratios, but their crystallization did not occur during combustion [29]. In the case of LaFeO_3 system, the formation of $\text{La}(\text{OH})_2\text{NO}_3$ is probably explained by a higher temperature in the reaction zone in comparison to that which can be implemented during synthesis in the YFeO_3 system. The higher temperature, in turn, can be rationalized to be due to the catalytic effect of the formed LaFeO_3 on the combustion process which leads to an acceleration of energy release and even when G/N ratio is far from stoichiometric, sufficient temperatures are reached in the system to cause the crystallization of lanthanum nitrate derivatives.

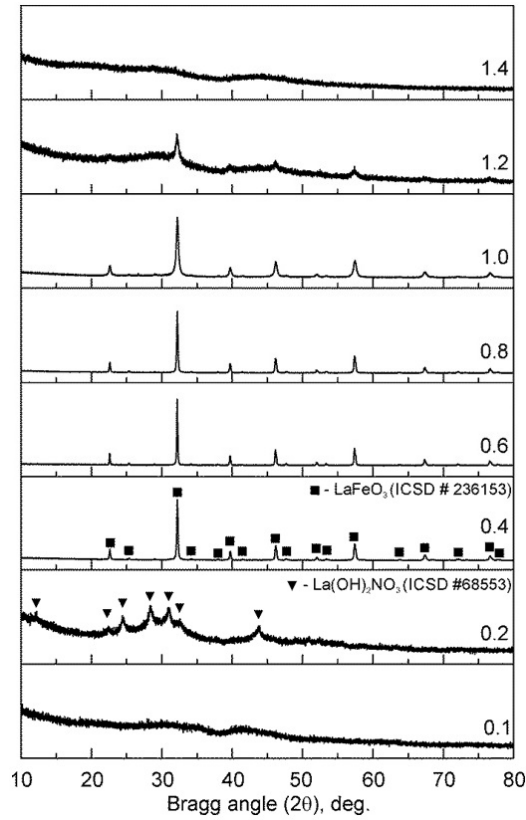


FIG. 1. X-ray diffraction patterns of products of LaFeO_3 glycine-nitrate synthesis obtained at different G/N ratios

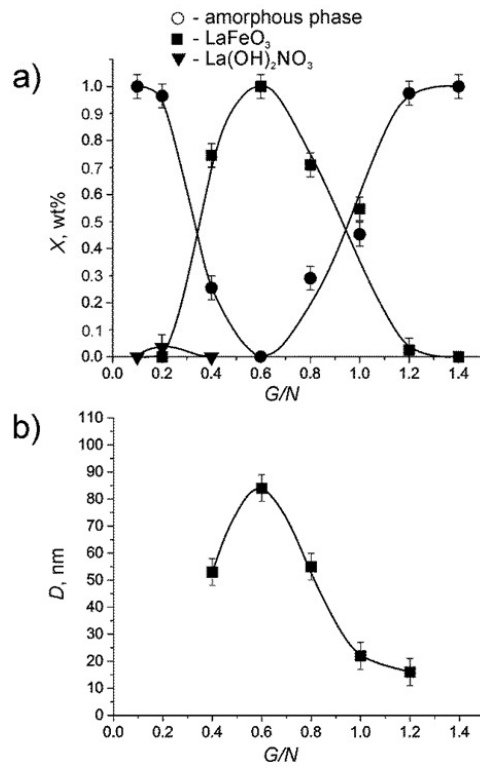


FIG. 2. Phase composition of glycine-nitrate synthesis products (a) and LaFeO_3 average crystal-size (b) depending on G/N ratio

The typical dependence of phase composition on G/N ratio (Fig. 2(a)), as was previously shown for the similar system [21], is connected with the dependence of temperature on this parameter. The temperature in the reaction zone is considered to be maximum at the stoichiometric point and decreases both towards the excess and the shortage of glycine. Therefore the most stable and defect-free crystalline phases are conventionally formed at the stoichiometric G/N ratio.

This trend is also noted in the dependence of the average crystallite size on the G/N ratio (Fig. 2), as far as at the stoichiometric point it usually reaches the maximum value and in the considered system the value is about 85 nm. For comparison, the average crystallite size reaches only about 50 nm in the $YFeO_3$ system. This considerable difference can also be explained by the catalytic activity of $LaFeO_3$ and higher temperature that intensify the recrystallization processes in the reaction zone and leads to the growth of the lanthanum orthoferrite nanocrystals. In other respects, the dependence of the average crystallite size on glycine-nitrate ratio repeats those known for other systems [21,26]. The samples obtained at G/N ratio of 0.4 and 0.8 have almost the same average crystallite size of about 55 nm. The powder with the smallest average crystallite size of about 20 nm and mostly consisting of crystalline $LaFeO_3$ was obtained at $G/N = 1.0$. At the same time, this sample is characterized by the narrowest shape of crystallite size distribution among other samples and the size of crystallite majority lies in the range of 10 – 35 nm (Fig. 3). The broadest crystallite size distribution, as it was expected, belongs to the sample obtained at stoichiometric G/N ratio and its crystallite size is varied from 50 to 110 nm. The sample obtained at $G/N = 1.2$ despite on the smallest size of crystallites is excluded from consideration as it contains an only trace amount of $LaFeO_3$. Thus, from a practical point of view, the lanthanum orthoferrite nanocrystals obtained at $G/N = 1.0$ are the most interesting since they have the smallest crystallite size and the narrowest crystallite size distribution among the whole set of samples, what meets important requirements for nanopowders using as a basis for magnetic and electric materials [4,5].

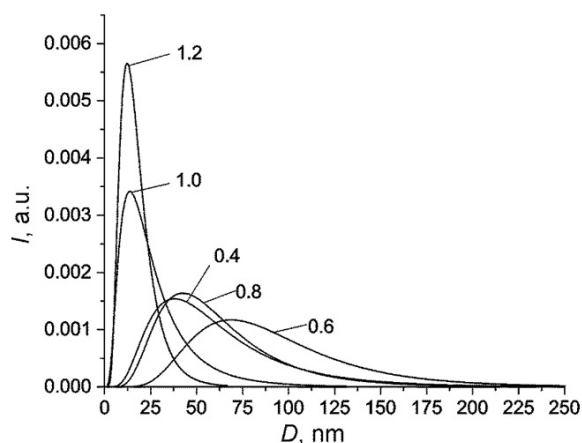


FIG. 3. Size distribution of $LaFeO_3$ nanocrystals obtained at different G/N ratios

Another practically important parameter of the obtained $LaFeO_3$ nanocrystals and compositions on their basis is the specific surface area. The results of measurements of the specific surface area are shown in Fig. 4(a). According to the shown data, the samples synthesized at a glycine-nitrate ratio close to the stoichiometric point ($G/N = 0.4 - 0.8$) have a relatively low specific surface area of about $10 \text{ m}^2/\text{g}$, which agrees with data reported previously [10,24]. At G/N below 0.4, a drastic decrease of the specific surface area to $0.5 \text{ m}^2/\text{g}$ ($G/N = 0.1$) is observed, which is related to the replacement of the bulk combustion mode inherent to the stoichiometric reaction by the smoldering mode. The smoldering mode is characterized by relatively low temperatures in the reaction zone and low reaction rate that promotes the formation of several by-products ($La(OH)_2NO_3$ and others) in the reaction and a poorly developed surface for the products. On the contrary, as G/N ratio exceeds stoichiometric value a dramatic increase of specific surface area to $33 \text{ m}^2/\text{g}$ is observed ($G/N = 1.0$), which can be explained by an increase of waste gases and maintaining enough high temperature at the same time. Thus, it was shown the possibility to increase the specific surface area of nanocrystalline $LaFeO_3$ by facile varying of redox composition of the initial solution, which was previously reached only by additional modification of glycine-nitrate synthesis [25]. Helium pycnometry data provide evidence for the high purity of obtained lanthanum orthoferrite nanocrystals, as the value of the pycnometric density of samples synthesized at $G/N = 0.4 - 1.0$ almost matches with the X-ray density ($\rho_{LaFeO_3}^{XRD} = 7.081 \text{ g/cm}^3$) of orthorhombic $LaFeO_3$ (Fig. 4(b)). However, as in the case of excess of

nitrate ($G/N < 0.4$), so in the case of their deficiency ($G/N > 1.0$) in the reaction mixture, the by-products of redox reaction such as nitrate and carbonate derivatives of iron and lanthanum reduce the pycnometric densities of the samples. The agreement between the average crystallite size of LaFeO₃ and the average thickness of interpore partition of foam-like samples (Fig. 5) within the limits of experimental error for the broad G/N range of 0.4 – 1.0 (Fig. 2(b) and Fig. 4(c)), as well as similar shape of dependence of these values on G/N argue that interpore partition is formed by layers of LaFeO₃ nanocrystals and thickness of the layers is comparable with the average crystallite size. Herewith, according to SEM data (Fig. 5), the morphology and the microstructure parameters of the glycine-nitrate synthesis products corroborate conclusions stated above about the influence of the glycine-nitrate ratio on the formation of nanocrystalline LaFeO₃. Thus, the sample obtained at $G/N = 0.1$ (Fig. 5(a)) is a dense low-porosity substance of micron size, which has an extremely low specific surface area and a large thickness of interpore partition. While the sample obtained at stoichiometric G/N ratio (Fig. 5(b)) already has rather developed porosity structure, but the thickness of interpore partition is still large enough (~ 100 nm). As opposed to the previous cases, synthesis at a G/N ratio = 1.0 leads to the formation of the sample with the most developed porosity and surface (Fig. 5(c)), the major bulk of which is formed by LaFeO₃ nanocrystals with the size of 20–25 nm. This peculiar structure of the product of glycine-nitrate synthesis – nanocrystals of lanthanum orthoferrite – allows one to suppose the successful application of materials based on the nanocrystals for photocatalysis. The assumption seems to be especially reasonable since successful results have been obtained elsewhere [11]. Finally, at $G/N = 1.4$ (Fig. 5(d)), i.e. in a large excess of glycine, the sample obtained was of micron size and with high porosity and specific surface. However, a considerable part of the sample consists of combustion by-products (mainly carbonate derivatives of iron and lanthanum), which was confirmed by the extremely low pycnometric density and the great fraction of the amorphous phase in the composition.

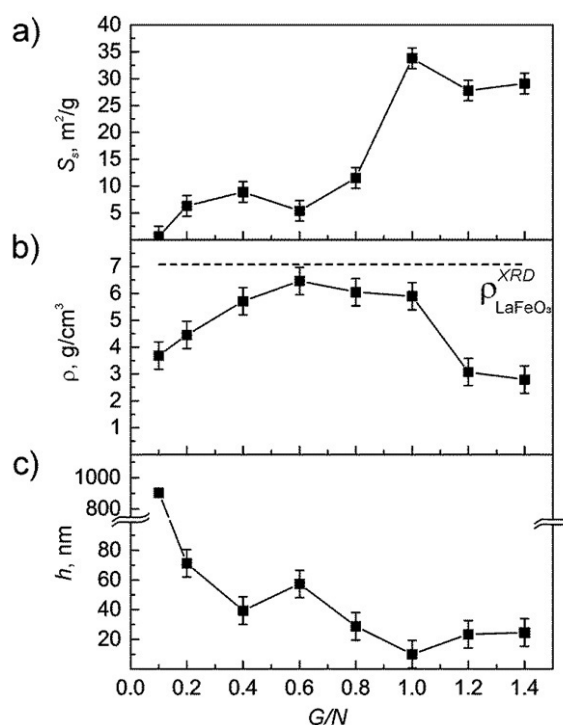


FIG. 4. Specific surface S_s (a), pycnometric density ρ (b) and thickness of interpore partition h (c) of glycine-nitrate combustion products depending on G/N ratio. Dashed line – X-ray density of orthorhombic LaFeO₃, equal to 7.081 g/cm³

Thus, in this paper, the possibility of nanocrystalline lanthanum orthoferrite synthesis from glycine and nitrate precursors was demonstrated. Additionally, it was also shown that by varying the glycine-nitrate composition of the initial solution, one can vary the selected properties of the obtained nanocrystals. Samples were obtained based on LaFeO₃ nanocrystals with different microstructure and the average crystallite size, ranging from 18 ± 2 to 85 ± 9 nm, which provided nanopowders with specific surface area values ranging from 8 – 33 m²/g. It was established that in the broad range of G/N ratio 0.4 – 1.0, high-porosity samples are mainly formed by nano-scale

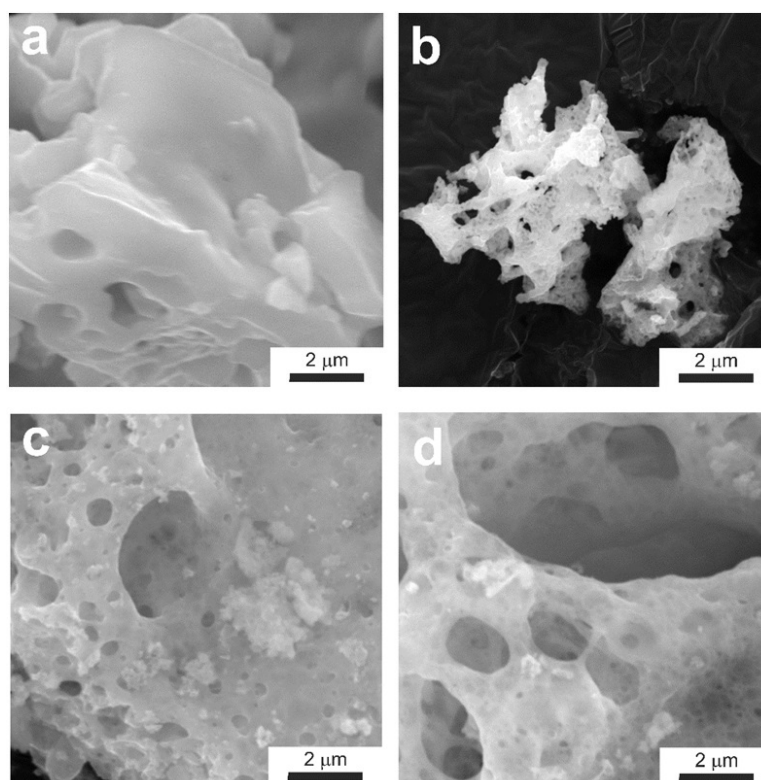


FIG. 5. SEM images of glycine-nitrate combustion products obtained at 0.1 (a), 0.6 (b), 1.0 (c) and 1.4 (d) G/N ratio

single crystal layers of LaFeO_3 , the thickness of which is comparable with the average crystallite size, making these nanocrystalline powders promising candidates for catalytic materials.

Acknowledgments

The reported study was funded by RFBR, according to the research Project No. 16-33-00345. The powder X-ray diffraction and SEM studies were performed on equipment of the Engineering Center of the Saint-Petersburg State Technological Institute (Technical University).

References

- [1] Pavlovska O.B., Vasylechko, Lutsyuk I. V., Koval N.M., Zhydachevskii Y.A., Pieniżek A. Structure Peculiarities of Micro- and Nanocrystalline Perovskite Ferrites $\text{La}_{1-x}\text{Sm}_x\text{FeO}_3$. *Nanoscale Res. Lett.*, 2017, **12**, P. 153–159.
- [2] Ciambelli P., Cimino S., De Rossi S., Lisi L., Minelli G., Porta P., Russo G. AFeO_3 (A=La, Nd, Sm) and $\text{LaFe}_{1-x}\text{Mg}_x\text{O}_3$ perovskites as methane combustion and CO oxidation catalysts: structural, redox and catalytic properties. *Appl. Catal. B: Environ.*, 2001, **29**(4), P. 239–250.
- [3] Wang J., Liu Q., Xue D., Li F. Synthesis and characterization of LaFeO_3 nano particles. *J. Mater. Sci. Lett.*, 2002, **21**(13), P. 1059–1062.
- [4] Rajendran M., Bhattacharya A.K. Nanocrystalline orthoferrite powders: Synthesis and magnetic properties. *J. Eur. Ceram. Soc.*, 2006, **26**(16), P. 3675–3679.
- [5] Khetre S.M., Jadhav H.V., Jagadale P.N., Kulal S.R., Bamane S.R. Studies on electrical and dielectric properties of LaFeO_3 . *Adv. Appl. Sci. Res.*, 2011, **2**(4), P. 503–511.
- [6] Markova-Velichkova M., Lazarova T., Tumbalev V., Ivanov G., Kovacheva D., Stefanov P., Naydenov A. Complete oxidation of hydrocarbons on YFeO_3 and LaFeO_3 catalysts. *Chem. Eng. J.*, 2013, **231**, P. 236–244.
- [7] Lomanova N.A., Pleshakov I.V., Volkov M.P., Gusarov V.V. Magnetic properties of Aurivillius phases $\text{Bi}_{m+1}\text{Fe}_{m-3}\text{Ti}_3\text{O}_{3m+3}$ with $m=5.5, 7, 8$. *Mater. Sci. Eng. B.*, 2016, **214**, P. 51–56.
- [8] Popkov V.I., Almjashcheva O.V., Semenova A.S., Kellerman D.G., Nevedomskiy V.N., Gusarov V.V. Magnetic properties of YFeO_3 nanocrystals obtained by different soft-chemical methods. *J. Mater. Sci. Mater. Electron.*, 2017, **28**(10), P. 7163–7170.
- [9] Nguyen A.T., Nguyen T.D., Mittova V.O., Berezhnaya M.V., Mittova I.Y. Phase composition and magnetic properties of $\text{Ni}_{1-x}\text{Co}_x\text{Fe}_2\text{O}_4$ nanocrystals with spinel structure, synthesized by Co-precipitation. *Nanosyst. Physics, Chem. Math.*, 2017, **8**(3), P. 371–377.
- [10] Parida K.M., Reddy K.H., Martha S., Das D.P., Biswal N. Fabrication of nanocrystalline LaFeO_3 : An efficient sol-gel auto-combustion assisted visible light responsive photocatalyst for water decomposition. *Int. J. Hydrogen Energy.*, 2010, **35**(22), P. 12161–12168.
- [11] Acharya S., Padhi D.K., Parida K.M. Visible light driven LaFeO_3 nano sphere/RGO composite photocatalysts for efficient water decomposition reaction. *Catal. Today.*, 2017, P. 1–12.

- [12] Iervolino G., Vaiano V., Sannino D., Rizzo L., Palma V. Enhanced photocatalytic hydrogen production from glucose aqueous matrices on Ru-doped LaFeO₃. *Appl. Catal. B Environ.*, 2017, **207**, P. 182–194.
- [13] Tien N.A., Mittova I.Y., Almjasheva O.V., Kirillova S.A., Gusarov V.V. Influence of the preparation conditions on the size and morphology of nanocrystalline lanthanum orthoferrite. *Glas. Phys. Chem.*, 2008, **34**, P. 756–761.
- [14] Van Tac D., Mittova V.O., Mittova I.Y. Influence of Lanthanum Content and Annealing Temperature on the Size and Magnetic Properties of Sol – Gel Derived Y_{1-x}La_xFeO₃ Nanocrystals. *Inorg. Mater.*, 2011, **47**(5), P. 590–595.
- [15] Zheng W., Liu R., Peng D., Meng G. Hydrothermal synthesis of LaFeO₃ under carbonate-containing medium. *Mater. Lett.*, 2000, **43**(1-2), P. 19–22.
- [16] Ji K., Dai H., Deng J., Song L., Xie S., Han W. Glucose-assisted hydrothermal preparation and catalytic performance of porous LaFeO₃ for toluene combustion. *J. Solid State Chem.*, 2013, **199**, P. 164–170.
- [17] Tugova E.A., Karpov O.N. Nanocrystalline perovskite-like oxides formation in Ln₂O₃-Fe₂O₃-H₂O (Ln = La, Gd) systems. *Nanosyst.: Physics, Chem. Math.*, 2014, **5**(6), P. 854–860.
- [18] Nguyen A.T., Knurova M.V., Nguyen T.M., Mittova V.O., Mittova I.Y. Synthesis and the study of magnetic characteristic of nano La_{1-x}Sr_xFeO₃ by co-precipitation method. *Nanosyst.: Physics, Chem. Math.*, 2014, **5**(5), P. 692–702.
- [19] Cherepanov V.A., Gavrilova L.Y., Volkova N.E., Urusov A.S., Aksenova T.V., Kiselev E. Phase equilibria and thermodynamic properties of oxide systems on the basis of rare earth, alkaline earth and 3d-transition (Mn, Fe, Co) metals. A short overview of, *Chim. Techno Acta.*, 2015, **2**(4), P. 273–305.
- [20] Wang J., Dong X., Qu Z., Liu G., Yu W. Electrospinning Preparation of LaFeO₃ Nanofibers, *Mod. Appl. Sci.*, 2009, **3**(9), P. 65–71.
- [21] Popkov V.I., Almjasheva O.V. Yttrium orthoferrite YFeO₃ nanopowders formation under glycine-nitrate combustion conditions. *Russ. J. Appl. Chem.*, 2014, **87**(2), P. 167–171.
- [22] Varma A., Mukasyan A.S., Rogachev A.S., Manukyan K.V. Solution Combustion Synthesis of Nanoscale Materials. *Chem. Rev.*, 2016, **116**(23), P. 14493–14586.
- [23] Khaliullin S.M., Zhuravlev V.D., Bamburov V.G. Solution-combustion synthesis of oxide nanoparticles from nitrate solutions containing glycine and urea: Thermodynamic aspects. *Int. J. Self-Propagating High-Temperature Synth.*, 2016, **25**(3), P. 139–148.
- [24] Kondakindi R.R., Karan K., Peppley B.A. A simple and efficient preparation of LaFeO₃ nanopowders by glycine-nitrate process: Effect of glycine concentration. *Ceram. Int.*, 2012, **38**(1), P. 449–456.
- [25] Komova O.V., Simagina V.I., Mukha S.A., Netskina O.V., Odegova G.V., Bulavchenko O.A., Ishchenko A.V., Pochtar' A.A. A modified glycine-nitrate combustion method for one-step synthesis of LaFeO₃. *Adv. Powder Technol.*, 2016, **27**(2), P. 496–503.
- [26] Zaboeva E.A., Izotova S.G., Popkov V.I. Glycine-nitrate combustion synthesis of CeFeO₃-based nanocrystalline powders. *Russ. J. Appl. Chem.*, 2016, **89**(8), P. 1228–1236.
- [27] Popkov V.I., Almjasheva O.V., Nevedomskiy V.N., Sokolov V.V., Gusarov V.V. Crystallization behavior and morphological features of YFeO₃ nanocrystallites obtained by glycine-nitrate combustion, *Nanosyst.: Physics, Chem. Math.*, 2015, **6**(6), P. 866–874.
- [28] Popkov V.I., Almjasheva O.V., Schmidt M.P., Izotova S.G., Gusarov V.V. Features of nanosized YFeO₃ formation under heat treatment of glycine-nitrate combustion products *Russ. J. Inorg. Chem.*, 2015, **60**(10), P. 1193–1198.
- [29] Wang X.J., Shen H.Y., Tian H.Y., Yang Q.H. Photocatalytic Degradation of Water-Soluble Azo Dyes by LaFeO₃ and YFeO₃. *Adv. Mater. Res.*, 2012, **465**, P. 37–43.

Nonlinear optical and quanta-dimensional effects in monoselenide of gallium and indium

A. G. Kyazim-zade¹, V. M. Salmanov¹, A. G. Huseynov¹, R. M. Mamedov¹,
A. A. Salmanova², F. Sh. Ahmedova¹

¹Baku State University, Z. Khalilov str. 23, AZ-1148, Baku, Azerbaijan

²Azerbaijan State University of Oil and Industry, 20 Azadliq ave., AZ-1010, Baku, Azerbaijan

vagif.salmanov@yahoo.com

PACS 71.55.Gs, 78.20.-e, 85.30.-z, 85.60.Dw

DOI 10.17586/2220-8054-2017-8-5-654-660

Nonlinear light absorption and its time evolution at high optical excitation levels in GaSe and InSe layered crystals have been experimentally investigated. It is shown that the nonlinear absorption observed in InSe in the region of exciton resonance is due to the exciton-exciton interaction. The effect of filling the zones detected in GaSe at high excitation intensities leads to a change in the absorption coefficient and the refractive index. For InSe nanoparticles obtained by the chemical deposition method, a quanta-dimensional effect was observed; the width of the forbidden band was dependent upon the dimensions of the nanoparticles.

Keywords: nonlinear absorption, GaSe, InSe, bandfilling effect, nanoparticles.

Received: 20 September 2017

Revised: 6 October 2017

1. Introduction

In semiconductors, photogenerated electron-hole pairs rapidly thermalize and relax into levels close to the band gap. Direct electron-hole pairs normally have a short recombination lifetime which, thus at low crystal lattice temperatures T_l , thermalization with the crystal lattice is not allowed. Thus, the temperature T_e of the electron-hole pairs is usually higher than T_l . Therefore, they will not only occupy bound states (excitons) which have the lowest energies, but also higher dissociated states (ionized excitons). The electron-hole pairs' density can be easily raised by increasing the photoexcitation intensity. A high electron-hole pair density will screen the Coulomb interaction between electrons and holes. For very strong screening, no bound electron-hole pair states exist [1, 2]. Thus, at low temperatures and with increasing pair density, the electron-hole fluid turns from an insulating gas of mostly bound electron-hole pairs or excitons into a metallic plasma of dissociated pairs. This phase transition is called the Mott transition of the excitons [3], even though the carriers are not at zero temperature.

GaSe and InSe crystals belonging to III-V compounds have received considerable attention recently as an interesting class of nonlinear optical materials. Possessing layered structure, high polarizability, optical homogeneity and naturally mirror-like surfaces, a number of nonlinear optical phenomena such as harmonic generation [4, 5], parametric light generation [6, 7], electron-hole plasma [8–12] and stimulated emission in the visible and terahertz region [13–19], etc., have been observed in these crystals.

Investigations of dimensional quantum phenomena in these semiconductors open up great prospects for constructing on their basis new devices with a wide range of functional capabilities. Scientists have established that the ultrathin nanosilic indium and gallium monoselenides have unique properties that qualitatively distinguish them among the remaining two-dimensional crystals. In the obtained samples of indium monoselenide, the electron mobility is the highest. This material parameter is extremely important in terms of improving the performance of devices that can be created on its basis. Another interesting property of indium monoselenide is that, unlike dichalcogenide and silicon, this crystal is a so-called direct-gap semiconductor. This makes it particularly promising for use in optoelectronics. In addition, the width of the InSe band gap depends essentially on the thickness of its layers. The ability to vary the width of the band gap of this material by selecting nanofilms of various thicknesses opens up wide possibilities for its application in optoelectronic devices that can function over a wide spectral range from the near infrared to the visible regions. Such an effect cannot be achieved in other graphene-like two-dimensional semiconductors [20]. This paper is devoted to an experimental study of nonlinear absorption and quanta-dimensional effects in gallium and indium monoselenides at high optical excitation levels.

2. Experimental method

The investigated single crystals were obtained by the Bridgman method. GaSe and InSe have a layered structure, where each layer contains two gallium (indium) and two selenium close-packed sublayers in the stacking sequence Se-Ga(In)-Ga(In)-Se. The bonding between two adjacent layers is of the Van der Waals type, while within the layer, the bonding is predominantly covalent. The ingots were cleaved along the planes of layers, obtaining slices about (10-50) μm thick. The presence of exciton line in the absorption spectrum is indicative of a good quality material [21,22]. Mobility and concentration of charge carriers measured by conventional methods at room temperature were $\sim 20 \text{ cm}^2/\text{V}\cdot\text{s}$, $1 \times 10^{14} \text{ cm}^{-3}$ and $\sim 1.2 \times 10^3 \text{ cm}^2/\text{V}\cdot\text{s}$, $\sim 7 \times 10^{14} \text{ cm}^{-3}$ GaSe and InSe, respectively. The samples were put into a helium cryostat equipped with a temperature controller which allows any temperature between 4.2 and 77 K to be maintained.

As an excitation source, a picosecond YAG:Nd laser with a pulse duration of 30 ps were used to excite InSe crystals. In this case, both the single beam and also double beam excitation were used [23]. In the first method, resonant excitation of excitons is performed by a parametric light generator. The second method (double beam method) uses pump-probe spectroscopy. After amplification, the light pulse is divided into two parts and two laser beams are focused on the same spot of a semiconductor sample. The laser labeled pump passes through a KDP crystal and doubles in frequency ($\hbar\omega = 2.34 \text{ eV}$). The pump pulse has a relatively large intensity and is usually tuned to an energy within the absorption region of the InSe. The pump beam is absorbed, resulting in the generation of electron-hole pairs. The second light beam, referred to as the probe beam, is used to monitor the changes in the optical properties caused by the pump. The probe intensity is very small, not inducing any changes by itself. The transmission spectrum of the probe beam detected in the presence of the pump beam is compared to the spectrum without pump beam, giving the frequency-dependent absorption of the sample for different intensities of the pump. For this purpose, it is convenient to have a probe beam that is either spectrally broad or easily tunable in wavelength, making it possible to monitor the entire band-edge absorption region. In our case, the probe pulse was formed by passing the second laser beam through deuterioxide, after which it was converted into a pulse having a wavelength in the range 0.75–1.5 μm . The pump-probe technique described above may also be employed to study the time evolution of the absorption spectrum. The time delay Δt between the probe and pump pulses is caused by a change in the path length of the pump pulse. Spectral distribution of probe pulse passing through the sample was investigated by a double-monochromator. All experimental data were processed and computer analyzed.

As an excitation source, Rhodamine 6G dye laser (PRA, LN-107) pumped by the output of a N_2 -laser (PRA, LN-1000), tuned through the region 594–643 nm with a repetition frequency of 10 Hz and a pulse width of 1 ns was used in the case of excitation of GaSe crystals. Lower excitation intensities were obtained by means of suitable calibrated neutral filters. Transmission spectra were obtained by shifting filters from the front to the rear of the samples and checking the experimental reproducibility in the region of transparency. The output signals were detected by a silicon photodiode and recorded by a storage oscilloscope (Le Groy 9400).

2.1. Nonlinear light absorption in InSe crystals at high optical excitation

Fig. 1(a) illustrates dependence of the magnitude of transmission coefficient on the emission intensity for an InSe single crystal excited by laser light having an energy $\hbar\omega = 1.327 \text{ eV}$ (resonant excitation of exciton) at 77 K. As it is seen from the figure, a nonlinear absorption in the exciton resonance region and occurrence of sample bleaching in the indicated light frequency at high excitation levels are observed. The observed bleaching saturates at the incident light intensity of $\sim 300 \text{ MW}/\text{cm}^2$. Diminishing of the magnitude of exciton absorption may be explained by the process of screening (Mott transition) for a high density exciton system (Fig. 1(b)). The density of the electron-hole pairs in our experiment reached $\sim 10^{20} \text{ cm}^{-3}$ which exceeds the density necessary for the Mott transition in InSe ($n_{\text{Mott}} = 2.5 \times 10^{16} \text{ cm}^{-3}$) [24]. The detailed investigation of the bleaching and dynamics of nonlinear absorption in the exciton resonance region have been realized by using double beam method at 4.2 K. Similar to single beam excitation, in this case, bleaching is also observed in the exciton absorption region at $T = 4.2 \text{ K}$.

Figure 1(c) illustrates clearly dependence of optical density on the excitation intensity in a frequency where the exciton absorption is maximum (the time delay between the probe and pump pulses is zero). The observed bleaching saturates at higher excitation levels with respect to the case of resonant excitation of exciton. This can be ascribed to the spatial inhomogeneity of the excitation in the sample. Typical absorption length of the excitation power is of the order $1 \sim 1/\alpha \sim 10^{-4} \text{ cm}$, $\alpha = 10^4 \text{ cm}^{-1}$ for $\hbar\omega = 2.34 \text{ eV}$ [5]. Disappearance of the exciton peak in this case may be explained by screening of the Coulomb interaction by free charge carriers. The screening length

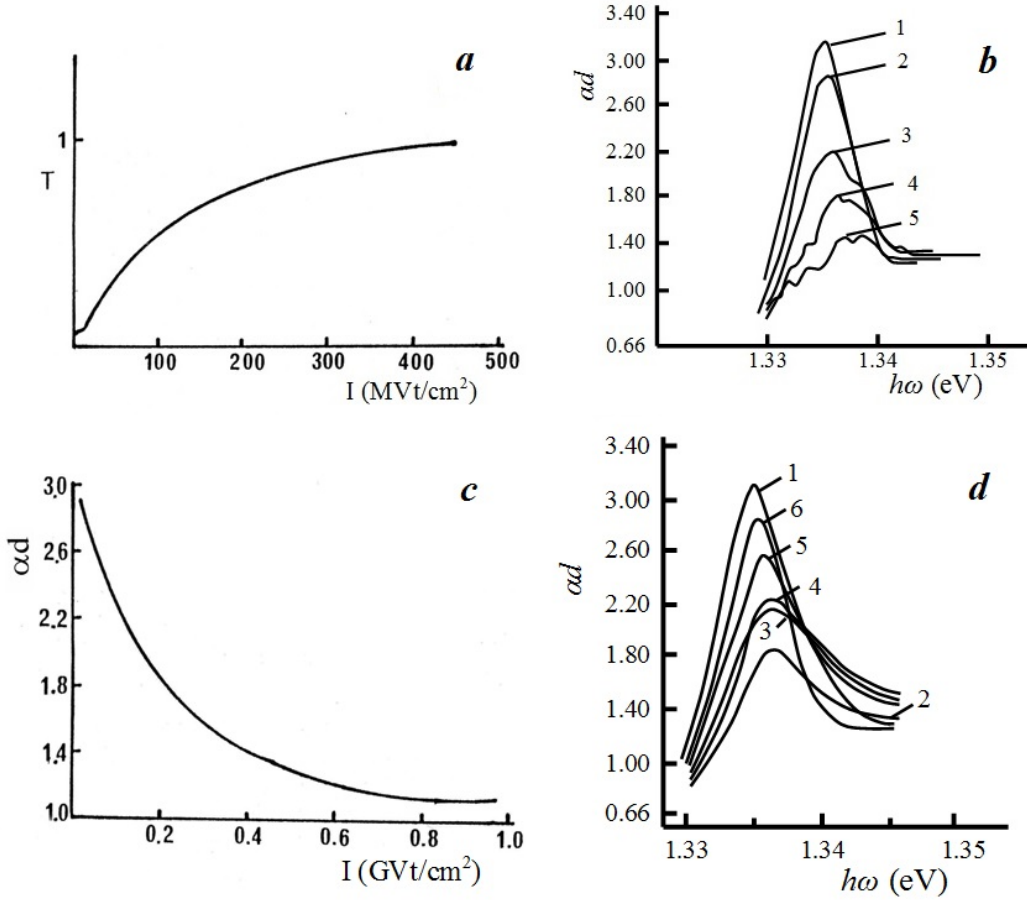


FIG. 1. (a) Dependence of the transmission coefficient on the excitation intensity in InSe (in the case of resonant excitation of exciton, $\hbar\omega = 1.327$ eV) at 77 K. (b) Absorption spectra of InSe at various excitation intensities I_{pump} . (MVt/cm²): 1 - 0; 2 - 12; 3 - 60; 4 - 250; 5 - 600, $T = 4.2$ K. (c) Dependence of the optical density on the excitation intensity ($\hbar\omega_{pump} = 2.34$ eV, $\hbar\omega_{probe} = 1.336$ eV, $\Delta t = 0$) at 4.2 K. (d) Absorption spectra of InSe for different time delays between the probe and pump pulses: 1 - $I_{pump} = 0$; 2 - $\Delta t = 24$ ps; 3 - $\Delta t = 98$ ps; 4 - $\Delta t = 297$ ps; 5 - $\Delta t = 660$ ps; 6 - $\Delta t = 910$ ps, $I_{pump} = 600$ MVt/cm², $\hbar\nu_{pump} = 2.34$ eV, $T = 4.2$ K.

can be defined by the following equation [25]:

$$L = \frac{\hbar}{2} \left(\frac{\pi}{3} \right)^{1/6} N^{-16} \frac{\varepsilon^{1/2}}{em^{*1/2}},$$

where, ε is the dielectric constant of the crystal and m^* is the effective mass. By substituting these values from [26,27] it is found that, $L \sim 10$ Å which is less than the exciton radius (~ 37 Å) [12]. In Fig. 1(d) the absorption spectra of InSe crystals for different time delays between the probe and pump pulses are shown. It is clear from the figure that, the exciton absorption peak broadens and shifts toward higher energies with respect to the nonexcitation case. In the energy region between the exciton level and edge of the conduction band, an induced absorption is appeared. It should be noted that at a light intensity $I \sim 600$ MW/cm², complete disappearance of the exciton peak is not observed. Thus, a situation is realized experimentally in which both the electron-hole plasma (EHP) and high density exciton gas are present in the sample.

3. Nonlinear light absorption in GaSe crystals at the fundamental absorption edge

The absorption spectra of GaSe at low (curve 1) and high (curve 2) excitation intensities are given in Fig. 2(a). As it is seen from the figure, at high excitation levels, the absorption coefficient is decreased, and along with the onset of absorption is also shifted towards higher energies. The change in the absorption coefficient $\Delta\alpha$ can be

obtained by direct subtraction of curves 1 and 2 in Fig. 2(a). The result is plotted in Fig. 2(b). It is seen that the maximum absorption change takes place in the vicinity of the band gap.

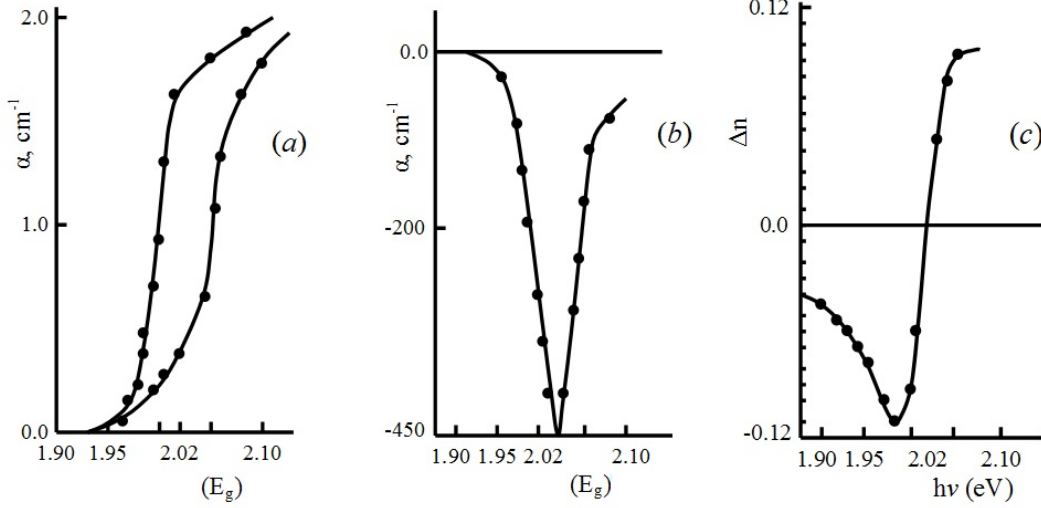


FIG. 2. (a) Absorption spectra of GaSe at low ($\sim 3,5$ mW/cm², curve 1) and high (~ 12 mW/cm², curve 2) intensity excitations. (b) The change in the absorption coefficient $\Delta\alpha$. (c) The change in the refractive index $\Delta n(\omega)$

The observed nonlinear absorption near the band gap at high excitation intensities can be attributed to optical saturation effects in GaSe, i.e. electrons and holes generated by absorption of light which relax rapidly to a thermal distribution, blocking absorption states near the band edge. Effectively, this is like a shift of the band edge to higher energies with increasing laser intensity, which causes the absorption at the vicinity of the band edge to decrease. From Fig. 2(b), it is clear that, the absorption change becomes negative. Negative absorption means amplification as can be seen from Beer-Lambert's law:

$$I(t) = I_0 \exp(-\alpha x). \quad (1)$$

For $\alpha < 0$, the transmitted intensity is higher than the input intensity. This optical gain can give the possibility of producing a semiconductor laser based on GaSe crystals.

The bandfilling effect predicts that the change in absorption coefficient due to free carriers (neglecting exciton interaction) at photon energy $\hbar\omega'$ above the band-gap energy is given by [28]:

$$\Delta\alpha(\hbar\omega') = -\alpha_0(\hbar\omega') 2^{1/2} \left(\frac{\pi\hbar}{k_B T} \right)^{3/2} \times \left[n_e m_e^{-3/2} \exp(-\Delta E_c/k_B T) + n_h m_h^{-3/2} \exp(-\Delta E_v/k_B T) \right], \quad (2)$$

where:

$$\Delta E_c = (\hbar\omega' - E'_g)/(1 + m_e/m_h), \quad (3)$$

$$\Delta E_v = (\hbar\omega' - E'_g)/(1 + m_h/m_e), \quad (4)$$

$\alpha_0(\hbar\omega')$ is the low-power absorption coefficient at photon energy $\hbar\omega'$, m_e is the effective mass of an electron, m_h is the effective mass of a hole, n_e , n_h are the integrated population density of free – electron and free – hole, respectively, E'_g is the renormalized band gap which results from exchange and correlation effects at high carrier densities [29]. Taking $m_e = 0.3m_0$, $m_h = 0.2m_0$ and calculated values of n_e , n_h , E'_g , ΔE_c , ΔE_v from Eqs. (4)–(11) of Ref. [30], the percentage relative absorbance change $\Delta\alpha/100\%/\alpha_0$ is evaluated to be $\sim 12\%$ in GaSe. This is in good agreement with the corresponding observed value of 15%. The small difference between these values can be due to the fact that, the exciton interactions were neglected in Eq. (2), while in wide-band-gap materials (such as GaSe). Coulomb electron-hole correlation effects should be taken into account which can eventually lead to the enhancement of the nonlinear absorption. Such saturation leads both to nonlinear absorption and to a strong intensity dependence of the refractive index. From the Kramers – Kronig relation [31] we may write the change in

refractive index at photon energy $\hbar\omega$ as:

$$\Delta n(\hbar\omega) = \frac{hc}{\pi} \int_0^{\infty} \frac{\Delta\alpha(\hbar\omega')}{(\hbar\omega')^2 - (\hbar\omega)^2} d(\hbar\omega'). \quad (5)$$

Using Eq. (5) to compute the index change related to the absorption change of Fig. 2(b), we obtain the result plotted in Fig. 2(c). As can be noted from Fig. 2(c), the change in the refractive index leads to nonlinear effects. $\Delta n(\omega)$ is negative at frequencies below the absorption edge and positive on the high-energy side. The laser-induced negative index change is referred to as a self-defocusing optical nonlinearity. The positive $\Delta n(\omega)$ on the high-energy side of the band gap corresponds to a self-focusing optical nonlinearity.

4. Quantum-dimensional effects in GaSe nanoparticles

The GaSe nanoparticles were obtained by a modified method of chemical deposition (Successive Ionic Layer Adsorption and Reaction-SILAR). Using the Debye-Scherrer formula, the sizes of the nanoparticles obtained were calculated [32]. Estimates show that the dimensions of GaSe nanoparticles range from 7–20 nm. Using the energy-dispersive X-ray spectroscopy (EDAX) and the scanning electron microscope (SEM), the internal structure and structure of the GaSe nanoparticles were studied. Images obtained with SEM show that the obtained substances consist of spherical nanocrystals that are collected in a polydisperse form (Fig. 3(a)). The laser irradiation of GaSe nanoparticles results in a homogeneous distribution of the nanoparticles. In this case, the dimensions of the nanoparticles practically become the same (Fig. 3(b)). The image of the GaSe and InSe nanoparticles, obtained from AFM studies, shows that the homogeneous particle distribution is not observed (Fig. 4(a,b)). The EDAX method shows that the ratio of gallium to selenium (Ga:Se) is 1:1, hence the composition of the substance is in the stoichiometric ratio. Images obtained by an atomic force microscope show that a homogeneous distribution of nanoparticles is not observed on the substrate surface.

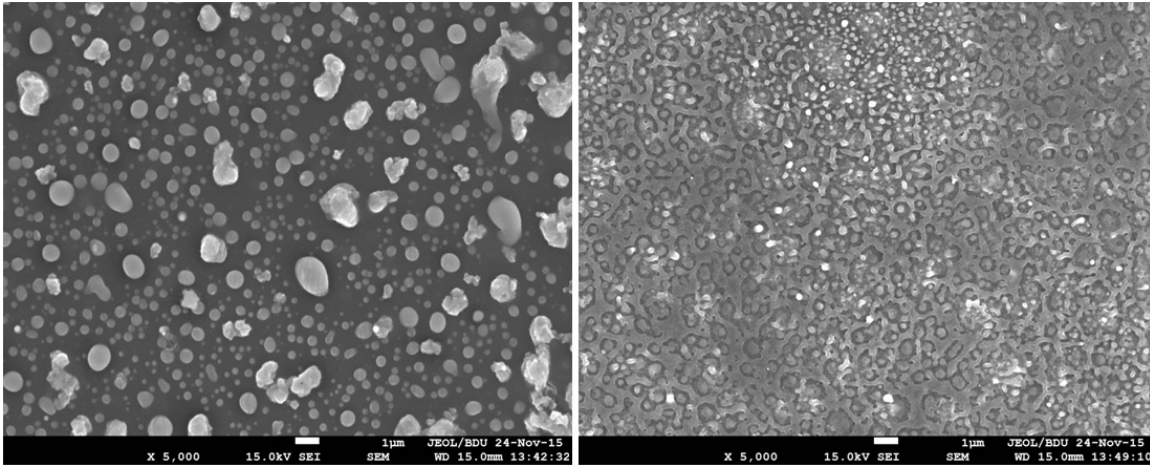


FIG. 3. SEM images of the GaSe nanostructure, grown on a glass substrate before (a) and after (b) laser light irradiation with a power of 6 MVt/cm²

As is known, many mechanical, thermodynamic and electrical characteristics of a substance are altered in nanoparticles. Their optical properties are not an exception to this behavior. Correspondingly, the frequency of light emitted by nanoparticles increases with decreasing particle size. Experiments conducted by us showed that a quasi-dimensional effect is observed in GaSe nanoparticles, the width of the forbidden band depends on the dimensions of the nanoparticles.

Calculation of the width of the band gap was carried out according to the following formula:

$$E_g = E_g^{(bulk)} + E_b \left(\frac{\pi a_B}{D} \right)^2, \quad (6)$$

where E_g is the width of the forbidden band of nanostructures, $E_g^{(bulk)}$ is the width of the same substance without nanostructures, E_b is the binding energy of the exciton, a_B – the Bohr radius of the exciton, and D is the size of the nanoparticles (~ 4 –20 nm).

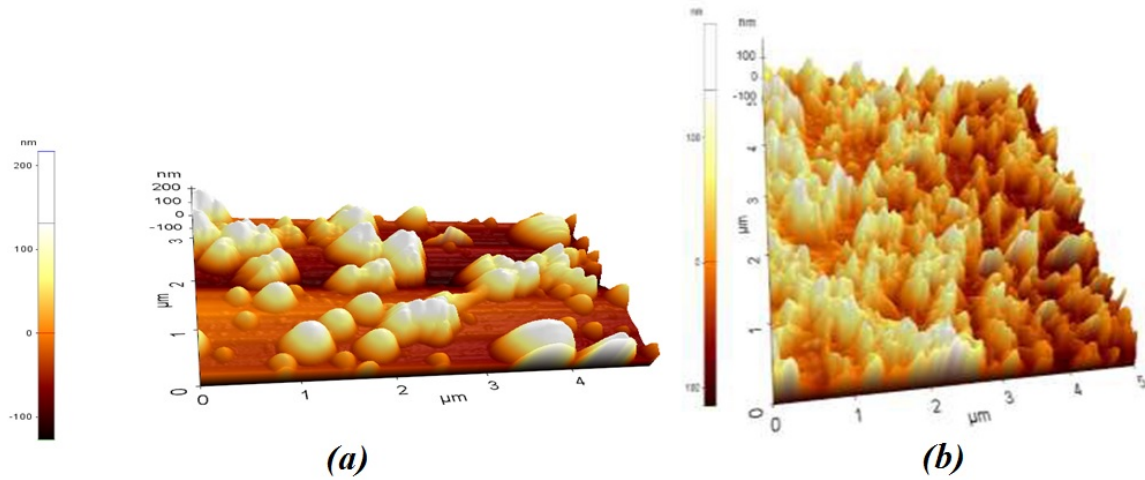


FIG. 4. AFM images of the nanostructure of GaSe (a) and InSe (b) grown on a glass substrate

The above parameters in GaSe have the following values: $E_g^{(bulk)} = 2.02$ eV, $E_b = 20$ meV, $a_B = 37$ Å. Fig. 5 shows the dependence of the width of the forbidden band of GaSe nanoparticles on the dimensions of nanoparticles. As can be seen from the figure, the quantum-size effect begins to significantly affect the width of the forbidden band when the dimensions of the nanoparticles become smaller than 10 nm.

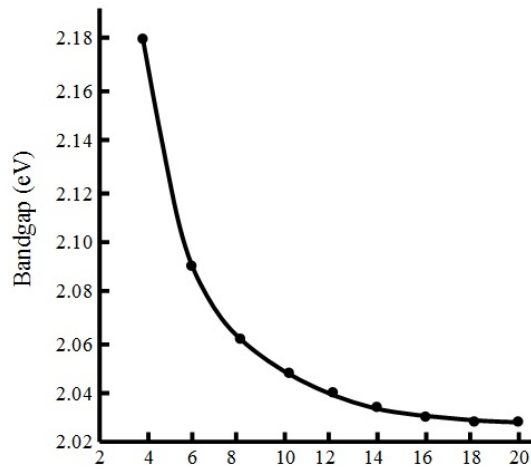


FIG. 5. Dependence of the width of the forbidden band of GaSe on the dimensions of nanoparticles

5. Conclusion

We note in conclusion that the nonlinear absorption observed in high-level optical excitation of InSe crystals in the region of exciton resonance is due to the exciton-exciton interaction. The density of the pairs generated by laser light in InSe ($3 \times 10^{19} \text{ cm}^{-3}$) is much higher than the density necessary for the Mott transition in these crystals. The induced absorption which appeared in the energy region between the exciton level and edge of the conduction band is due to the appearance of continuum states caused by shifting the energy band edges for InSe. The time dynamics of bleaching in the both the exciton absorption and induced absorption regions may be explained by recombination processes taking place in EHP and high density exciton gas. The illumination of the edge of the absorption band of GaSe, with its simultaneous shift to the high-energy region of the spectrum, is associated with the filling of energy bands at high optical excitation levels. It is shown that the observed band-filling effect allows a semiconductor laser to be created on the basis of GaSe crystals. In the nanoparticles of GaSe, obtained by a modified method of chemical deposition, a quanta-dimensional effect was observed. Reducing the size of nanoparticles from 20 nm to 4 nm leads to an increase in the width of the forbidden band from 2.02 eV to 2.18 eV.

References

- [1] Rogers F.J., Graboske H.C., Harwood D.J. Bound eigenstates of the static screened coulomb potential. *Phys. Rev. A1*, 1970, P. 1576–1586.
- [2] Keldish L.V. *Excitons in Semiconductors*. Nauka, Moscow, 1971, 143 p.
- [3] Mott N.F. *Metal-Insulator Transitions*. Taylor, Francis, London, 1974, 34 p.
- [4] Abdullaev G.B., Gulevski L.A., Prokhorov A.P., Saveliev A.D., Salaev E.Yu., Smirnov V.V. GaSe-new effective material for nonlinear optics. *JETP lett.*, 1972, **16**, P. 130–133.
- [5] Akhundov G.A., Agaeva A.A., Salmanov V.M., Scharonov Ju.P. and Jarochetski I.D. Generation of the second harmonic in compounds of the A^3B^6 type. *Sov. Phys. Semicond.*, 1973, **7**, P. 1229–1231.
- [6] Abdullaev G.B., Allakhverdiyev K.R., Gulevski L.A., Prokhorov A.P., Salaev E.Yu., Saveliev A.D. and Smirnov V.V. Parametric IR conversion in a GaSe crystal. *Quantum Electronics*, 1975, **2**, P. 1228–1233.
- [7] Bereglyin E.B., Valov P.M., Ribakova T.B., Salmanov V.M., and Jarochetski I.D., Experimental study of the conversion of infrared light into the near-IR range in crystals of gallium selenide // *Sov. Phys. Semicond.* **9** (1975), pp. 2288–2291
- [8] Baltramieyunas R., Narkevicius V., Skaistys E., Vaitkus J. and Viscakas J. Polarization of Luminescence Spectra and Electron-Hole Plasma Radiation in GaSe Single Crystals at High Level of Excitation. *Nuovo Cimento B*, 1977, **38**, P. 603–609.
- [9] Frova A., Schmid Ph., Grisel A., Levy F. The electron-hole system in GaSe at high densities. *Solid State Commun.*, 1977, textbf23, P. 45–48.
- [10] Yao S.S., Buchert J. and Alfano R.R. Time-resolved picosecond absorption spectroscopy of the layered compound gallium selenide. *Phys. Rev. B*, 1982, **25**, P. 6534–6537.
- [11] Dneprovskii V.S., Furtichev A.I., Klimov V.I., Nazvanova E.V., Okorokov D.K. and Vandinchev U.V. Room temperature self – screening and screening of excitons in GaSe. *Phys. Status Solidi B*, 1988, **146**, P. 341–345.
- [12] Pavesi L., Staehly J.L., Mott transition of the excitons in GaSe. *Phys. Rev. B*, 1989, **39**, P. 10982–10994.
- [13] Nahory R.E., Shaklee K.L., Leheny R.F. and De Winter J.C. Stimulated emission and the type of bandgap in GaSe. *Solid State Commun.*, 1971, **9**, P. 1107–1111.
- [14] Catalano I.M., Cingolani A., Ferrara M. and Minafra A. Luminescence by exciton-exciton collision in GaSe. *Phys. Status Solidi (b)*, 1975, **68**, P. 341–346.
- [15] Lu X.Z., Rao R., Willman B., Lee S., Doukas A.G. and Alfano R.R. Photoluminescence due to exciton-exciton scattering in GaSe under picosecond laser excitations. *Phys. Rev. B*, 1987, **36**, P. 1140–1146.
- [16] Bobrysheva A.I., Golubev G.P., Dobinda I.I., Zhukov E.A., Luchinski D.G. and Shekun Yu.G., Picosecond Kinetics of Photoluminescence in GaSe. *Phys. Status Solidi (a)*, 1990, **117**, P. 587–592.
- [17] Abdullaev G.B., Godzhaev I.O., Kakhramanov N.B. and Suleimanov R.A. Stimulated radiation in layered semiconductors InSe and GaSe. *Fiz. Tverd. Tela*, 1992, **34**, P. 75–82.
- [18] Wei Shi, Ding J., Nils Fernelius, Konstantin Vodopyanov. Efficient, tunable, and coherent 0,18-5,27 THz source based in GaSe crystal. *Opt. Lettr.*, 2002, **27**, P. 1454–1459.
- [19] Ding J. and Wei Shi. Widely-tunable, monochromatic and high-power terahertz sources and their applications. *Journal of Nonlinear optical physics and materials*, 2003, **12**, P. 557–585.
- [20] Bandurin D.A., Tyurina A.V., Geliang L.Yu., Mishchenko A., Zolyomi V., Kumar R.K., Gorbachev R.V., Kudrynskiy Z.R., et al. High Electron Mobility, Quantum Hall Effect and Anomalous Optical Response in Atomically Thin InSe. *Nature Nanotechnology*, 2016, P. 242–260. doi: 10/1038/nano
- [21] Bakumenko V.L., Kovalyuk Z.D., Kurbatov L.N. and Chisko V.F. Optical properties of InSe single crystals in the region of fundamental absorption edge. *Sov. Phys. Semicond.*, 1976, **10**, P. 1045–1049.
- [22] Dzhafarova S.Z., Ragimova N.A., Abutalybov G.I., Guseynov A.M. and Abidinov A.Sh. Effect of Doping on Exciton States in InSe and GaSe Lamellar Semiconductors. *Phys. Stat. Sol. (a)*, 1995, **128**, P. 235–242
- [23] Ivanov S.V., Kopjev P.S., Nekrasov.Yu., Paxomov A.G., Trukhin V.N. and Jaroshetskii I.D. Energy relaxation and transport of electrons and holes in short-period semiconductor superlattices. *Sov. Phys. Semicond.*, 1989, **23**, P. 1564–1569.
- [24] Cingolani A., Cingolani R., Ferrera M. and Lugara M. Excitons and electron-hole plasma in InSe. *Solid Stat. Commun.*, 1985, **55**, P. 1011–1015.
- [25] Gross P. *Free electrons in solids*. Moscow, 1982, p. 135.
- [26] Ottaviani G., Canali C., Nava F., Schmid Ph., Mooser E., Minder R. and Zschokke. Comparison of nonlinear optical properties of sulfide glasses in bulk and thin film form. *Solid Stat. Commun.*, 1974, **13**, P. 933–936.
- [27] Staehli J.L. and Capozzi V. Coexistence of Direct and Indirect Electron-Hole Plasma Components in GaSe. *Helv. Phys. Acta.*, 1985, **58**, P. 262–265.
- [28] Miller A., Parry G. and Daley R. Nonlinear absorption in semiconductors. *IEEE J. Quantum Electron*, 1984, **QE-20**, P. 710–715.
- [29] Vashista P. and Kalia R.K. Universal behavior of exchange-correlation energy in electron-hole liquid. *Phys. Rev. B*, 1982, **25**, P. 6492–6495.
- [30] Hilinski F.E., Lucas P.A. and Ying Wang. A picosecond bleaching study of quantum-confined cadmium sulfide microcrystallites in a polymer film. *J. Chem. Phys.*, 1988, **89**, P. 3435–3440.
- [31] Peyghambarian N., Koch S.W. and Mysyrovicz A. *Introduction to semiconductor optics, Series in Solid State Physical Electronics*. New Jersey, 1993, P. 325–331.
- [32] Samuel S. Mao. Nanolasers: lasing from nanoscale quantum wires. *Int. J. of Nanotechnology*, 2004, **1**, P. 42–85.

SnO₂ quantum dots for nano light emitting devices

S. S. Nath¹, A. Ganguly², G. Gope¹, M. R. Kanjilal³

¹Central Instrument Lab, Assam University, Silchar, Assam-788011, India

²National Institute of Technology, Silchar, Silchar, Assam-788010, India

³Narula Institute of Technology, Agarpara, Kolkata-700109, India

nathss01@rediffmail.com,avigyan.ganguly@hotmail.com, gopemail@gmail.com

DOI 10.17586/2220-8054-2017-8-5-661-664

We prepared SnO₂ quantum dots embedded in polyvinylpyrrolidone (PVP) matrix and report its operation as a Nano Light emitting device. The samples have been prepared via quenching technique where bulk ZnO powder is sintered at a very high temperature of 1000 °C and then quenched into ice cold polyvinylpyrrolidone solution. The specimen was then characterized using UV/VIS spectroscopy, X-ray diffraction study and high resolution transmission electron microscopy (HRTEM). These studies indicate the sizes of quantum dots to be within 9 nm. The prepared quantum dot samples have been evaluated as nano light emitting devices by exploring the variation of electroluminescence (light emission phenomenon) with supply voltage at room temperature.

Keywords: quantum dot, polyvinylpyrrolidone, quenching, nano LED.

Received: 19 May 2017

Revised: 17 August 2017

Final revision: 4 September 2017

1. Introduction

The synthesis of semiconductor quantum dots and their different applications as various electronic and optoelectronic devices including different kinds of sensors, devices are among the top research areas at present [1–6]. Recently, many techniques [1–4] like molecular beam epitaxy (MBE), radio frequency sputtering (RF), liquid phase epitaxy (LPE), quenching etc. have been adopted to synthesize semiconductor quantum dots. But due to its manifold advantages [3,6] viz. like simplicity and low cost, quenching method draws the interest of current researchers. In the present investigation, we discuss the preparation of SnO₂ quantum dots in a polyvinylpyrrolidone (PVP) matrix (which embeds the quantum dots) by quenching method and their functioning as Nano light emitting devices which is a new area of nano research. The advantage of PVP over other polymer matrices viz. SBR latex matrix is that circular and uniform quantum dots can be fabricated on PVP. The prepared samples have been examined using different characterization methods to reveal their nano natures [2]. These studies infer the formation of quantum dots within the dimension of 8 nm. Next, the ability of SnO₂ samples to function as nano light-emitting diodes (LED's) has been tested by performing electroluminescence studies at room temperature. Testing of SnO₂ quantum dots for nano LED, which has not been focused in any report earlier, is interesting, and technically very important.

2. Materials and method

To synthesize [3] SnO₂ quantum dots by quenching method, 4 gms of SnO₂ powder (99.99 % pure, E Merck) was calcined at ~ 1000°C for 10 hours and then quenched into 4 wt% aqueous solution of polyvinylpyrrolidone (PVP) matrix (99.9% pure, E Merck) kept at ice cold temperature followed by its moderate stirring (~ 175 rpm). This solution contains SnO₂ quantum dots embedded in a polyvinylpyrrolidone matrix (chemical structure is shown in Fig. 1). The film is developed on the laboratory glass slides by placing a few drops of SnO₂ quantum dot solution (embedded in PVP) on a clean slide and by stretching over it, another clean slide.

3. Results and discussions

The SnO₂ specimen was characterized by UV/VIS optical absorption spectroscopy (Perkin Elmer Lambda 35 1.24), X-ray diffraction study (Bruker AXS, X-ray source: CuK α) and high resolution transmission electron microscopy (HRTEM) (JEM 1000 C XII).

Optical absorption spectroscopy [6] shows sharp blue shifted absorption edge of the prepared samples (Fig. 1). A blue shift is a distinct signature of quantum dot formation [1, 3, 4] (Fig. 2a). By considering shifted absorption

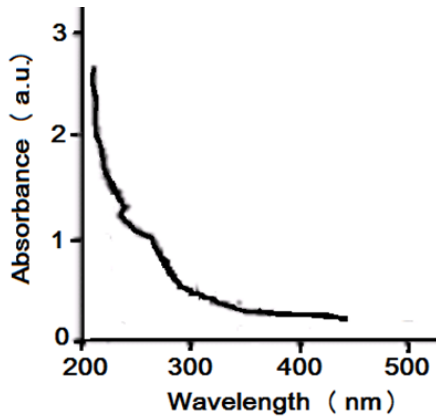


FIG. 1. UV/VIS absorption spectra of SnO₂ quantum dots

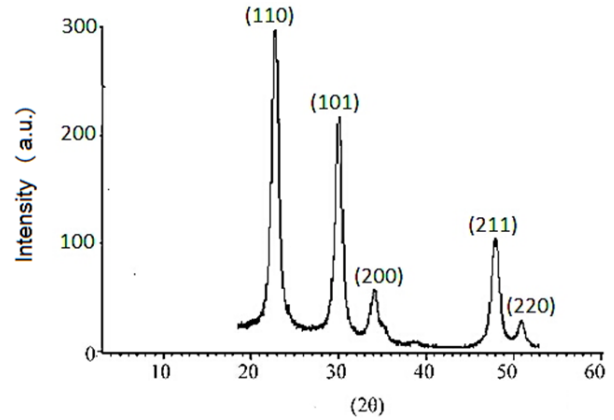


FIG. 2. XRD spectra of SnO₂ quantum dots

edge (at 210 nm) of SnO₂ sample, average crystallite (particle) size has been estimated and found to be 10 nm by using the following hyperbolic band model [5]:

$$R = \sqrt{\frac{2\pi^2 h^2 E_{gb}}{m^*(E_{gn}^2 - E_{gb}^2)}}, \quad (1)$$

where R is quantum dot radius ($2R$ is the diameter and hence the particle size), E_{gb} is the bulk band gap, E_{gn} is quantum dot band gap (calculated from the sharp absorption edge which is 210 nm as shown in Fig. 1.), h is Planck's constant, m^* is effective mass. Similarly, from X-ray diffraction study (Fig. 3) average particle size (crystallite size) is calculated by using Scherrer formula [2], $D = \frac{0.9\lambda}{W \cos \theta}$, λ is wave length of X-ray (0.1541 nm), W is FWHM (full width at half maxima), θ (theta) is the glancing angle and D is particle diameter (crystallite size). Considering all the peaks [3] (2θ in degree) in the X-ray diffractogram, the average crystallite (quantum dot) size has been calculated to be 9 nm. Further, by analyzing the X-ray diffractogram with the help of ICDD (International Center Diffraction Data) it has been revealed that SnO₂ quantum dots are "wurtzite" in structure. HRTEM images of PVP film (c) and SnO₂ quantum dots (a) are shown in Fig. 3. It is evident in the HRTEM image (a) that SnO₂ crystallites (quantum dots) are circular in shape with sizes within 10 nm.

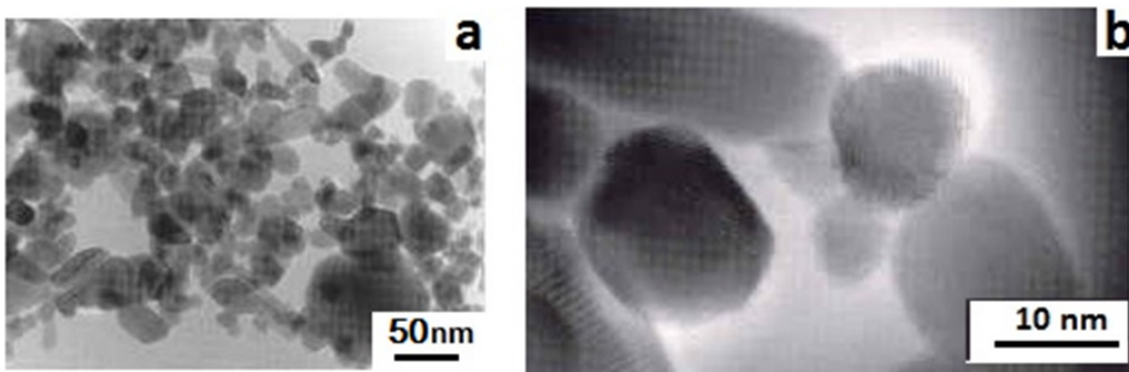


FIG. 3. HRTEM images of SnO₂ QDs in PVP matrix

SnO₂ sample sizes assessed from these three studies are reasonably similar, which is a distinct advantage over earlier reports [2, 3]. This matching occurs due to the formation of well uniformed and circular shaped quantum dots by using PVP matrix instead of PVA (polyvinyl alcohol) matrix [3]. All these characterizations infer that SnO₂ quantum dot sizes (diameters) are within 10 nm.

To test the operation of SnO₂ quantum dots as Nano Light emitting devices, the electroluminescence (EL) of the sample [5, 6, 19] at room temperature was determined (Fig. 4). SnO₂ has been shown to display appreciable electroluminescence at around 580 nm at room temperature and we believe that this emission is a result of the

oxygen vacancy. It has been reported elsewhere that emission intensity is a function of bias voltage and the luminescence intensity increases at higher bias voltages [4, 18]. But the disadvantage is that, high bias voltages causes damage to the sample at longer operating times. This investigation obviously indicates that SnO₂ quantum dots can act as nano light emitting devices at a very low bias, which is our new achievement with fast response speed on the order of 10⁻⁹ sec. Variation of EL intensity with bias voltage is plotted in Fig. 5. The data from the electroluminescence study of the quantum dots is given in Table 1.

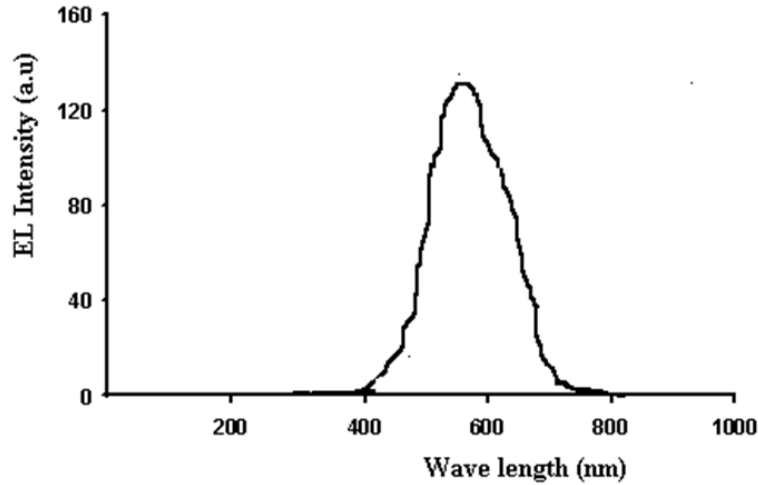


FIG. 4. EL spectra (0.5 V) of SnO₂ samples

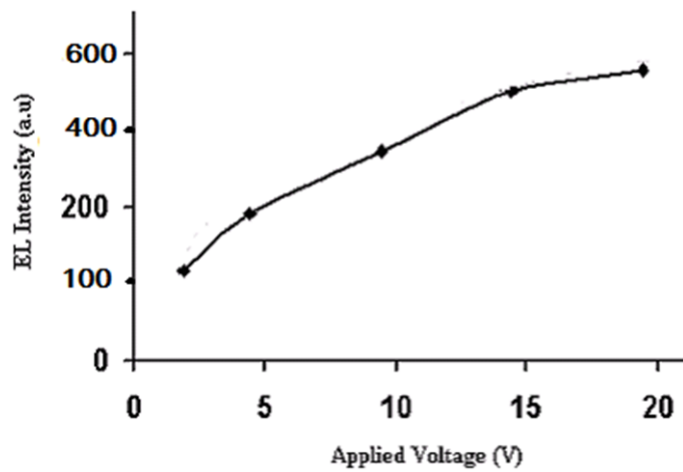


FIG. 5. EL intensity Vs applied voltage

4. Conclusion

SnO₂ shows appreciable electroluminescence at room temperature and the relationship between EL intensity and applied voltage up to 20 V appears to be almost linear. Thus, SnO₂ quantum dots can act as Nano light emitting devices at room temperature.

TABLE 1. Data from Electroluminescence (EL) spectra of SnO₂ quantum dots

Sample	Applied voltage (V)	EL intensity (a.u)	Relative quantum efficiency (times)	Response speed
SnO ₂	2.5	145	3.2	Of the order of 10 ⁻⁹ sec
	5	310	6.8	
	10	410	9.1	
	15	520	11.5	
	20	580	12.9	

References

- [1] Zhang K., Chang H.Y., et al. Continuous distribution of emission states from single CdSe/ZnS quantum dots. *Nano Lett.*, 2006, **6**, P. 843–847.
- [2] Debye P. Zerstreung von Roentgenstrahlen. XRD study of Nanomaterials. *Annalen der Physik B*, 1915, **46** (1), P. 809–823.
- [3] Nath S.S., Chakdar D., et al. Green luminescence of ZnS and ZnS: Cu quantum dots embedded in Zeolite matrix. *J. Appl. Phys.*, 2009, **105**, P. 094305–94309.
- [4] Lee E., Wang C., et al. “Greener” Quantum dot enabled LCDs with BT. 2010 color gamut. *SID Symposium Digest of Tech. Papers*, 2016, **47**, (1), P. 549–551.
- [5] Liu A.Y., Peters J., et al. Electrically pumped continuous wave 1.3 μm quantum dot lasers epitaxially grown on on-axis (001) GaP/Si. *Optical Letters*, 2017, **42** (2), P. 338–341.
- [6] Nath R.K., Nath S.S. Tin dioxide thin film-based ethanol Sensor prepared by spray pyrolysis. *Sensors and Materials*, 2009, **21**, P. 95–104.
- [7] Sayhay P.P., Tewari S., Nath R.K. Optical and electrical studies on spray deposited ZnO thin films. *Cryst. Res. Tech.*, 2007, **42**, P. 723–729.
- [8] Sahay P.P., Nath R.K. Al-doped ZnO thin films as methanol sensors. *Sens. Actuators B: Chem.*, 2008, **134**, P. 654–659.
- [9] Fang Y.K., Lee J. A tin oxide thin film sensor with high ethanol sensitivity. *Thin Solid Films*, 1989, **169**, P. 51–56.
- [10] Chakraborty S., Mandal S., et al. Improvement of recovery time of nanostructured tin dioxide-based thick film gas sensors through surface modification. *Sens. Actuators B: Chem.*, 2007, **127**, P. 554–558.
- [11] PengIndium L., Xie T.F., et al. Light induced enhancing gas sensitivity of copper-doped zinc oxide at room temperature. *Sens. Actuators B: Chem.*, 2008, **131** (2), P. 659–660.
- [12] Zaiats G., Ikeda S., Kinge S., Kamat P.V. Quantum Dot Light Emitting Devices: Beyond alignment of energy levels. *ACS Appl. Mater. Interfaces*, 2017, **9** (36), P. 30741–30745.
- [13] Hulser T.P., Wiggers H., Kruis F.E., Lorke A., Nanostructured gas sensors and electrical characterization of deposited SnO₂ nanoparticles in ambient gas atmosphere. *Sens. Actuators B: Chem.*, 2005, **109**, P. 13–18.
- [14] Chou S.M., Teoh L.G., et al. ZnO:Al Thin Film Gas Sensor for Detection of Ethanol Vapor. *Sensors*, 2006, **6**, P. 1420–1427.
- [15] Shouli B., Liangyuan C., et al. Sn/In/Ti nanocomposite sensor for CH₄ detection. *Sens. Actuators B: Chem.*, 2008, **135**, P. 1–6.
- [16] Gong X., Yang Z., et al. Highly efficient quantum dots near – If light emitting diodes. *Nature Photonics*, 2016, **10**, P. 253–257.
- [17] Sahay P.P., Tewari S., Jha S., Shamsuddin M. Sprayed ZnO thin films for ethanol sensors. *J. Mat. Sci.*, 2005, **40**, P. 4791–4793.
- [18] Nath S.S., Chakdar D., Gope G., Avasthi D.K. Preparation of Quantum dots and their uses in Electronics. *Nanotrends – A journal of nanotechnology and its application*, 2008, **3** (3).
- [19] Nath S.S., Chakdar D., Gope G., Avasthi D.K. Effect of 100 MeV Nickel Ions on Silica Coated ZnS Quantum Dots. *Journal of Nanoelectronics and optoelectronics*, 2008, **3** (2), P. 180.

The influence of substrate material on the resistance of composite films based on reduced graphene oxide and polystyrene

M. N. Nikolaeva¹, E. V. Gushchina², M. S. Dunaevskii², A. T. Dideikin², A. N. Bugrov^{1,3}, T. D. Anan'eva¹

¹Institute of macromolecular compounds RAS, Bolshoy pr. 31, 199004 St. Petersburg, Russian Federation

²Ioffe Institute RAS, Politekhnicheskaya ul. 26, 194021 St. Petersburg, Russian Federation

³Saint Petersburg Electrotechnical University "LETI",

ul. Professora Popova 5, 197376 St. Petersburg, Russian Federation

marianna_n@mail.ru*, katgushch@yandex.ru, Mike.Dunaeffsky@mail.ioffe.ru,

dideikin@mail.ioffe.ru, alexander.n.bugrov@gmail.com, anthracene@hq.macro.ru

PACS 36.20.-r; 68.65.Pq; 71.20.Rv; 72.80. Tm; 74.78.-w

DOI 10.17586/2220-8054-2017-8-5-665-669

Current and surface topographies of composite based on polystyrene with reduced graphene oxide were investigated using atomic force microscopy. Different substrates such as gold, silicon and graphite were used for this purpose. The strong influence of the substrate's nature on the current distribution map $I(x, y)$ and the current-voltage characteristics was observed. This effect can be related to different adhesion of composite on the investigated substrates.

Keywords: reduced graphene oxide, polystyrene, composite, resistance, atomic force microscopy.

Received: 16 September 2017

Revised: 9 October 2017

1. Introduction

There are many studies devoted to the conductivity of graphene oxide in polymer composites [1–8]. Graphene oxide is a dielectric, but with appropriate treatment its band gap can be decreased to zero [9,10]. In this regard, the conductivity of the reduced graphene oxide (RGO) varies from that of a semiconductor to a metal. This can be one of the reasons for the discrepancies in the conductivity values of graphene-containing polymer composites, which are fixed by the authors. Also, not only the chemical and thermal pre-history of graphene inclusions affects the conductivity of polymer composites, but also the introduction approach, distribution uniformity and adhesion at the polymer-graphene interface play an important role. For example, it was shown in [11] that the conductive properties of a polystyrene composite with RGO (named in this paper as "graphene flakes") are significantly dependent on the dispersion degree and homogeneity distribution of the filler in the polymer matrix. The filler localization near the surface of the polymer films leads to high conductivity in the case of styrene copolymerization with graphene functionalized by vinyl groups. It is worth noting that RGO functionalized by 3-(trimethoxysilyl)propyl methacrylate can form covalent bonds with styrene under predetermined polymerization conditions, similar to the work [12]. At the same time, the mechanical mixing of the modified RGO with polymer matrix, as well as the copolymerization of styrene with unmodified filler, give weakly conducting compositions.

A large number of articles devoted to graphene/polymer or RGO/polymer composites have shown that their conductivity is proportional to the filler content. At the same time, there are articles where very small amounts of graphene (0.01 wt.%) contribute to the appearance of high conductivity [13,14] and even superconductivity [15,16]. In our case, the object of study is the composites demonstrating superconducting features based on polystyrene with RGO combining graphene fragments and oxidized groups. Thus, the goal of this article is to measure resistance values of polystyrene/RGO films and to determine the influence of substrate on the composite conductivity. We suppose that various substrates will provide different adhesion degree for the RGO/polystyrene composite. Since polystyrene is dielectric itself, for any changes in the conductivity under the influence of the substrate material, one can expect RGO inclusions only. It is important to mention that electron tunneling is possible if the distance between electron states is less than 2 nm, thus the conductivity of composite film is limited by this distance. It is important because the key point of getting the charge into the composite film is its electrification by the substrate metal even with a simple metal/polymer contact [17]. We assume the adhesion degree can correlate with the amount (area) of conducting regions on the composite film along with the conductivity value. The conductive atomic force microscopy (CAFM) method was used for detailed study of the conductivity of composite films on various substrates. Previously, it was shown by CAFM analysis of polystyrene/RGO thin films that high-conductivity regions exhibit ohmic current-voltage characteristics, starting with weak electric fields [13]. In

addition, this method allowed that non-conducting regions to become conductive when a threshold pre-destructive electric field was reached. The effect can be reversible, when the electric field is reduced below the threshold value. The reverse switching to a non-conducting state occurs by analogy with results of A. N. Ionov et al. [18].

2. Experimental

Natural crystalline graphite was used as an initial material for GO production. Modified Hummers wet chemical method was used to produce graphene oxide [10,19]. After series of chemical reactions in liquid medium, prepared RGO was extracted from an aqueous suspension by drying at room temperature in air. Synthetic details were described previously [13,14]. Surface modification of RGO by 3-(trimethoxysilyl)propyl methacrylate was carried out using the method presented in our previous work [11]. Synthesis of polymer-inorganic composite based on polystyrene with surface-modified particles of RGO was performed by in-situ polymerization in solution. We put 0.5 ml of styrene, 0.5 ml of toluene and 5 mg of 2,2'-azobis(2-methylpropionitrile) as an initiator into an ampule containing 5 mg of RGO (1 wt.%). Then, the ampule with the reaction mixture was purged with argon for 10 min, sealed and sonicated. Polymerization was carried out for 35 hours at 70 °C, every hour for 15 minutes the ampule was sonicated. The content of the covalently bound RGO in the composite was about 0.01 wt.%.

Graphite and silicon plates have been used as substrates, as well as a vacuum deposited gold coating on glass. All substrates had a surface roughness not exceeding several nanometers, which was confirmed by the AFM data. Atomic force microscope Solver P47-Pro was used for surface and current topography measurements. The surfaces of the electrodes before the composite film deposition were thoroughly cleaned with acetone and ethanol. Films of the composite were deposited on electrodes through the dispenser by casting from 1 % polymer solution in toluene. The films' thicknesses were evaluated from concentration of composite solution and surfaces profiles of substrate electrodes as well were controlled by the interference microscope according to the method described in [20]. Thus, the thicknesses of investigated films were approximately 2 μm . The diamond AFM tip doped by nitrogen with curvature radius 50 nm was used as an upper electrode in CAFM measurements. The Ohm's nature of obtained current-voltage characteristics exclude the presence of a breakdown in films which have been investigated.

3. Results and discussion

The obtained RGO/polystyrene composite exhibited a different level of resistance depending on the lower electrode nature, according to CAFM measurements. The composite does not form percolation cluster in our case, since the concentration threshold of graphene is much higher, 0.9 wt.% [7]. Therefore, conductivity is possible only on areas containing RGO inclusions.

The surface topography (a) of the polymer composite on gold substrate and the current distribution (b) taken at the voltage value at the electrodes $U = 3$ V are shown in Fig. 1. Here, as well as on the following figures, more protruding parts of the surface and the largest currents are colored by white in grayscale palette. It can be seen that there is a correlation between the topography of the surface and the current distribution. The greatest currents are observed in places protruding above the surface and associated with the inclusion of RGO in the polymer matrix. The resistance value (R) on the gold coating is $5 \times 10^6 \Omega$ for used probe geometry of the atomic force microscope [21]. If measurements are made on electrodes with a larger contact area (S), the resistance of the polymer composite will decrease in proportion to the increase in S . For example, the calculated value resistance will be $\sim 1 \Omega$ for macroscopic electrodes with a contact area of $\sim 400 \mu\text{m}^2$.

The topography of the composite surface on silicon (a), as well as the current distribution (b) on it at a voltage $U = 3$ V is shown in Fig. 2(a). The current-voltage characteristic of the most conductive region of composite film on a silicon substrate and the silicon one are shown in Fig. 3. These current-voltage characteristics demonstrate non-linear behavior that may indicate the Schottky barrier presence in this case. Fig. 4 shows the composite surface topography on graphite (a), as well as the current distribution on it (b) taken at the voltage value of the electrode $U = 1$ V.

The dark areas in the Fig. 1(b), Fig. 2(b), and Fig. 4(b) correspond to low conductivity. Current distribution maps $I(x, y)$ were taken at voltages not exceeding the value of 10^6 V/cm to exclude electrical breakdown of the film.

There is a correlation between the topography of the surface and the current distribution: a current exceeding the noise is observed only at those points which dominate the nearest surrounding surface. A similar correlation between surface topography and current distribution is observed, even when the polymer was deposited onto other metal substrates. Moreover, the current-voltage characteristics at the points demonstrating high conductivity obey Ohm's law (Fig. 5). In addition, forward and reverse motions of the current-voltage characteristics have also been reproduced.

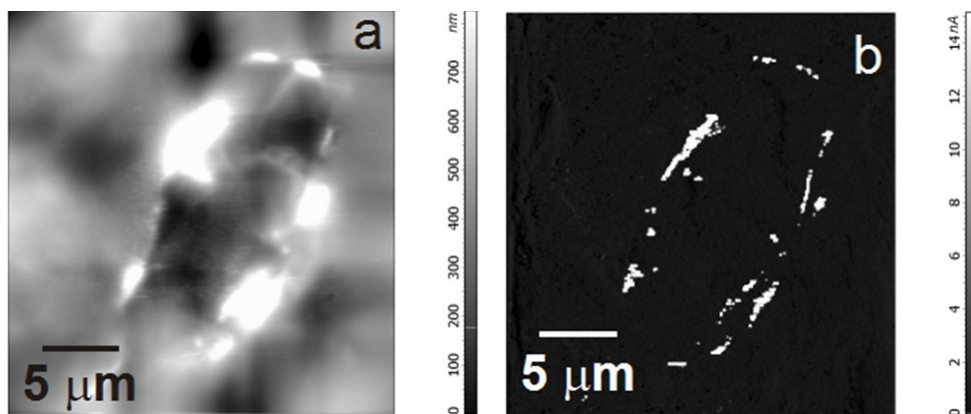


FIG. 1. Surface (a) and current (b) topography of a composite film deposited on a gold substrate at voltage of 3 V

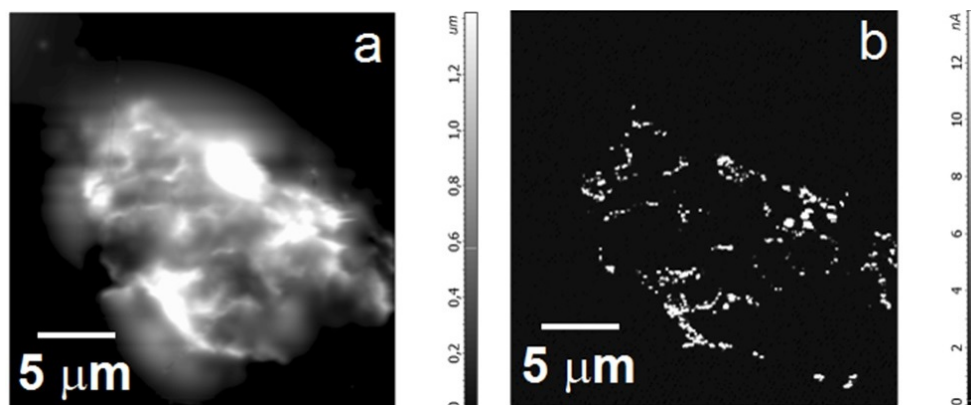


FIG. 2. Surface (a) and current (b) topography of a composite film deposited on silicon substrate at voltage of 3 V

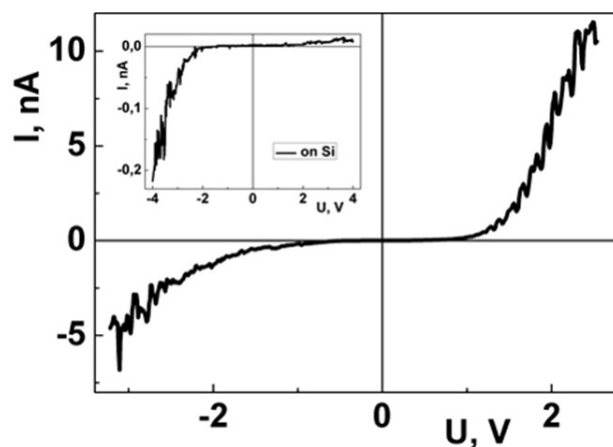


FIG. 3. Current-voltage characteristics of the conductive area of composite film on silicon substrate and the current-voltage characteristics of silicon (in insertion)

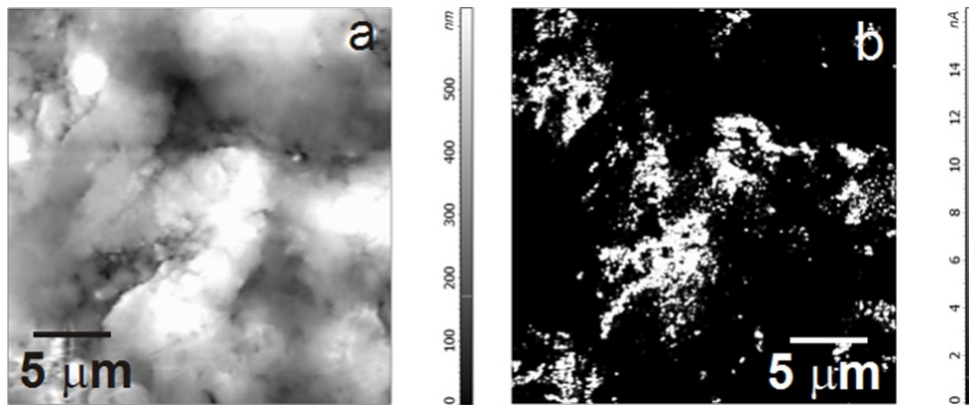


FIG. 4. Surface (a) and current (b) topography of composite film deposited on graphite substrate at a voltage of 1 V

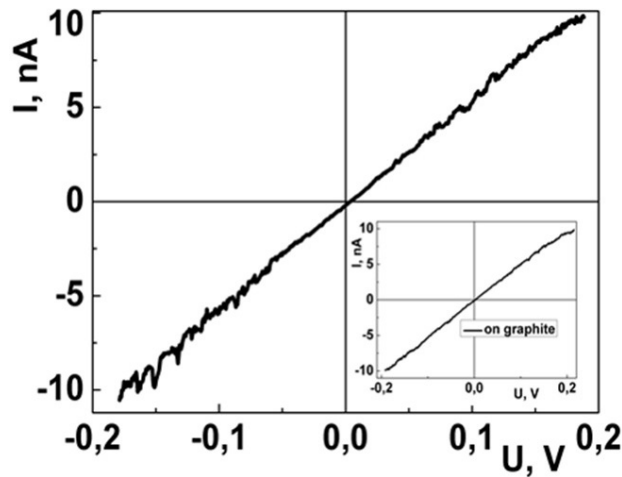


FIG. 5. Current-voltage characteristic of the conductive area of composite film on graphite substrate (a) and the current-voltage characteristic of graphite (in insertion)

Despite gold's high conductivity, the RGO/polystyrene resistance values on gold turned out to be comparable to the values for the composite film on silicon (Fig. 1(b), 2(b)) and amounted to approximately $2 \times 10^8 \Omega$. This result can be explained by weak adhesion of the RGO particles to the gold substrate. Thus, the resistance of the film conductive areas related to RGO is higher than the resistance of gold by more than one and a half orders of magnitude. The resistance of gold in our case is $5 \times 10^6 \Omega$, as was indicated above. It is also important to note that conductive areas for films on gold are much less than for films on graphite, in which the measured resistance of the composite conducting inclusions was of $3 \times 10^7 \Omega$. This is almost an order of magnitude lower than the RGO resistance on the gold substrate. The graphite substrate is obviously the most suitable material for achieving the high-conductivity state for polystyrene-based RGO composite films. The results obtained for the resistance and the conductive areas of composite films are probably related to the fact that both styrene rings and graphene inclusions are close in chemical nature to the graphite, creating the greatest surface adhesion. This facilitates the creation of numerous conducting channels through the composite film from the one electrode to the other. At the same time, the gold substrate for our type of composite does not promote good adhesion and gives high resistance values. One of the factors which improve adhesion, film contact force with silicon substrate and its conductivity obviously is 3-(trimethoxysilyl)propyl methacrylate.

It can be concluded that there is no relation between the conductivity of the RGO/polystyrene composite and the electron work function of substrate material, as was shown in [22]. For example, gold has an electron work function of about 4.7 eV. Thus, viewed composite films exhibit a low resistance on a gold substrate according to [22]. In fact, we see in present work the inverse situation.

The conductive area resistance of RGO/polystyrene film on a graphite substrate at room temperature is approximately 2 orders of magnitude lower, than its resistance on gold, and is equal to the neat graphite resistance.

In addition to the semiconductor values of conductivity that are typical for RGO at room temperature, the metallic type of conductivity is observed in composites with decreasing temperature to that of liquid nitrogen [13], as well as superconducting properties when their thickness is about 150 nm [15, 16]. This unusual character for the temperature dependences of resistance requires theoretical explanations. The authors of [23] propose that sufficiently high density of states for such systems as considered RGO/polystyrene composite results in the high temperature of either spin ordering or superconducting pairing.

4. Conclusions

Films of RGO/polystyrene composite which demonstrate superconducting features under special conditions were investigated by the CAFM method. The experiments showed that the density of the conductive areas on the surface of the polymer films with the same thicknesses and the absolute values of the current intensity depend on the substrate's nature, as well as the applied electric field at the metal/polymer contact area. The minimum resistance of the RGO/polystyrene film areas was $3 \times 10^7 \Omega$ when using this tip geometry and under the conditions of the best adhesion on graphite, which approximately corresponds to the graphite resistance.

Acknowledgements

We are grateful to Alexander N. Ionov and to Leonid N. Ionov (Ioffe Institute) for useful discussion and for gold substrate preparation. A. T. Dideikin acknowledges RFBR, grant 15-02-05153, for support.

References

- [1] Rani A., Nam S., et al. Electrical conductivity of Chemically reduced graphene powders under compression. *Carbon Lett.*, 2010, **11**(2), P. 90–95.
- [2] Neustroev E.P., Nogovitsyna M.V., Solovyova Yu.S., et al. Study of electrical conductivity of thermally reduced graphene oxide. *RENSIT*, 2015, **7**(2), P. 162–167.
- [3] Chen Y., Fu K., Zhu S., et al. Reduced graphene oxide films with ultrahigh conductivity as Li-ion battery current collectors. *Nano Lett.*, 2016, **16**(6), P. 3616–3623.
- [4] Jungo S.T., Oh S.H., Kim H.B., et al. The optical and electrical properties of graphene oxide with water-soluble conjugated polymer composites by radiation. *J. Nanosci. Nanotechnol.*, 2013, **13**(11), P. 7358–7364.
- [5] Nirmala R., Navamathavan R., Kim H.Y., Park S.J. Electrical properties of conductive nylon66/graphene oxide composite nanofibers. *J. Nanosci. Nanotechnol.*, 2015, **15**(8), P. 5718–22.
- [6] Chamingkwan P., Matsushita K., Taniike T., Terano M. Enhancement in mechanical and electrical properties of polypropylene using graphene oxide grafted with end-functionalized propylene. *Materials*, 2016, **9**, P. 240–253.
- [7] Syurik Ju., Alyabyeva N., Alekseev A., Ageev O.A. AFM-based model of percolation in graphene-based polymer nanocomposites. *Composite Science and Technology*, 2014, **95**, P. 38–43.
- [8] Song M. Graphene functionalization and its application to polymer composite materials. *Nanomater. and en.*, 2013, **2**, P. 97–111.
- [9] Mikoushkin V.M., Shnitov V.V., Nikonov S.Yu. et al. Controlling graphite oxide bandgap width by reduction in hydrogen. *Tech. Phys. Lett.*, 2011, **37**(10), P. 942–945.
- [10] Aleksenskii A.E., Brunkov P.N., Dideikin A.T. et al. Single-layer graphene oxide films on a silicon surface. *Tech. Phys.*, 2013, **58**(11), P. 1614–1618.
- [11] Nikolaeva M.N., Anan'eva T.D., Bugrov A.N. et al. Correlation between structure and resistance of composites based on polystyrene and multilayered graphene oxide. *Nanosystems: physics, chemistry, mathematics*, 2017, **8**(2), P. 266–271.
- [12] Yevlampieva N., Bugrov A., Anan'eva T., et al. Soluble poly (methyl methacrylate) composites containing covalently associated zirconium dioxide nanocrystals. *Am. J. Nano Res. and Appl.*, 2014, **2**(2), P. 1–8.
- [13] Khairullin A.R., Nikolaeva M.N., Bugrov A.N. Resistance of the composite films based on polystyrene and graphene oxide. *Nanosystems: physics, chemistry, mathematics*, 2016, **7**(6), P. 1055–1058.
- [14] Nikolaeva M.N., Bugrov A.N., et al. Conductive properties of the composite films of graphene oxide based on polystyrene in a metal-polymer-metal structure. *Russ. J. Appl. Chem.*, 2014, **87**(8), P. 1151–1155.
- [15] Ionov A.N. Josephson current-voltage characteristic of a composite based on polystyrene and graphene oxide. *Tech. Phys. Lett.*, 2015, **41**(7), P. 651–653.
- [16] Ionov A.N. Josephson-Like Behaviour of the Current-Voltage Characteristics of Multi-graphene Flakes Embedded in Polystyrene. *J. Low Temp. Phys.*, 2016, **185**(5-6), P. 515–521.
- [17] Duke C.B., Fabish T.J. Charge-induced relaxation in polymers. *Phys Rev Lett.*, 1976, **37**, P. 1075–1078.
- [18] Ionov A.N., Nikolaeva M.N., Rentzsch R. Local distribution of high-conductivity regions in polyamide thin films. *JETP Letters*, 2007, **85**(12), P. 636–638.
- [19] Hummers W., Offeman R. Preparation of graphitic oxide. *J. Am. Chem. Soc.*, 1958, **80**(6), P. 1339–1339.
- [20] Nikolaeva M., Boiko Y., Martynenkov A. Supramolecular structure and conductive properties of dielectric polymers in metal/polymer/metal systems. *Int. J. Polym. Mater.*, 2013, **62**(13), P. 706–710.
- [21] Ionov A.N., Nikolaeva M.N., Rentzsch R. Local distribution of high-conductivity regions in polyamide thin films. *JETP Letters*, 2007, **85**(12), P. 636–638.
- [22] Ionov A.N., Dunaevskii M.S., Nikolaeva M.N., et al. The dependence of polymer conductivity on the work function of metallic electrodes. *Ann. Phys.*, 2009, **18**(12), P. 959–962.
- [23] Volovik G.E., Pudalov V.M. Graphite on graphite. *JETP Letters*, 2016, **104**(12), P. 880–882.

Revisiting preparation routes of SERS materials

A. A. Semenova¹, I. A. Semenova², A. P. Semenov², E. A. Gudilina³, E. A. Goodilin^{1,4,*}

¹Lomonosov Moscow State University, Faculty of Materials Science, Lenin Hills, Moscow, 119991, Russia

²Institute of Physical Materials Sciences of Siberian Branch of the Russian Academy of Sciences, Buryatia Republic, Ulan-Ude, 670047, Russia

³FSBI “N. N. Blokhin National Medical Research Center of Oncology” of the Ministry of Health of the Russian Federation, Moscow, 115478, Russia

⁴Kurnakov Institute of General and Inorganic Chemistry of the Russian Academy of Sciences, Moscow, 119992, Russia

*goodilin@yandex.ru

PACS 61.46.Hk, 62.23.St, 68.35.bd

DOI 10.17586/2220-8054-2017-8-5-670-676

For the first time, a systematic study of a background noise to signal ratio is given for various preparation histories of consolidated silver nanoparticles and artificially prepared nanostructures to rate the best and the worst routes of deposition of surface-enhanced Raman spectroscopy (SERS) active layers. It is shown that most of common preparation schemes face with a high intensity of extra peaks in the ca. 900–1100 and 1400–1700 cm^{-1} range as related to residual adsorbed / chemisorbed nitrate, nitrite ions and organic oxidation products of various pollutants formed in the course of Ag^+ redox reactions. Finally, Leopold–Lendl and the original USR (Ultrasonic Silver Rain) methods would be recommended for the highly sensitive SERS analysis of diluted solutions and impurities.

Keywords: SERS, silver, nanostructures, nanoparticles, preparation methods, background.

Received: 20 August 2017

Revised: 23 August 2017

1. Introduction

The Surface-enhanced Raman spectroscopy (SERS) method has become one of the most powerful and universal tool for modern analytics in pharmacology, ecology and potentially noninvasive biomedical diagnostics for screening and personal medicine [1–5]. Silver nanoparticles and nanostructured materials are a common choice for SERS measurements due to their broad plasmon resonance, high stability, facile fabrication methods and the largest enhancement for special molecules [3–5]. A complex morphology such as nanoflowers, nanorices, cubes, multipods and nanodendrites, mesocages is achieved by kinetically controlled, aggregation-based, heterogeneously seeded, template-directed growth, selective etching and colloidal system aging; the polyol technique allows one to synthesize silver nanoparticles of a wide variety of shapes and sizes [6–16]. Despite of all possible advantages, the nanoparticles themselves are likely to aggregate uncontrollably in solutions, making it difficult to reproduce SERS results [5, 6, 11, 14]; nanoparticle sols exhibit limited plasmonic tunability as compared to a new class of nanomaterials – colloidosomes composed of a dielectric core and a concentric metal shells with hybridization of plasmon modes supported by an inner cavity and an outer surface of the nanoshell [5, 7, 9, 10]. However, SERS still suffers a lack of reproducibility due to the masking of SERS signals by surfactants or by-products, gradients of electric fields near the nanoparticles and variations of molecule positions with respect to the nanoparticles; commonly used linkers, surfactants, reducing agents and their oxidized forms, halide ions can change the characteristic properties of nanoparticles because of their aging, recrystallization or random formation of aggregates [5, 11–14]. Nanostructured substrates promise much better reproducibility and less toxicity promoting their SERS applications in biology and medicine, especially in highly sensitive lab-on-a-chip devices [5, 11, 13–15]. However, the coming wave of SERS development admits a challenge of development of highly sensitive and reproducible low cost nanomaterials vitally demanded for SERS. In this paper, a systematic study of a background noise to signal ratio is given for various preparation histories of consolidated silver nanoparticles to rate the routes of deposition of SERS active layers in the sake of practical development of SERS active materials for novel operating sensor devices.

2. Experimental

Silver nitrate (AgNO_3), sodium hydroxide (NaOH), ammonium hydroxide (NH_4OH , 30 %), ascorbic acid, polyvinylpyrrolidone (PVP), sodium borohydride (NaBH_4), sodium citrate, hydrogen peroxide (H_2O_2 , 10 %), hydrochloric acid (HCl), Rhodamine 6G (Rh6G) were of high purity grade. In all the experiments, ultra-pure

water with resistivity ca. 18 M Ω -cm (Milli-Q, Millipore) was used. Several series of silver nanoparticles and nanostructures were prepared (Table 1) according to known (Series A–C, I) [1–3, 6, 7, 11–17] and new schemes (Series D–H, J).

TABLE 1. Series of experimental nanostructured silver samples and their preparation schemes

Series	Preparation scheme
Series A	Direct reduction of silver nitrate (0.01 – 0.001 M) with ascorbic acid (0.01 – 0.001 M)
Series B	Direct reduction of silver nitrate (0.01 – 0.001 M) with NaBH ₄ (0.01 – 0.001 M)
Series C	Silver platelets preparation by grain selective regrowth of nuclei [11, 14]
Series D	Direct reduction of fresh water suspension of solid silver (I) oxide with an excess of H ₂ O ₂ (0.1 – 0.01 M)
Series E	Direct reduction of silver nitrate (0.01 – 0.001 M) with water suspension of SnCl ₂
Series F	Reduction of diamminesilver hydroxide with hot microfiber cellulose suspension
Series G	Reduction of diamminesilver hydroxide with hot graphene oxide suspension
Series H	Reduction of suspension of silver (I) chloride in hydrochloric acid (0.01 M) with metallic aluminum (hydrogen <i>in situ</i>)
Series I	The Leopold–Lendl method, reduction of silver nitrate with alkali solution of hydroxylamine hydrochloride [6, 8, 16]
Series J	Soft thermal pyrolysis of diamminesilver hydroxide [5, 12, 15]

The samples of Series A and B were prepared by simple reduction of silver (I) nitrate in aqueous solution with commonly used organic and inorganic substances as noted in Table 1.

In accordance with our previous publications [11, 14], highly pure water, silver (I) nitrate, sodium citrate, PVP, NaBH₄, ascorbic acid were used as reagents to prepare silver nanoplates in the Series C (Table 1). Initially, silver (I) nitrate was reduced by NaBH₄ in the presence of sodium citrate to form a seeding solution of spherical silver nanoparticles. In particular, 11 ml aqueous solution of 0.11 mM AgNO₃ and 2.05 mM sodium citrate were mixed quickly, under vigorous stirring, with 0.3 ml of freshly prepared 5 mM aqueous solution of NaBH₄. The stirring has been stopped in 10 min. The yellow sol thus obtained was maintained for 5 hrs at room temperature and then placed in a dark place at 4 °C for storage as a seeding solution. On the second stage, a mixture of aqueous solutions of 0.25 ml of 5 mM AgNO₃, 0.75 ml of 30 mM sodium citrate, 0.75 ml of 0.7 mM (with respect to repeating fragment – chain) of PVP in 9.25 ml of pure water was added to a series of aliquots of the seeding solution, namely 0.9, 2.7, 3.6, 5.3, 6.9, 12.9, 18.2, 22.9, 30.8, 37.2, 52.7 vol.%, followed by an addition of 6.25 ml of 1 mM of ascorbic acid. The solution color was found to start its changing immediately after ascorbic acid injection then it has become permanently stable after about 15 min. Thus, prepared sols were purified by repeated centrifugation (19,900 rpm for 10 min, Sartorius Sigma 3–30 K) followed by gentle dilution with pure water, after that they were stored at 4 °C in darkness.

In the Series D, silver (I) oxide prepared as in the Series C, was reduced to nanoparticles using hydrogen peroxide solutions while in the Series E, a suspension of soft reducing species SnCl₂ was used to get a composite with silver nanoparticles from silver nitrate solution (Table 1). In the Series F and G diamminesilver hydroxide solution was heated at 90–95 °C together with either suspension of microfiber cellulose or graphene oxide for about 30–60 min to deposit silver nanoparticles reduced by superficial groups of the substances onto the surface of cellulose or graphene (Table 1). In the Series H, silver chloride suspension was rapidly reduced by hydrogen “in situ” in the environment of hydrochloric acid, metallic aluminum was applied to generate hydrogen (Table 1). The Series I was exactly the silver colloid prepared by the classical Leopold and Lendl scheme [16] (Table 1).

In order to prepare silver ring nanostructures in the Series J, our original procedure [5, 12, 15, 17] was slightly modified (Table 1). SERS-active substrates containing nanostructured silver were prepared using spray pyrolysis deposition of aqueous diamminesilver hydroxide. Aqueous sodium hydroxide solution (0.1 M) was added dropwise to a freshly prepared aqueous silver nitrate solution (10 mM) until complete precipitation of a black-brown silver (I) oxide. Then, the prepared oxide was thoroughly washed with deionized water and dissolved in a two-fold molar excess of a 10 % aqueous ammonia solution (prepared from 30 % ammonium hydroxide) to give a

0.0125 M solution of a silver (I) complex; a higher concentration deteriorates the silver ring structure formation while superstoichiometric ammonia is needed to prevent Ag_2O precipitation at the aerosol production stage. The obtained transparent silver complex solution was filtered through Millex-LCR syringe driven filter units (Millipore, 0.45 μm pores). In the ultrasonic silver rain (USR method) deposition process, this initial ammonia solution of silver (I) oxide was nebulized into mist and 1–5 μm droplets were streamed onto “warm” (270–290 $^\circ\text{C}$) glasses.

The obtained materials were examined by XRD measurements using Rigaku D/MAX 2500 (Japan) with a rotating copper anode ($\text{CuK}\alpha$ irradiation, 5–90 $^\circ 2\theta$ range, 0.02 $^\circ$ step). Diffraction maxima were indexed using the PDF-2 database. UV-vis absorption spectra were recorded using the UV-vis spectrophotometer Lambda 950 (Perkin-Elmer) with an attached diffuse reflectance accessory. Measurements were in the spectral range 250–850 nm with a step scan of 1 nm. Raman and SERS experiments were performed using InVia Raman microscope (Renishaw, UK) equipped with a 20 mW 514 nm argon laser and power neutral density filter (10 %). All the spectra were collected using $\times 50$ objective lens and 10 s of acquisition time. A silicon wafer was used for calibration.

3. Results and discussion

It is almost a common belief that formation of silver nanoparticles of a certain size by most of preparation methods guarantees SERS amplification of any substance [1–3]. Unfortunately, it is not as simple and certain as reported, and a lot of criteria should be satisfied prior achieving essential SERS effects [5–15, 17, 18]. It is also obvious that intense background peaks would be one of the most serious reasons to expect worsening analytical signals of SERS-based sensors. The data of Fig. 1 and Table 1 demonstrate that such drawbacks are unexpectedly common for many usual preparation schemes despite of the feelings one could expect after reading the literature; such unsatisfactory backgrounds are observed with no respect to application of either organic or inorganic reducing agents [1–3].

Silver itself has lattice vibrations and some special modes only in the range of 50–250 cm^{-1} , these modes (especially the 230–235 cm^{-1} line) are clearly seen if silver is nanodispersed (Fig. 1) while all other peaks would not be related to metallic silver [19]. Thus the most expected reasons of the observed high background signals (Fig. 1) include the tremendous affinity of nanoparticle ensemble, possessing highly developed surface area values, with respect to the preparation byproducts. This is, in turn, connected with unsaturated superficial silver bonds, the existence of high zeta-potentials and a double layer for the nanoparticles in reacting solutions, moreover formation of aggregated nanoparticle structures results in capillary absorption and all of these factors lead to blocking the nanoparticle surface with the chemisorbed molecules of reactants, product impurities or surfactants applied for the synthesis. This finally means that these impurities should provide a certain number of Raman peaks strongly enhanced in intensities due to the SERS effect, thus creating a noisy background including an important spectral range of 1000–1700 cm^{-1} and the fingerprint area of 2500–3000 cm^{-1} (Fig. 1, Table 2).

As evident from Fig. 1 and Table 2, the most widely used reductants like ascorbic acid, NaBH_4 and hydrogen peroxide give a risk of a noisy background. In the case of hydrogen peroxide, the background appears because of substances stabilizing H_2O_2 such as polyphosphates, salicylic acid, etc. contributing their own modes to the spectra. The same reason leads to the peaks in the case of ascorbic acid which is one of the carbon acids with typical vibrations of the $-\text{CO}_2$ fragment, some other peaks could be given by its oxidation products chemisorbed onto the silver surface. NaBH_4 is degradable in surrounding moisture and CO_2 atmosphere giving carbonate-like peaks and some peaks near 3000 cm^{-1} due to the precipitation of $\text{B}_2\text{O}_3 \cdot x\text{H}_2\text{O}$ with internal hydrogen bonds; peaks near 1000 cm^{-1} would be related to chemisorbed nitrates. The least intense background is demonstrated by the nanostructured silver prepared by reduction with hydroxylamine hydrochloride in ammonia environment of silver chloride purified by repeated washing and centrifugation after its precipitation with an excess of hydrochloric acid from silver nitrate. Such a procedure gets rid of nitrates and other impurity ions; the inorganic reductant forms gaseous nitrogen which could not disturb SERS spectra measurements. Small peaks at 1300–1550 cm^{-1} are most probably related to amide bonds forming between silver and residual ammonia. The peaks near 3000 cm^{-1} seem to be attributed to hydrogen bonds in water absorbed with aggregated structure of silver nanoparticles [20]. For example, an application of hydroxyethylcellulose, swelling in both hydrophilic and hydrophobic environment, combined with the Series I samples, gives a small worsening of the background signal mostly because of hydrogen bonds associated with residual water. Microcellulose carriers are cheap and easily available materials with a small Raman cross-section. Precipitation of silver nanoparticles by a direct reaction of cellulose suspension with a hot (80–90 $^\circ\text{C}$) 0.001–0.01 M solution of diamminesilver hydroxide for 10–15 min gives latter a dry material with a high absorption ability and a low background signal (Table 2).

Finally, thermal decomposition of diamminesilver hydroxide solutions (see the Experimental part) allows preparing nanostructured silver materials with a uniformly low background signal not exceeding 3–5 % of analyte

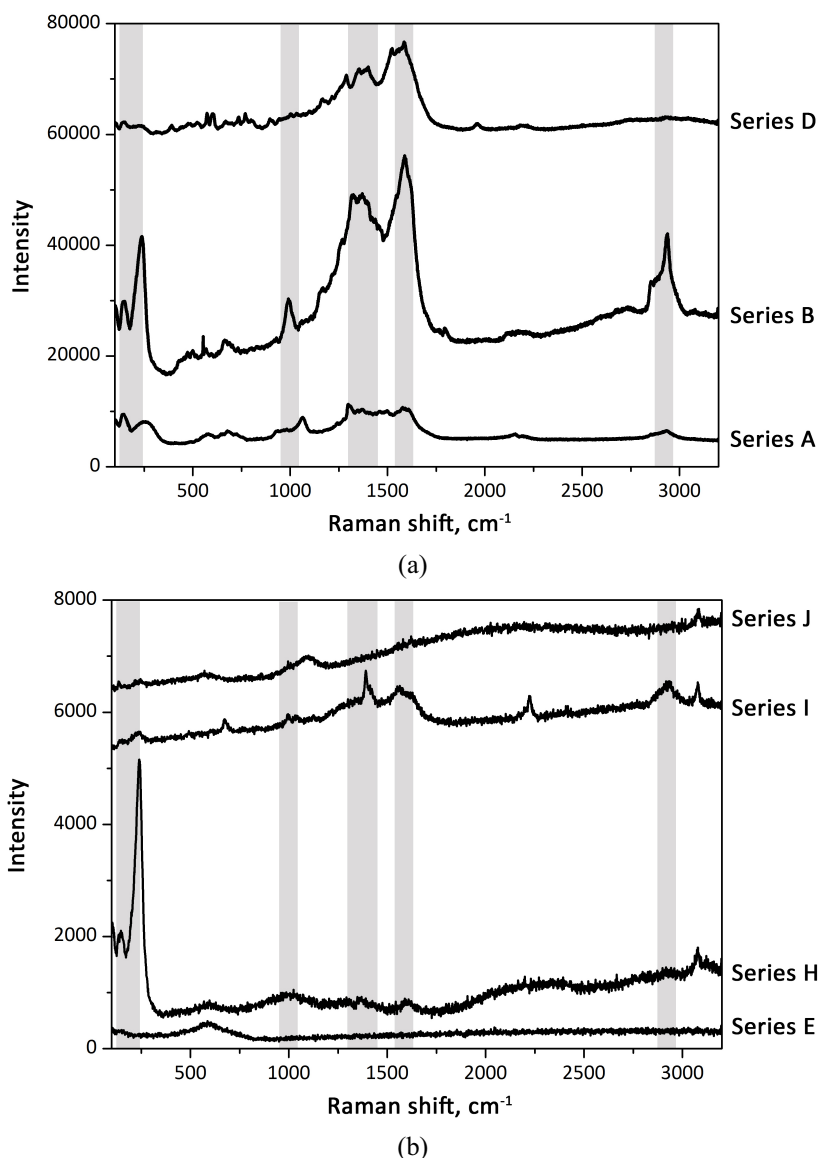


FIG. 1. Typical raw background signals of dried powdered silver nanoparticles with a different preparation history: (a) series with a large backgrounds, (b) series with smooth and low background signal

signals in the whole working range of our spectrometer. The latter becomes possible because of a combination of highly nonequilibrium preparation conditions guaranteeing a small size for the formed nanoparticles and their aggregates and also high enough temperatures prevent the physical adsorption and chemisorption of byproducts. Moreover, pyrolytic deposition is a scalable method suitable for preparation of either nanoparticles of a complex shape or planar nanostructures [12, 13, 15]. All of such nanostructures reveal the large number of “hot spots” and are free of nonvolatile impurities since there are no special reductants or surfactants applied in the preparation route of these original materials. Fig. 2 evidently demonstrates that the nanostructured samples with selected preparation histories diminishing background signals show remarkable enhancement coefficients and seem to be effective materials for the development of new SERS sensors.

From a chemical perspective, thermal treatment of ultrasonic mists of the diamminesilver hydroxide complex provides irreversible decomposition and solvent evaporation. The products of this transformation include silver nanostructured particles, water, ammonia and oxygen. Quenching of such products yields nanostructured particles and their aggregates formed in a shock manner, since the whole transformation occurs for few seconds at high temperatures [12, 13, 15]. High-temperature silver microspheres of about 100 nm in size are typical for aerosol spray pyrolysis because of solvent evaporation from mist droplets and spontaneous formation of silver nuclei

TABLE 2. Functional properties of samples with different preparation schemes

Series of samples	Background signal / observed Raman background peaks for pure consolidated sample of nanostructure silver nanoparticles or nanostructures	SERS activity with respect to Rhodamine 6G (Rh6G)
A	Strong, peaks at 150, 240, 1300–1400, 1600, 2900 cm^{-1}	Average, 10^{-6} M
B	Strong, peaks at 150, 240, 1300–1400, 1600, 2900 cm^{-1}	Average, 10^{-6} M
C	Average, peaks at 150, 240, a wide double peak at 1300–1600, 2900 cm^{-1}	Average, 10^{-6} M
D	Strong, peaks at 150, 240, 1300–1400, 1600, 2900 cm^{-1}	Average, 10^{-6} M
E	Weak, peaks at 150, 240 cm^{-1}	Small, 10^{-4} M
F	Average, peaks at 1300 – 1400, 1600, 2900 cm^{-1}	Good, 10^{-8} M
G	Average, peaks at 1400, 1600 (D, G modes) cm^{-1}	Average, 10^{-6} M
H	No obstacles from background	No activity, bulk metallic silver
I	Weak, peaks at 150, 240, 1100, 2900 cm^{-1}	High, 10^{-8} – 10^{-10} M
J	No obstacles from background	High, 10^{-8} – 10^{-10} M

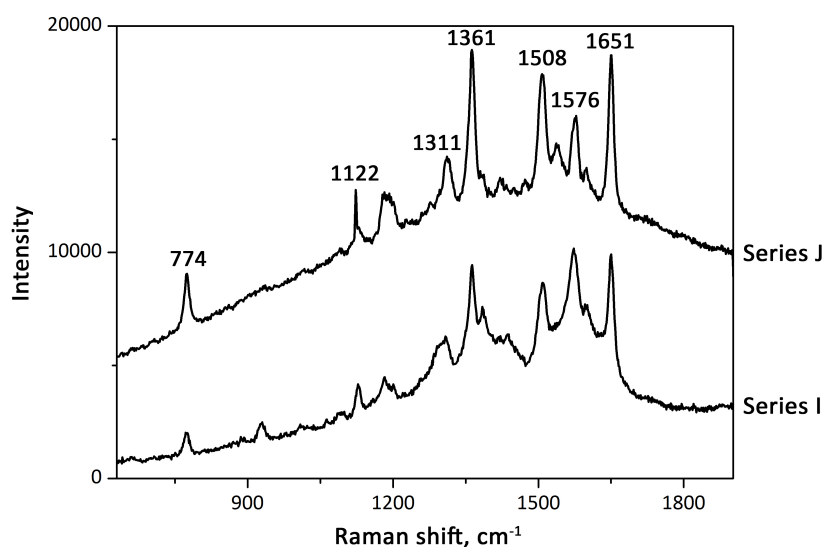


FIG. 2. Typical SERS spectra of model analyte (Rh6G dye) in different concentrations recorded using silver nanostructures: 1 % of laser power, 10 s of acquisition time, 10^{-7} M Rh6G (Series J), 5 % of laser power, 10 s recording, 10^{-8} M Rh6G (Series I)

joining into a porous “orange skin” layer. Polyhedral aggregates formed could be a consequence of primary silver (I) oxide formation within the mist droplets prior its decomposition. In the case of application of warm substrates (see the Experimental part), silver ring structures caused by the known “coffee ring” effect are formed at moderate temperatures of 200–250 °C due to the deposition of the mist droplets onto a preheated substrate (Fig. 3). The coatings consist of overlapping silver rings of a complex morphology originated from decomposition of micron-sized droplets of ultrasonic mist of silver (I) solution. This resembles a rain making rings on a flat dusty surface hence we call it UltraSonic Silver Rain (USR method). Usually, silver deposition gives intersecting circles of 30–100 μm in diameter. This value is several times larger than the expected size of 1–10 μm of the falling mist droplets as occurred because the liquid from the droplets spreads laterally over the substrate. Solvent evaporation increases concentration of the silver complex and then metallic silver resides on rims of the spreading circles producing walls of silver craters. The thickness of walls lies typically in a range of 1–3 μm while the

residual part is covered with sparse silver nanoclusters gradually increasing in their sizes from 10–20 nm in the centers of circles to about 100 nm in the wall vicinities. The nanoclusters increase the role of capillary forces and, afterwards, more droplets stack onto the surface, boil, decompose; an increase of sputtering time leads to rough and porous layers. This deposition mode has several advantages in terms of manufacturing SERS-active structures for promising applications: silver micro- and nanostructures are immobilized onto a substrate and form a rather stable metallic film on cheap materials like glass; there is no need to filter or separate nanoparticles; the nanostructure consists of porous silver sponge only; the temperatures are high enough for the one-stage formation of metallic silver nanostructured layer. The negligible background of the USR substrates allowed to use small laser power that prevents photoinduced damage of biological objects and ensures repeated measurements of SERS even from the same point [7, 15]. Thus, this preparation technique is the method of choice for preparation of functional components for new SERS devices.

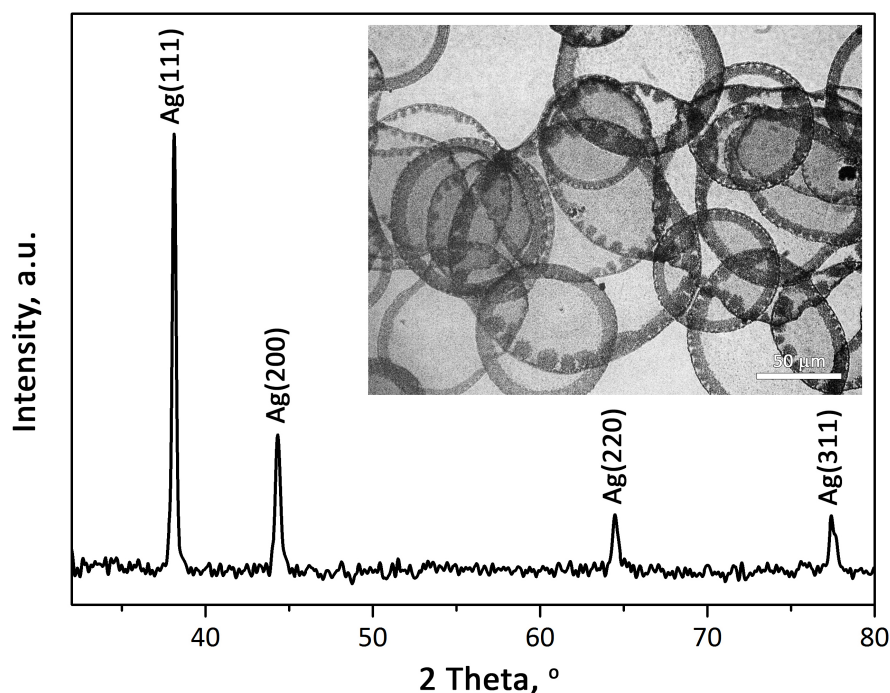


FIG. 3. Microstructural features of SERS-active samples with the pyrolysis preparation history (Series J): typical XRD data of the chemically coated silver substrates and transmission optical images of the ring structures (inset)

4. Conclusions

A systematic study of a background noise to signal ratio for various preparation histories of consolidated silver nanoparticles and artificially prepared nanostructures allowed us to rate the best and the worst routes of deposition for SERS active layers. It is shown that most of common preparation schemes face a high intensity of parasitic unidentified peaks in the ca. 900–1100 and 1400–1700 cm^{-1} regions as related to residual adsorbed/chemisorbed nitrate, nitrite ions and organic oxidation products of various pollutants formed in the course of Ag^+ redox reactions. Finally, the Leopold–Lendl route and the original USR spray deposition method would be recommended for the highly sensitive SERS analysis of dilute solutions and impurities. The USR synthesis seems to be the method of choice for preparing functional components for new SERS devices.

Acknowledgements

This research is supported by the Grant of the President of Russian Federation for the governmental support of young scientists (#MK-1146.2017.3).

References

- [1] Alvarez-Puebla R.A., Liz-Marzan L.M. SERS-based diagnosis and biodetection. *Small*, 2010, **6** (5), P. 604–610.
- [2] Sharma B., Frontiera R.R., et al. SERS: Materials, applications, and the future. *Mater. Today*, 2012, **15** (1–2), P. 16–25.
- [3] Yuan Y., Panwar N., et al. SERS-based ultrasensitive sensing platform: An insight into design and practical applications. *Coord. Chem. Rev.*, 2017, **337**, P. 1–33.
- [4] Tretyakov Y.D., Goodilin E.A. Chemical principles of the metall-oxide superconductors preparation. *Uspekhi khimii*, 2000, **69** (1), P. 3–40.
- [5] Semenova A.A., Semenov A.P., et al. Nanostructured silver materials for noninvasive medical diagnostics by surface-enhanced Raman spectroscopy (focus article). *Mendeleev Communications*, 2016, **26** (3), P. 177–186.
- [6] Brazhe N.A., Parshina E.Y., et al. Tuning SERS for living erythrocytes: Focus on nanoparticle size and plasmon resonance position. *Journal of Raman Spectroscopy*, 2013, **44** (5), P. 686–694.
- [7] Brazhe N.A., Evlyukhin A.B., et al. Probing cytochrome c in living mitochondria with surface-enhanced Raman spectroscopy. *Scientific reports*, 2015, **5**, 13793.
- [8] Parshina E.Y., Sarycheva A.S., et al. Combined Raman and atomic force microscopy study of hemoglobin distribution inside erythrocytes and nanoparticle localization on the erythrocyte surface. *Laser Physics Letters*, 2013, **10** (7), 075607(6 pp.).
- [9] Sarycheva A.S., Brazhe N.A., et al. New nanocomposites for SERS studies of living cells and mitochondria. *Journal of Materials Chemistry B*, 2016, **3** (4), P. 539–546.
- [10] Sarycheva A.S., Ivanov V.K., et al. Microbead silica decorated with polyhedral silver nanoparticles as a versatile component of sacrificial gel films for SERS applications. *RSC advances*, 2015, **5** (110), P. 90335–90342.
- [11] Semenova A.A., Goodilin E.A. Surface enhanced Raman spectroscopy substrates with advanced spectral sensitivity prepared from five years old silver nanoplatelets. *Functional materials letters*, 2016, **9** (6), 1642003(4 pp.).
- [12] Semenova A.A., Ivanov V.K., Savilov S.V., Goodilin E.A. Unusual silver nanostructures prepared by aerosol spray pyrolysis. *Cryst. Eng. Comm.*, 2013, **15** (39), P. 7863–7871.
- [13] Semenova A.A., Brazhe N.A., et al. Aqueous diamminesilver hydroxide as a precursor of pure silver nanoparticles for SERS probing of living erythrocytes. *Plasmonics*, 2014, **9** (2), P. 227–235.
- [14] Semenova A.A., Brazhe N.A., et al. A new route of SERS analysis of intact erythrocytes using polydisperse silver nanoplatelets on biocompatible scaffolds. *RSC advances*, 2016, **6** (88), P. 85156–85164.
- [15] Semenova A.A., Goodilin E.A., et al. Planar SERS nanostructures with stochastic silver ring morphology for biosensor chips. *Journal of Materials Chemistry*, 2012, **22** (47), P. 24530–24544.
- [16] Leopold N., Lendl B. A new method for fast preparation of highly surface-enhanced Raman scattering (SERS) active silver colloids at room temperature by reduction of silver nitrate with hydroxylamine hydrochloride. *Journal of Physical Chemistry B*, 2003, **107** (24), P. 5723–5727.
- [17] Semenova A.A. Silver based nanostructured materials for biomedical diagnostics by Surface-enhanced Raman spectroscopy, PhD thesis, Moscow, 2012, 199 pp.
- [18] Sidorov A.V. Chemically modified nanocomposites of silver for Surface-enhanced Raman spectroscopy of raw oil products, PhD thesis, Moscow, 2016, 220 pp.
- [19] Kurbatova N.V., Galyautdinov M.F., et al. Low-temperature Raman spectroscopy of copper and silver nanoparticles ion-synthesized in a silica glass and subjected to laser annealing. *Physics of the Solid State*, 2010, **52** (6), P. 1255–1259.
- [20] Kochkina N.E., Skobeleva O.A., Khokhlova Yu.V. Synthesis of silver nanoparticles in DMSO solutions of starch: a comparative investigation of native and soluble starches. *Nanosystems: Physics, chemistry, mathematics*, 2015, **6** (3), P. 405–411.

Universal mechanism of tetrahedral metal cluster formation in structures with breathing pyrochlore sublattices

M. V. Talanov¹, V. M. Talanov²

¹Research Institute of Physics, Southern Federal University, Rostov-on-Don, Russia

²South-Russian State Polytechnical University, Novocherkassk, Russia

tmikle-man@mail.ru, valtalanov@mail.ru

PACS 61.50.Ks; 36.40.-c

DOI 10.17586/2220-8054-2017-8-5-677-687

A universal mechanism of tetrahedral metal cluster formation in crystal with geometrically frustrated pyrochlore sublattices is proposed. It has been shown that the critical irreducible representation τ , which generated the formation of metal clusters in non-centrosymmetrical $F\bar{4}3m$ -phases from high symmetry phases with $Fd\bar{3}m$ space group, is a one dimensional irreducible representation $\kappa_{11}(\tau_4(A_{2u}))$ (in Kovalev notation). The structural theory of metal cluster formation based on group theoretical calculations was published earlier for the case of A-ordered spinel. In this work, the theory is generalized in the case of any high symmetry $Fd\bar{3}m$ structures that include pyrochlore sublattices. We presented a brief review of such structures and mechanisms of the tetrahedral metal cluster formation. The existence of so called “breathing” pyrochlore sublattices in ordered phases is predicted theoretically. The groups of atoms, between which bond clusters, are found. These groups of atoms define electron correlation effects. Examples of tetrahedral metal cluster formation in ordered spinels, ordered lacunar spinels, ordered Laves phases ($MgCu_4Sn$ structural type) and ordered pyrochlore are considered. The theoretical results are confirmed by the known experimental facts.

Keywords: tetrahedral clusters, ordered spinel, ordered Laves phases, ordered pyrochlore, geometrical frustration, breathing pyrochlore sublattices.

Received: 10 August 2017

Revised: 1 September 2017

1. Introduction

Geometric frustration is an old topic of physics and solid state chemistry [1–4]. L. Pauling, using the example of crystalline ice, has shown the existence of different orientations of water molecules, which do not lead to a change in the energy of the system [5, 6].

The paradigm of geometric frustration is used in different scientific fields: for the description of the non-trivial packing of polyhedra in three-dimensional space in systems such as quasi-crystals; for amorphous metals and nematic disclination networks in densely packed 3D colloidal lattices; in the theory of magnetism when the arrangement of spins on a lattice does not satisfy all interactions at the same time; for the study of the orientation order in the proton configurations in ordinary hexagonal ice and for spins in magnetic molecules and artificial magnetic architectures.

The term “geometrical frustration” describes the structures with local order generated by the lattice geometry. Frustration arises when the geometry of any system allows for a set of degenerate ground states. Such highly degenerate systems are extremely sensitive to thermal and quantum fluctuations, and thereby intriguing classical and quantum ground states may emerge via “order by disorder”.

The important physical properties of many inorganic crystals are connected with a structural feature – a three-dimensional network of the tetrahedra formed by cations. A network of these tetrahedra is called a pyrochlore sublattice. Some such pyrochlore sublattices are in the following: spinels AB_2X_4 (where the B site displays a pyrochlore sublattice); pyrochlores $A_2B_2O_7$ (where both A and B sites form corner-sharing tetrahedra); and Laves phases (C15) AB_2 (where B-metal atoms form a pyrochlore sublattice). There are hundreds of compounds crystallizing in these structural types. The geometrical frustration of spins results in the formation of exotic electronic and structural state in these substances. One of these states is spin liquid.

P. W. Anderson was the first to show that B-sublattice (pyrochlore sublattice) in spinel structure is geometrically frustrated and causes the unusual physical properties of this class of materials [4].

In this paper, we theoretically establish the universal structural mechanism for the formation of metal clusters namely metal tetrahedra in inorganic crystals with $F\bar{4}3m$ space group. This short paper is written from a solid state chemist’s point of view, with an emphasis on crystalline materials and structural chemistry aspects.

2. Symmetry of order parameter of $Fd\bar{3}m \leftrightarrow F\bar{4}3m$ phase transition

The crystal structures of spinels, pyrochlores and Laves phases (C15) are characterized by the space group $Fd\bar{3}m$. The subject of our investigation is the ordered phases of these structural types with the $F\bar{4}3m$ space group. By using the concept of one critical irreducible representation (irrep) we will derive theoretically the structures of low-symmetry ordered cubic $F\bar{4}3m$ -phases from structures of high-symmetry disordered $Fd\bar{3}m$ -phases. The structure of low-symmetry $F\bar{4}3m$ -phase is determined by the ordering of atoms and their displacements in the initial (parent) structure. The structural mechanism of $F\bar{4}3m$ -phase formation is generated by critical and noncritical (improper) irreps of $Fd\bar{3}m$ space group.

The phases with $F\bar{4}3m$ symmetry can be generated by one-dimensional irrep $\kappa_{11}(\tau_4(A_{2u}))$ and can also be generated by two four-dimensional irreps $\kappa_9(\tau_1)$ and $\kappa_9(\tau_4)$ [7–10]. Below, we will only discuss the phase induced by the irrep $\kappa_{11}(\tau_4)$ of group $Fd\bar{3}m$. The expression $\kappa_j(\tau_i)$ means the star of wave vectors κ_j , where i is number of corresponding irrep τ for given star j [7]. Critical irrep $\kappa_{11}(\tau_4)$ determines the symmetry and structure of low-symmetry phase near point of phase transition.

The Wyckoff positions splitting takes place in the low-symmetry phase as a result of phase transition. To find the splitting of Wyckoff positions in the structure of the highly-symmetric phase it is necessary to analyze the composition of permutation and mechanical representations of high-symmetry structure. We have found that the critical one dimensional irrep $\kappa_{11}(\tau_4)$ enters into the mechanical representation on 16c, 16d, 32e, 48f Wyckoff positions and enters into the permutation representation on 8a, 8b, 32e, 48f Wyckoff positions [11–15].

Therefore the low-symmetry $F\bar{4}3m$ -phases formation is accompanied by simultaneous displacements of atoms spaced on 16c, 16d, 32e, 48f Wyckoff positions as well as by ordering of atoms spaced on 8a, 8b, 32e, 48f Wyckoff positions.

3. B_4 -clusters in A-ordered spinel structures

The structural formula of cubic centrosymmetric $Fd\bar{3}m$ -spinel AB_2X_4 is $(A)^{8a}[B_2]^{16d}X_4^{32e}$. The formation of a low-symmetry non-centrosymmetric $F\bar{4}3m$ -phase is accompanied by ordering of tetrahedral cations (1:1 order type) and anions (1:1 order type), and also by displacements of octahedral B-cations and anions. The calculated structure of the ordered $F\bar{4}3m$ -phase is shown in Fig. 1. The results of the calculations demonstrate that the tetrahedral cations in the ordered phase occupy nonvariant 4a and 4c Wyckoff positions (site symmetry $\bar{4}3m$). The octahedral cations are displaced by equal distances along the four threefold axes and occupy monovariant Wyckoff positions 16e with local symmetry 3m in the ordered structure (Figs. 1, 2). The free parameter x_1 is approximately equal to 0.675. It is interesting that the B-cations and anions form specific clusters (Fig. 2(a, c, e)). The anionic lattice is separated into two sublattices in the ordered phase. The anions occupy the 16c Wyckoff positions (site symmetry 3m). The anions' arrangement in each sublattice is described by the free parameters $x_2 \approx 0.875$ and $x_3 \approx 0.375$. The anions are displaced along the diagonals of the octants in the [111]-directions (Fig. 2a). It has been stated by calculation that general structural formula of the A-ordered spinel is $A^{14a}A^{4c}B_4^{16e}X_4^{16e}X_4^{16e}$ (Fig. 3) [16].

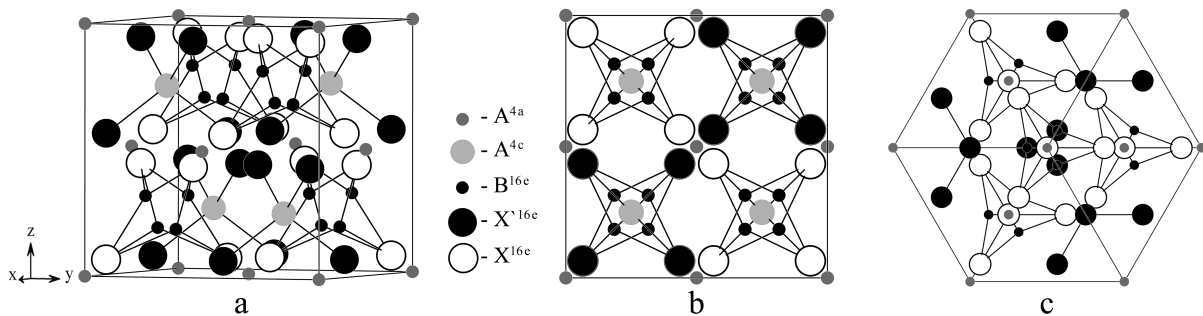


FIG. 1. Calculated structure of an A-ordered spinel (space group $F\bar{4}3m$). Atom presentation of the structure (a) and projections along (001) (b) and along (111) (c) of the ordered spinel structure

Features of the $F\bar{4}3m$ -phase structure are discussed in [14, 16]. The metal clusters are the most interesting feature of this structure. Two neighboring groups of octahedral cations and anions form the expanded (Fig. 2(c, d)) and contracted (Fig. 2(b, e)) regular tetrahedra. Net of such alternative tetrahedra (expanded and contracted) forms the unusual pyrochlore sublattice with two different B–B distances [16] (Fig. 3, Table 1). In the work [17] this was termed “breathing” pyrochlore sublattice. Also it is interesting that the structural feature of ordered phase is “breathing” ring of tetrahedra (Fig. 4).

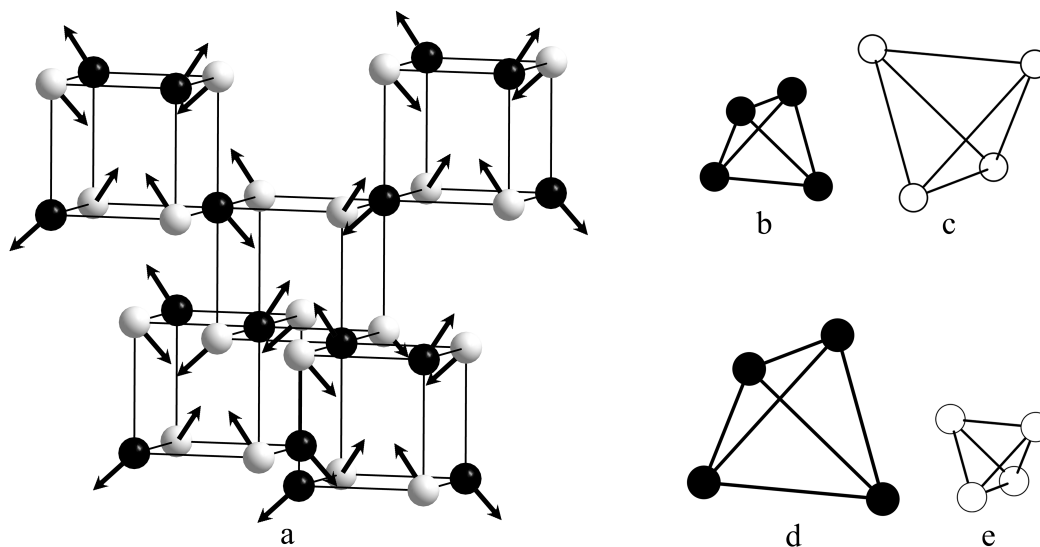


FIG. 2. Structural mechanism of atom cluster formation. Displacements of octahedral cations and anions in the adjacent octants of the spinel structure (a); compressed cluster B_4^{16e} (b), expanded cluster X_4^{16e} (c), expanded cluster B_4^{16e} (d) and compressed cluster X_4^{16e} (e)

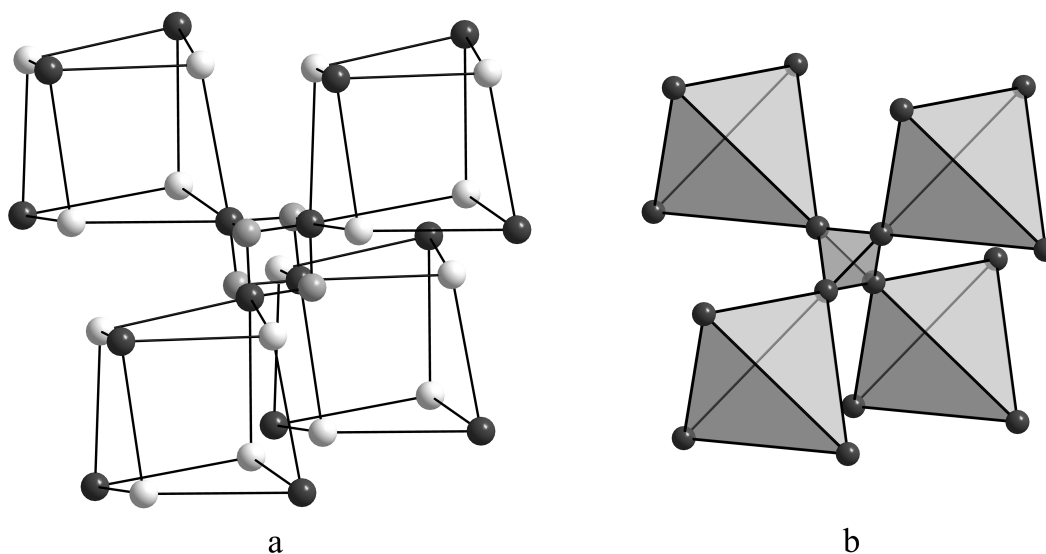


FIG. 3. Part of the crystal structure of spinel type with space group $F\bar{4}3m$ (a); expansion and contraction of the B_4 tetrahedra are overdrawn (b). The designation of atoms is the same as in Fig. 1

The expanded and contracted tetrahedra of B-cations are considered as a metal cluster. Contracted tetrahedra have the linear size $(2^{1/2}/4)a$ and are located in the distance $(6^{1/2}/4)a$, where a is the parameter of a cubic elementary cell of a spinel structure.

The chemical bonding between metal tetrahedra is realized with the help of bridge from two atoms X^{16e} (Fig. 5). This bond influences the correlation of electron movement and the participant in the hopping mechanism of electrical conductivity for A-ordered spinels.

Metal tetrahedra form hyper-tetrahedra (Fig. 6). The hyper-tetrahedra are formed by 4 B-tetrahedra. The hyper-tetrahedra formed by B-cations may participate in the formation of magnetic properties of the ordered phase.

Metal clusters were experimentally observed in ordered spinels $LiXY_4O_8$ ($X = Ga, Fe, In; Y = Cr, Rh$), Cr_4GaLiO_8 , Cr_4InLiO_8 , Rh_4InLiO_8 , $Ag_{0.5}In_{0.5}Cr_2S_4$ and $Cu_{0.5}In_{0.5}Cr_2S_4$ [18–20] and their existence, apparently, causes unusual magnetic properties of these compounds. If such metal clusters have a magnetic moment, then it

TABLE 1. Interatomic distances in the ordered structure of the spinel $A_{1/2}A'_{1/2}B_2X_4$

Atom pair	Distances	
	$F\bar{4}3m$ from $Fd3m$	$F\bar{4}3m$
A - X	$3^{1/2}(1/8 + \delta - d)$	$3^{1/2}(1 - x_2)$
A' - X	$3^{1/2}(1/8 + \delta - d)$	$3^{1/2}(x_2 - 1/4)$
A - X	$[19/64 + 3(\delta - d)^2 + 5/4(d - \delta)]^{1/2}$	$[3/2 + 3x_2^2]^{1/2}$
A' - X	$[11/64 + 3(\delta - d)^2 + 1/4(\delta - d)]^{1/2}$	$[11/16 - (3/2)x_2 + 3x_2^2]^{1/2}$
B - X	$[(1/4 - \delta + d - b)^2 + 2(d + b - \delta)^2]^{1/2}$	$[(x_2 - x)^2 + 2(x_2 + x - 1/2)^2]^{1/2}$
B - X	$3^{1/2}(1/4 + d - \delta - b)$	$3^{1/2}(x_2 - x)$
B - X	$[2(3/8 + \delta + d - b)^2 + (-1/4 + \delta + d - b)^2]^{1/2}$	$[2(x - x_1 - 1/2)^2 + (x - x_1)^2]^{1/2}$
A - A; A' - A'	$(1/2)2^{1/2}$	$(1/2)2^{1/2}$
A - A'	$(1/4)3^{1/2}$	$(1/4)3^{1/2}$
B - B	$2^{3/2}(1/8 - b)$	$2^{3/2}(3/4 - x)$
B - B	$2^{3/2}(1/8 + b)$	$2^{1/2}(2x - 1)$
X - X	$2^{3/2}(1/8 - \delta + x)$	$2^{1/2}(2x_2 - 1/2)$

Note: $x = 5/8 + b$; $x_1 = u + d$; $x_2 = 1/4 - u + d$, where b, d - displacements of B-cations and X-anions, $u = 3/8 + \delta$ - anion parameter (free parameter).

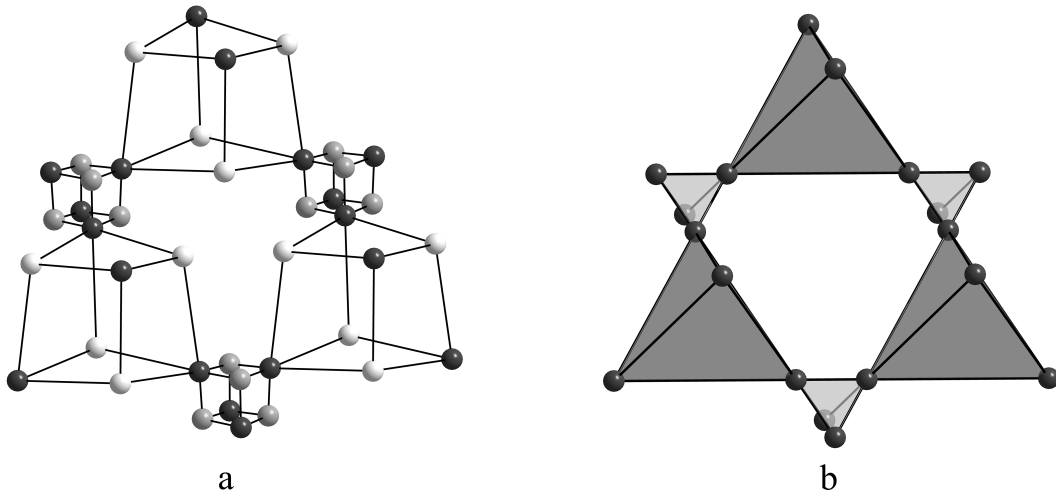


FIG. 4. B-cations in ordered spinel form “breathing” ring of tetrahedra. The designation of atoms is the same as in Fig. 1

is possible to expect that distribution of the magnetic moments on space of a crystal should be chaotic. In the results, the crystal which does not have a long ferromagnetic order, but has clusters with a certain degree of the local magnetic order, is formed. Such magnetic state is named spin glass. Thus, structural ordering of cations in spinel tetrahedral sites naturally causes an opportunity for the existence of a magnetic spin-glass state. In the case of magnetic interaction of metal tetrahedra unusual magnetic states of ordered spinels can be observed.

4. B_4 -clusters in some lacunar ordered spinel structures

The structure of some lacunar phases can be considered as a particular case of ordered spinel structures. The structure of these phases can be represented as a structure of defect spinels with the 1:1 ordering of cations in

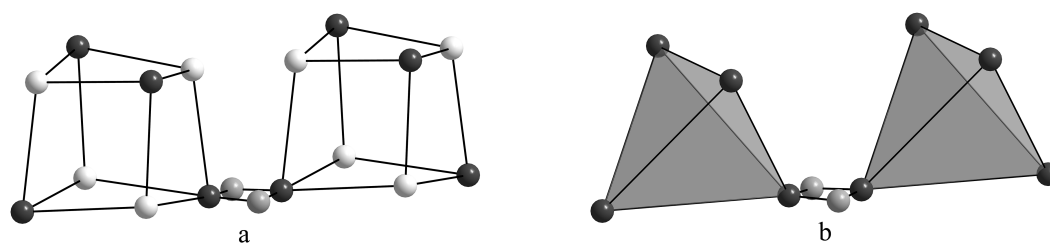


FIG. 5. The chemical bridge between two metal tetrahedra

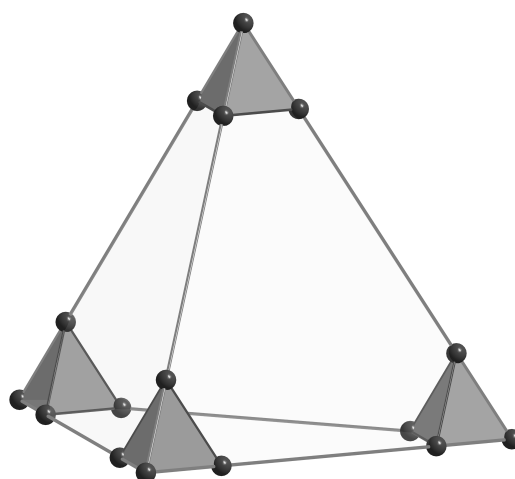


FIG. 6. The hyper-tetrahedra formed by B-cations

TABLE 2. The distribution of atoms in Wyckoff positions of some lacunar phases

Examples of the chemical compounds	Structural formula	Wyckoff positions of $\overline{F}43m$ -phase					References
		$A^{4(a)}$	$A^{4(c)}$	$B_4^{16(e)}$	$X_4^{16(e)}$	$X_4^{\prime 16(e)}$	
$\text{Re}_4\text{S}_4\text{Te}_4$	$B_4^{16e}X_4^{\prime 16e}X_4^{16e}$	\square	\square	Re_4	S_4	Te_4	[21,22]
$\text{Ga}_{1.33}\text{Cr}_4\text{S}_8$	$A^{\prime 4a}A^{4c}B_4^{16e}X_4^{\prime 16e}X_4^{16e}$	$\text{Ga}_{1.33} + \square$		Cr_4	S_4	S_4	[23–25]
GaMo_4O_8	$A^{4c}B_4^{16e}X_4^{\prime 16e}X_4^{16e}$	\square	Ga	Mo_4	O_4	O_4	[26,27]
$\text{Re}_4\text{As}_6\text{S}_3$	$A^{4c}B_4^{16e}X_4^{\prime 16e}X_4^{16e}$	\square	As	Re_4	As_4	AsS_3	[28]

tetrahedral sites. Therefore, the lacunar structures and their properties are inherently associated with the structure of A-ordered spinels. All varieties of possible compositions of lacunar phases are theoretically deduced from the structural formula of A-ordered defect spinel with space group $\overline{F}43m$ (Table 2). Lacunar phases of different types are obtained depending on the types of atoms that are absent in the structural formula of the A-ordered spinel. For example, Table 2 presents the experimentally revealed distributions of atoms on Wyckoff positions for some lacunar phases as particular cases of defect A-ordered spinel [21,22]. Defects in the table are designed by a symbol \square .

The lacunar structures “inherits” from the structure of the ordered spinel four types clusters, which have been established as a result of theoretical research of the structural mechanism of the spinel formation with the type 1:1 order in 8a and 32e Wyckoff positions (Section 3). There are two types of metal clusters – extended and compressed metal tetrahedra $B_4^{16(e)}$ and two types of extended and compressed anion clusters $X_4^{16(e)}$ and $X_4^{\prime 16(e)}$. We believe that the formation of these clusters is the main reason of the unusual physical properties of these phases. There are many experimental examples which confirm with the considered concept of the universal mechanism of cluster formation [21–28].

The Re_4 clusters in the $Re_4Te_4S_4$ (Fig. 7). The arrangement of the ReS_3Te_3 octahedra is the same as that in the BX_6 octahedra in the spinel structure AB_2X_4 , where A is a tetrahedrally coordinated metal atom and B is an octahedrally coordinated metal atom. According to our concept the B atom is at the centre of the BX_6 octahedron in the spinel structure, but the Re atom is shifted from the centre of the S_3Te_3 octahedron to form Re_4 cluster. The sites which are occupied by A atoms in the spinel structure are empty in $Re_4Te_4S_4$ structure (Table 1, Fig. 5). In this structure Re_4S_4 moieties are linked by bridging Te-groups. The part of rhenium atoms of this cluster may be replaced by molybdenum atoms, which lead to the formation of $Re_{4-x}Mo_x$ heterometallic cluster in $Re_{4-x}Mo_xS_4Te_4$ ($0 \leq x \leq 1.25$) structure [22,29].

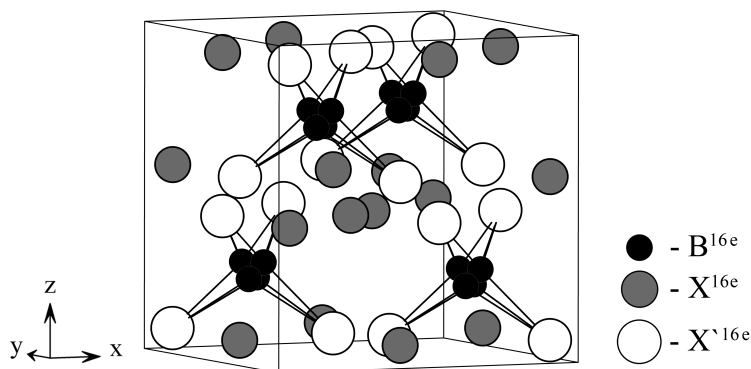


FIG. 7. The calculated structural motif of $Re_4S_4Te_4$ structure

The structure of the $Re_4S_4Te_4$ has been determined using X-ray diffraction [21,22]. The compound contains tetrahedral Re_4 clusters with the Re–Re distance of 2.785 Å [21]. The distance between the Re_4 clusters is equal to 4.345 Å [30]. The geometry and arrangement of these Re_4 clusters corresponds exactly to the B_4 -clusters arrangement on Figs. 1, 2. By introducing halogens into such rhenium-chalcogenide systems, related compounds, such as $Re_4Te_4(TeBr_2)_4Br_8$ [31] are obtained. It is interesting to note that the structure of $Re_4Te_4S_4$ is isotopic with those of the chalcogenohalides of niobium and molybdenum, $M_4X_4X'_4$ ($M = Nb, Mo; X = S, Se; X' = Cl, Br, I$) [21,32,33].

The Re_4 clusters in the $Re_4As_6S_3$ structure [28]. The $Re_4As_6S_3$ structure is isostructural to $GaMo_4S_8$ and may be written as $AsRe_4(As_{0.25}S_{0.75})_4As_4$ according to the family of compounds $AB_4X_4Y_4$. Anions in 32e Wyckoff position spinel splits into two 16-fold positions in the $F\bar{4}3m$ -phase. These two positions are occupied by the same atoms in the thio-spinel AB_2S_4 ; but they may also contain chemically different atoms in case of more general family of compounds with structural formula $AA'B_4X_4X'_4$. In $Re_4As_6S_3$, one of these positions is occupied entirely by arsenic atoms (IV) whereas the other contains a random mixture of sulfur and arsenic atoms (II) in a 3:1 ratio. As a consequence, the simple close packed anion lattice in the thio-spinels now consists of two distinct sublattices, producing a distorted close packed anion lattice (Fig. 8).

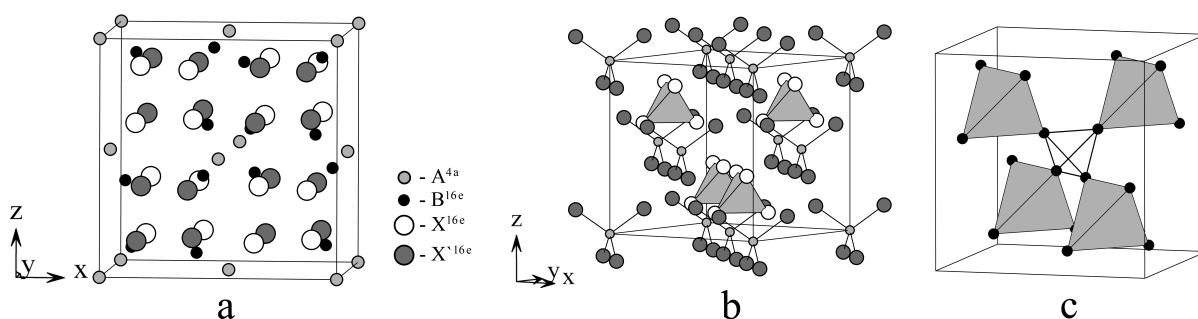


FIG. 8. Calculated low-symmetrical anion ordered spinel structure with the space group $F\bar{4}3m$ and with the structural formula $A^{4(a)}B_4^{16(e)}X_4^{16(e)}X'_4^{16(e)}$. Atom presentation of ordered spinel structures (a), tetrahedra in ordered spinel structure (b), $B^{16(e)}$ -metallic tetrahedral (nanoclusters) (c). A substance with composition $Re_4As_6S_3$ has a similar structure. In this structure there are Re_4 -clusters

The position of atom A in the spinel-type (previously the 8a position) splits into two different positions of multiplicity 4 each, one at (0, 0, 0), surrounded by four atoms from the first sublattice (in $\text{Re}_4\text{As}_6\text{S}_3$, 4 arsenic atoms), the other at (3/4, 3/4, 3/4), surrounded by 4 atoms from the second sublattice (in $\text{Re}_4\text{As}_6\text{S}_3$ 4 As/S atoms) [28]. A central arsenic is found in (0, 0, 0), producing an As_5 clusters. The atom B, in the ideal spinel at the octahedral site 16d (at 3/8, 3/8, 3/8), is moved out of its ideal position, shifting along the body diagonal of the unit cell (coordinates (x, x, x)). This produces different interatomic distances, allowing contacts with other atoms in symmetry-related B positions [28]. In $\text{Re}_4\text{As}_6\text{S}_3$, the rhenium atoms have short contacts at a distance of 2.776 Å [28].

The B_4 and $B_2B'_2$ clusters in lacunar AB_4X_8 spinels. The structural formula of these compounds is $A^{4a}B_4^{16e}X_4^{16e}X_4^{16e}$. The filling of half of the A sites with metal atoms gives the GaMo_4S_8 type of structure, which is found for AB_4X_8 (A = Ga, Al, Ge; B = V, Nb, Na, Mo; X = S, Se) (Fig. 9) and $\text{AMo}_2\text{Re}_2\text{S}_8$ (A = Zn, Fe, Co, Ni) [26,27].

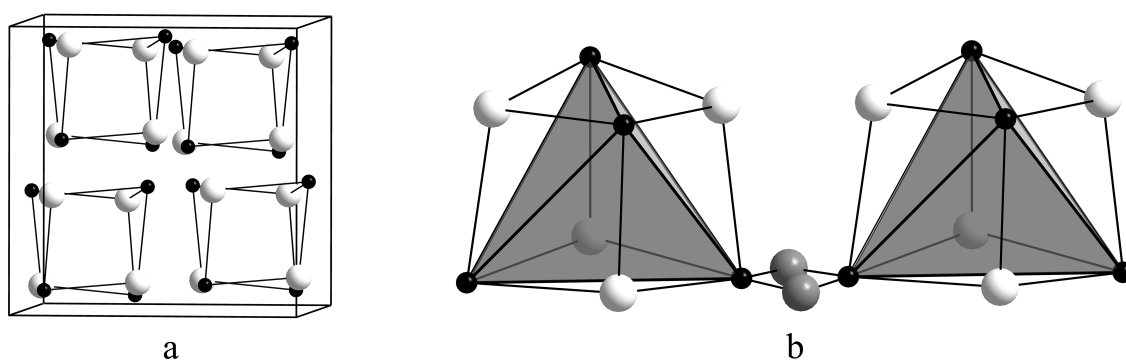


FIG. 9. Calculated crystal structure of the AB_4X_8 type compounds containing B_4^{16e} clusters (a), the bridge between two B_4^{16e} clusters mediated by two X^{16e} atoms (b)

The structure of these a cation-deficient ordered spinels consists of heterocubane-like $B_4X_4^{n+}$ units and AX_4^{n-} tetrahedra arranged in a similar manner to the ions in the rock-salt structure (Fig. 9(a)). The 8a site (0, 0, 0) of the spinel splits into sites 4a (0, 0, 0) and 4c (1/4, 1/4, 1/4) in $F\bar{4}3m$ -phase, where only 4a is occupied by atoms. The 16d site (5/8, 5/8, 5/8), occupied by the B atoms, becomes the 16e site (x, x, x) in $F\bar{4}3m$, which allows the B atoms in this site to dislocate along the body diagonal of the unit cell. Within these clusters the B–B distances are compatible with the formation of metallic bonds, while the large intercluster distances prevent metal-metal bonding. This peculiar topology leads to the formation of molecular-like electronic states within the clusters.

The formation of B_4 clusters causes significant changes in the physical properties. The metal electrons not incorporated in M–S bonds localize in cluster molecular orbitals. Because the clusters are widely separated, orbitals of different clusters do not overlap and the compound becomes nonmetallic. Electric conduction takes place in case the electrons hop between the clusters. These materials are Mott insulators, in which electrical conduction occurs by the hopping of electrons between clusters separated by relatively large distances (≈ 4 Å) and not between single atoms as in classical Mott insulators like NiO.

It has been suggested that GaV_4S_8 behaves as an electron glass at low temperatures, while GaNb_4S_8 as recently has been shown to undergo a pressure-induced transition to a superconducting state ($T_c \approx 4$ K at 23 GPa) [34]. The large separation of the tetrahedral metal B_4 clusters is believed to be the origin of strong electron correlations (Fig. 9(b)).

Recently, several correlation effects have been reported for AB_4X_8 lacunar spinels, including pressure-induced superconductivity [35], bandwidth-controlled metal-to-insulator transition [36, 37], large negative magnetoresistance [38], a two-dimensional topological insulating state [39], resistive switching through electric field-induced transition [40–42], emergence of orbitally driven ferroelectricity [43], and an extended Néel-type skyrmion phase [44].

Contrary to the spinel structure, the B atoms of the cubes shift toward the cube center creating a B_4 regular tetrahedral cluster with short metal-metal bond lengths (2.8 to 2.9 Å), and the B atoms of the other type cubes shift toward the cube outside, leading to the metal–metal distances of about 4 Å, which is too long to be considered as bonds.

Ordered spinels of $A_xB_2X_4$ type, where $A = Al, Ga, B = Mo, V, Cr$ and $X=S, Se$. The structural formula ordered spinels in this case is $A_{2x}\square_{2(1-x)}B_4^{16e}X_4^{16e}X_4^{16e}$. The examples of such type ordered spinels are $Ga_{0.67}Mo_2S_4$, $Ga_{0.5}V_2S_4$, $Al_{0.75}Mo_2S_4$ and $Ga_{0.67}Cr_2S_4$ [23–25]. According to our concept, B_4 -clusters are also in the structures of these substances.

5. B_4 -clusters in ordered Laves phases with $MgCu_4Sn$ structure type

The crystal structure of Laves phases can be either a cubic C15 ($MgCu_2$), hexagonal C14 ($MgZn_2$) or dihedral C36 ($MgNi_2$). The C15 phase has more than 1000 binary and ternary forms among the three types of Laves phases. The $MgCu_2$, type structure (Strukturbericht symbol C15) is face-centered cubic, belonging to the space group $Fd\bar{3}m$ with 8 formula units per non-primitive cubic unit cell. The A sublattice of the $MgCu_2$ has the structure of diamond net, while the B-sublattice can be described in terms of B-tetrahedra connected by their vertices. So far, more than 80 of such ordered compounds have been reported [45].

The structure formula of ordered Laves phases C15 may be obtained from structural formula ordered spinel $A'^{4a}A^{4c}B_4^{16e}X_4^{16e}X_4^{16e}$ if we will consider atoms positions X_4^{16e} and X_4^{16e} as vacant. The structural formula of the ordered Laves phases is $A'^{4a}A^{4c}B_4^{16e}$. The $A'^{4a}A^{4c}B_4^{16e}$ structure is presented as an example in Fig. 10. The B-atoms build up the three-dimensional network of slightly distorted corner-sharing B_4 -tetrahedra. The A and A' atoms fill larger cages with coordination number 16 (Frank–Kasper polyhedra [46, 47]) within this network. The small distortion of the B-tetrahedra is due to the difference in size between A and A' atoms [48]. For a more detailed discussion on the crystal chemistry and chemical bonding in such Laves phases we refer to review articles [49–51] and references which present there in.

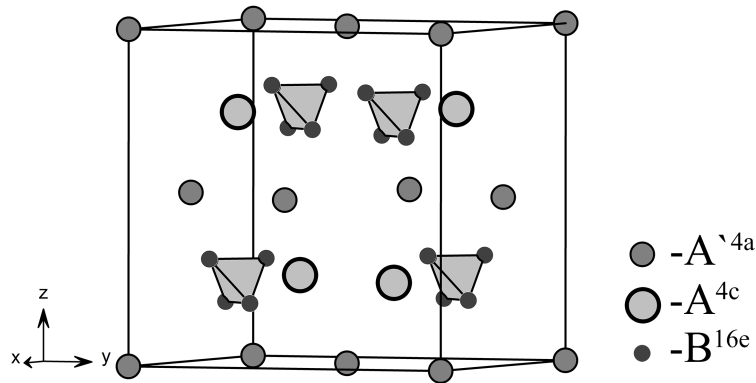


FIG. 10. The crystal structure of $A'^{4a}A^{4c}B_4^{16e}$ (the structural type of $MgCu_4Sn$). The three-dimensional network of corner-sharing B_4 -tetrahedra is emphasized

6. A_4 and B_4 -clusters in ordered pyrochlore structures

Compounds $A_2B_2O_6X$ with pyrochlore structure are notable for the significant variety of their physical properties: electric (semiconductors, metals, superionics), ferroelectric, magnetic (ferromagnetic), piezoelectric, catalytic. Recently in this family of materials superconductors with structures $Cd_2Re_2O_7$ ($T_c = 1$ K) and KOs_2O_6 ($T_c = 9.6$ K) were opened [52, 53]. Such a wide spectrum of properties is caused substantially by processes of the structural ordering of atoms.

The crystal structure of cubic pyrochlore-type oxides, which have the general formula $A_2B_2O_6X$, is composed of a framework of corner shared BO_6 octahedra. Here, the X site is partially or fully occupied by an oxygen atom. The space group of pyrochlore was originally suggested to be $Fd\bar{3}m$ [54, 55], in which the X site is randomly and partially occupied. Later investigation by a powder neutron diffraction experiment [56] showed that the space group is $F\bar{4}3m$; in this model vacancies in the X site are ordered. In $Fd\bar{3}m$ -pyrochlore structure $A_2^{16c}B_2^{16d}O_6^{48f}X^{8a}$ atoms occupy four nonequivalent crystallographic positions: cations A and B occupy 16c and 16d Wyckoff positions, and anions occupy 48f and 8a Wyckoff positions. The metal atoms forming clusters, occupy in pyrochlores, as well as in spinel, 16d Wyckoff positions of space group $Fd\bar{3}m$. Also, clusters are formed by atoms occupying 16c Wyckoff positions. The frustrated geometry arises from sublattices of corner-sharing tetrahedra, which are present for both the A and B cations.

We have made the prediction of the existence of a new type of cluster materials on the basis of pyrochlore family with the ordered arrangement of anions O and X (type of order 1:1); we have also submitted a calculated structure of pyrochlore (Fig. 11).

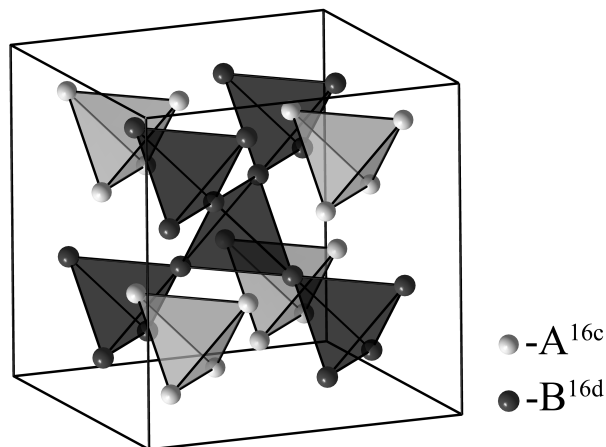


FIG. 11. A calculated elementary cell of pyrochlore, a network of B_4 - and A_4 -tetrahedra. Atoms in 48f and 8a Wyckoff positions are not shown

Metal clusters in the structure of ordered pyrochlore are formed due to displacement of cations in 16d and 16c Wyckoff positions. Thus, the theory predicts the existence of four types of metal clusters – compressed and expanded tetrahedra. These tetrahedra form two a three-dimensional network as it is schematically shown on Fig. 11. To explain the unusual physical properties of pyrochlore, it is essential to have direct interactions of metal – metal. These interactions are realized in two networks of A_4 - and B_4 -tetrahedra.

7. Summary

Various interesting phenomena concerning the spin, orbital and charge degrees of freedom on these sublattices have been observed in structures with pyrochlore sublattices caused by geometrical frustration. Typical examples are the Verwey transition in Fe_3O_4 [57,58], a heavy-fermion state in LiV_2O_4 [59], and a heptamer formation in AlV_2O_4 [60].

In this work we have established that the structural mechanism of B_4 -cluster formation in crystals with geometrically frustrated pyrochlore sublattices has universal character. The reason of universal character for B_4 -cluster formation is caused by the fact of one the same critical irreducible representation ($\kappa_{11}(\tau_4)$) which generates the same changes in the geometry of pyrochlore sublattices of high-symmetry $Fd\bar{3}m$ -phases. This conclusion has been illustrated for crystals that belong to different structural types.

We have also showed that cluster formation accompany changes in the geometry of pyrochlore sublattices – by appearance of two different B–B-distances. It is so called “breathing” pyrochlore sublattice which are in all structural types with low-symmetry $F\bar{4}3m$ space group. The “breathing” pyrochlore lattice must be an important factor to explore interesting phenomena in frustrated magnets.

We believe that to understand of the origin of magnetic and electrical properties in a given class of materials are important theoretical results as well (hypertetrahedron formation, bridges between tetrahedral metal clusters, “breathing” rings of tetrahedra).

Future tasks will be connected with investigation of the symmetry reduction from space group $Fd\bar{3}m$ to $F\bar{4}3m$ in pyrochlore family and the magnesium aluminum-chromium system with composition intermetallic compound $Mg_3Cr_2Al_{18}$ [61] more detailed.

Acknowledgements

The reported study was funded by RFBR, according to research project no. 16-32-60025 mol.a.dk (Talanov M. V.).

References

- [1] Sadoc J.F., Mosseri R. *Geometrical Frustration*. Cambridge: Cambridge University Press, 2006, 319 p.
- [2] Lacroix C., Mendels P., Mila F. *Introduction to Frustrated Magnetism. Materials, Experiments, Theory*. Springer-Verlag, Berlin, 2011, 128 p.
- [3] Ramirez A.P. *Handbook on Magnetic Materials*. Amsterdam: Elsevier Science, 2001, **13**, 423 p.
- [4] Anderson P. Ordering and Antiferromagnetism in Ferrites. *Phys. Rev.*, 1956, **102**, P. 1008–1013.
- [5] Bernal J.D., Fowler R.H. A Theory of Water and Ionic Solution, with Particular Reference to Hydrogen and Hydroxyl Ions. *J. Chem. Phys.*, 1933, **1**, P. 515–548.
- [6] Pauling L.J. The Structure and Entropy of Ice and of Other Crystals with Some Randomness of Atomic Arrangement. *Am. Chem. Soc.*, 1935, **57**, P. 2680–2684.
- [7] Kovalev O.V. *Representations of Crystallographic Space Groups. Irreducible Representations, Induced Representations and Co-representations*. London, Taylor and Francis Ltd., 1993, 390 p.
- [8] Talanov V.M., Shirokov V.B. Tilting structures in spinels. *Acta Cryst. A*, 2012, **68**, P. 595–606.
- [9] Talanov V.M., Shirokov V.B. Atomic order in spinel structure - a group-theoretical analysis. *Acta Cryst. A*, 2014, **70**, P. 49–63.
- [10] Talanov V.M., Shirokov V.B., Talanov M.V. Unique atom hyper-kagome order in $\text{Na}_4\text{Ir}_3\text{O}_8$ and in low-symmetry spinel modifications. *Acta Cryst. A*, 2015, **71**, P. 301–318.
- [11] Talanov V.M. Anion ordering in spinels. *Phys. Stat. sol. (a)*, 1989, **115**, K1–K4.
- [12] Talanov V.M. Calculation of Structural Parameters of Spinel. *Phys. Stat. sol. (a)*, 1981, **106**, P. 99–106.
- [13] Talanov V.M. Theoretical Grounds of the Natural Classification of Structure Types. *Kristallografiya*, 1996, **44** (6), P. 979–997; *Crystallogr. Rep.*, 1996, **44**, P. 929–946.
- [14] Talanov V.M. Structural Mechanism of Cluster Formation in Ordered Chalcogenide Spinel. *Phys. Chem. Glass*, 2005, **31**, P. 323–325.
- [15] Talanov M.V., Shirokov V.B., Talanov V.M. Phenomenological thermodynamics and the structure formation mechanism of the CuTi_2S_4 rhombohedral phase. *Phys. Chem. Chem. Phys.*, 2016, **18**, P. 10600–10606.
- [16] Talanov V.M. Structural mechanism of the ordering of ions in tetrahedral holes in spinels. *J. Struct. Chem.*, 1986, **2**, P. 172–176.
- [17] Okamoto Y., Nilsen G.J., Attfield J.P., Hiroi Z. Breathing Pyrochlore Lattice Realized in A-Site Ordered Spinel Oxides $\text{LiGaCr}_4\text{O}_8$ and $\text{LiInCr}_4\text{O}_8$. *Phys. Rev. Letters*, 2013, **110**, 097203(1–5).
- [18] Plumier R., Sougi M., Lecomte M. Observation of an unusual range magnetic ordering in spinel $\text{Cu}_{1/2}\text{In}_{1/2}\text{Cr}_2\text{S}_4$. *Phys. Rev. Letters A*, 1977, **60**, P. 341–344.
- [19] Plumier R., Lecomte M., Miedan-Gros A., Sougi M. Observation of a first order macro to microdomain transition in chalcogenide spinel $\text{Ag}_{1/2}\text{In}_{1/2}\text{Cr}_2\text{S}_4$. *Physica B*, 1977, **86–88**, P. 1360–1362.
- [20] Nauciel-Bloch M., Plumier R. Magnetic structure in spinel B-site lattice with ordered diamagnetic ions at the A-sites. *Solid State Communication*, 1971, **9**, P. 223–226.
- [21] Federov V.E., Mironov Y.V., et al. $\text{Re}_4\text{S}_4\text{Te}_4$. *Acta Crystallogr. C*, 1996, **52**, P. 1065–1067.
- [22] Fedorov V.Y., Mironov Y.V., et al. Cluster Transition Metal Chalcogenide Halides. *Russ. Chem. Rev.*, 2007, **76**, P. 529–552.
- [23] Brasen D., Vandenberg J.M., et al. Magnetic and Crystallographic Properties of Spinel of the Type $\text{A}_x\text{B}_2\text{X}_4$ where A = Al, Ga, and B = Mo, V, Cr. *J. Solid State Chemistry*, 1975, **13**, P. 298–303.
- [24] Barz H. New ferromagnetic molybdenum spinels. *Mater. Res. Bull.*, 1973, **8**, P. 983–988.
- [25] Okuda K., Noguchi S., Asano M., Endo S. Phase transitions of Mo-cluster compounds $\text{Ga}_{0.5}(\text{Mo},\text{Re})_2\text{S}_4$. *J. Magn. Magnetic Materials*, 1990, **90 & 91**, P. 148–150.
- [26] Ben Yaich H., Jegaden J.C., et al. Nou-veaux chalcogénures et chalcobalagénures à clusters tétraédriques Nb_4 ou Ta_4 . *J. Less-Common Met.*, 1984, **102**, P. 9–22.
- [27] Aminov T.G., Shabunina G.G., Busheva E.V., Novotortsev V.M. Magnetic properties of $\text{Co}_x(\text{Cu}_{0.5}\text{In}_{0.5})_{1-x}\text{Cr}_2\text{S}_4$ solid solutions. *Russian Journal of Inorganic Chemistry*, 2016, **61** (4), P. 461–469.
- [28] Besnard C., Svensson C., Stahl K., Siegrist T. $\text{Re}_4\text{As}_6\text{S}_3$, a thio-spinel-related cluster system. *J. Solid State Chemistry*, 2003, **172**, P. 446–450.
- [29] Fedorov V.E., Mironov Yu.V., et al. Chalcogenide clusters of Group 5 – 7 metals. *Russian Chemical Reviews*, 2007, **76**, P. 529–552.
- [30] Fedorov V.E., Mironov Yu.V., Fedin V.P., Mironov Yu.I. $\text{Re}_4\text{S}_4\text{Te}_4$. A new mixed rhenium chalcogenide containing a tetrahedral Re_4 cluster. *J. Struct. Chem.*, 1994, **35** (1), P. 146–147.
- [31] Schulz Lang E., Abram U., Strahle J. Synthese und Struktur von $\text{Re}_4(\mu_3\text{-Te})_4(\text{TeBr}_2)_4\text{Br}_8$. *Z. Anorg. Allg. Chem.*, 1996, **622**, P. 251–253.
- [32] Fedorov V.E., Naumov N.G., et al. Inorganic Coordination Polymers Based on Chalcocyanide Cluster Complexes. *J. Struct. Chem.*, 2002, **43**, P. 669–684.
- [33] Novotortsev V.M., Kalinnikov V.T., Aminov T.G. Spin glass state in multinary chromium compounds. *Russian Journal of Inorganic Chemistry*, 2005, **50**, P. 54–80.
- [34] Pocha R., Johrendt D., Ni B., Abd-Elmeguid M.M. Crystal Structures, Electronic Properties, and Pressure-Induced Superconductivity of the Tetrahedral Cluster Compounds GaNb_4S_8 , GaNb_4Se_8 , and GaTa_4Se_8 . *J. Am. Chem. Soc.*, 2005, **127** (24), P. 8732–8740.
- [35] Abd-Elmeguid M.M., Ni B., et al. Transition from Mott insulator to superconductor in GaNb_4Se_8 and GaTa_4Se_8 under high pressure. *Phys. Rev. Lett.*, 2004, **93**, 126403(1–4).
- [36] Ta Phuoc V., Vaju C., et al. Optical conductivity measurements of GaTa_4Se_8 under high pressure: Evidence of a bandwidth-controlled insulator-to-metal Mott transition. *Phys. Rev. Lett.*, 2013, **110**, 037401(1–5).
- [37] Camjayi A., Acha C., et al. First-order insulator-to-metal Mott transition in the paramagnetic 3D system GaTa_4Se_8 . *Phys. Rev. Lett.*, 2014, **113**, 086404(1–5).
- [38] Dorolti E., Cario L., et al. Halfmetallic ferromagnetism and large negative magnetoresistance in the new lacunar spinel GaTi_3VS_8 . *J. Am. Chem. Soc.*, 2010, **132**, P. 5704–5710.
- [39] Kim H.-S., Im J., Han M.J., Jin H. Spin-orbital entangled molecular jeff states in lacunar spinel compounds. *Nat. Commun.*, 2014, **5**, P. 3988–3995.

- [40] Dubost V., Cren T., et al. Resistive switching at the nanoscale in the Mott insulator compound GaTa₄Se₈. *Nano Lett.*, 2013, **13**, P. 3648–3653.
- [41] Stoliar P., Cario L., et al. Universal electric-field-driven resistive transition in narrow-gap Mott insulators. *Adv. Mater.*, 2013, **25**, P. 3222–3226.
- [42] Guiot V., Cario L., et al. Avalanche breakdown in GaTa₄Se_{8-x}Te_x narrow-gap Mott insulators. *Nature Commun.*, 2013, **4**, P. 1722–1728.
- [43] Singh K., Simon C., et al. Orbital ordering-driven multiferroicity and magnetoelectric coupling in GeV₄S₈. *Phys. Rev. Lett.*, 2014, **113**, 137602(1–6).
- [44] Kézsmárki S., Bordács Milde P., et al. Néel-type skyrmion lattice with confined orientation in the polar magnetic semiconductor GaV₄S₈. *Nat. Mater.*, 2015, **14**, P. 1116–1122.
- [45] Linsinger S., Eul M., et al. Structure, homogeneity ranges, magnetic, and electrical properties of the ordered Laves phases ReNi₄Mg with MgCu₄Sn type structure. *Intermetallics*, 2011, **19**, P. 1579–1585.
- [46] Frank F.C., Kasper J.S. Complex Alloy Structures Regarded as Sphere Packings. I. Definitions and Basic Principles. *Acta Crystallogr.*, 1958, **11**, P. 184–190.
- [47] Frank F.C., Kasper J.S. Complex alloy structures regarded as sphere packings. II. Analysis and classification of representative structures. *Acta Crystallogr.*, 1959, **12**, P. 483–499.
- [48] Emsley J. *The Elements*. Oxford University Press, Oxford, 1989, 256 p.
- [49] Nesper R. Bonding patterns in intermetallic compounds. *Angew. Chem.*, 1991, **30**, P. 789–817.
- [50] Johnston R.L., Hoffmann R. Structure-Bonding Relationships in the Laves Phases. *Z. Anorg. Allg. Chem.*, 1992, **616**, P. 105–120.
- [51] Nesper R., Miller G.J. A covalent view of chemical bonding in Laves phases CaLi_xAl_{2-x}. *J. Alloys Compd.*, 1993, **197**, P. 109–121.
- [52] Hanawa M., Muraoka Y., et al. Super-conductivity at 1 K in Cd₂Re₂O₇. *Phys. Rev. Lett.*, 2001, **87**, 187001(1–4).
- [53] Yamaura J.-I., Yonezawa S., Muraoka Y., Hiroi Z. Crystal structure of the pyrochlore oxide superconductor KOs₂O₆. *Journal of Solid State Chemistry*, 2006, **179**, P. 336–340.
- [54] Shah J.S., Hahn W.C. Material characterization of thick film resistor pastes. *IEEE Trans. Compon. Hybrides and Manuf. Technol.*, 1978, **303** P. 383–385.
- [55] Longo J.M., Raccach P.M., Goodenough J.B. Pb₂M₂O_{7-x} (M = Ru, Ir, Re) – preparation and properties of oxygen deficient pyrochlores. *Mat. Res. Bull.*, 1969, **4**, P. 191–202.
- [56] Beyerlein R.A., Horowitz H.S., et al. Neutron diffraction investigation of ordered oxygen vacancies in the defect pyrochlores, Pb₂Ru₂O_{6.5} and PbT₁Nb₂O_{6.5}. *Solid State Chem.*, 1984, **51**, P. 253–266.
- [57] Verwey E.J.W. Electronic Conduction of Magnetite (Fe₃O₄) and its Transition Point at Low Temperatures. *Nature (London)*, 1939, **144**, P. 327–328.
- [58] Senn M.S., Wright J.P., Attfield J.P. Charge order and three-site distortions in the Verwey structure of magnetite. *Nature (London)*, 2012, **481**, P. 173–176.
- [59] Kondo S., Johnston D.C., et al. LiV₂O₄: A Heavy Fermion Transition Metal Oxide. *Phys. Rev. Lett.*, 1997, **78**, P. 3729–3732.
- [60] Horibe Y., Shingu M., et al. Spontaneous Formation of Vanadium Molecules in a Geometrically Frustrated Crystal: AlV₂O₄. *Phys. Rev. Lett.*, 2006, **96**, 086406(1–4).
- [61] Samson S. The Crystal Structure of the Intermetallic Compound Mg₃Cr₂Al₁₈. *Acta Cryst.*, 1958, **11**, P. 851–857.



NANOSYSTEMS:

PHYSICS, CHEMISTRY, MATHEMATICS

INFORMATION FOR AUTHORS

The journal publishes research articles and reviews, and also short scientific papers (letters) which are unpublished and have not been accepted for publication in other magazines. Articles should be submitted in English. All articles are reviewed, then if necessary come back to the author to completion.

The journal is indexed in Web of Science Core Collection (Emerging Sources Citation Index), Chemical Abstract Service of the American Chemical Society, Zentralblatt MATH and in Russian Scientific Citation Index.

Author should submit the following materials:

1. Article file in English, containing article title, the initials and the surname of the authors, Institute (University), postal address, the electronic address, the summary, keywords, MSC or PACS index, article text, the list of references.
2. Files with illustrations, files with tables.
3. The covering letter in English containing the article information (article name, MSC or PACS index, keywords, the summary, the literature) and about all authors (the surname, names, the full name of places of work, the mailing address with the postal code, contact phone number with a city code, the electronic address).
4. The expert judgement on possibility of publication of the article in open press (for authors from Russia).

Authors can submit a paper and the corresponding files to the following addresses: nanojournal.ifmo@gmail.com, popov1955@gmail.com.

Text requirements

Articles should be prepared with using of text editors MS Word or LaTeX (preferable). It is necessary to submit source file (LaTeX) and a pdf copy. In the name of files the English alphabet is used. The recommended size of short communications (letters) is 4-6 pages, research articles– 6-15 pages, reviews – 30 pages.

Recommendations for text in MS Word:

Formulas should be written using Math Type. Figures and tables with captions should be inserted in the text. Additionally, authors present separate files for all figures and Word files of tables.

Recommendations for text in LaTeX:

Please, use standard LaTeX without macros and additional style files. The list of references should be included in the main LaTeX file. Source LaTeX file of the paper with the corresponding pdf file and files of figures should be submitted.

References in the article text are given in square brackets. The list of references should be prepared in accordance with the following samples:

- [1] Surname N. *Book Title*. Nauka Publishing House, Saint Petersburg, 2000, 281 pp.
- [2] Surname N., Surname N. Paper title. *Journal Name*, 2010, **1** (5), P. 17-23.
- [3] Surname N., Surname N. Lecture title. In: Abstracts/Proceedings of the Conference, Place and Date, 2000, P. 17-23.
- [4] Surname N., Surname N. Paper title, 2000, URL: <http://books.ifmo.ru/ntv>.
- [5] Surname N., Surname N. Patent Name. Patent No. 11111, 2010, Bul. No. 33, 5 pp.
- [6] Surname N., Surname N. Thesis Title. Thesis for full doctor degree in math. and physics, Saint Petersburg, 2000, 105 pp.

Requirements to illustrations

Illustrations should be submitted as separate black-and-white files. Formats of files – jpeg, eps, tiff.



NANOSYSTEMS:

PHYSICS, CHEMISTRY, MATHEMATICS

Журнал зарегистрирован

Федеральной службой по надзору в сфере связи, информационных технологий и массовых коммуникаций

(свидетельство ПИ № ФС 77 - 49048 от 22.03.2012 г.)

ISSN 2220-8054

Учредитель: федеральное государственное автономное образовательное учреждение высшего образования

«Санкт-Петербургский национальный исследовательский университет информационных технологий, механики и оптики»

Издатель: федеральное государственное автономное образовательное учреждение высшего образования

«Санкт-Петербургский национальный исследовательский университет информационных технологий, механики и оптики»

Отпечатано в Учреждении «Университетские телекоммуникации»

Адрес: 197101, Санкт-Петербург, Кронверкский пр., 49

Подписка на журнал НФХМ

На первое полугодие 2018 года подписка осуществляется через

ОАО Агентство «Роспечать»

Подписной индекс 57385 в каталоге «Издания органов научно-технической информации»